Analysis and Synthesis of a Planar Reconfigurable Mechanism with a Variable Joint

Peter William Malak
Marquette University

ANALYSIS AND SYNTHESIS OF A PLANAR RECONFIGURABLE MECHANISM WITH A VARIABLE JOINT

by

Peter W. Malak, B.S.

A Thesis submitted to the Faculty of the Graduate School,
Marquette University,
in Partial Fulfillment of the Requirements for
the Degree of Master of Science

Milwaukee, Wisconsin

August 2016

ABSTRACT
ANALYSIS AND SYNTHESIS OF A PLANAR RECONFIGURABLE MECHANISM WITH A VARIABLE JOINT

Peter W. Malak, B.S.

Marquette University, 2016

Currently, there is a demand for mechanisms with variable topology that can perform multiple tasks with the least amount of actuators. These devices have the ability to provide numerous motion profiles within one device. In the following thesis, a specific planar reconfigurable mechanism with a kinematic reconfigurable joint was mathematically modeled. This mechanism functions as a RRRP mechanism in one configuration and as a RRRR in the other and is known as a RRRR-RRRP Mechanism. The kinematics and kinetics of the RRRR-RRRP Mechanism were analyzed with a Lagrangian approach. The models are simulated and verified using a trajectory planner and control system. In order to verify the effectiveness of the models, a prototype driven by a geared DC motor was constructed. The RRRR-RRRP Mechanism was experimentally tested by changing the starting position and velocity. The experimental angular position of each joint on the Mechanism was compared to the models position analysis. The error was found to be in an acceptable range. The resulting models can be used to improve RRRR-RRRP Mechanism design and analysis. A suite of design tools was created based on the previously generated models.

ACKNOWLEDGMENTS

Peter W. Malak, B.S.

I would like to thank my mom, dad, and siblings Matthew and Hanna for their continued support. I would like to thank Shaoli Wu, Tony Buchta, and Clark Andrews for the great discussions. I would also like to thank my committee members, Dr. Mark Nagurka and Dr. Brian Slaboch, and advisor Dr. Philip Voglewede for always pushing me to be a better person and engineer. My thanks also go to the Graduate School and all of the Marquette University administration for guiding me through this process. Finally and foremost, I would like to thank my fiancé Rachel for her encouragement, patience, and unwavering love.

DEDICATION

I would like to dedicate this work to my ever-supporting family and friends. In addition, this is written in memory of one of the best engineers I have ever known, Girard Zimmerman.

TABLE OF CONTENTS

LIST OF TABLES

LIST OF FIGURES

CHAPTER 1

INTRODUCTION

1.1 Motivation

There is a demand for mechanisms with low cost and weight that can perform multiple tasks with the least number of actuators. For example, these mechanisms can be used in manufacturing applications, robotic end effectors, medical equipment and devices, tools, space exploration and industrial automation. These mechanisms must have the ability to produce complex motion profiles without adding degrees of freedom (DOF) and/or redundant actuation. Reconfigurable mechanisms are a way to fill this void. In this context, reconfigurable mechanisms are defined as a mechanism that has the ability to achieve different motion profiles within one mechanism. Reconfigurable mechanisms as a whole will be discussed in the literature review.

1.2 Problem Statement

The current problem with reconfigurable mechanisms is that only limited theoretical framework has been developed for analysis and synthesis. Often times these mechanisms are developed ad-hoc [3]. Some researchers have tried to focus on the synthesis of kinematically reconfigurable joints (KRJ) or variable joints and how they are a viable method for better understanding reconfigurable mechanisms [1]. This area will be examined in the thesis. The thesis will focus on the analysis and synthesis of a specific type of KRJ in a reconfigurable mechanism. Through the analysis of a specific reconfigurable mechanism, the goal is to establish a more complete framework for synthesis that enables practical reconfigurable mechanisms to be created. The research consists of two

different distinct areas. The first area is analysis of reconfigurable mechanisms and the second is synthesis of reconfigurable mechanisms. Through the work in the first area, it is expected that a specific set of techniques will be developed for analyzing and developing a mathematical model for reconfigurable mechanisms. Once these analysis techniques are known, reconfigurable mechanisms can be better synthesized. They will be able to be created (i.e., synthesized) more efficiently due to the knowledge gained through the analysis.

The research will focus on one specific planar reconfigurable mechanism with a KRJ [1]. This mechanism functions as a RRRR[1] mechanism in one configuration and as a RRRP[2] mechanism in another. An example of a RRRR mechanism is a crank rocker mechanism depending on the physical configuration. An example of a RRRP mechanism is a crank slider mechanism depending on the physical configuration. The reconfigurable mechanism with a KRJ will be referred to as the RRRR-RRRP Mechanism, or as the Mechanism for short, in the rest of the thesis. The Mechanism is shown in Figure 1.1. The RRRR-RRRP Mechanism was developed to complete two rigid body guidance tasks within a single mechanism for a specific pick and place type of industrial application [1]. The design goal is to be able to replace a two degree of freedom (DOF) automation application with the Mechanism; the RRRR-RRRP Mechanism only uses one actuator to achieve this specific complex motion profile.

The research provides insight into an understudied field that is reconfigurable mechanism analysis and synthesis. Through understanding of the RRRR-RRRP Mechanism a suite of tools will be developed for examining and designing future RRRR-RRRP Mechanisms. The research will uncover the different analysis techniques that are most appropriate for RRRR-RRRP

[1]R- Represents a revolute joint
[2]P- Represents a prismatic joint

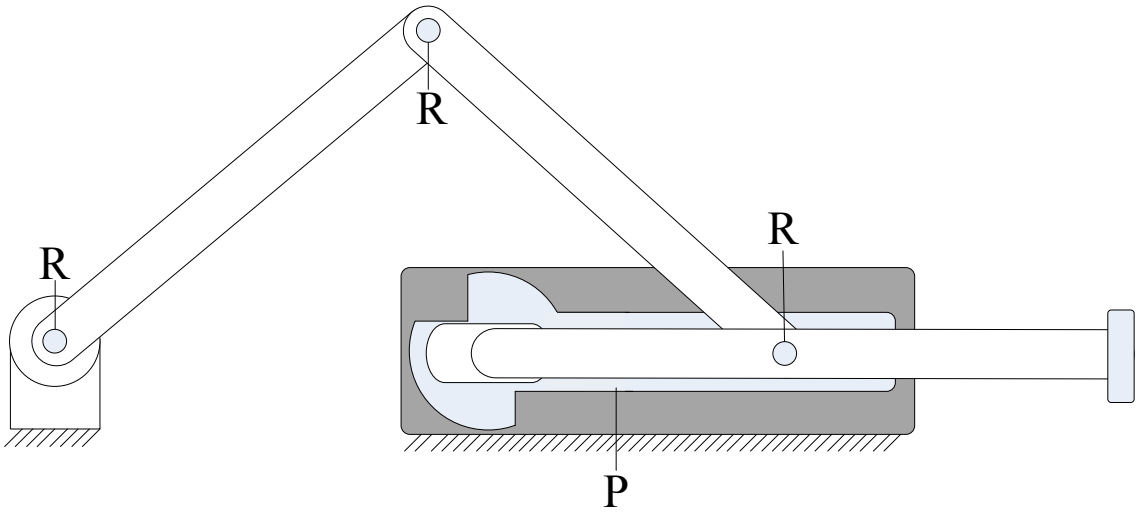

Figure 1.1: RRRR-RRRP Mechanism

Mechanisms first. These techniques will then lead to the design tools for future RRRR-RRRP Mechanisms. Understanding one specific reconfigurable mechanism in detail could lead to the development of a larger suite of tools for designing future reconfigurable mechanisms. This is the ultimate goal of this research.

1.3 Organization

The thesis is organized as follows. Chapter 2 outlines reconfigurable mechanisms and examines relevant literature. Chapter 3 completes a mechanism analysis of the RRRR-RRRP Mechanism. In addition, the RRRR-RRRP Mechanism is simulated using the developed analytical Model in Matlab and SimMechanics. Chapter 4 examines the system as whole and simulates the motion of the Mechanism. Chapter 5 outlines the experimental results of the prototype of the Mechanism. Chapter 6 compares the simulation and experimental prototype results. Chapter 7 provides analysis and design tools future RRRR-RRRP Mechanisms. Chapter 8 draws conclusions and suggestions for future work. Appendix A supplies a detailed mechanical derivation of the

RRRR configuration. Appendix B provides a detailed mechanical derivation of the RRRP configuration. Appendix C demonstrates a detailed examination of the plant modeling of the Mechanism including individual motor modeling. Appendix D outlines the experimental data gathered from the prototyped Mechanism.

CHAPTER 2

LITERATURE REVIEW

2.1 Introduction

As stated previously, there is a demand for mechanisms with low cost and weight that can perform multiple tasks with the least number of actuators. For example, these mechanisms can be used in manufacturing applications, robotic end effectors, medical equipment and devices, tools, space exploration and industrial automation. These mechanisms must have the ability to produce complex motion profiles without adding degrees of freedom (DOF) and/or redundant actuation. Reconfigurable mechanisms are a way to fill this void.

The chapter is outlined as follows. First, a classification of reconfigurable mechanisms is discussed. Second, a brief history of reconfigurable mechanisms is presented. Finally, current reconfigurable mechanism research is presented and examined from two different views. The first is analysis and the second synthesis.

2.2 Reconfigurable Mechanism Classifications

Reconfigurable mechanisms can now be categorized in the following groups per Slaboch[1]: kinematotropic mechanisms [4, 5, 6, 7, 8], metamorphic mechanisms [3] and mechanisms with variable topology (MVTs) [9]. Classifications of mechanisms allow researchers to apply different analysis and synthesis techniques easier. If one technique works on a specific mechanism in a classification it may potentially work on a different mechanism of the same classification. While the classifications are close, there are small differences between them. Kinematotropic mechanisms are defined as:

> "Mechanisms that, in passing a singularity position (in which a certain transitory infinitesimal mobility is attained) these mechanisms permanently change their global mobilities." [4]

Metamorphic mechanisms are:

> "A mechanism whose number, the total of all effective links, changes as they move from one configuration to another or a singular condition makes it behave differently." [3]

A Mechanisms with Variable Topology:

> "is a mechanism whose topology changes during operation." [9]

2.3 Brief History of Reconfigurable Mechanisms

Reconfigurable mechanisms can be found throughout history (the Chu state repeating crossbow dates back to the fourth century BC [4]), but only recently has the design process been more formalized. In the early 1990s, engineers needed innovative ways to solve complex spatial problems. For example, Gosselin focused on workspace analysis of mechanisms and Wohlhart examined kinematotropic linkages [10, 11, 12, 5]. In addition, Dai and others were starting to examine metamorphic mechanisms in coordination with mobility [3]. The need to solve the complex spatial problems has spawned a multitude of work into reconfigurable mechanisms.

In the early 2000s, Howell led the research on synthesis of compliant mechanisms [13]. Yan et al. introduced mechanisms with variable topology in 2001 [12]. In addition, Galletti and Fanghella demonstrated how to generate single-loop kinematotropic mechanisms [7]. In 2006, Kuo presented how to use graph theory and generalized transition pairs. These were used to form a semi-automated procedure in synthesizing new mechanisms [14]. Murray and Schmiedeler explored shape changing mechanisms in 2008 [15].

2.4 Current Reconfigurable Mechanism Research

Current reconfigurable mechanism research can be split into two distinct categories: analysis and synthesis. Mechanism analysis is the process of decomposing a mechanism and examining its topology. Many have tried to develop methods for classification of mechanisms based on topology. These will be explored. In addition, a mechanism's kinematics and kinetics are explored. These are absolutely necessary for controlling a device effectively. In addition, through the derivation of kinematics and kinetics of a mechanism design insights can be made. For example, if one mechanism is analyzed and is modeled effectively those design analysis methods could be applied to other reconfigurable mechanisms.

Synthesis is the process of creating a new mechanism based on external constraints. While analysis and synthesis are distinct research areas, their results cross over. For example, an analysis technique could lead the development of a new synthesis technique [16]. This is consistent with other research fields. In this research, a mechanism is first analyzed and a set of analysis and design tools are developed. These design tools could be used to develop future mechanisms. Understanding the motion and forces acting on a mechanism will allow the designer to select the appropriate motor or link lengths.

Two different conference series have helped drive reconfigurable mechanism design. The first is the ASME International Design and Engineering Technical Conferences (IDETC) - Mechanisms and Robotics (MR) conference series and the second Reconfigurable Mechanisms and Robotics (ReMAR) conference series. Numerous works have arisen out of these conferences and will be referenced in the following paragraphs.

2.4.1 Current Analysis Techniques

Within analysis of reconfigurable mechanisms, there are specific sub-sections. The two main sub-sections are reconfigurable mechanism structure decomposition and reconfigurable mechanism kinematic and kinetic analysis. Mechanism structure decomposition is a method for expressing a mechanisms topology characteristics in matrix form. For example, a reconfigurable four bar mechanism could be represented with a matrix. The advantage of analyzing a mechanism as a matrix is to remove the complexity of reconfigurable joints and identify isomorphisms. In addition, the matrix representation strips down the mechanism to the fundamental kinematics to allow a more understanding in analysis.

Slaboch and Voglewede [17], Yan and Kuo [14, 18, 19, 20], Dai and Jones [21], and Lan and Du [22] have used matrix notation to complete representation of topological configurations. Each of the groups presents different theories on which representation is the best. Slaboch and Voglewede combine all of the previous representations to create Mechanism State Matrices [17]. Mechanism State Matrices have since been referenced in other publications and are becoming more commonplace. Mechanism structure decomposition is an active area of research but is not the focus of the thesis [23].

Kinematics is the study of mechanics concerned with the motion of objects without reference to the forces that cause the motion [24]. Kinetics is the study of mechanics concerned with forces and torques acting on an object [24]. Reconfigurable mechanism kinematic and kinetic analysis is the study of kinematics and kinetics in the context of reconfigurable mechanisms. Currently, it is difficult to quantify the transition point in reconfigurable mechanisms.

An example of reconfigurable kinematic analysis can be found in a reconfigurable mechanism that can provide pure translation and pure rotation. The researchers developed a reconfigurable Hooke Joint [25]. The reconfigurable Hooke Joint is different from the classical Hooke Joint in the fact that it can be reconfigurable by changing the direction of the radial axis. The researchers used screw theory to understand the motion/force transmission through the mechanism. Six different reconfigurable Hooke Joints are used to create a mechanism that is very similar to a Stewart-Gough Platform. Using screw theory is one approach to analyzing a reconfigurable mechanism.

Another idea is to separate a reconfigurable mechanism into individual lower pair joints and analyze the mechanism separately [26]. This concept will be examined in the current research. The kinematics and kinetics optimal approach is still unknown and will be examined in further detail in the thesis.

2.4.2 Current Synthesis Techniques

Other researchers have focused on the synthesis of reconfigurable mechanisms and have used the structure decomposition analysis technique to continue this. Yang et al. [27] demonstrated how to use a genetic algorithm approach to decide an optimal reconfigurable mechanism. Ma et al. [28] demonstrated how to use characteristic matrices to generate new designs. All of these methods are complex and require in-depth knowledge of mechanism analysis techniques and matrix representation. In addition, these synthesis techniques rely on the classic lower and higher pairs.

Critical to the design of many reconfigurable mechanisms is the use of variable joints. In 2006, Yan and Kuo [19] first introduced variable joints which have the ability to change either their representation or kinematic pair with respect to a local coordinate frame. Slaboch and Voglewede continued work on

variable joints publishing several related papers [1, 17]. Slaboch proposed profile synthesis of variable joints that change from rotational to translational motion. Once the profiles of the joints have been determined, the joints can be used to create new reconfigurable mechanisms. This type of synthesis work was novel, and the synthesized joint profiles are intended to help in the reconfigurable mechanism synthesis process. Ultimately a new variable joint was designed by Slaboch and Voglewede. This new joint and corresponding mechanism is the topic of the current research.

CHAPTER 3

MECHANISM ANALYSIS

3.1 Introduction

As stated in Chapter 1, this thesis investigates the analysis and synthesis of reconfigurable mechanisms. The focus of this chapter will be on the analysis. Specifically, the analysis of the RRRR-RRRP Mechanism, referenced Figure 1.1. The Mechanism was developed to complete two rigid body guidance tasks within a single mechanism [1]. This approach allows the mechanism to be able to provide unique rotational and translational motion with one actuator.

As discussed in Chapter 2, there are several analysis techniques that have been applied to reconfigurable mechanisms. A classical approach will be taken with the Mechanism. The Mechanism will be considered in two different configurations for the analysis purposes. First, the mechanism will be examined in a RRRR configuration and then in a RRRP configuration. This technique was chosen because the Mechanism functions in these specific configurations depending on the location of the slider. The biggest area this technique does not account for is the Transition Point. The Transition Point is when the Mechanism changes from the RRRR configuration to the RRRP configuration or vice versa.

This chapter will include the following topics. First, a specific problem using the RRRR-RRRP Mechanism is presented. Next, the kinematics of the RRRR and RRRP configurations are determined. Then using the kinematics of each configuration, the kinetics of each configuration were solved using a Lagrangian dynamics approach. The equations of motion (EOM) were developed from the hand calculated equations for each configuration [26]. The EOM models are necessary to fully understand the geometric motions and forces. Through

understanding the forces on the Mechanism, a motor can be appropriately sized and the links can be sized to withstand the forces applied. In addition, the individual EOM models will be needed for modeling the physical Mechanism as a whole with a motor attached. The combination of the two EOM models and a motor model will be known as the Plant Modeling and is completed in Chapter 4. Finally, each individual EOM model was verified for accuracy. Within any hand derivation of dynamics, there are numerous opportunities for error. For example, ensuring the signs are correct in the derivation. Verification is necessary to ensure accuracy of the dynamics and was completed used SimMechanics, a multi-body dynamics solver.

3.2 Specific Problem Setup

The design of the RRRR-RRRP Mechanism was motivated by a hypothetical manufacturing application [1]. The goal of the manufacturing application is to apply a bonding agent to a part (Component A) and then rotate it 90 degrees to adhere it to a different component (Component B). The result is an assembly with two components glued together. An example of the physical configuration of the process is shown in Figure 3.1. This setup was modified from Slaboch and Voglewede's work [1]. The use of the Mechanism in this application will only use one actuator to complete the necessary motion profile. Comparatively, the procedure would normally take two actuators to complete the task using a gantry or other robotic system.

Figure 3.2 shows the Mechanism in various configuration states necessary to complete the manufacturing application. The process requires the glued assembly of Component A to Component B. The following steps must be taken in order to properly adhere Component A to Component B. An even layer of a bonding agent must be applied to Component A by a dispenser that is at a height

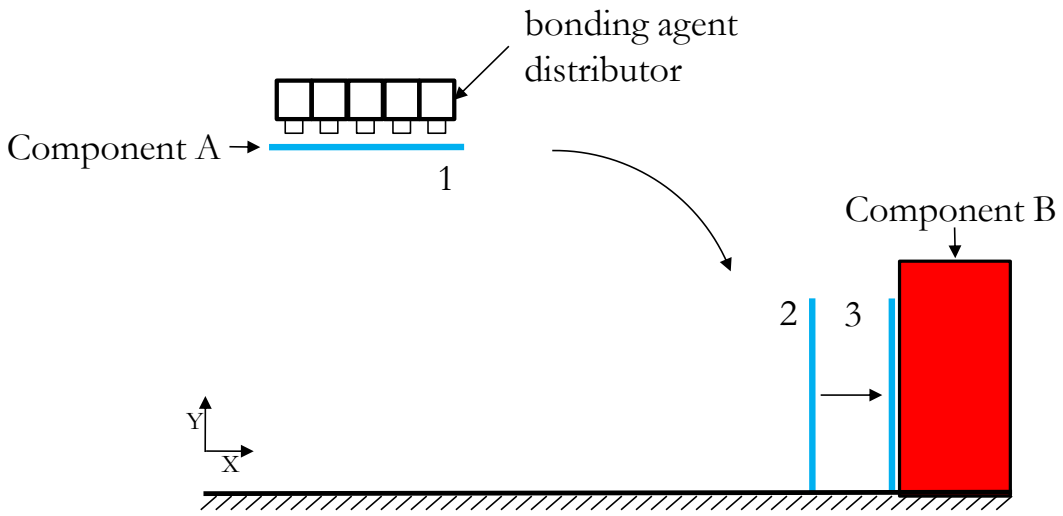

Figure 3.1: Manufacturing Application (Adapted from [1])

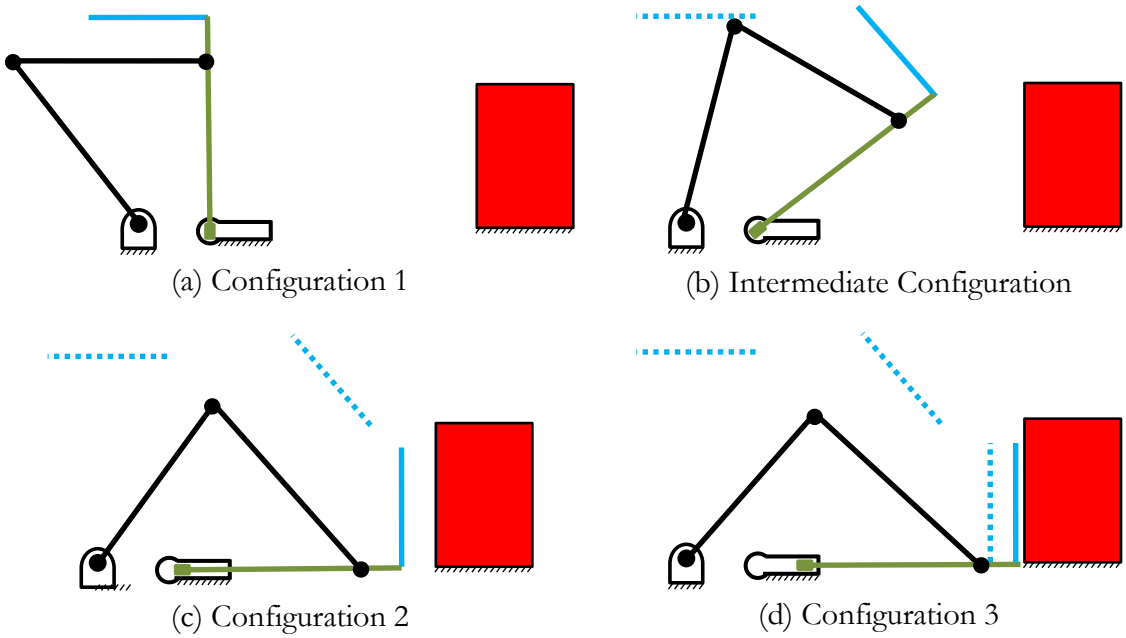

Figure 3.2: Manufacturing Application: Mechanism's Motions (Adapted from [1])

above the ground. Distributing the bonding agent in the vertical orientation allows for a uniform application of the bonding agent to Component A. Component A must be moved from Configuration 1 to Configuration 2 where it will be able to slide a distance. This allows Component A to make even surface contact with Component B as shown in configuration 3. This process must be automated to ensure speed and the accuracy of the manufacturing operation [29].

The discussed task could use two actuators to complete the task using a gantry or other robotic system. For example, two pneumatic slides could be used to move vertically and translate horizontally. However, using the Mechanism only one actuator is necessary. In addition, the Mechanism allows for complex motions not possible by a conventional four-bar mechanism. The use of the Mechanism adds complexity to the joints but simplifies the overall mechanism. All of these things drive the use of the Mechanism.

3.3 Kinematics

Kinematics is the geometry of motion [24]. Understanding the Mechanism's kinematics is vital to being able to predict and control the Mechanism at any input angle or velocity. The Mechanism (shown in Figure 3.3) is a one degree of freedom system. If the input angle and velocity (θ, $\dot{\theta}$) are known, the positions and velocities of all the other links in the Mechanism can be found. The kinematics are necessary and will be used to understand the dynamics of the system. In the following sections a planar position and velocity analysis of the Mechanism in the RRRR and RRRP configuration will be completed.

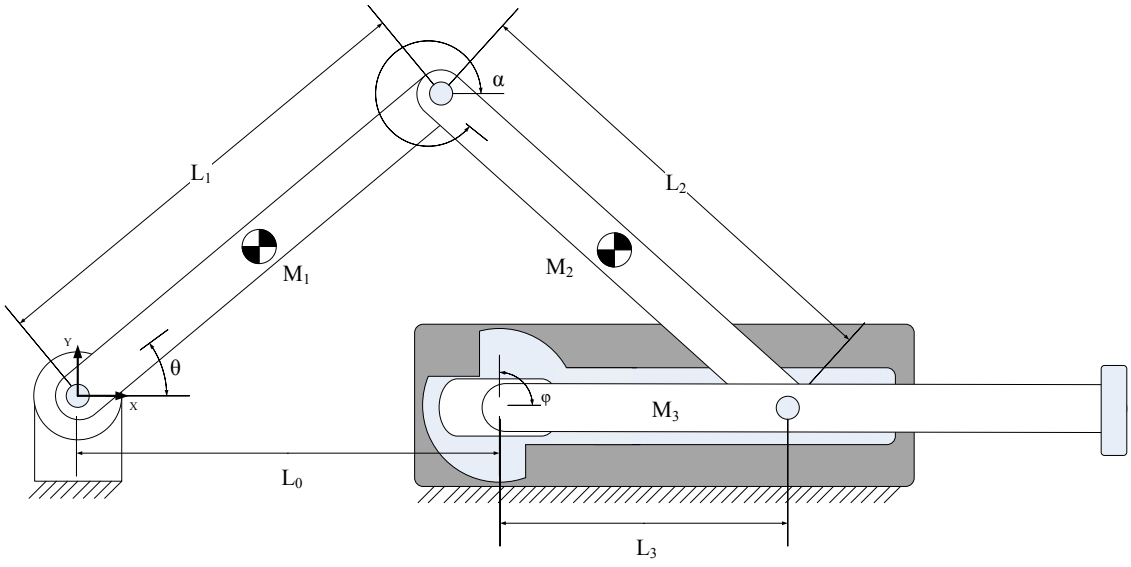

Figure 3.3: RRRR-RRRP Mechanism

3.3.1 Position Analysis

First, the positional analysis will be completed. This will provide insight into the angular position and locations of the links and slider in space. A fixed coordinate system following right hand rule is located at the left revolute joint shown in Figure 3.3 and is denoted with an XY arrows. The system will be analyzed in two dimensional (2D) space in the XY-plane. Overall, the kinematics require extensive manipulation of equations but are necessary for properly understanding the Mechanism. Rather than showing all, Appendix A and Appendix B contain a complete step by step derivation of the positional kinematics for the RRRR and RRRP configurations, respectively. Only the final positional equations have been provided in the following sections.

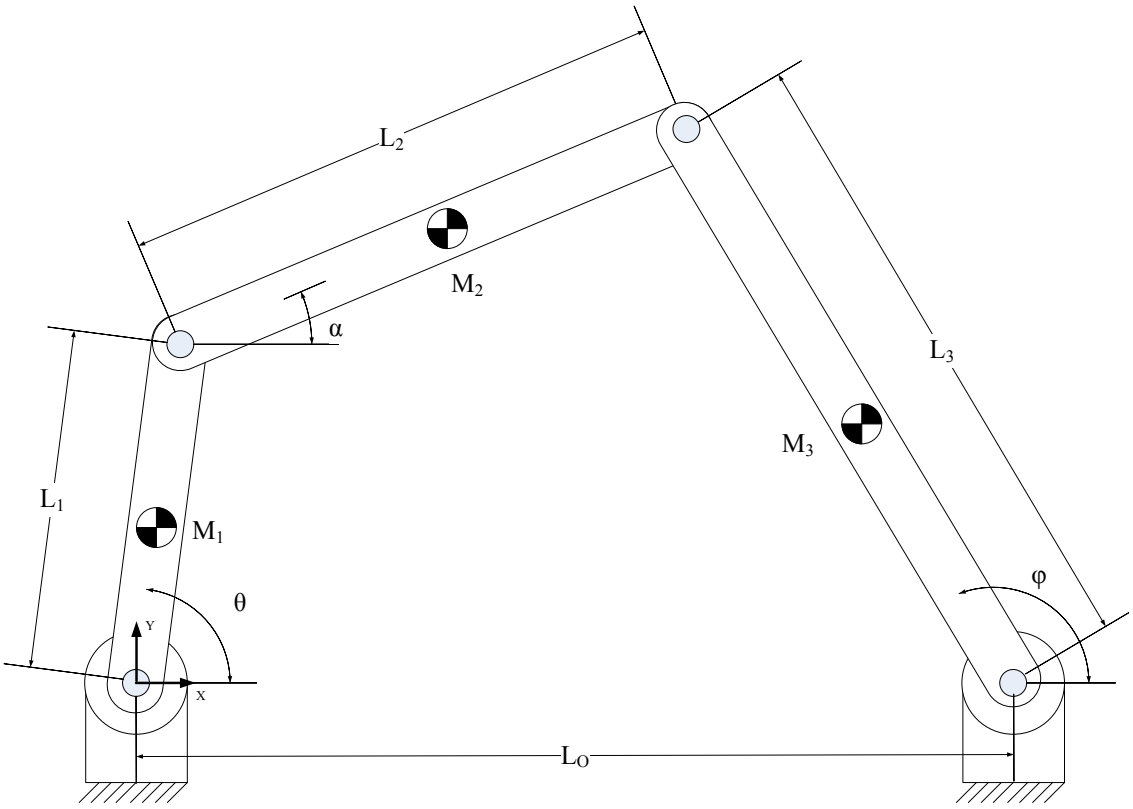

Figure 3.4: RRRR Configuration

Position Analysis: RRRR Configuration

The Mechanism will now only be examined in the RRRR configuration and is shown in Figure 3.4. A fixed coordinate system is located at the left revolute joint shown in Figure 3.4 and is consistent with Figure 3.3. The RRRR configuration will be analyzed in the XY-plane. Note, normal four-bar mechanism angle convention could also be used. Using the vector loop method, a method for solving closed kinematic chains [30], kinematic equations were developed for the RRRR configuration [31]. Appendix A contains a step by step derivation of the kinematics.

The input driver of RRRR configuration is assumed as θ. α and ϕ are the outputs and will be expressed in terms of θ to fully describe the position of the RRRR configuration in one coordinate (θ). In addition, it is assumed all link lengths are known.

Using the vector loop method, two equations can be written in terms of X and Y components.

For x:

$$0 = -L_1 \cos\theta - L_2 \cos\alpha + L_3 \cos\phi + L_0 \tag{3.1}$$

For y:

$$0 = -L_1 \sin\theta - L_2 \sin\alpha + L_3 \sin\phi \tag{3.2}$$

From algebraic manipulation of Equations 3.1 and 3.2, the output angle ϕ is:

$$\boxed{\phi(\theta) = 2 \cdot arctan2(A_1 \pm \sqrt{A_1^2 + A_2^2 - A_3^2}, A_3 - A_2)} \tag{3.3}$$

where:

$$A_1 = -2L_1L_3 \sin\theta \tag{3.4}$$

$$A_2 = 2L_3(L_0 - L_1 \cos\theta) \tag{3.5}$$

$$A_3 = L_0^2 + L_1^2 - L_2^2 + L_3^2 - 2L_0L_1 \cos\theta \tag{3.6}$$

Using θ and the derived angle ϕ, α can be found. Through algebraic manipulation of Equations 3.1, 3.2, and 3.3 the output angle α is:

$$\boxed{\alpha(\theta, \phi) = arctan2(-L_1 \sin\theta + L_3 \sin\phi, L_0 - L_1 \cos\theta + L_3 \cos\phi)} \tag{3.7}$$

The outputs (α and ϕ) are fully expressed and provide the angular positions of the RRRR configuration in the terms of the input (θ).

Position Analysis: RRRP Configuration

The Mechanism will now only be examined in the RRRP configuration and is shown in Figure 3.5. Similar to the RRRR configuration a fixed coordinate system is located at the left revolute joint shown in Figure 3.5. The RRRP configuration will be analyzed in the XY-plane. Using the vector loop method, kinematic equations were developed for the RRRP configuration [31]. Appendix B contains a step by step derivation of the kinematics.

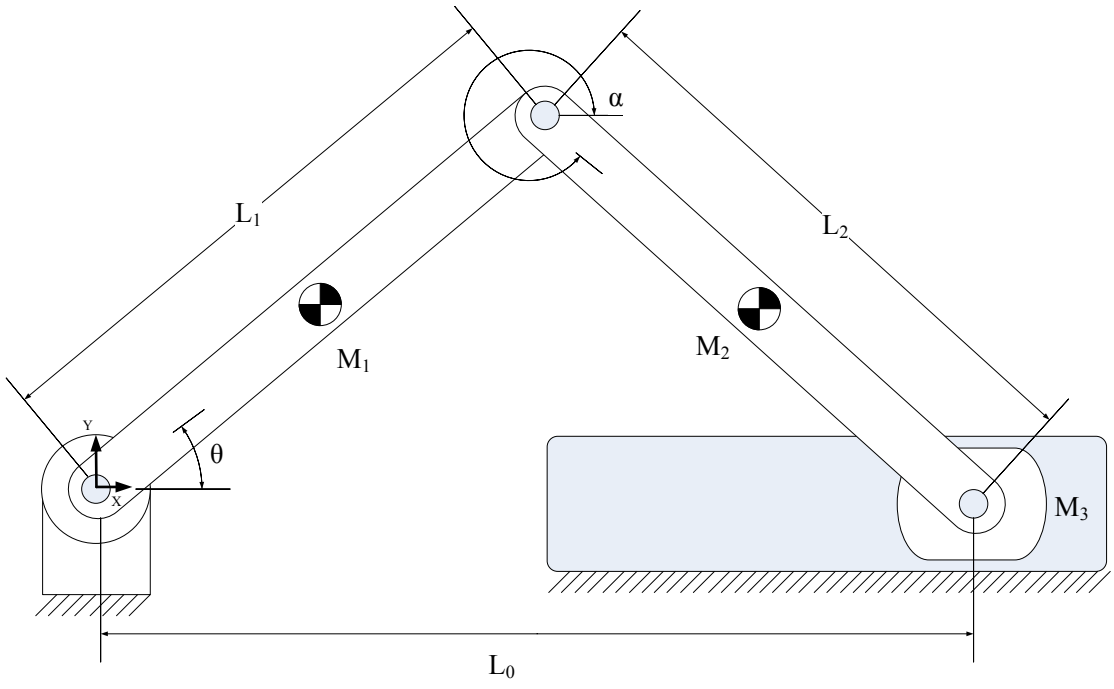

Figure 3.5: RRRP Configuration

The input driver of RRRP configuration is assumed as θ. In addition, it is assumed all link lengths are known. α and L_0 are outputs and will be expressed in terms of θ to fully describe the position of the RRRP configuration in one coordinate (θ).

Using a similar procedure from the previous section, the vector loop equations can be written in terms of X and Y components.

For x:

$$0 = L_1 \cos\theta + L_2 \cos\alpha - L_0 \tag{3.8}$$

For y:

$$0 = L_1 \sin\theta + L_2 \sin\alpha \tag{3.9}$$

From algebraic manipulation of Equations 3.8 and 3.9, the position of the slider relative to the fixed coordinate system, L_0, is:

$$\boxed{L_0(\theta) = L_1 \cos\theta \pm \sqrt{L_1^2 \cos\theta^2 - L_1^2 + L_2^2}} \tag{3.10}$$

Similarly, the intermediate angle α is found in the form:

$$\boxed{\alpha(\theta, L_0) = arctan2(-L_1 \sin\theta, L_0 - L_1 \cos\theta)} \tag{3.11}$$

The outputs (α and L_0) are fully expressed and provide the angular position and slider position of the RRRR configuration in the terms of the input (θ).

3.3.2 Velocity Analysis

A velocity analysis is necessary for understanding how any mechanism functions in time. In addition, the velocities are needed for deriving the kinetics of a mechanism. The velocity equations can be found by taking the derivative of the positional kinematics and some algebraic manipulation. This process has been followed and the results for the RRRR and the RRRP configurations are provided. Again, the Appendices contain step by step derivations.

Velocity Analysis: RRRR Configuration

For the RRRR configuration, θ and $\dot{\theta}$ are are assumed as the inputs and ϕ, $\dot{\phi}$, α, $\dot{\alpha}$ are the outputs. From differentiation of Equations 3.1 and 3.2 and with

algebraic manipulation results in the following velocity equations:

$$\dot{\alpha}(\theta, \dot{\theta}, \phi, \alpha) = \frac{L_1 \sin(\phi - \theta)}{L_2 \sin(\alpha - \phi)} \dot{\theta} \tag{3.12}$$

and

$$\dot{\phi}(\theta, \dot{\theta}, \phi, \alpha) = \frac{L_1 \sin(\alpha - \theta)}{L_3 \sin(\alpha - \phi)} \dot{\theta} \tag{3.13}$$

Velocity Analysis: RRRP Configuration

Following the same procedure outline in the previous section. For the RRRP configuration, θ and $\dot{\theta}$ are are assumed as the inputs and L_0, $\dot{L_0}$, α, $\dot{\alpha}$ are the outputs. From differentiation of Equations 3.8 and 3.9 and with algebraic manipulation results in the following velocity equations:

$$\dot{\alpha}(\theta, \dot{\theta}, \alpha) = \frac{-L_1 \cos(\theta)}{L_2 \cos(\alpha)} \dot{\theta} \tag{3.14}$$

and

$$\dot{L_0}(\theta, \dot{\theta}) = \ -L_1 sin\theta \ \dot{\theta} \overline{+} \frac{-L_1^2 sin\theta \ cos\theta \ \dot{\theta}}{\sqrt{{L_1}^2 \ (cos\theta \ )^2 - {L_1}^2 + \ {L_2}^2}} \tag{3.15}$$

For $\dot{L_0}$, the sign in front of the quotient will change depending on the slider position relative to the origin. If the slider is on the right side of the origin, the sign will be positive. If the slider is on the left side of the origin, the sign will be negative. For this thesis, it is assumed that the slider is always on the right hand side of the origin, thus a positive sign.

3.4 Kinetics: Lagrangian Dynamics Approach

Kinetics or dynamics is the study of the interaction between forces and moments and the resulting motion [24]. The kinematics are the first needed part to derive the kinetics. When analyzing a mechanism, the kinetics are vital to truly understanding the motion and forces of that mechanism. Understanding of the

forces allows for proper sizing of components. For example, if the force acting on a link can be analytically determined, the link can then be sized to withstand that particular force. This allows designers to create better quality and safer products. In addition, if the kinematics and kinetics are known, one can predict where a mechanism will be in time and space. This is incredibly important when designing any system.

Specifically for the RRRR-RRRP Mechanism, understanding the forward dynamics will provide insight into the motion. A torque will be applied at the input joint (θ) and the system will move. Through the derivation of the kinematics and kinetics, one is able to predict the other angles of the and forces acting on the system. Similar to before, the Mechanism will be analyzed as two individual configurations: the RRRR and RRRP configurations. This approach is consistent with the kinematics.

The individual configurations can be analyzed using a Lagrangian dynamics approach. Rather than using constrained coordinates, the dynamics for each configuration are analyzed using a single constrained coordinate following the approach by Tang [31]. While a single dynamic equation is only needed to fully describe a system with one degree of freedom, these equations can be quite complicated due to the nonlinearity of the kinematic vector loop equations. Mathematical gymnastics are often necessary in order to complete this for closed kinematic chains. This method was selected to provide insight into Transition Point of the configurations. That is the point in which the Mechanism switches from the RRRR configuration to the RRRP configuration or vice versa.

Certain assumptions must be made when kinetically modeling the Mechanism. In the kinetic analysis, the friction in the joints was neglected and the torque supplied was considered an ideal source. Also, the links are considered rigid.

When simulating the kinetics of a system, the initial conditions must be known and are provided in Section 3.6. For each of the the configurations only the positional input (θ), the velocity input ($\dot{\theta}$) and any external forces or torques are needed to completely describe the system. Thus, each model was evaluated using the generalized coordinate θ. In addition, a torque (τ) will be applied at the revolute joint described by angle θ in each model.

In the next sections, the following variables will be used to describe the system. I_i represents the inertia of the corresponding link. g represents the gravitational constant. All other terms are defined in the figures.

3.4.1 RRRR Configuration: Equation of Motion

The RRRR configuration dynamic analysis is shown below [31]. As stated before, the EOM provides insight into how the mechanism functions in time with external forces applied. This is beneficial to better understanding the Mechanism. The following equations are general forms of the kinetic energy (T) potential energy (V) and the generalized Lagrange equations. These equations are are necessary for deriving the final EOM. Shown in Appendix A is a step by step derivation of each of the equations and the EOM. Figure 3.4 show the specific lengths and naming convention.

The kinetic energy of each link (T_1, T_2, T_3) has been found and the sum can be expressed as (T).

$$\sum T = T_1 + T_2 + T_3 \tag{3.16}$$

where:

$$T_1 = \frac{1}{8} M_1 L_1^2 \dot{\theta}^2 + \frac{1}{2} I_1 \dot{\theta}^2 \tag{3.17}$$

$$T_2 = \frac{1}{2} M_2 L_1^2 \dot{\theta}^2 + \frac{1}{8} M_2 L_2^2 \dot{\alpha}^2 + \frac{1}{2} I_2 \dot{\theta}^2 + M_2 L_1 L_2 \cos(\theta - \alpha) \dot{\theta} \dot{\alpha} \tag{3.18}$$

$$T_3 = \frac{1}{8} M_3 L_3^2 \dot{\phi}^2 + \frac{1}{2} I_3 \dot{\phi}^2 \tag{3.19}$$

The potential energy of each link number (V_1, V_2, V_3) can be expressed as the sum of all potential energies (V).

$$\sum V = V_1 + V_2 + V_3 \tag{3.20}$$

where:

$$V_1 = \frac{1}{2} M_1 g \sin\theta L_1 \tag{3.21}$$

$$V_2 = M_2 g (L_1 \sin\theta + \frac{L_1}{2} \sin\alpha) \tag{3.22}$$

$$V_3 = \frac{1}{2} M_3 g L_3 \sin\phi \tag{3.23}$$

The kinetic energy (Equation 3.16) and potential energy (Equation 3.20) terms can then be substituted into Lagrange's equation (Equation 3.24) [24].

$$\mathcal{L} = T - V \tag{3.24}$$

The final equation of motion can be found by solving Equation 3.25.

$$\tau = \frac{d}{dt}\left(\frac{\partial \mathcal{L}}{\partial \dot{\theta}}\right) - \frac{\partial \mathcal{L}}{\partial \theta} \tag{3.25}$$

Once solved, the general form of the final EOM is represented by Equation 3.26 where A, B, C represent specific terms derived.

$$\boxed{A(\theta)\ddot{\theta} + B\left(\theta,\ \dot{\theta}\right)\dot{\theta}^2 - C = \tau} \tag{3.26}$$

3.4.2 RRRP Configuration: Equation of Motion

Similarly to the RRRR configuration dynamic analysis the RRRP configuration dynamic analysis is shown below [31]. The assumptions made for the RRRR configuration were also used for the RRRP configuration. The following equations are general forms of the kinetic energy (T) potential energy (V) and the generalized Lagrange equation. These equations are are necessary for

deriving the final EOM. Shown in Appendix B is a step by step derivation of each of the equations and the EOM. Figure 3.5 shows specific lengths and naming convention for the derivation.

The kinetic energy of each link (T_1, T_2, T_3) has been found and can be expressed as the sum of all kinetic energies (T). Note that Link L_3 (from Figure 3.3) mass has been added into the end mass, M_3 of the RRRP Configuration for the Mechanism.

$$\sum T = T_1 + T_2 + T_3 \tag{3.27}$$

where:

$$T_1 = \frac{1}{8} M_1 L_1^2 \dot{\theta}^2 + \frac{1}{2} I_1 \dot{\theta}^2 \tag{3.28}$$

$$T_2 = \frac{1}{2} M_2 L_1^2 \dot{\theta}^2 + \frac{1}{8} M_2 L_2^2 \dot{\alpha}^2 + \frac{1}{2} I_2 \dot{\theta}^2 + M_2 L_1 L_2 \cos(\theta - \alpha) \dot{\theta} \dot{\alpha} \tag{3.29}$$

$$T_3 = \frac{1}{2} M_3 (L_1^2 \sin^2 \theta \dot{\theta}^2 + L_2^2 \sin^2 \alpha \dot{\alpha}^2 + 2 L_1 L_2 \sin\theta \dot{\theta} \sin\alpha \dot{\alpha}) \tag{3.30}$$

The potential energy of each link(V_1, V_2, V_3) has been found and can be expressed as the sum of all potential energies (V).

$$\sum V = V_1 + V_2 + V_3 \tag{3.31}$$

where:

$$V_1 = \frac{1}{2} M_1 g \sin\theta L_1 \tag{3.32}$$

$$V_2 = M_2 g (L_1 \sin\theta + \frac{L_1}{2} \sin\alpha) \tag{3.33}$$

$$V_3 = 0 \tag{3.34}$$

The kinetic energy (Equation 3.27) and potential energy (Equation 3.31) terms can then be substituted into Lagrange's equation (Equation 3.35) [24].

$$\mathcal{L} = T - V \tag{3.35}$$

The final equation of motion can be found by completing Equation 3.36.

$$\tau = \frac{d}{dt}\left(\frac{\partial \mathcal{L}}{\partial \dot{\theta}}\right) - \frac{\partial \mathcal{L}}{\partial \theta} \tag{3.36}$$

Once solved, the general form is expressed by Equation 3.37 where A, B, C represent specific terms derived.

$$\boxed{A(\theta)\ddot{\theta} + B\left(\theta,\ \dot{\theta}\right)\dot{\theta}^2 - C = \tau} \tag{3.37}$$

3.4.3 Kinetics: Summary

In conclusion, the equation of motion for the RRRR and RRRP configurations were determined. These EOM models were then coded in Matlab. In Section 3.6, the EOM models will be verified by comparing them to the results of the SimMechanics models of the individual configurations.

3.5 SimMechanics

As discussed in Section 3.1, the Mechanism was analyzed in two separate configurations. The equations of motion were found for each configuration using the Lagrangian approach. These equations were coded in Matlab for further analysis. Verification of these equations is necessary to ensure the controls of the Mechanism. Understanding the dynamics will help properly size a motor and understand the forces in the Mechanism.

SimMechanics is a commercially available software used for modeling and simulating multi-body systems [32]. SimMechanics provides a three-dimensional (3D) simulation environment for systems. These systems can range from hydraulic to electrical to mechanical. SimMechanics is an extension of Matlab and allows for sharing of data between the two. SimMechanics is optimal for the research application.

SimMechanics allows the user to create models of systems using blocks to represent joints, constraints, links and specific geometry. Once a model has been created a 3D representation of the model is generated. Next, SimMechanics allows the user to simulate the response to different external forces. For example, in a mechanical system a torque can be applied at a specified joint. Understanding the motion of the system will be extremely useful in the research application. Once the external forces have been applied, the model can be simulated. The simulation results provide specific joint forces and torques. Essentially, SimMechanics solves multi-bodied dynamic problems through numeric simulation [32]. In understanding of the Mechanism, the internal forces can be quickly found through SimMechanics. Finding the internal forces quickly is especially usefully because the Lagrangian dynamics do not inherently provide these.

In order to verify the equations of motion for the Mechanism, SimMechanics was used. First, individual models of the RRRR configuration, shown in Figure 3.6, and the RRRP configuration, shown in Figure 3.7, were constructed. These were then simulated to ensure the SimMechanics model was working properly. Next, the hand derived EOM models and the SimMechanics models were compared and examined for error. If the error was within an acceptable range, the hand derived EOM would be considered valid. This is shown in Section 3.6.

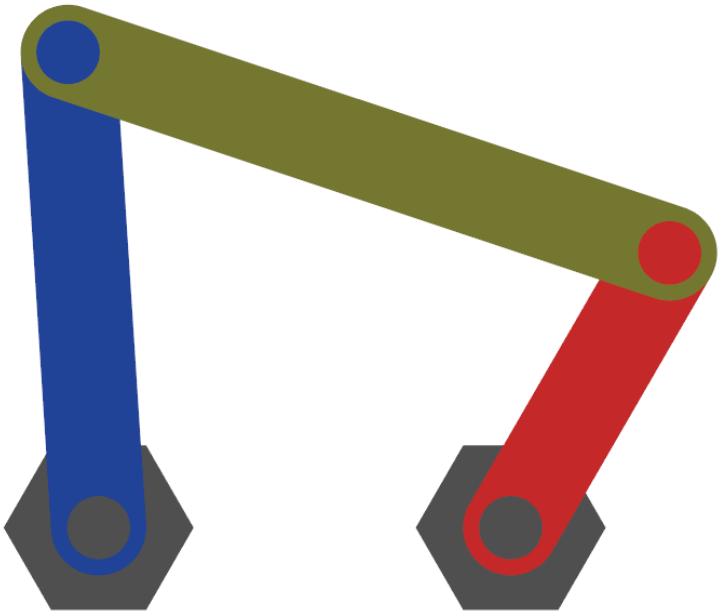

Figure 3.6: RRRR SimMechanics Depiction

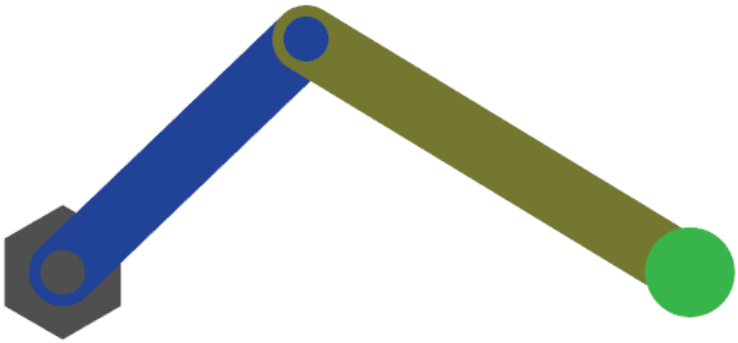

Figure 3.7: RRRP SimMechanics Depiction

3.6 Verification of Individual Dynamic Models

As discussed previously, verification of the individual dynamic models is necessary. The hand derived equations were coded in Matlab for simulation and comparable models were generated in SimMechanics. These models will be simulated and compared for accuracy. First, the RRRR equation of motion will be verified, shown in Section 3.6.1. Second, the RRRP equation of motion will be validated, shown in Section 3.6.1. The techniques used to validate each model are identical and will be outlined in the following paragraphs.

In order to validate any two dynamic models, the simulation must be configured properly. First, individual parameters and initial conditions need to be defined. In addition, a numerical differential equation solver for the models must be selected. Then, external forces or moments can be applied to the system. For example, the external force could even be gravity. Once defined, the models can be simulated and the response of the models can be compared.

Specifically for the RRRR and RRRP models, the initial conditions are defined in their respective sections. Next, a solver was selected. When comparing the two models, it is of the utmost importance that they are compared at the same time steps. This will ensure that the dynamics compared are accurate. A fixed step solver, a fifth-order Runge-Kutta method (ODE5), was used with a step size of 0.0001 seconds to compare the models. Each simulation, was conducted over 10 simulation time seconds. As stated previously, it was found that the ODE5 solver allowed for consistent comparison of data at any time interval. Using a variable step size solver would not provide the same ease of comparison. Next, a constant torque (τ_θ) was applied to the revolute joint described by the angle θ in both the Matlab code and SimMechanics. This constant torque simulates an ideal motor attached to the input θ. Finally, the response of the systems was analyzed

and compared.

3.6.1 Verification of RRRR Equation of Motion

Shown in Table 3.1 are the parameters and initial conditions used for the SimMechanics and Matlab code model verification. As stated previously, a constant torque (τ_θ) was applied to the revolute joint described by the angle θ. These parameters are comparable to Tang's work on RRRR mechanisms [31]. Matlab was used to generate a graphic of the corresponding link lengths of the RRRR configuration in Figure 3.8. The RRRR Matlab and SimMechanics models were compared to the overall responses of Tang's simulations. It was found they were comparable.

Table 3.1: RRRR Dynamic Model Parameter Input

Parameters	Units	Value
Link Lengths	m	L_0=3.0, L_1=1.0, L_2=4.0, L_3=2.5
Mass Centers	m	L_{ci}=$L_i/2$, i=1,2,3
Link masses	kg	M_1=M_2=M_3=1
Moment of Inertia	$\mathrm{kg}\cdot\mathrm{m}^2$	I_i=$M_i L_i^2/12$, i=1,2,3
Initial configuration	rad	$\theta(0) = 1.5708$
Initial configuration	rad	$\alpha(0) = 0.3494$
Initial configuration	rad	$\phi(0) = 0.9531$
Initial velocity	rad/s	$\dot{\theta} = \dot{\phi} = \dot{\alpha}$= 0
Torque input	$\mathrm{N}\cdot\mathrm{m}$	τ_θ= 6.0
Gravity	m^2/s	g= 9.81

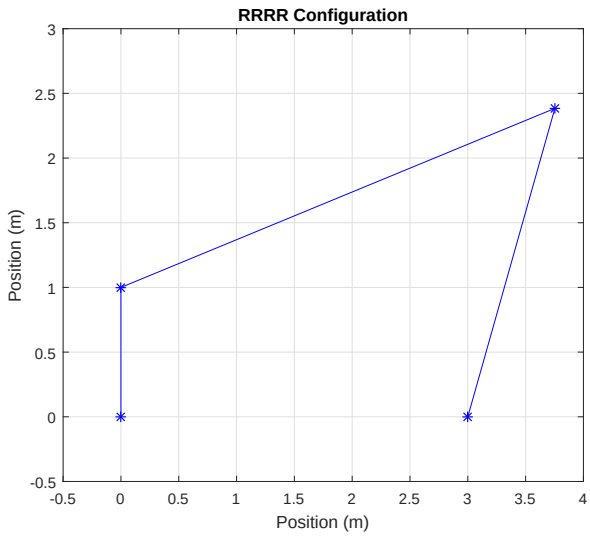

Figure 3.8: RRRR Configuration using Table 3.1 parameters

The simulation results of the SimMechanics simulation and Matlab code simulation are provided. Shown in Figure 3.9 is the response of the angle θ. The overall shape of the response follows the expected result. The angular position is increasing and the link is accelerating. This is consistent with Tang's work and follows the expected result. Shown in Figure 3.10 is the response of the angle α. Shown in Figure 3.11 is the response of the angle ϕ. Again, both α and ϕ follow the expected result and are consistent with the overall shape of Tang's work. Note, it is difficult to differentiate between the SimMechanics and the Matlab code data on the plots. The figures show that the error between the models is insignificant (the order of 10^{-4}). This means that either the Matlab coded model or the SimMechanics model for the RRRR mechanism configuration can be used for the final combined RRRR-RRRP dynamic model. Being able to use the SimMechanics model is extremely beneficial for understanding internal forces. Using the proper conditions SimMechanics will provide the internal forces very quickly.

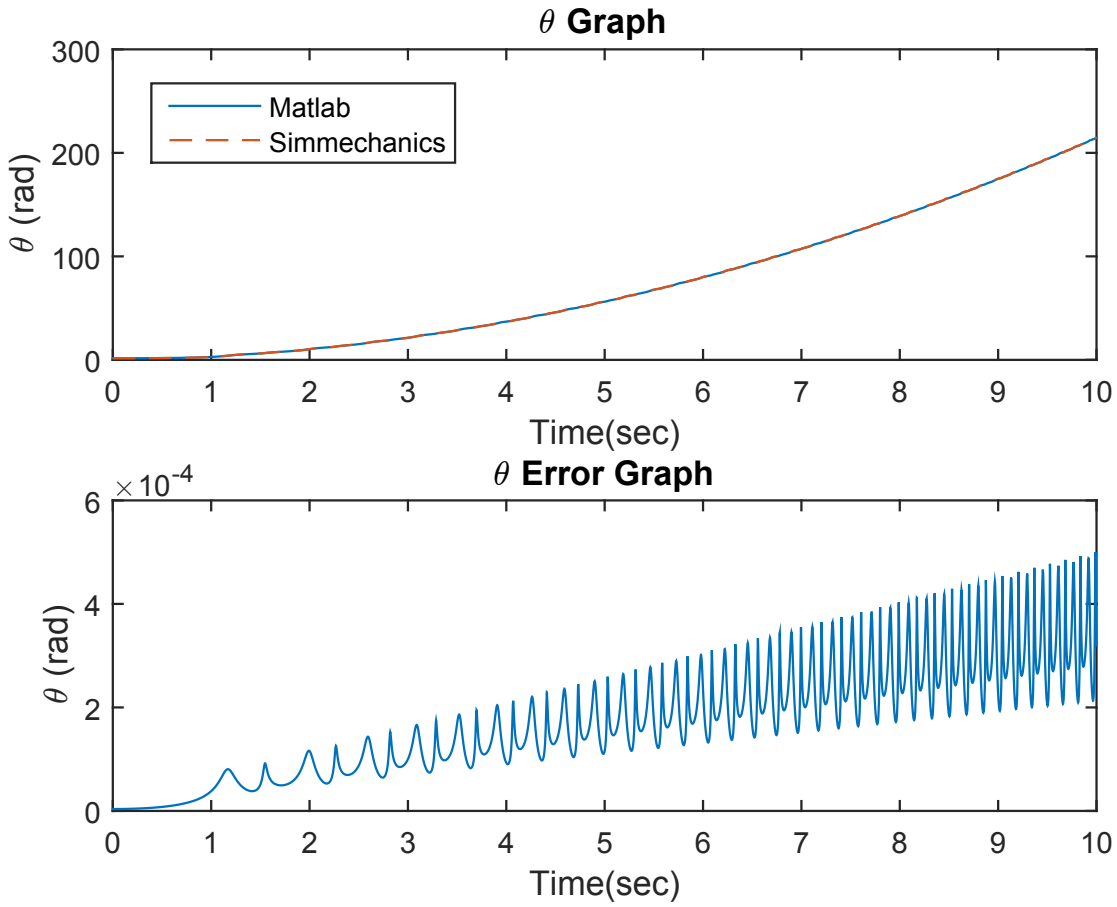

Figure 3.9: RRRR Configuration - Dynamic Model Verification: θ

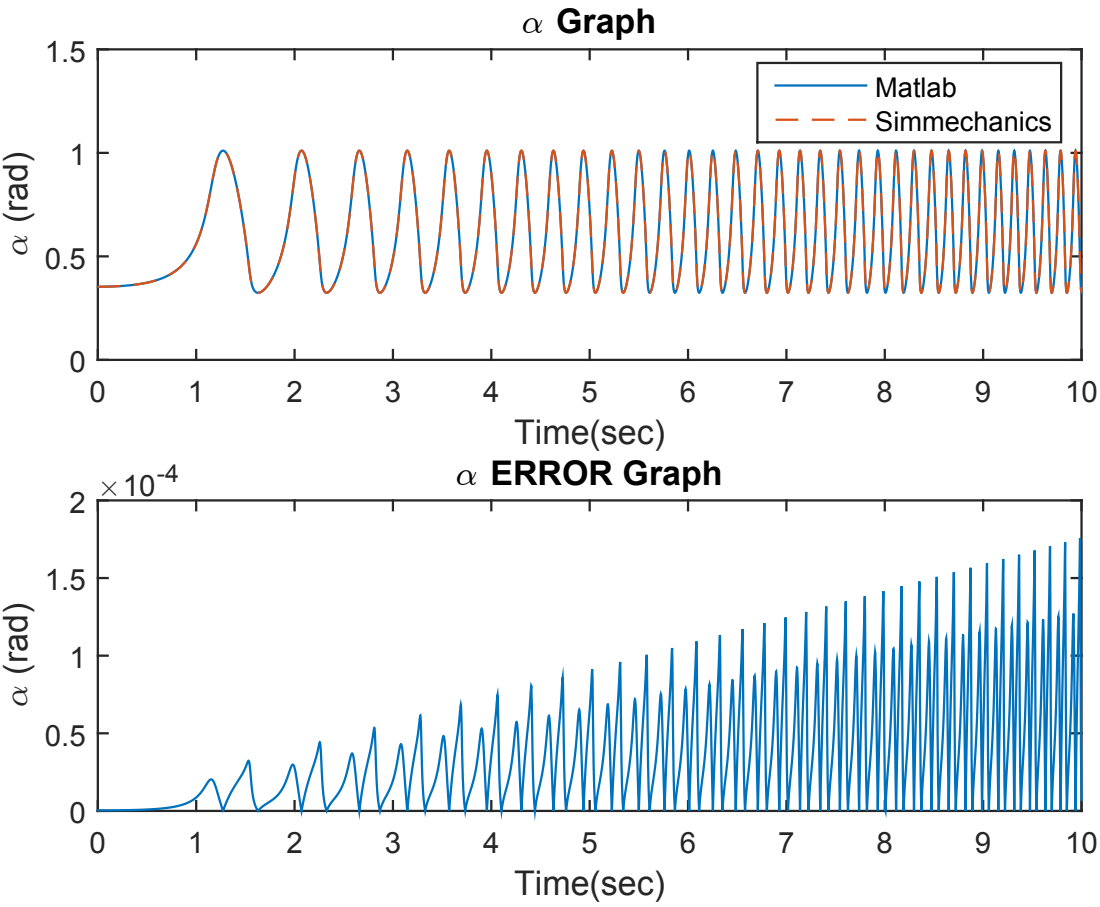

Figure 3.10: RRRR Configuration - Dynamic Model Verification: α

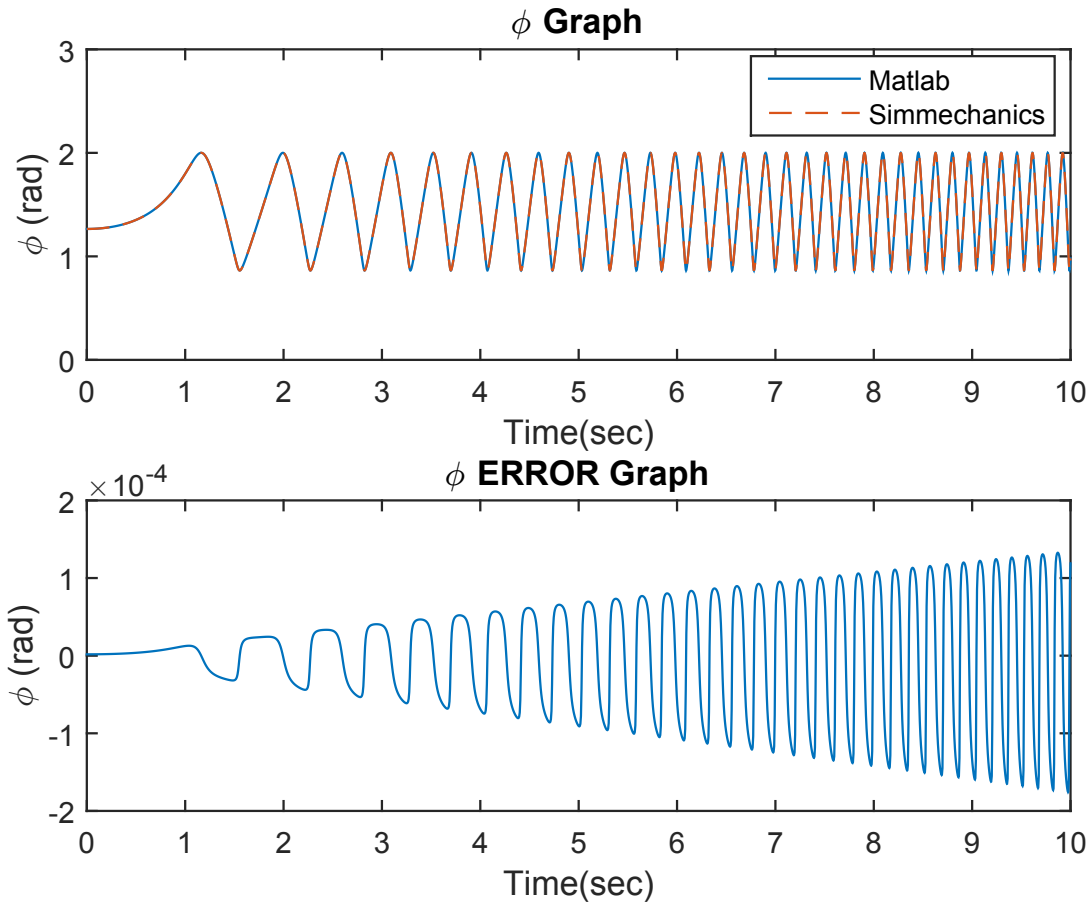

Figure 3.11: RRRR Configuration - Dynamic Model Verification: ϕ

3.6.2 Verification of RRRP Equation of Motion

Now that the RRRR models have been validated, the overall response for RRRP configuration are compared. Shown in Table 3.2 are the parameters and initial conditions used for the SimMechanics and Matlab code model verification. Again, a constant torque (τ_θ) was applied to the revolute joint described by the angle θ. Applying a constant torque should provide a comparable response of θ in the RRRP to θ in the RRRR model.

Table 3.2: RRRP Dynamic Model Parameter Input

Parameters	Units	Value
Link Lengths	m	L_1=1.0, L_2=4.0
Mass Centers	m	L_{ci}=$L_i/2$, i=1,2,3
Link masses	kg	M_1=M_2=1
Moment of Inertia	$\text{kg} \cdot \text{m}^2$	I_i=$M_i L_i^2/12$, i=1,2,3
Initial configuration	rad	$\theta(0) = 1.5708$
Initial configuration	rad	$\alpha(0) = 0.3494$
Initial velocity	rad/s	$\dot{\theta} = \dot{\alpha}$= 0
Torque input	$\text{N} \cdot \text{m}$	τ_θ= 6.0
Gravity	m^2/s	g= 9.81

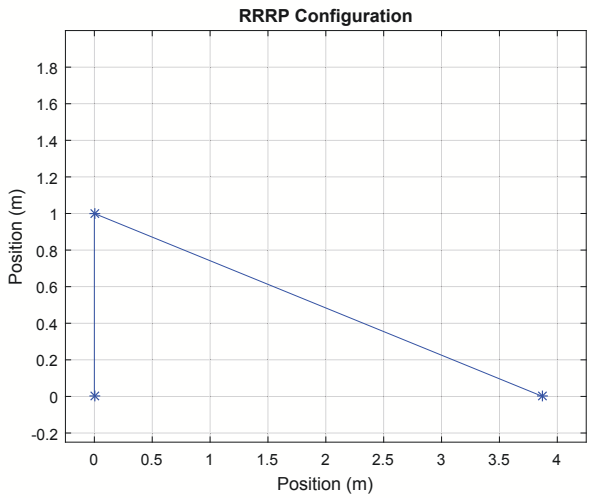

Figure 3.12: RRRP Configuration using Table 3.2 parameters

The simulation results of the SimMechanics simulation and Matlab code simulation are provided. Shown in Figure 3.13 is the response of the angle θ. The overall shape of the response follows the expected result. The angular position is increasing and the link is accelerating. This is consistent with the RRRR configuration and follows the expected result. Shown in Figure 3.14 is the response of the angle α. α also follows the expected result. Figure 3.15 is the displacement of the slider relative to the origin (L_0). L_0 can be quickly verified by examining the peaks and troughs of the simulation. The max peak should correspond to $L_1 + L_2$ and the minimum should correspond to $L_2 - L_1$. Note, when examining the RRRP response figures, it is difficult to differentiate between the SimMechanics and the Matlab code data. The figures show that the error between the models is insignificant (the order of 10^{-4}). This means that either the Matlab coded model or the SimMechanics model for the RRRR mechanism configuration can be used for the final combined RRRR-RRRP dynamic model. Being able to use the SimMechanics model is extremely beneficial for understanding internal forces.

Overall, either the Matlab coded models or the SimMechanics models for the RRRR and RRRP configurations can be used for the final combined Mechanism plant model.

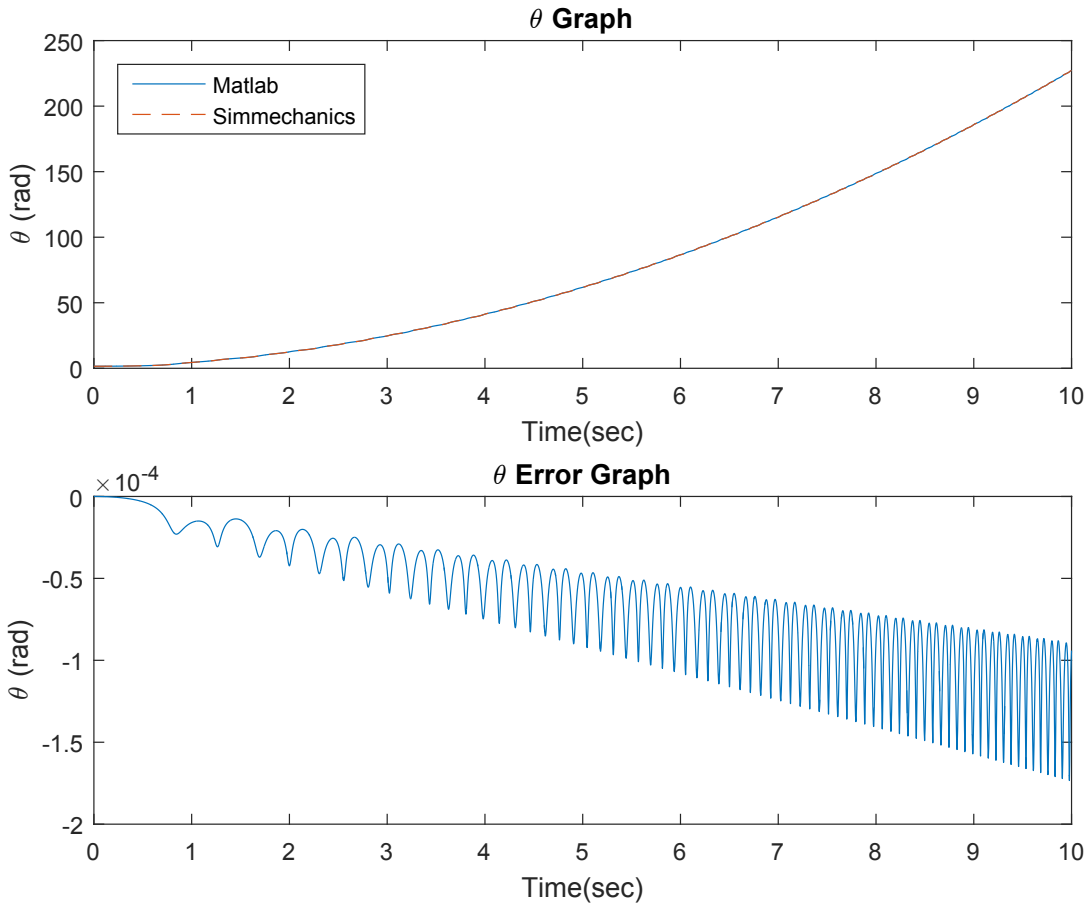

Figure 3.13: RRRP Configuration - Dynamic Model Verification: θ

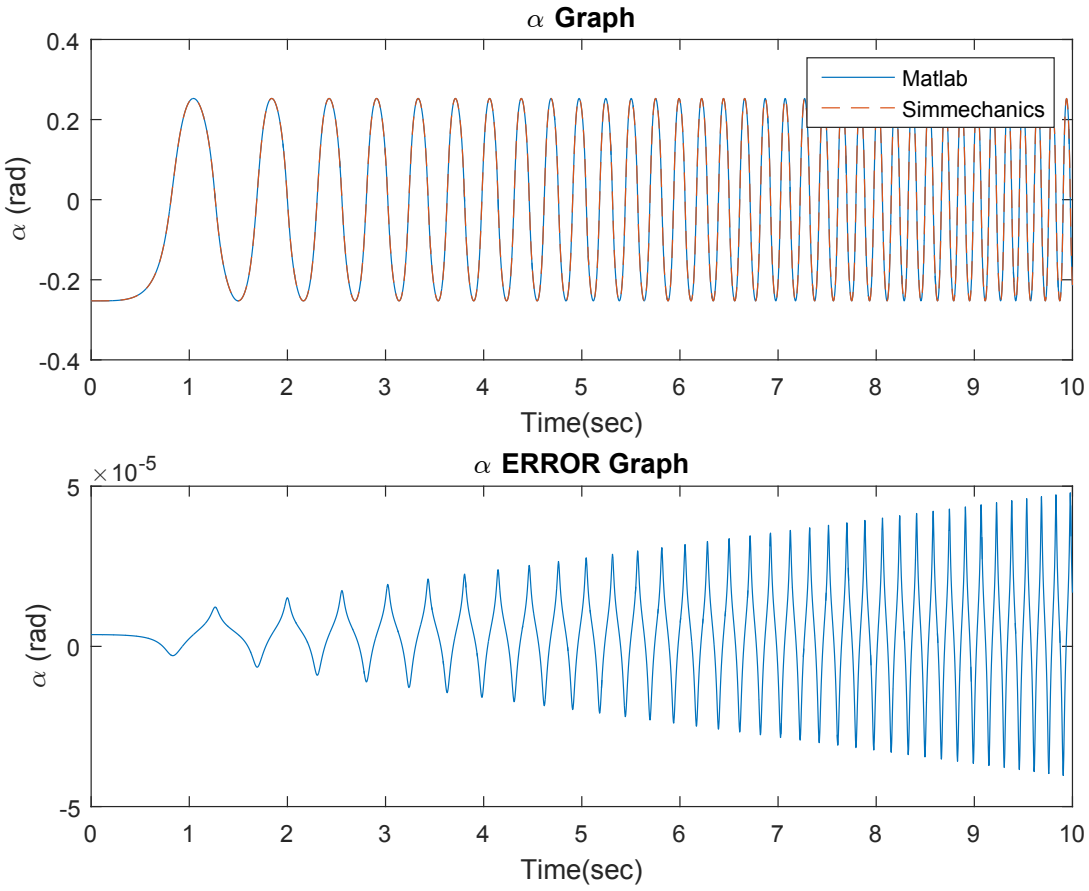

Figure 3.14: RRRP Configuration - Dynamic Model Verification: α

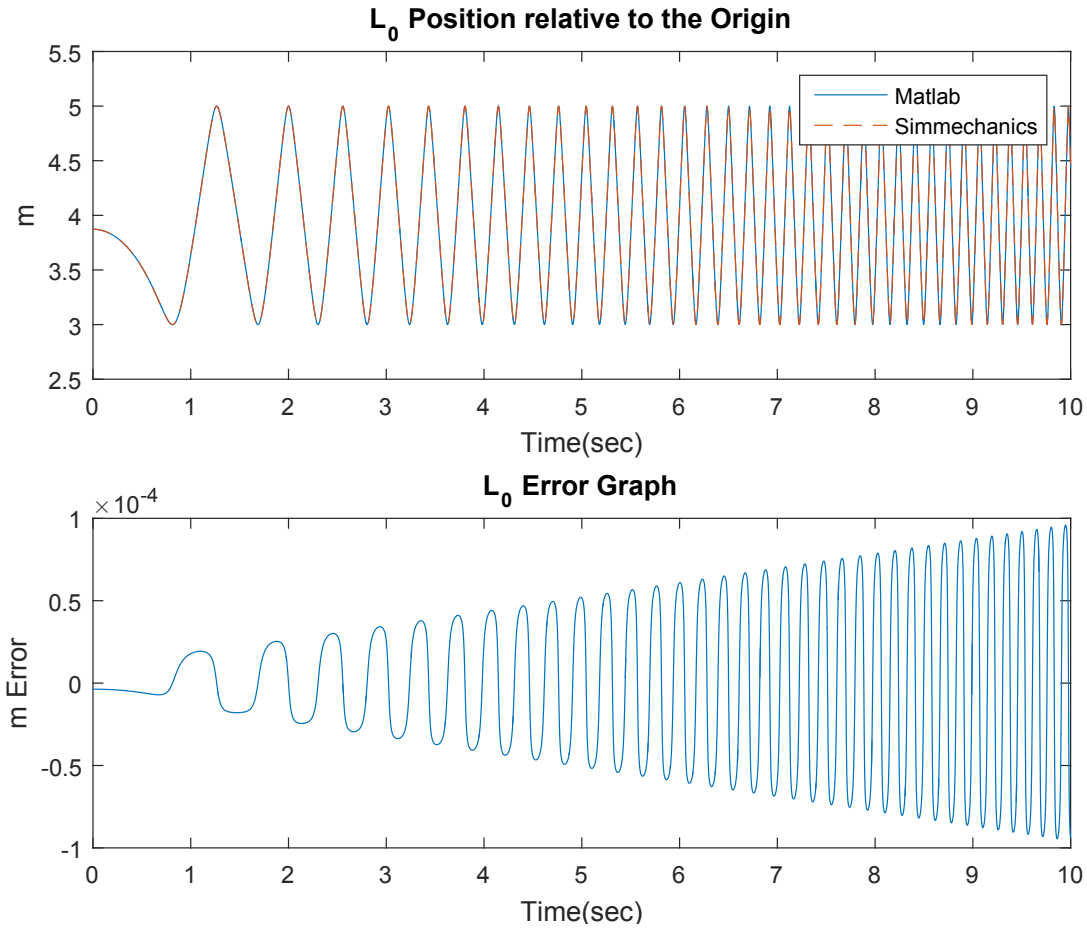

Figure 3.15: RRRP Configuration - Dynamic Model Verification: L_0

3.7 Mechanism Analysis Summary

In summary, the Mechanism was examined in two different configurations: the RRRR and RRRP configurations. First, the kinematics were found for each configuration. Next, the dynamics were determined using a classical Lagrangian approach. A full derivation of the kinematics and kinetics for the RRRR and RRRP configurations can be found in Appendices A, and B respectively. The dynamics were then verified using SimMechanics. The dynamics are necessary for future controls applications and will assist in developing the design guidelines. In addition, the EOM models are necessary to fully understanding the geometric motions and forces of the systems. A complete Plant model of the Mechanism will be shown in Chapter 4.

CHAPTER 4

MECHANISM SYSTEM MODELING AND SIMULATION

4.1 Introduction

The Mechanism's configurations were analyzed from a dynamics perspective in Chapter 3. The Mechanism will be examined with a geared DC motor attached to its input from a system level. The goal of this chapter is to derive and simulate a mathematical model of the complete system. The complete system contains the following components: a trajectory planner, controller and a plant model. These components will represent the RRRR-RRRP Mechanism system.

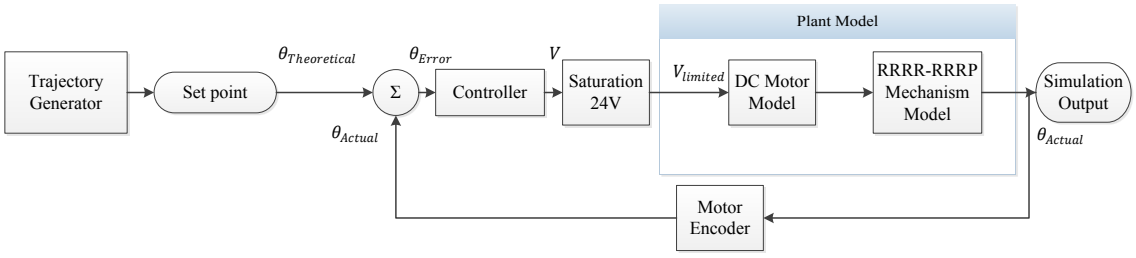

Figure 4.1: System Model Block Diagram

Shown in Figure 4.1 is a block diagram of the processes necessary to simulating the complete RRRR-RRRP Mechanism system. The angular position (θ) of the DC motor will be controlled and examined. First, a desired trajectory must be created using the trajectory planner. The desired trajectory then becomes the set point ($\theta_{Theoretical}$) for the controller. The error (θ_{Error}) is then computed and the controller mathematically manipulates the error. The manipulation is dependent on the type of controller. The control signal is then converted into a

voltage and a saturation limit ($V_{limited}$). For the physical system, the saturation block ensures that the voltage sent to the motor does not exceed a specified voltage and will not burn out the motor. For the simulation, the saturation limits the numeric voltage to the system. The limited voltage ($V_{limited}$) is supplied to the plant model. The plant model will be developed that incorporates the DC motor and the Mechanism. Incorporating both will provide a highly accurate representation of the system as a whole. The angular position (θ_{Actual}) response is measured and fed back to the controller. The controller examines the next set point and the system repeats the process. The system is run in a loop until the generated trajectory profile has completed its specified values.

Each component will be examined in greater detail in individual sections. First, the trajectory generation will be examined in detail. A cubic polynomial profile is used but there are many more options. Next, two different plant models will be developed and examined in detail. The first plant model will only represent the first link of the Mechanism. The second plant model will represent the Mechanism in its entirety. Then, the controller is examined. While there are many controller options, in this thesis, a PID controller will be used. Finally, the system will be simulated in Matlab with both plant models and the controller. The results will be compared to experimental results .

4.2 Trajectory Generation

Trajectory planning is a necessary part of any controlled system. Trajectory planning allows the definition of a mechanism's motion path from one point to another. In addition, trajectory planning can also define the velocity and acceleration of a joint. Defining the motion profile of any mechanism allows for a controlled and predicted path to be achieved. Through definition of motion profiles, increased efficiency and safety is achieved.

There are numerous motion trajectories planning schemes that can be used. Selection of a trajectory planner usually depends on the number of parameters the user wants to control. The parameters range from controlling position, velocity, acceleration and even jerk through a motion profile. In the Mechanism's system, it is vital to control the starting and ending angular position and velocity of the system. Through control of the input angle (θ) and velocity ($\dot{\theta}$), the whole Mechanism will be controlled due to its one degree of freedom nature. To achieve control of θ and $\dot{\theta}$, a third-order polynomial trajectory planner is used [30]. The following paragraphs outline how a third-order trajectory planner works and an example is demonstrated.

Using a third-order polynomial trajectory planner allows for the selection of the desired starting and ending angular positions and velocities. The desired starting position is denoted as θ_i and the ending position is represented by θ_f and will be selected by the user. The velocities are the time derivative of these respective parameters and are $\dot{\theta}_i$ and $\dot{\theta}_f$. For the Mechanism application, the starting and ending velocity is desired to be zero ($\dot{\theta}_i = \dot{\theta}_f = 0$). Using the initial and final conditions (θ_i, $\dot{\theta}_i$, θ_f, $\dot{\theta}_f$) allows one to solve the equations shown in Equations 4.1 and 4.2. Equation 4.1 is the general representation of the third-order polynomial and Equation 4.2 is its time derivative. Time is represented as t. The starting time is defined as t_i. The ending time is defined as t_f. The following equations are adapted from Niku [30].

$$\theta(t) = b_0 + b_1 t + b_2 t^2 + b_3 t^3 \tag{4.1}$$

$$\dot{\theta}(t) = b_1 + 2b_2 t + 3b_3 t^2 \tag{4.2}$$

where the initial and final conditions are:

$$\theta(t_i) = \theta_i \tag{4.3}$$

$$\theta(t_f) = \theta_f \tag{4.4}$$

$$\dot{\theta}(t_i) = 0 \tag{4.5}$$

$$\dot{\theta}(t_f) = 0 \tag{4.6}$$

Through substitution of the initial and final conditions into Equations 4.1 and 4.2 a matrix of equations is developed. Solving the matrix yields the coefficients (b_0, b_1, b_2, b_3) of the third-order polynomial for Equations 4.1 and 4.2. Shown in Equation 4.7 is the matrix.

$$\begin{bmatrix} \theta_i \\ \dot{\theta}_i \\ \theta_f \\ \dot{\theta}_f \end{bmatrix} = \begin{bmatrix} 1 & 0 & 0 & 0 \\ 0 & 1 & 0 & 0 \\ 1 & t_f & t_f^2 & t_f^3 \\ 0 & 1 & 2t_f & 3t_f^2 \end{bmatrix} \begin{bmatrix} b_0 \\ b_1 \\ b_2 \\ b_3 \end{bmatrix} \tag{4.7}$$

An example of a third-order polynomial trajectory planner is shown in Figure 4.2. Equations 4.8, 4.9, 4.10, and 4.11 are the initial and final conditions of the example shown. In Figure 4.2, time is in units of seconds and angular position is in units of radians.

$$\theta(0) = 0 \tag{4.8}$$

$$\theta(14) = \pi \tag{4.9}$$

$$\dot{\theta}(0) = 0 \tag{4.10}$$

$$\dot{\theta}(14) = 0 \tag{4.11}$$

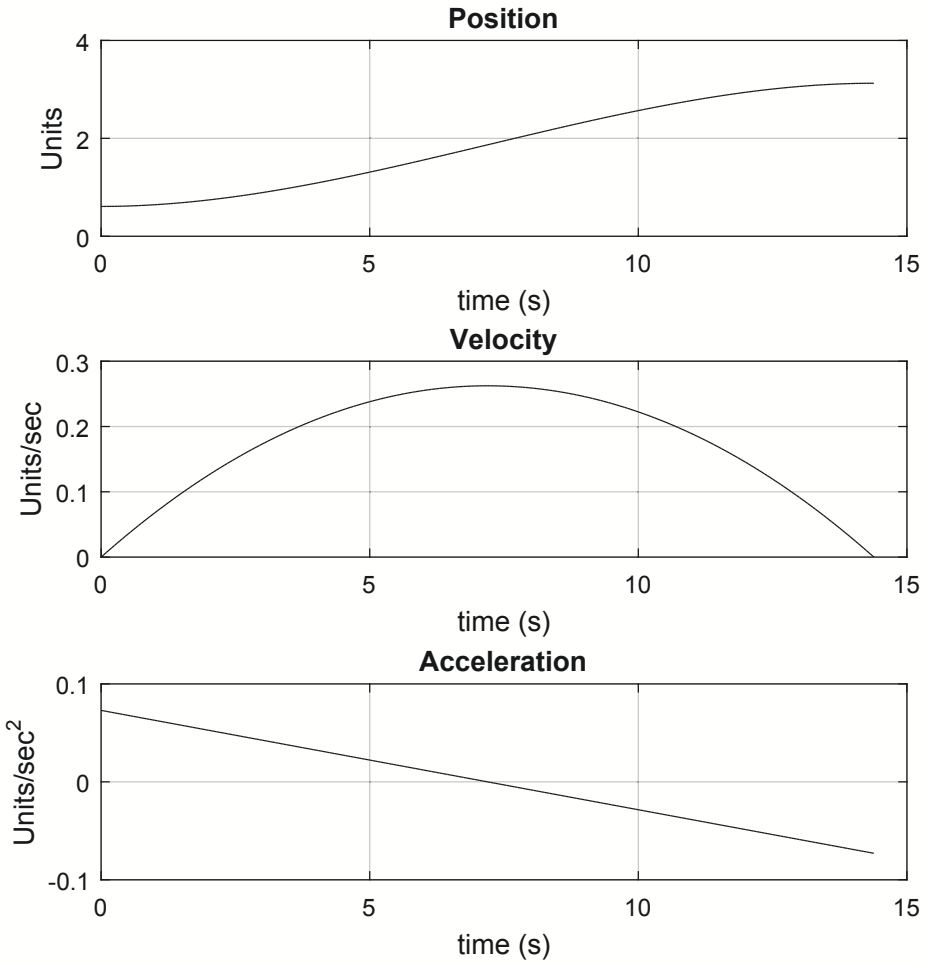

Figure 4.2: Trajectory Planning: Third-Order Polynomial ("Units" are radians)

4.3 Plant Modeling

4.3.1 Introduction

The following section outlines the development of the Plant Model for the system. The goal of the plant model is to represent a physical RRRR-RRRP Mechanism with a geared DC motor attached to the input driver (θ). Two different plants will be developed and compared for accuracy. In order to generate the plant models several intermediate modeling steps are needed. First,

a geared DC motor is modeled. Within the DC motor model, a general DC motor electrical circuit is developed and is consistent with industry standards [30, 33]. The DC motor model is then verified through open loop experimentation using a Pittman Ametek 8543 series 24.0 Volt DC motor [34].

Once the DC motor model is verified, the two different plant models are developed to represent the RRRR-RRRP Mechanism. The two different plant models are Case A: Mechanical Modeling with Simplified Dynamics and Case B: Mechanical Modeling with Full Dynamics. Case A represents a single external link attached to the output shaft of the motor. Using a geared motor, the external load should not play a large factor in the results but will be examined. The low loading felt by the motor is due to the divisor in the equations being the gear ratio term squared. Case B represents the entire Mechanism attached to the output shaft of the motor. Using the dynamics previously developed in Appendices A and B, the effective load applied can be determined in each case. Case B is considered the more accurate of the two models but its accuracy will be evaluated. Finally, the general electrical motor circuit can be combined with each case to develop state equations that represent the plant model.

The purpose of the two different plant models is to provide better understanding. If Case A is sufficient, future analysis techniques will be easier. Only the mass, inertia, and length of first link would be necessary for modeling the system. If it proves to be insufficient, Case B is necessary. That is, all masses, link lengths and inertias will need to be known to model the system accurately. Ideally Case A will prove sufficient. In this chapter, each case will be simulated and discussed. In Chapter 6, the simulated models will be compared to the experimental results for verification of the models. Once the two plant models have been analyzed, a final recommendation for the optimal plant model will be made.

In the following sub-sections, each area will be discussed and only the final equations presented. A step by step derivation of each subcase can be found in Appendix C.

4.3.2 DC Motor with a Gearbox Modeling

The modeling of the DC motor is examined as two systems (electrical and mechanical). First, an electrical derivation of a general DC motor is completed. Second, the mechanical modeling of a DC motor with a gearbox is completed. Initially, a generic mechanical model is developed and then revised based on open loop experimentation using a Pittman-Ametek 8543 24.0 volt motor with a 36:1 gearbox [34]. The revised DC motor model is then verified through experimentation in open loop. Shown in Appendix Section C.2 is a step by step derivation of the model.

DC Motor: Electrical Modeling

Figure 4.3 is a general DC motor model and the corresponding electrical circuit. The electrical model is consistent with industry standards for armature controlled DC motors [30, 35, 33]. The mechanical side is currently represented by a general DC motor. Figure 4.3 parameters are defined in Table 4.1.

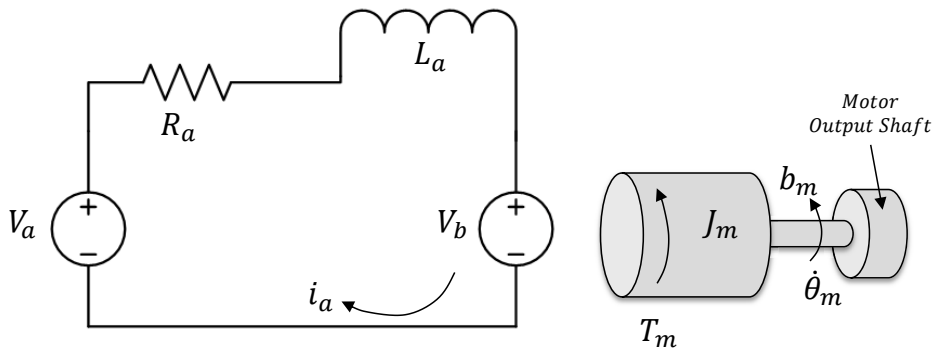

Figure 4.3: Electrical Circuit of DC Motor Model

Table 4.1: Figure 4.3 Parameters

Variable	Variable Description	Units
V_a	Supply Voltage	V
R_a	Motor Resistance	Ω
L_a	Motor Inductance	H
V_b	Motor Back EMF Voltage	V
i_a	Motor Current	A
T_m	Motor Torque	$\mathrm{N \cdot m}$
J_m	Rotor Inertia	$\mathrm{kg \cdot m^2}$
b_m	Viscous Damping Factor	$\mathrm{N \cdot m \cdot s/rad}$
θ_m	Angular Position	rad
$\dot{\theta}_m$	Angular Velocity	rad/s
$\ddot{\theta}_m$	Angular Acceleration	$\mathrm{rad/s^2}$

Through derivation and substitution, a final state equation (Equation 4.12) is found to represent the electrical side of the motor.

$$\boxed{\frac{di_a}{dt} = \frac{1}{L_a}V_a - \frac{R_a}{L_a}i_a - \frac{K_b}{L_a}\dot{\theta}_m} \tag{4.12}$$

DC Motor: Mechanical Modeling

The following section is the development of the mechanical model of a DC motor with a gearbox. The motor will be modeled with no load on the output shaft of the motor. Modeling no load on the motor will allow for verification quickly with simple experiments. Shown in Figure 4.4 is the model of the DC motor. The figure's parameters are explained in Table 4.2. The mechanical model is coupled with the previously developed electrical model.

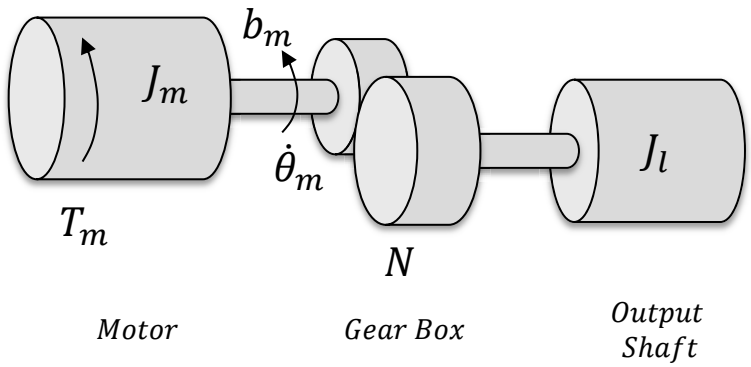

Figure 4.4: Mechanical DC Motor Model with Gearbox

Table 4.2: Figure 4.4 Parameters

Variable	Representation	Units
T_m	Motor Torque	$\mathrm{N \cdot m}$
J_m	Rotor Inertia	$\mathrm{kg \cdot m^2}$
b_m	Viscous Damping Factor	$\mathrm{N \cdot m \cdot s/rad}$
N	Gear Ratio	-
J_l	Inertia of gearbox shaft	$\mathrm{kg \cdot m^2}$
θ_m	Angular Position	rad
$\dot{\theta}_m$	Angular Velocity	rad/s
$\ddot{\theta}_m$	Angular Acceleration	$\mathrm{rad/s^2}$

Through derivation and substitution, a final state equation (Equation 4.13) is found to represent the mechanical side of the motor.

$$\boxed{\ddot{\theta}_l = \frac{NK_t}{N^2J_m - J_l} i_a - \frac{N^2 b_m}{N^2 J_m - J_l}\dot{\theta}_l} \tag{4.13}$$

DC Motor: Equations of Motion

The state variables are chosen to be $\theta_l, \dot{\theta}_l, i_a$. Collecting all of the terms from the previously developed equations, they are:

$$\frac{di_a}{dt} = \frac{1}{L_a}V_a - \frac{R_a}{L_a}i_a - \frac{K_b}{L_a}N\dot{\theta}_l \tag{4.14}$$

$$\dot{\theta}_l = \frac{d\theta_l}{dt} \tag{4.15}$$

$$\ddot{\theta}_l = \frac{NK_t}{N^2J_m - J_l} i_a - \frac{N^2 b_m}{N^2 J_m - J_l}\dot{\theta}_l \tag{4.16}$$

DC Motor: Revision of Equations of Motion

The developed equations of motion equations for the DC Motor Model were simulated and then compared to experimental results. The experimentation was conducted open loop. A specific voltage was used as a step input into the physical motor and the angular position and velocity response tracked. The same was done for the simulation. After examination of the results, it was found that additional parameters were necessary for increased fidelity of the model.

Through analysis and experimentation, the friction model of the motor was found to be inadequate. Initially, only the viscous friction and static Coulomb friction torque were modeled. These were the only parameters in the Pittman motor data sheet [34]. These parameters provided do not account for the addition of the gearbox which will significantly affect the the viscous friction and static Coulomb friction torque. In addition, the dynamic Coulomb friction torque was not provided. Revision of the model was necessary.

An experimentation process to find the necessary friction terms (viscous friction, static Coulomb friction torque and dynamic Coulomb friction torque) was conducted. The process is outlined in detail in Prisco's work [2]. Viscous friction is related linearly to the speed ($\dot{\theta}$). Static Coulomb friction torque is the torque required to start motion. Static Coulomb friction torque is also referred to as the breakaway force [35]. Dynamic Coulomb friction torque is the torque that is in constant opposition when the motor is moving. This friction is independent of the velocity and only dependent on the direction of motion [35]. The Stribeck effect was neglected as the measurement devices could not adequately capture the phenomenon. In addition, this will not be a factor when the final experimentation of the Mechanism is conducted.

Shown in Appendix section C.2 are the experimental results and comparison to data sheet parameters. The additional friction term ($T_{friction}$) term was adapted from Prisco's work [2] and represents the various friction terms added. In addition, B_{Total} represents the total viscous friction in the motor and the gearbox. The mechanical model was then re-derived to include these additional terms and new equations of state were developed.

With the updated friction term, the DC Motor Model was simulated and then compared to experimentation results. It was found that the motor model responded too fast. Upon examination, the gearbox inertia was not accounted for in the provided data sheet inertia, thus an effective motor inertia was experimentally determined.

In order to find the effective motor inertia experimental data was necessary. The DC motor was set to several voltages and given a step input. The rise time of three trials from the various voltages was recorded. A Matlab code was developed to find assist in finding the effective inertia. The equations of motion were simulated and the rise time found. A looping method was then used

to compare the motor model simulation's rise time to the experimental rise time based on the various input voltages. If the rise times differed, the inertia of the model was varied by a defined increment and the simulation rerun. Once the simulations rise time was within one percent of experimental rise time the inertia was recorded. The new effective inertia is the inertia that best represents the specific Pittman 8543 motor and is mathematically represented by $J_m + J_c$ and can be found in Equation 4.19. J_m is the motors rotor inertia and J_c is the inertia correction term.

In summary, corrective terms ($T_{friction}$, B_{Total}, J_c) are needed for increased fidelity in the DC motor model. The updated state equations are shown in the following section.

DC Motor: Updated Equations of Motion

As discussed in the previous section, adaptation of the original motor model is necessary. Updating the previous equations result in an accurate representation of the Pittman 8543 DC motor. The following are the updated state equations:

$$\frac{di_a}{dt} = \frac{1}{L_a}V_a - \frac{R_a}{L_a}i_a - \frac{K_b}{L_a}N\dot{\theta}_l \tag{4.17}$$

$$\dot{\theta}_l = \frac{d\theta_l}{dt} \tag{4.18}$$

$$\ddot{\theta}_l = \frac{NK_t}{N^2(J_m + J_c) - J_l}i_a - B_{Total}\dot{\theta}_l + \frac{1}{N(J_m + J_c) - J_l}T_{friction} \tag{4.19}$$

The equations presented were verified through open loop experimentation of the Pittman motor without load but with the gearbox attached. A step input at varying voltages was input to both the model and the physical motor. The response of the angular position and angular velocity were examined. Figure 4.5 is an example of the verification of the angular velocity with a 22 volt step input. When viewing Figure 4.5, the noise of the measurement system is seen by the

jagged points. If a better encoder or increased sampling time was used a cleaner response could be seen. The encoder and measurement system will be examined further in Chapter 5. Overall, the error is minimal. The DC motor model has now been validated and can be used to help develop the two plant models.

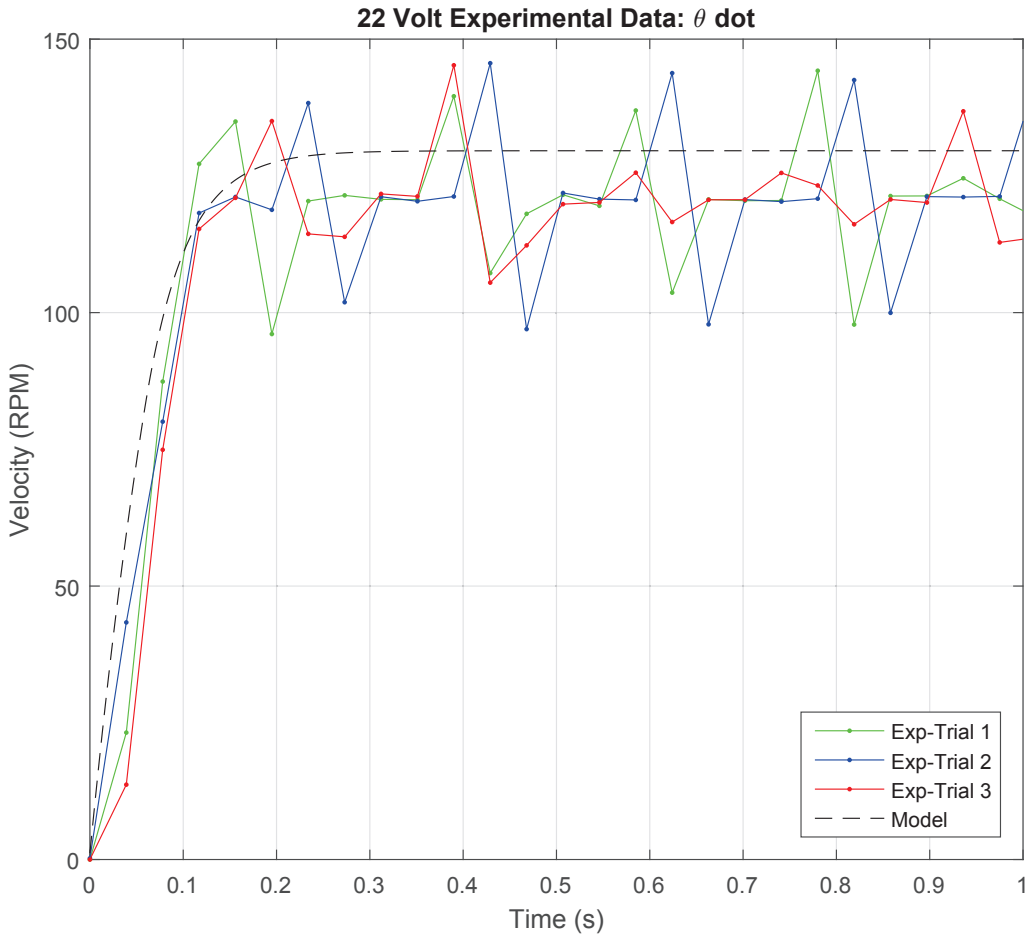

Figure 4.5: Angular Velocity- Comparison of Experimental and Simulation Results at 22 Volts

4.3.3 Plant Model- Case A: Mechanical Modeling with Simplified Dynamics

As discussed before, two different plant models are examined. The first, Mechanical Modeling with Simplified Dynamics (Case A), represents a single external link attached to the output shaft of the motor and will be examined in this specific section. Case A is comparable to the previously derived DC motor model. The only updates are the external link and an external load torque. An updated diagram of the mechanical side with an external link can be found in Figure 4.6. The parameters of the figure are explained in Table 4.3. First, the model's equations of motion were derived and then the additional terms (J_c, $T_{friction}$, B_{Total}) were added to the model. The addition of the terms is done after the initial derivation of the equation of motion to demonstrate the general form of the equations. The derivation is shown step-by-step in Appendix Section C.3. The finalized equations will be presented and then simulated.

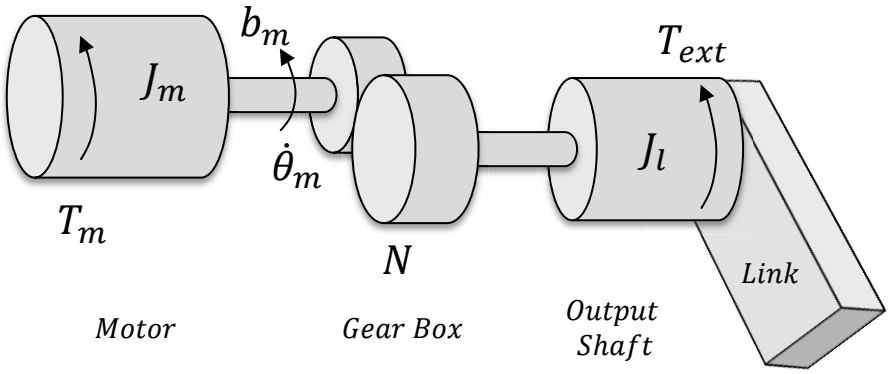

Figure 4.6: Case A: Mechanical DC Motor Model with Simplified Dynamics

Table 4.3: Figure 4.6 Parameters

Variable	Representation	Units
T_m	Motor Torque	$\mathrm{N \cdot m}$
J_m	Rotor Inertia	$\mathrm{kg \cdot m^2}$
b_m	Viscous Damping Factor	$\mathrm{N \cdot m \cdot s/rad}$
N	Gear Ratio	-
J_l	External Inertia of Link and Inertia of gear shaft	$\mathrm{kg \cdot m^2}$
T_{ext}	External applied Torque	$\mathrm{N \cdot m}$
θ_m	Angular Position	rad
$\dot{\theta}_m$	Angular Velocity	rad/s
$\ddot{\theta}_m$	Angular Acceleration	$\mathrm{rad/s^2}$

Case A: General Equations of Motion

The general state equations are presented and correspond to the model based on Figure 4.6.

$$\frac{di_a}{dt} = \frac{1}{L_a}V_a - \frac{R_a}{L_a}i_a - \frac{K_b}{L_a}N\dot{\theta}_l \tag{4.20}$$

$$\dot{\theta}_l = \frac{d\theta_l}{dt} \tag{4.21}$$

$$\ddot{\theta}_l = \frac{1}{N^2J_m - J_l}T_{ext} + \frac{NK_t}{N^2J_m - J_l}i_a - \frac{N^2b_m}{N^2J_m - J_l}\dot{\theta}_l \tag{4.22}$$

Case A: Updated Equations of Motion

Through the experimentation and analysis of the DC motor, it was found the addition of corrective terms (J_c, $T_{friction}$, B_{Total}) are necessary for increased fidelity. These terms correspond specifically to the 8543 Pittman motor; if a different motor was used these terms would need to be re-evaluated. Modification to the previous generated equations of motion result in the updated state equations. These equations are used in any simulation referenced as Case A

and will be simulated in a future section.

$$\frac{di_a}{dt} = \frac{1}{L_a}V_a - \frac{R_a}{L_a}i_a - \frac{K_b}{L_a}N\dot{\theta}_l \tag{4.23}$$

$$\dot{\theta}_l = \frac{d\theta_l}{dt} \tag{4.24}$$

$$\ddot{\theta}_l = \frac{1}{N^2(J_m + J_c) - J_l}T_{ext} + \frac{NK_t}{N^2(J_m + J_c) - J_l}i_a - B_{Total}\dot{\theta}_l + T_{friction} \tag{4.25}$$

4.3.4 Plant Model- Case B: Mechanical Modeling with Full Dynamics

The second plant model developed is Mechanical Modeling with Full Dynamics (Case B). Case B represents the full Mechanism connected to the output shaft of the motor. An updated diagram of the mechanical side with a representation of the Mechanism is shown in Figure 4.7. The parameters of the figure are explained in Table 4.4. First, the model's equations of motion will be derived in general and then the additional terms (J_c, $T_{friction}$, B_{Total}) will be added to the model. The method is comparable to the previous section. A complete step-by-step derivation is shown in Appendix Section C.4.

Case B incorporates the equations of motion of the RRRR and RRRP configurations and will be denoted as J_{mech}. The EOM of the configurations can be found in their entirety in Appendices A and B. A Matlab code was developed to select the equations of motion based on the angle ϕ. Shown in Figure 3.3 is the complete Mechanism and is a reference for the specific angle ϕ. If ϕ is greater than zero than the Mechanism is in the RRRR configuration. If ϕ is less than or equal to zero than the Mechanism is in the RRRP configuration. Figure 4.8 is a graphical representations of the determination for the parameter J_{mech}. J_{mech} will be incorporated into the step by step derivation of the equations of motion.

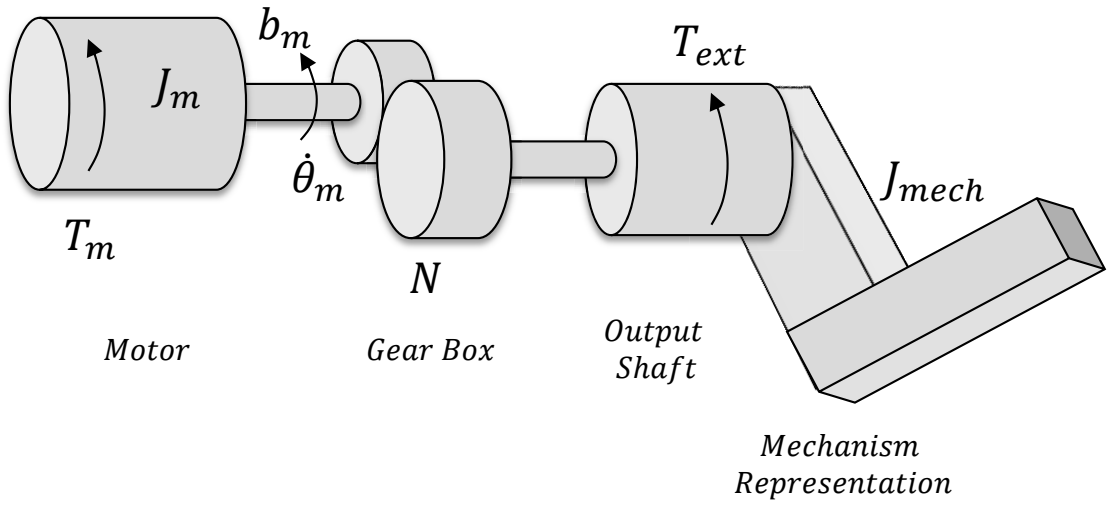

Figure 4.7: Case B- Mechanical Modeling with Full Dynamics

Table 4.4: Definition of Figure 4.7 Parameters

Variable	Representation	Units
T_m	Motor Torque	$\mathrm{N \cdot m}$
J_m	Rotor Inertia	$\mathrm{kg \cdot m^2}$
b_m	Viscous Damping Factor	$\mathrm{N \cdot m \cdot s/rad}$
N	Gear Ratio	-
T_{ext}	External applied Torque	$\mathrm{N \cdot m}$
θ_m	Angular Position	rad
$\dot{\theta}_m$	Angular Velocity	rad/s
$\ddot{\theta}_m$	Angular Acceleration	$\mathrm{rad/s^2}$
J_{mech}	Mechanism's Dynamics	-

Case B: Equations of Motion

As stated previously, the Mechanism's dynamics are represented by J_{mech} where A, B, C are coefficients of the dynamics model. Depending on the configuration of the Mechanism, A, B, and C will change accordingly. J_{mech} is

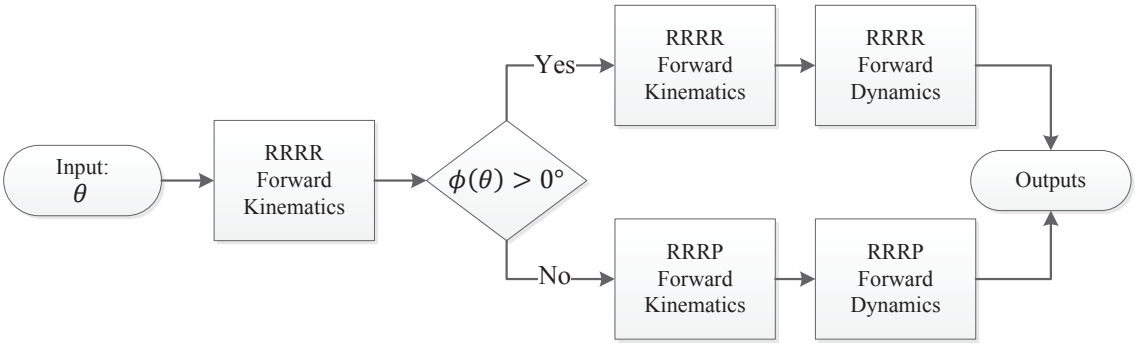

Figure 4.8: Configuration Selector for the Mechanism

shown in Equation 4.26. Shown in Figure 4.8 is a graphical representation for switching between configurations. The output of Figure 4.8 is the different coefficients (A, B, C) depending on the dynamics and kinematics.

$$J_{mech} = A\ddot{\theta}_l + B\dot{\theta}_l^2 + C \tag{4.26}$$

Through the experimentation and analysis of the DC motor, it was found the addition of corrective terms (J_c, $T_{friction}$, B_{Total}) are necessary for increased fidelity. These terms correspond specifically to the 8543 Pittman motor; if a different motor was used these terms would need to be re-evaluated. Modification to the previous generated equations of motion result in the updated state equations. These equations are used in any simulation referenced as Case B and will be simulated in a future section.

$$\frac{di_a}{dt} = \frac{1}{L_a}V_a - \frac{R_a}{L_a}i_a - \frac{K_b}{L_a}N\dot{\theta}_l \tag{4.27}$$

$$\dot{\theta}_l = \frac{d\theta_l}{dt} \tag{4.28}$$

$$\ddot{\theta}_l = \frac{B}{(J_m + J_c)N^2 - A}\dot{\theta}_l^2 + \frac{C}{(J_m + J_c)N^2 - A} + \frac{1}{(J_m + J_c)N^2 - A}T_{ext} + \frac{K_t N}{(J_m + J_c)N^2 - A}i_a + T_{friction} - B_{Total}\dot{\theta}_l \tag{4.29}$$

4.4 Controller

As seen in Figure 4.1, a controller is necessary to regulate the process. There are numerous controllers that exist but one of the most common controllers in industry is the Proportional-Integral-Derivative (PID) Controller [36]. Shown in Figure 4.9 is a generic PID controller. The PID controller requires a set point and a process variable. A set point is the desired value of the controller. A process variable is the value after a process or plant model has changed it. The error ($e(t)$) is calculated between the set point and process variable. The error is then manipulated by the gains mathematically (K_p, K_i, K_d). The output of the manipulation is then summed and output. The output is referred to as the control signal ($u(t)$). The control signal is then sent to the process or plant. The plant then has a response and is fed back for the next loop of the control system. One challenge of PID control is determining the specific gain values. A process called Ziegler-Nichols can be used to determine an starting point for tuning the gains and will be used to experimentally determine the gains.

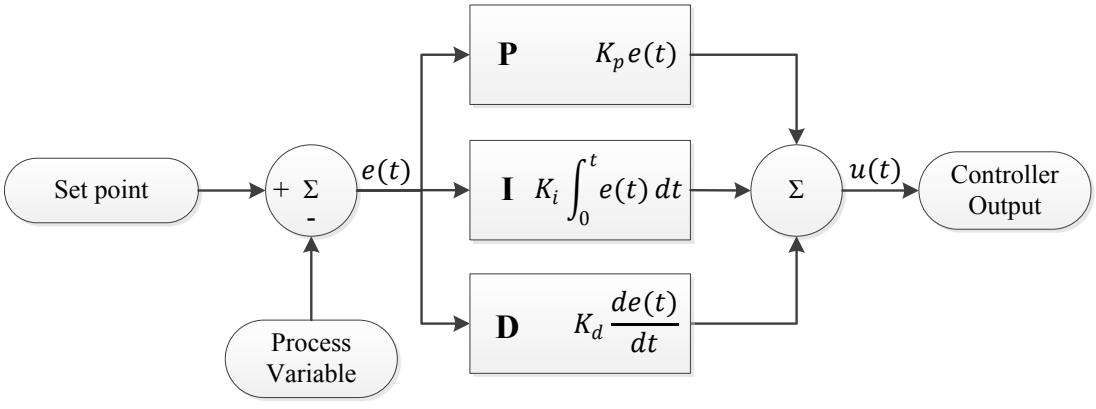

Figure 4.9: PID Controller

In the specific application of the Mechanism, some variation of the PID controller will be used to control the angular position (θ). In addition, the angular position will be measured by an encoder and fed back to the controller. The Ziegler-Nichols process outlined by Prisco [2] was used in coordination with the Pittman 8543 motor to experimentally determine a baseline for the gains value. Once a baseline was established through Ziegler-Nichols, the motor was tuned. A Proportional (P) controller was found to be sufficient and selected as the controller. The P controller assists in stability and increases response time [36]. Once the gain ($K_p = 0.0101$) was found, the DC motor was tested with a generated third-order polynomial trajectory. The angular position of the motor versus time was logged. Then, the control system was simulated in Matlab with the previously generated geared DC motor model. The experimental results and DC motor simulation had comparable results and are shown in Figure 4.10. The tracking error is minimal but a time delay was present. Overall, the control system used in Matlab is acceptable.

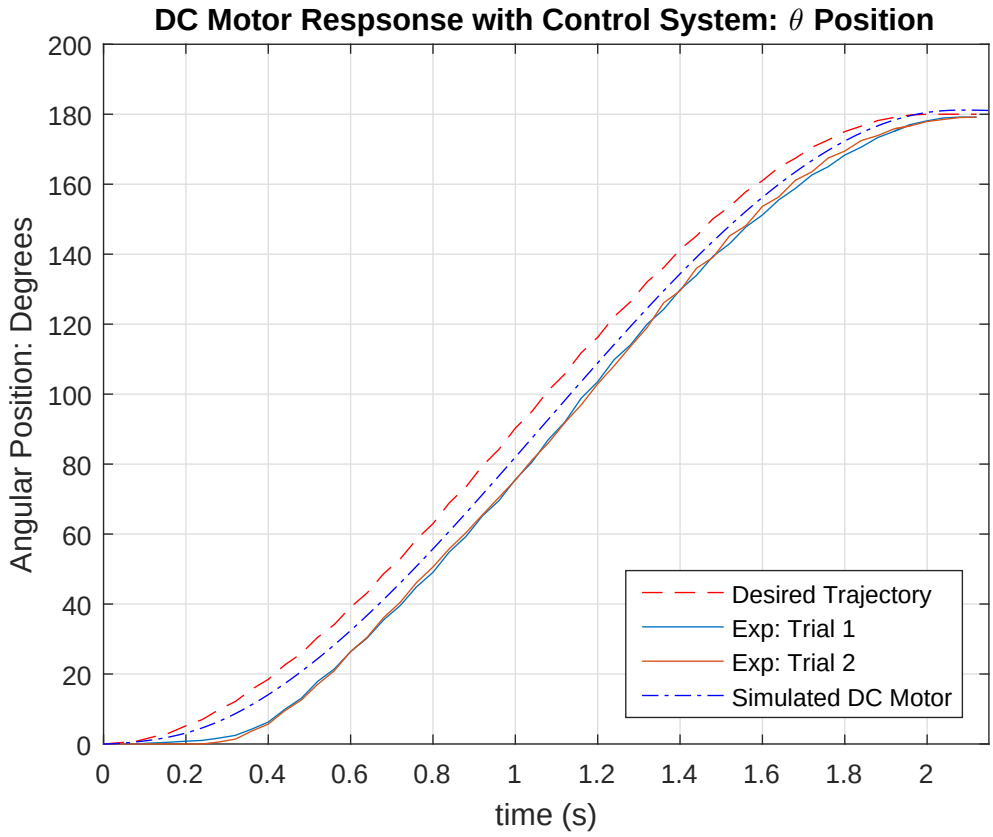

Figure 4.10: Verification of Control System

4.5 Simulated Model Results

4.5.1 Introduction

The goal of the modeled system is to be able to conduct the simulated experiments in Matlab that will correlate to physical experiments. The experiments entail simulating the Mechanism from the RRRR configuration to the RRRP configuration and vice versa with the closed loop control system. The approach taken for modeling and representing the system will be very similar to the experimental implementation. Using Case A, Case B, the trajectory planner and the controller, the models will be simulated to represent the Mechanism

going from the RRRR configuration to the RRRP configuration and vice versa.

For both simulations, a fixed step solver (ODE5) with a step size of 0.0001 seconds was used. In addition, a closed loop proportional controller with a gain of 0.0101 was used. Table 4.5 is the simulated physical configuration for the Mechanism. These parameters are necessary for understanding the dynamics of the system. Note, M_3 and L_{3c} have been examined and calculated based on link length three and the mass of the slider to adjust for the different masses and lengths depending on the configuration. In all figure titles, CS denotes the control system response with the plant models.

Table 4.5: Simulation Configuration Inputs

Parameter	Units	Numeric
Link Lengths	m	$L_0 = 0.15 + \Delta L_0$
Link Lengths	m	L_1=0.1000, L_2=0.2500, L_3=0.0600
Mass Centers	m	L_{ic}=$L_i/2$, i=1,2
Mass Centers	m	L_{3c}=0.0106
Link masses	kg	M_1=0.0600, M_2= 0.1330 ,M_3=0.1320
Moment of Inertia	$\text{kg} \cdot \text{m}^2$	I_i=$M_i L_i^2/12$, i=1,2,3

4.5.2 RRRP to RRRR Configuration

The initial conditions of a dynamic system directly affect the response of the system. Shown in Table 4.6 are the initial and final conditions for the RRRP to RRRR configuration. In all of the figures, the trajectory generation value shown is the calculated kinematic solution for the desired θ value. No kinetics are accounted for in the trajectory generation result and can be considered the baseline response for the system. Case A and Case B are the two different plant models and incorporate the kinetics of the Mechanism with a control. Figure 4.11

shows the simulated results of the Mechanism switching from RRRP configuration to the RRRR configuration. Figure 4.12 are snapshots of the graphical representation create in Matlab for the Mechanisms motion. Figure 4.13 specifically shows the angle θ and the error between the specific case and the desired generated trajectory. Figure 4.14 shows the simulated voltage, current and torque.

Table 4.6: Desired Trajectory Parameters for RRRP to RRRR Simulation Model

Description	Value	Units
Desired Starting Angular Position	$\theta_i(t_i = 0) = 50^\circ$	deg
Desired Ending Angular Position	$\theta_f(t_f = 2) = 125^\circ$	deg
Desired Starting Angular Velocity	$\dot{\theta}_i(t_i) = 0$	deg/s
Desired Ending Angular Velocity	$\dot{\theta}_f(t_f) = 0$	deg/s

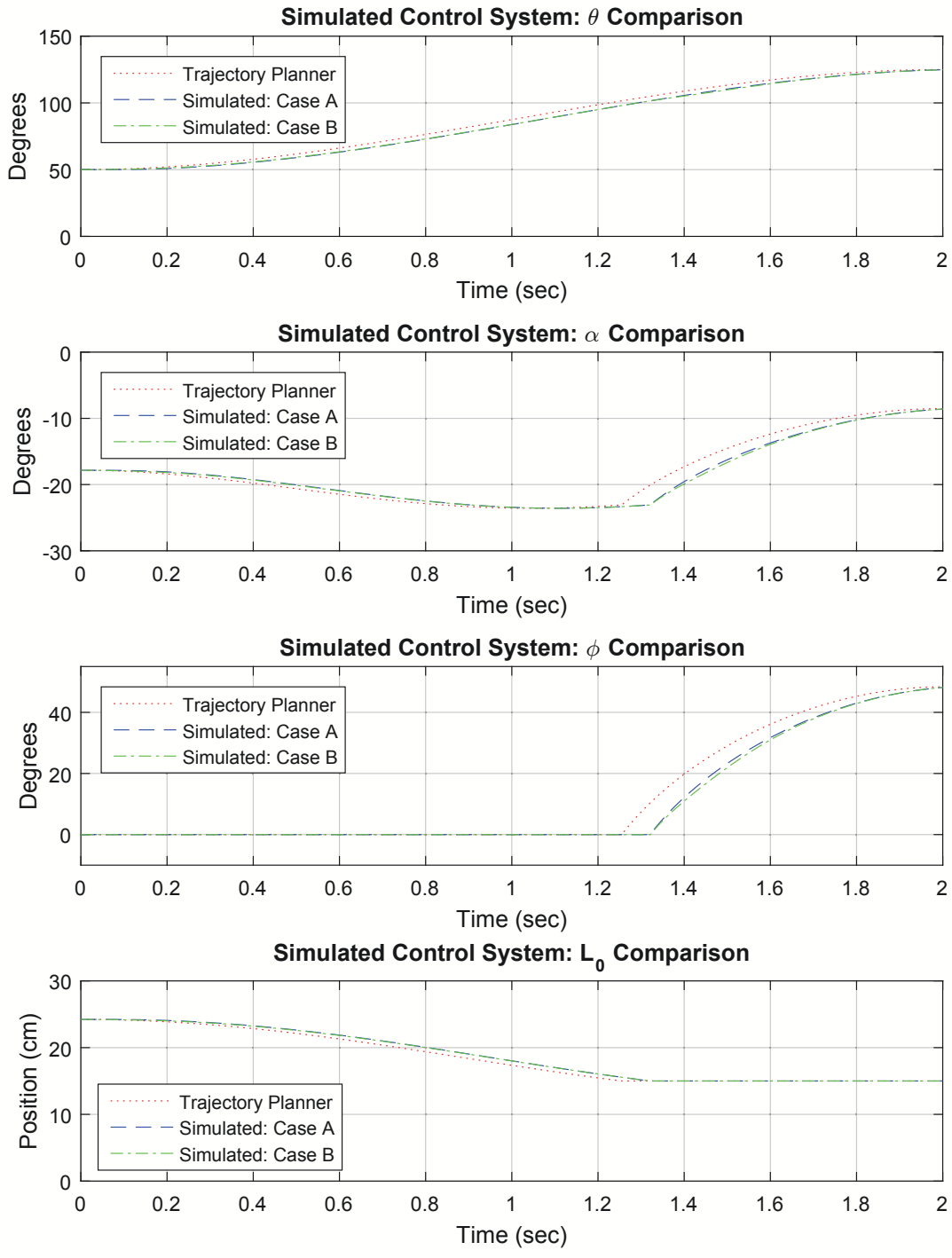

Figure 4.11: Simulated Kinematic Results for RRRP to RRRR

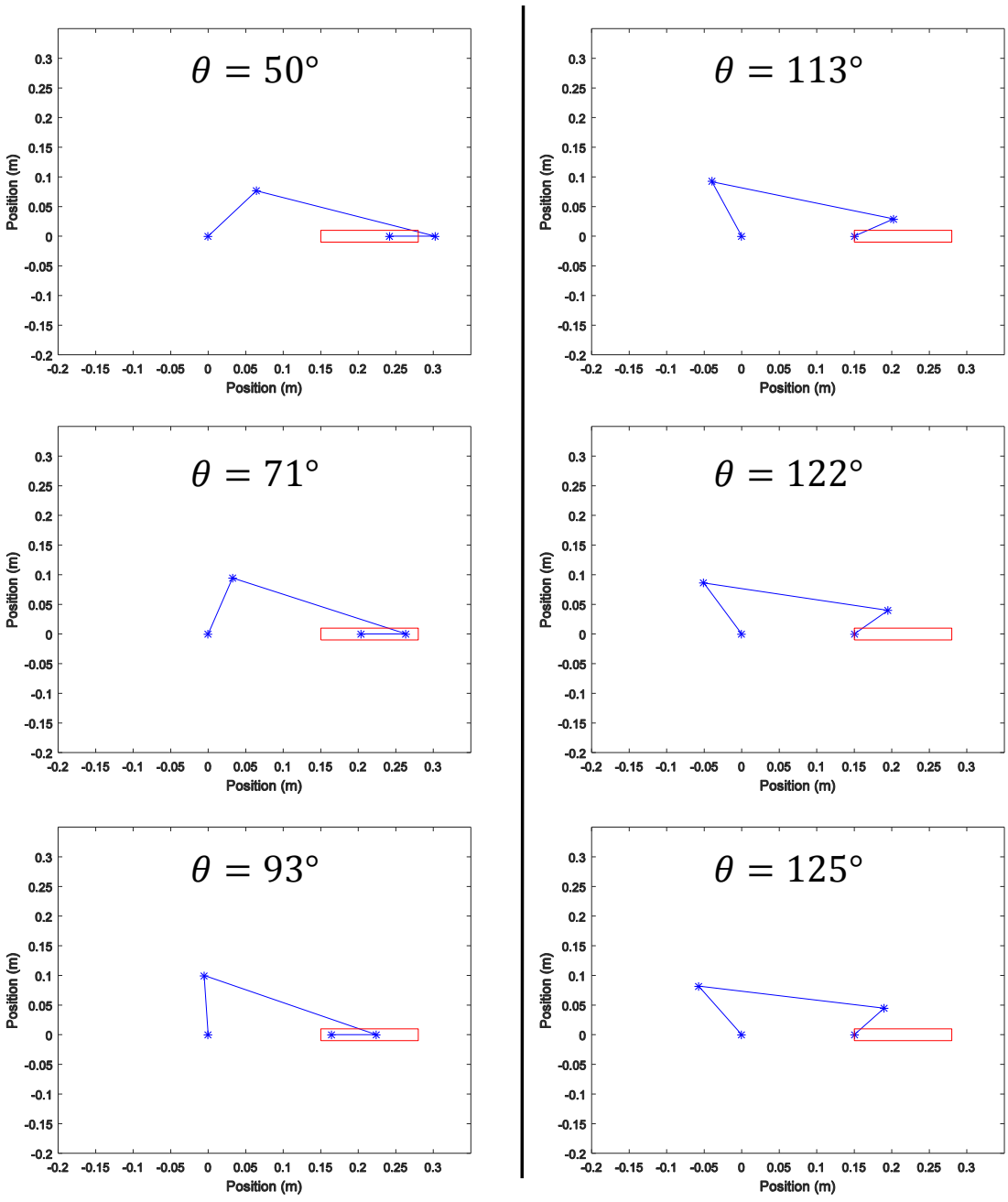

Figure 4.12: Simulated Results for RRRP to RRRR: Mechanism View

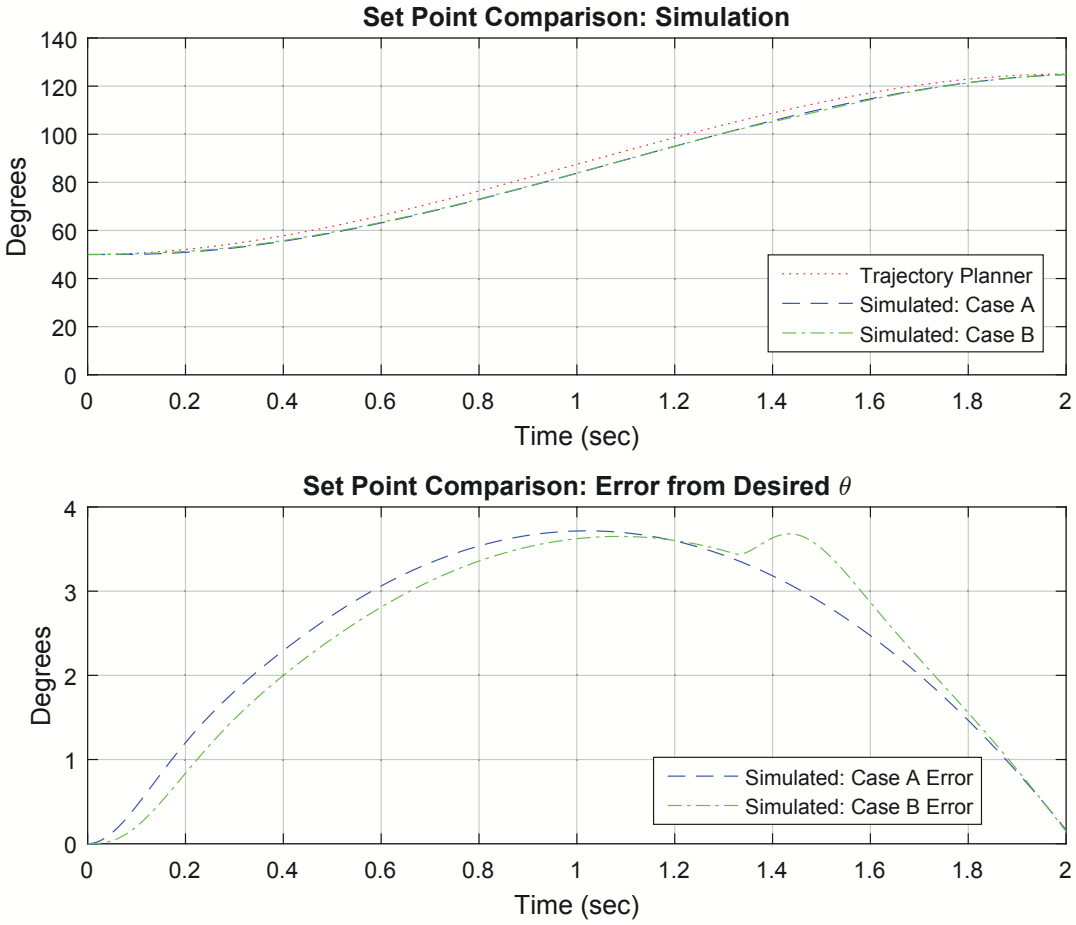

Figure 4.13: Simulated θ Results for RRRP to RRRR

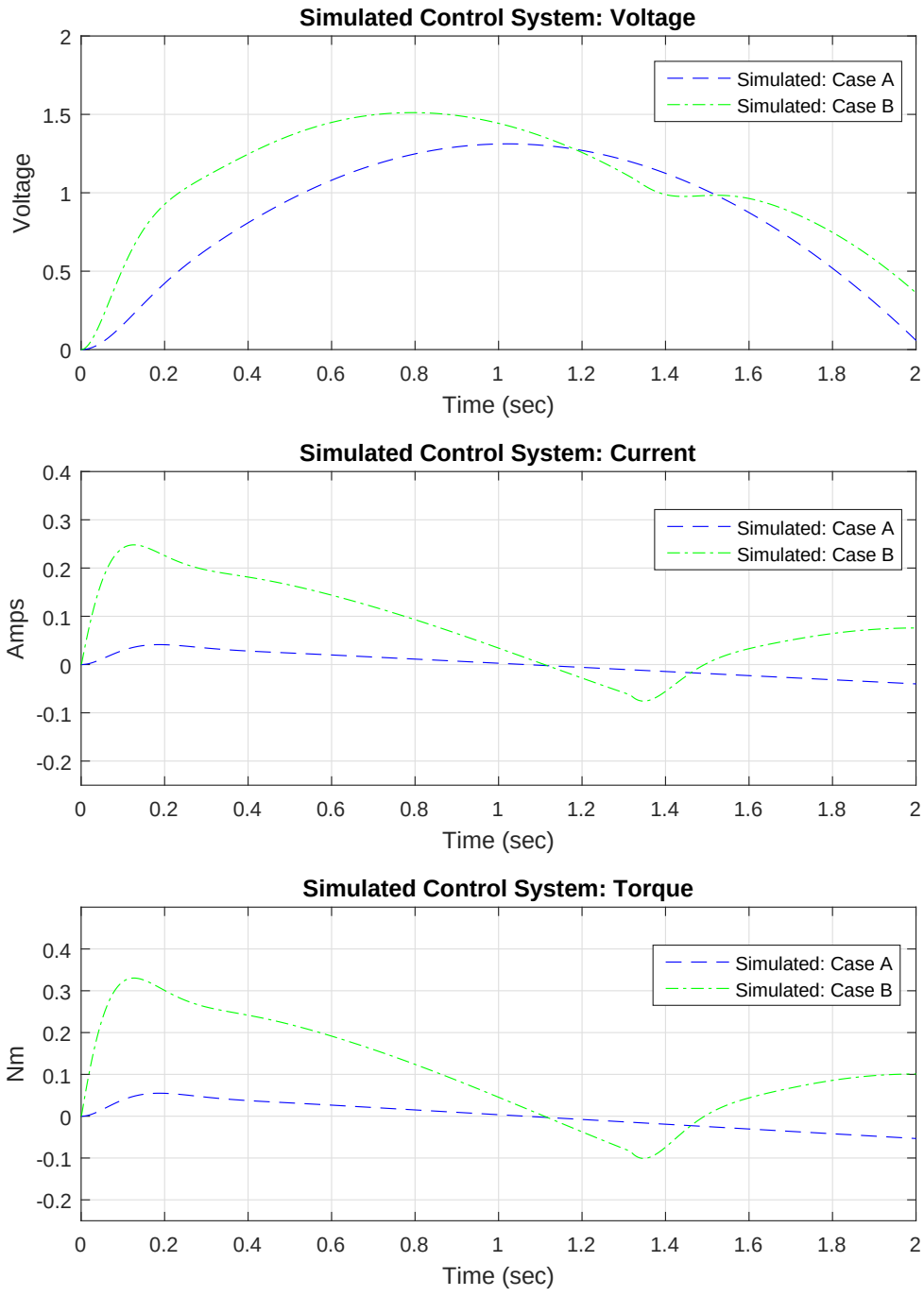

Figure 4.14: Simulated Electrical Results for RRRP to RRRR

4.5.3 RRRR to RRRP Configuration

The Mechanism will be simulated from the RRRR configuration to the RRRP configuration. Shown in Table 4.7 are the initial and final conditions for the simulation. The description of the trajectory generation, Case A, and Case B still hold true for the following model. Figure 4.15 shows the simulated results of the Mechanism switching from RRRR configuration to the RRRP configuration. Figure 4.16 specifically shows the angle θ and the error between the specific case and the desired generated trajectory. Figure 4.17 shows the simulated voltage, current and torque. Figure 4.12 are snapshots of the graphical representation create in Matlab for the Mechanism's motion. For the specific initial conditions, the graphics would be viewed in reverse order.

Table 4.7: Desired Trajectory Parameters for RRRR to RRRP Simulation Model

Description	Value	Units
Desired Starting Angular Position	$\theta_i(t_i = 0) = 125^\circ$	deg
Desired Ending Angular Position	$\theta_f(t_f = 2) = 50^\circ$	deg
Desired Starting Angular Velocity	$\dot{\theta}_i(t_f) = 0$	deg/s
Desired Ending Angular Velocity	$\dot{\theta}_f(t_f) = 0$	deg/s

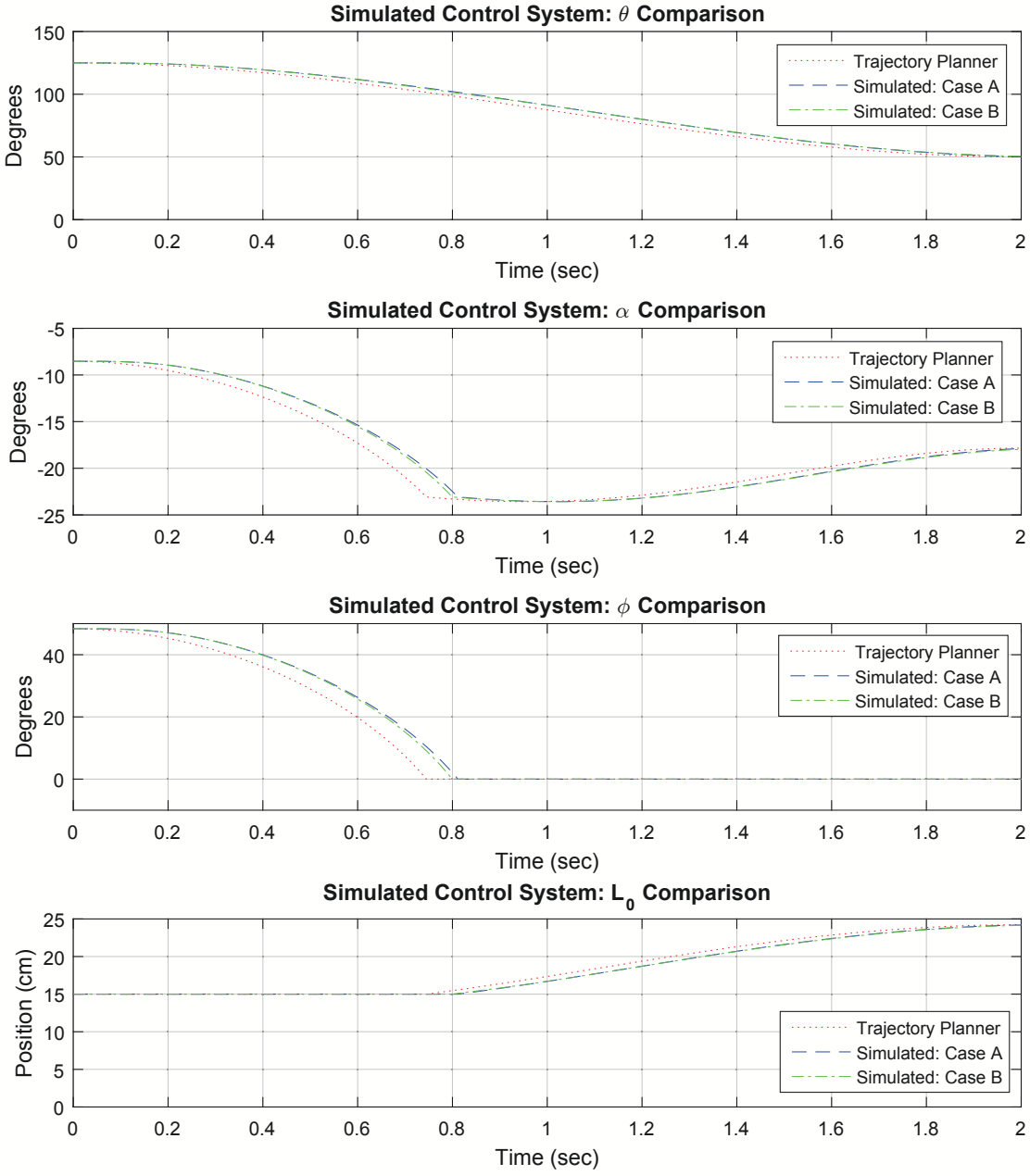

Figure 4.15: Simulated Kinematic Results for RRRR to RRRP

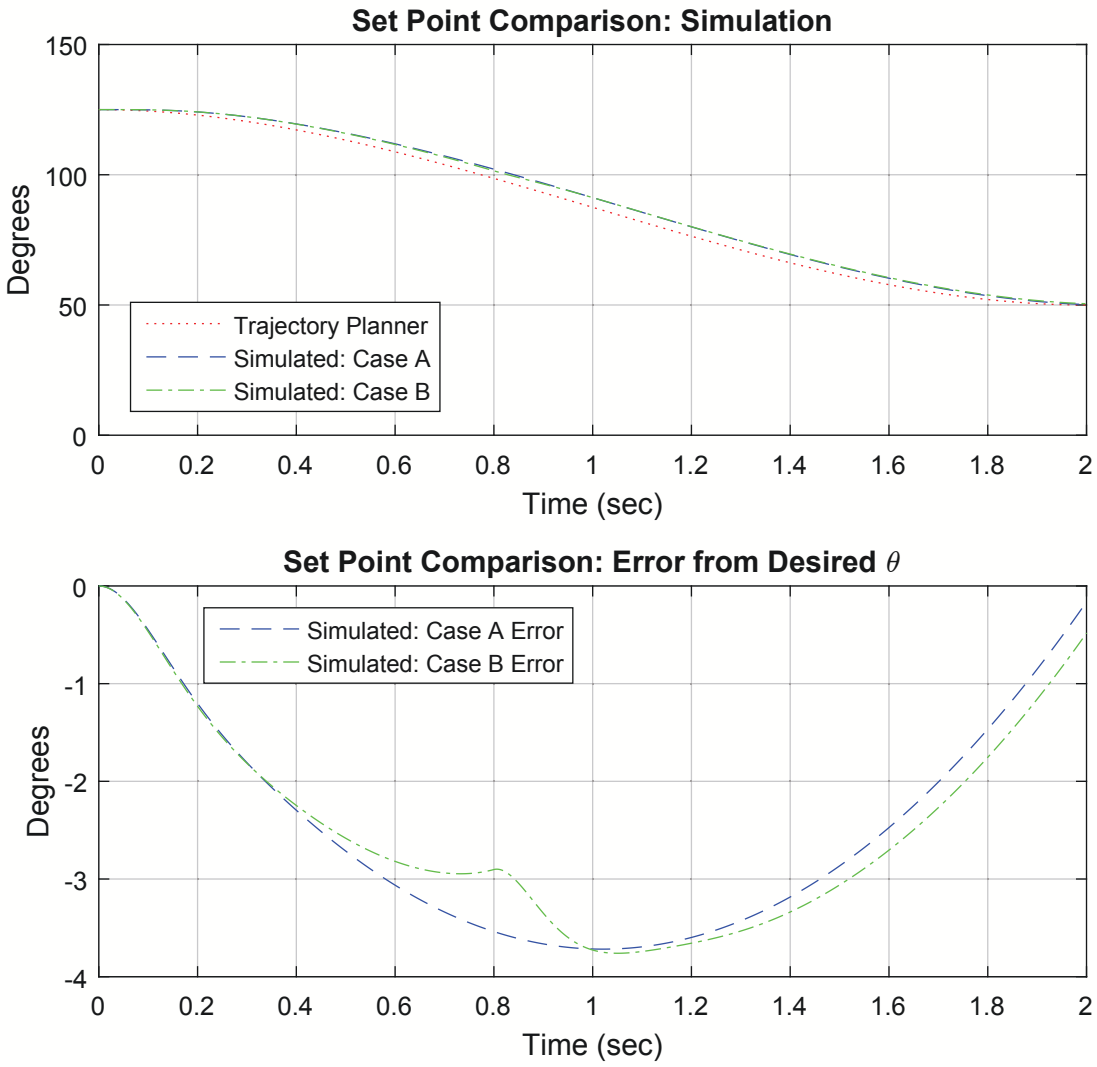

Figure 4.16: Simulated θ Results for RRRR to RRRP

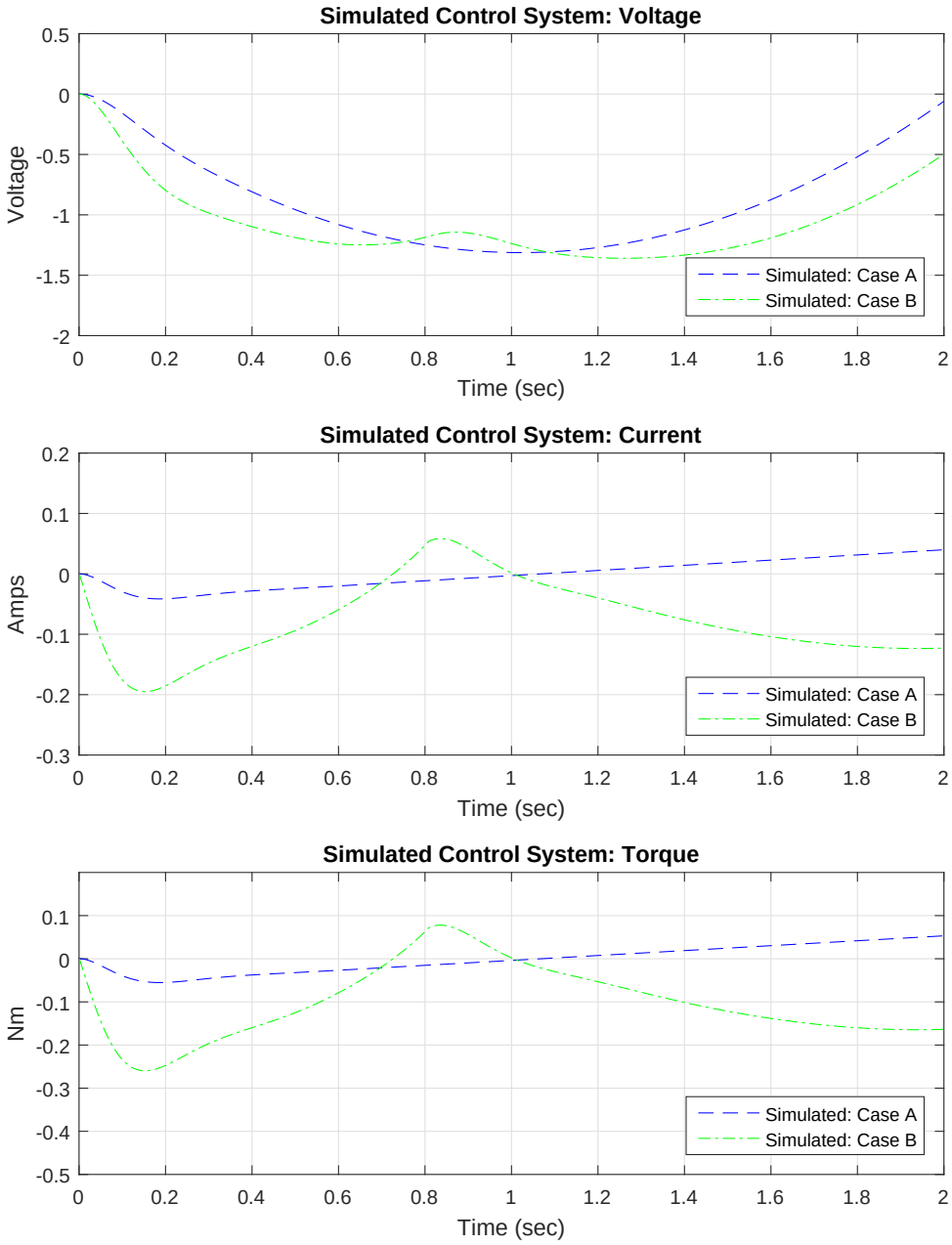

Figure 4.17: Simulated Electrical Results for RRRR to RRRP

4.5.4 Discussion of Simulation Results

Figures 4.11 and 4.15 show the results of the dynamically simulated RRRR-RRRP model. The figures show a clear transition point between dynamic models. These results were expected as the assumptions directly affect the results of the model. For example, the assumption that when $\phi = 0$ the model kinematically transitions from the RRRR configuration to the RRRP configuration. This is an idealized assumption and the true transition point is unknown.

Upon further examination, Case A lags behind the desired trajectory generation and Case B even further. The result is consistent with expectations. The larger the additional load the slower the system will respond. Case A has a smaller modeled mass and inertia, as it only incorporates the first link. Case B has a larger modeled mass and inertia, as it incorporates the entire Mechanism. The voltage and current are consistent with preliminary expectations. Further investigation is needed to better understand how much they differ from experimental results.

In addition, tolerances and bounce in a physical mechanism will cause error and are not currently modeled in the two different plants. Experimentation is necessary for better understanding and is completed in Chapter 5.

4.6 Summary of Mechanism System Modeling and Simulation

In summary, a trajectory planner was investigated and a third-order polynomial was selected. In addition, two plant models of the Mechanisms system were generated. A control system was implemented in code to represent a physical system. Finally, the two plant models were simulated with the control system and the results gathered. In the following chapter, experimentation of the Mechanism will be examined and is a necessary step to validating the models.

CHAPTER 5

MECHANISM EXPERIMENTATION

5.1 Experimental Introduction

Experimental verification of a plant model is necessary in any engineering application. The plant model of the RRRR-RRRP mechanism was dynamically simulated in the previous chapter. The dynamics were previously verified using SimMechanics, an extension of Matlab [26]. While SimMechanics was essential to validating the individual dynamic configurations, there is no substitute for a physical prototype validation. Therefore, a test stand containing the RRRR-RRRP mechanism with a DC motor was manufactured. The links are machined out of ABS plastic. The slider enclosure is 3D printed out of ABS plastic as well. The slider and motor fixture are machined out of aluminum for its material properties and durability. Pictures of the prototyped RRRR-RRRP Mechanism are shown in Figures 5.1 and 5.2. In addition, other pictures of the prototyped Mechanism are shown in Appendix Section D.4.

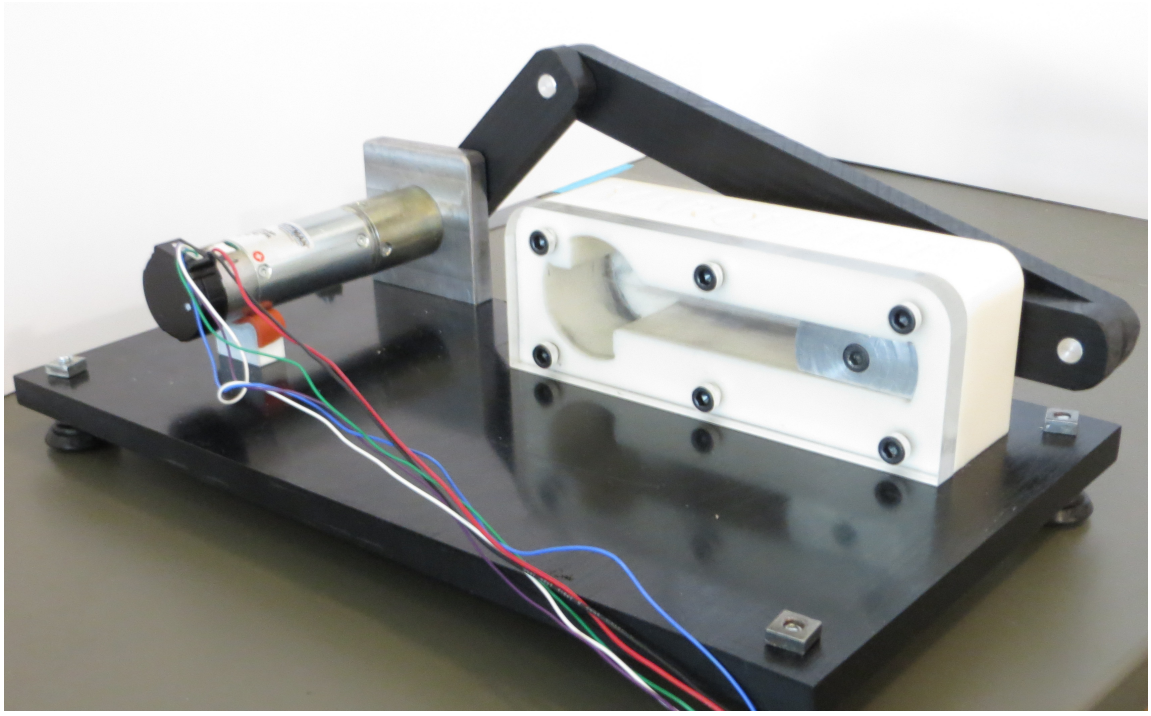

Figure 5.1: Prototyped RRRR-RRRP Mechanism

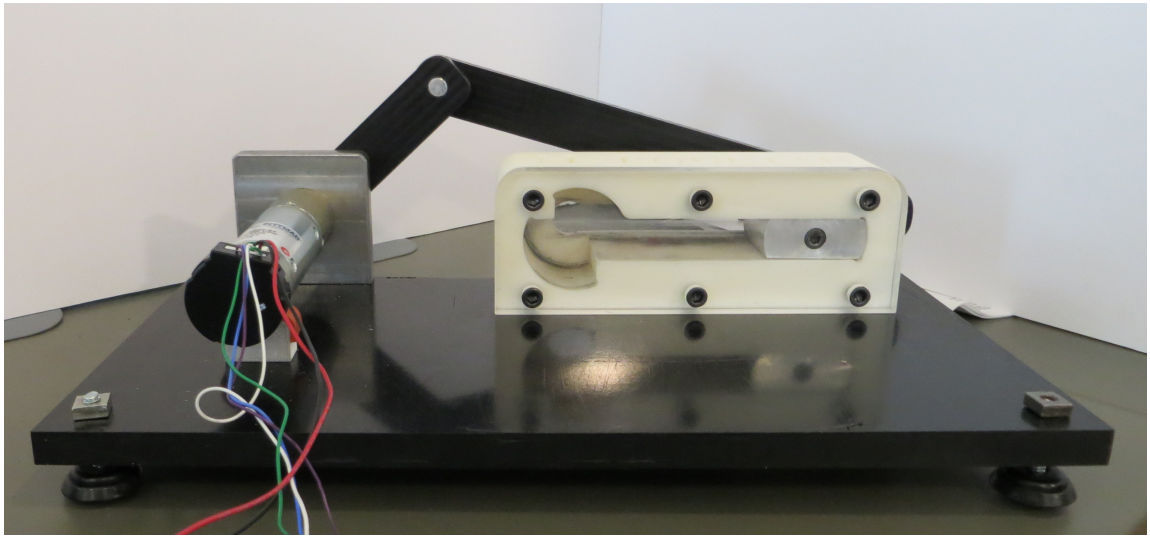

Figure 5.2: Prototyped RRRR-RRRP Mechanism

A single motor with an encoder drives the system because it only has one degree of freedom. Using the encoder the motor's rotational angle can be calculated. Using the derived kinematic equations and the encoder's angular position reading, the Mechanism's other angles can be calculated. In addition, a current sensor will indirectly provide data for the torque at the motor output shaft.

The chapter outline is as follows. First, the experimental setup will be examined in terms of hardware and software. The needed components will be listed and an overview of the software is provided. Finally, the prototyped RRRR-RRRP mechanism will be physically tested. The Mechanism will be positioned in the RRRR configuration and then run until the RRRP configuration and vice versa. The angular position, current, and torque will be logged for examination. Numerous trials were conducted to verify repeatability. The trials will be discussed in more detail in the following sections. Chapter 6 will compare model simulations to the results.

5.2 Experimental Setup

The experimental setup can be broken into two main sections: hardware and software. The necessary components will be examined in the Experimental Hardware section. In the Experimental Software section, a brief overview of the code implemented in LabView will be examined.

5.2.1 Experimental Hardware

The major hardware components of the Mechanisms test stand are the NI cRIO 9074, NI 9505, a Pittman 8543 brushed direct current (DC) motor and a Pittman E35A encoder. The NI cRIO 9074 is a real time processor and a field-programmable gate array (FPGA) which allows the user to plug in various

input or output (IO) modules. The cRIO 9074 acts as the communication hub between the computer and motor driver. Real time control can be implemented using this processor. The NI 9505 module is a motor driver with a full H-bridge design. The NI 9505 module is plugged directly into the cRIO 9074. The Pittman 8543 series brushed DC motor can be directly connected to the NI 9505; no additional circuity is necessary. Using the NI 9505 and cRIO 9074 allows for direct connectivity to and from the human machine interface (HMI) to the control of the DC motor. In addition, the NI 9505 provides a current sensing functionality and is vital to relate to torque. The current measurements were verified with a multi-meter from one to seven amps. The NI 9505 provides an instantaneous value of current and must be filtered using a smoothing function to determine the average value. At low currents, readings fluctuated on both the NI 9505 and a multi-meter. A high-side current shunt was also examined for additional verification of current. After examination, the current shunt was found to not be accurate enough for the necessary application. The NI 9505 will be used but the results will need to be examined carefully.

Figure 5.3 provides an overview of the hardware components and how they are connected together. A user selects inputs on the human-machine interface (HMI). The cRIO then communicates to the motor drive and signals a voltage to the motor. The motor then is actuated and turns. The encoder reads the pulse train and sends it back to the cRIO for processing. Figure 5.4 is a more detailed diagram of the the hardware implementation.

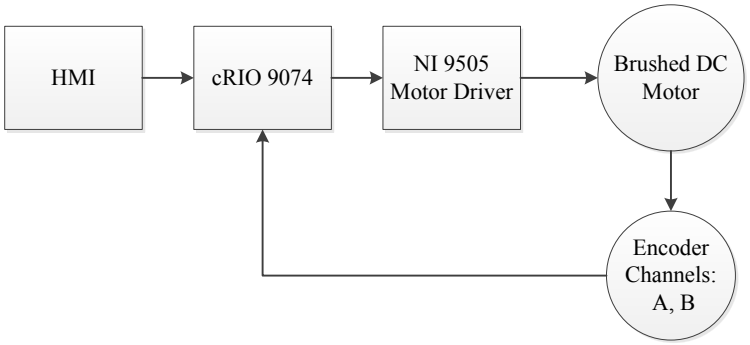

Figure 5.3: Hardware Implemented Overview

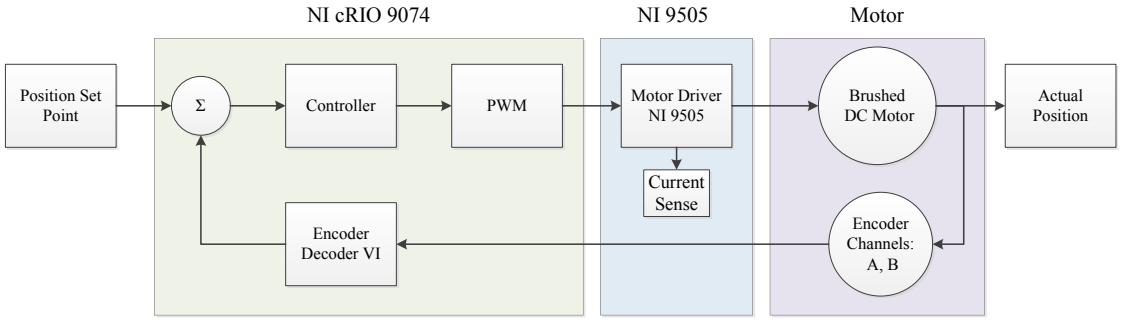

Figure 5.4: Hardware Implemented

Experimental Hardware: Motor Selection

The 8543 DC Pittman motor was selected because it is able to output high torque at low speeds due to its 36:1 gear ratio. As discussed previously, Pittman also provides detailed technical data for motor specifications. These are necessary to controlling a motor effectively. The Pittman encoder, E35A, is an incremental optical encoder that generates a quadrature signal. The encoder reads at 500 counts per revolution (cts/rev). The encoder sends its signals to the NI 9505 where the signal is decoded. The angular position and direction of the motor's shaft can be found.

5.2.2 Experimental Software

LabVIEW 2014 was used to implement the control algorithms for the experiment. The software is a visual based programming language with a development environment and a system-design platform. A motor position controller was implemented using LabVIEW. While modeling the system, a block diagram was created to represented the physical satem and is shown in Figure 4.1. The physical system follows the flow chart very closely. First, a cubic polynomial trajectory planner was used to develop a set path of what the motor should follow; an example trajectory is found in Figure 4.2. The cubic polynomial was selected because of the ability to control the starting and ending angle of the motor. In addition, a cubic polynomial can also be implemented quickly and efficiently. Next, a P controller was implemented to minimize tracking error. An output PWM signal proportional to the angular position error is sent to the NI 9505 motor driver. The driver converts the signal to a voltage and drives the motor. Next, the motor encoder reads the actual position of the motor. The process is repeated and the data logged. Through the implementation of the hardware and software, minimal positional tracking error was the obtained for the Mechanism. Matlab was then used to calculate the remaining kinematics of the RRRR-RRRP mechanism.

Shown in Figure 5.5 is the control systems verification of the cRIO. A desired trajectory is supplied and the controller drives the motor correctly. A slight time delay is present initially but then corrects itself at the end.

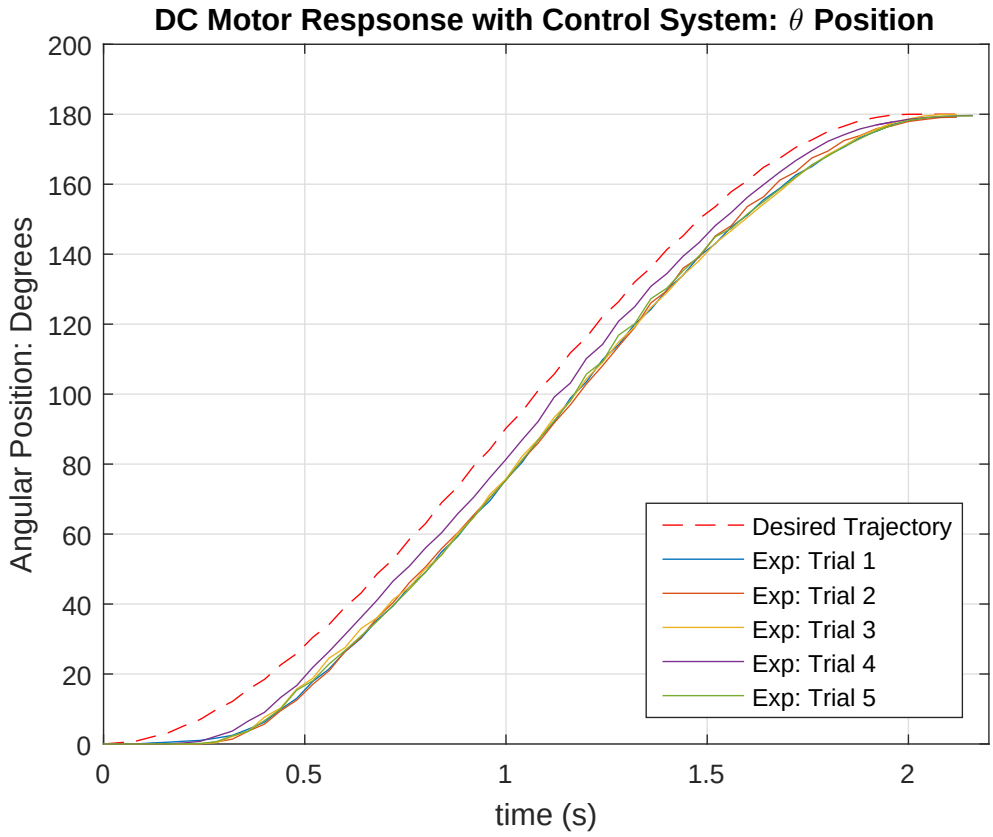

Figure 5.5: Control System Verification using the Pittman 8543 24.0 V DC Motor

5.3 Experimental Testing and Results

5.3.1 Introduction

As stated previously, the prototype RRRR-RRRP mechanism was to be experimentally tested. The goal of the experimentation was to record pertinent data and verify the systems repeatability. The Mechanism was positioned in two different starting positions for the tests. First, the Mechanism was positioned in the RRRP configuration then moved using the DC motor to the RRRR configuration. A third order trajectory was generated a priori and then implemented in real time. The positional data in addition to other parameters

were logged for examination. Once logged, Matlab was used to calculate the remaining kinematics of the Mechanism. The derived kinematics of the Mechanism were considered ideal when calculating the other components. Several different trials with varying lengths of time were completed to see how velocity plays a factor in the Mechanism. Each new final time, five trials were conducted to measure repeatability.

Second, the Mechanism was positioned in the RRRR configuration then moved using the DC motor to the RRRP configuration. Similarity, the trajectory was generated a priori and then implemented in real time. The data was logged for examination and the kinematics were calculated based on the input angle θ. Again, numerous trials were logged. Only one sample set of data has been provided in its entity for both configurations. The complete set of data can be found in Appendix D.

5.3.2 Experimental Results

Table 5.1 is the experimental parameters for the Mechanism and are used for the experimental tests. The parameters are necessary for understanding the dynamics of the system and will be vital when simulating the system. Note that M_3 and L_{3c} have been examined and calculated based on link length three and the mass of the slider to adjust for the different masses and lengths depending on the configuration.

RRRP to RRRR Configuration

The following is the experimental data gathered from the prototype Mechanism for the RRRP to RRRR configuration. Table 5.2 parameters are the initial conditions of the third-order polynomial trajectory planner. The notation used in the table is consistent with Section 4.2 for trajectory generation. The

Table 5.1: Experimental Parameter Inputs

Parameter	Units	Numeric
Link Lengths	m	$L_0 = 0.127 + \Delta L_0$
Link Lengths	m	L_1=0.0890, L_2=0.2280, L_3=0.0503
Mass Centers	m	L_{ic}=$L_i/2$, i=1,2
Mass Centers	m	L_{3c}=0.0106
Link masses	kg	M_1=0.060, M_2= 0.1330 ,M_3=0.1320
Moment of Inertia	$kg \cdot m^2$	I_i=$M_i L_i^2/12$, i=1,2,3

trajectory planner are the input set points to the controller. The only parameter changed for each set of experimental trials was the final generated trajectory time (t_f or T_{final} in the figures). Figure 5.6 is the compiled pictures of the prototyped Mechanism at different phases. The pictures provide insight into how the Mechanism truly moves. Shown in Figures 5.7 and 5.9 are examples of the experimental raw data. Numerous other data sets are shown in Appendix D. Figure 5.8 uses the data from trial one with a t_f of 1.5 seconds. The data set is comparable to other values at a t_f of 1.5 seconds.

Table 5.2: Desired Trajectory Parameters

Description	Value	Units
Desired Starting Angular Position	$\theta_i(t_i) = 46^\circ$	deg
Desired Ending Angular Position	$\theta_f(t_f) = 179^\circ$	deg
Desired Starting Angular Velocity	$\dot{\theta}_i(t_i) = 0$	deg/s
Desired Ending Angular Velocity	$\dot{\theta}_f(t_f) = 0$	deg/s

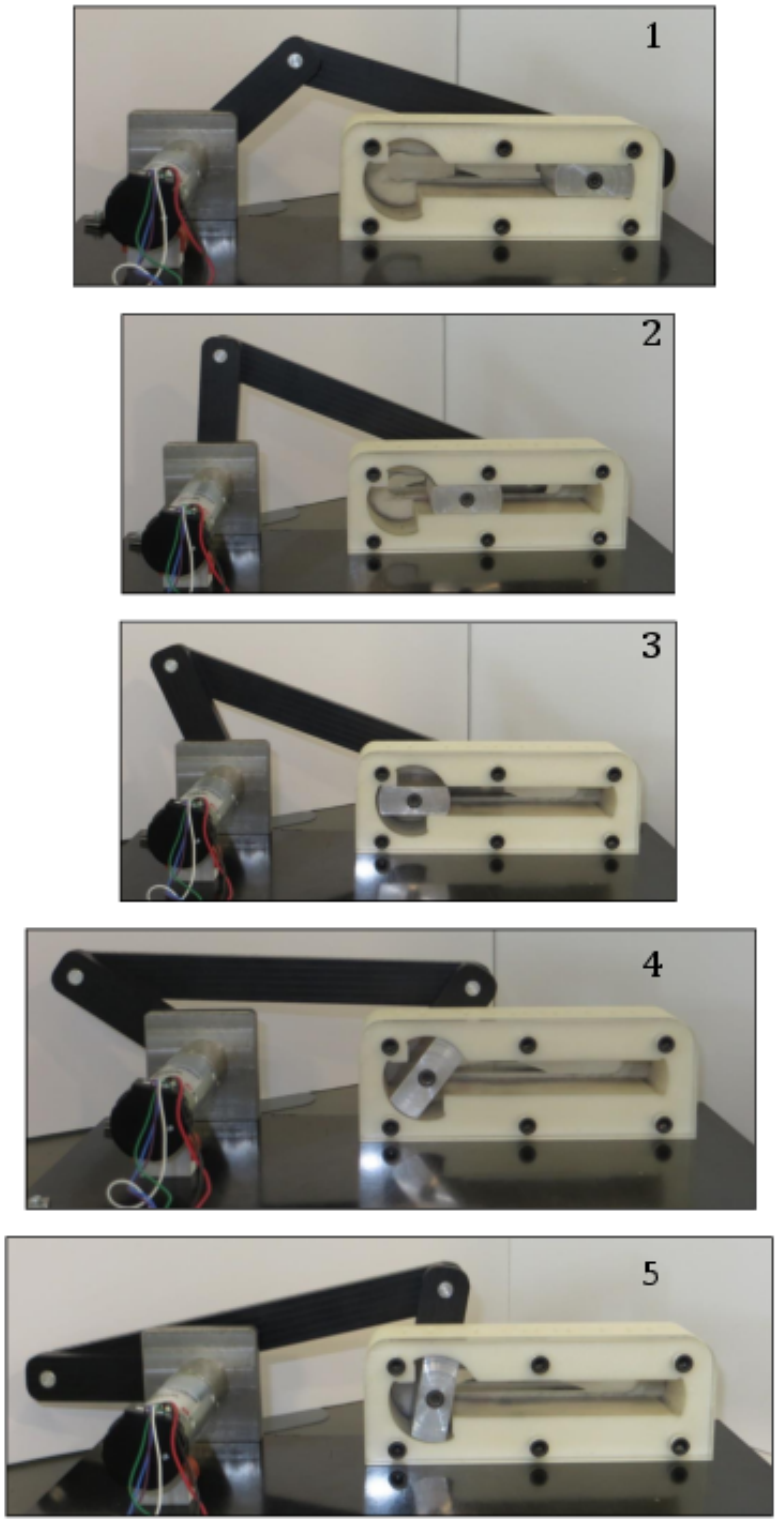

Figure 5.6: Compiled Pictures of RRRP to RRRR Configuration

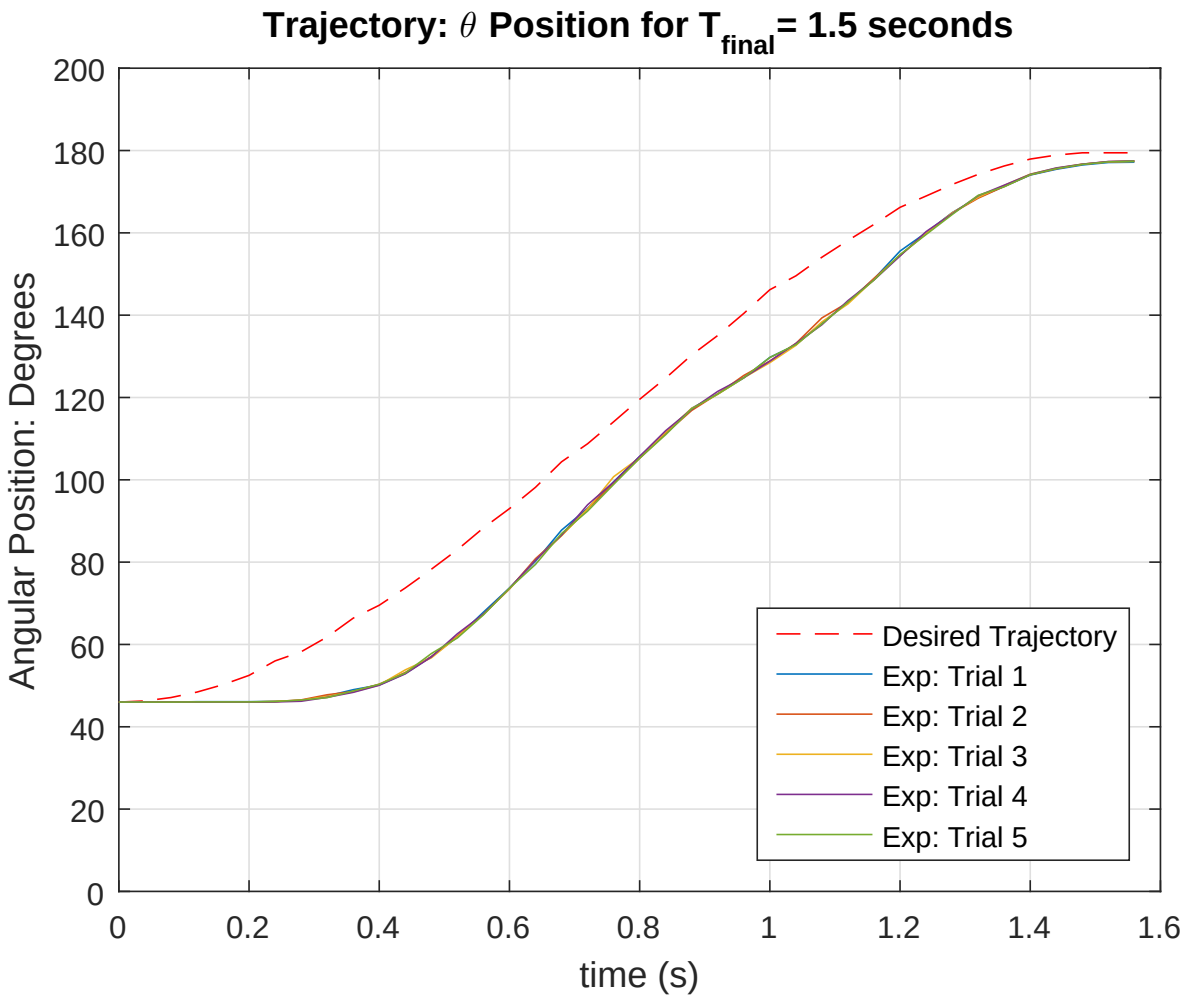

Figure 5.7: Experimental RRRP to RRRR- θ measurement, $t_f = 1.5$ seconds

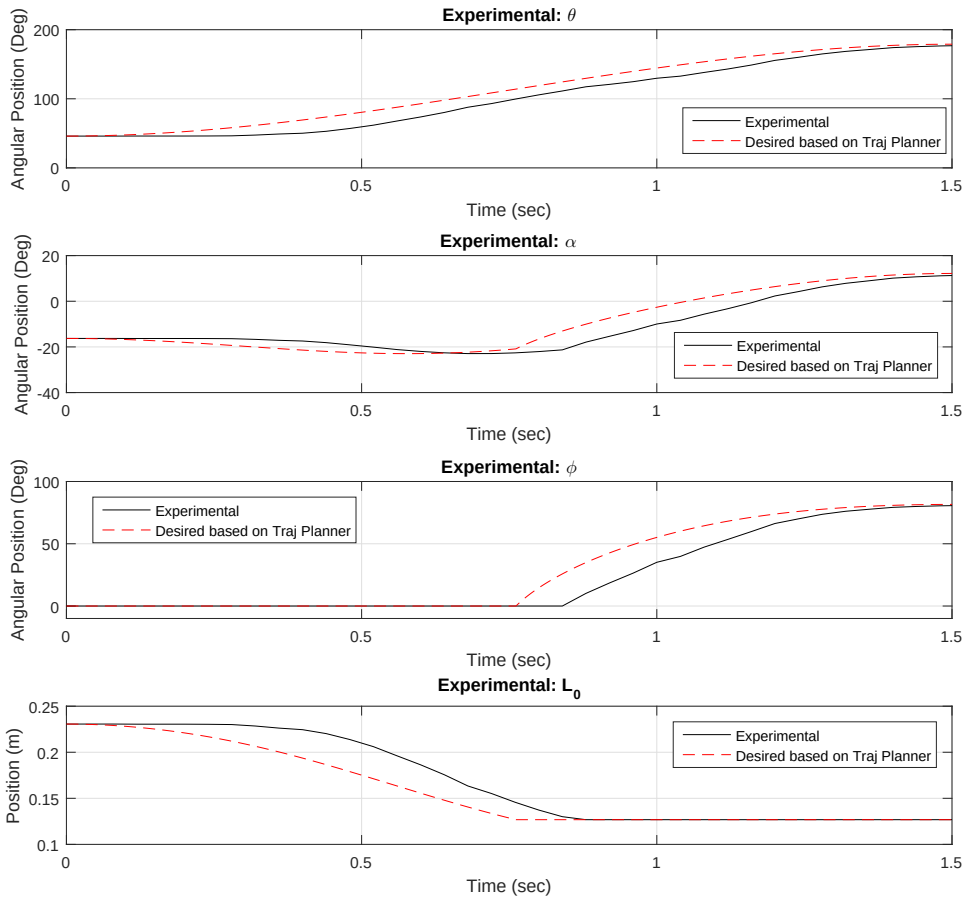

Figure 5.8: Experimental RRRP to RRRR- Full kinematics measurement, Trial 1:$t_f = 1.5$ seconds

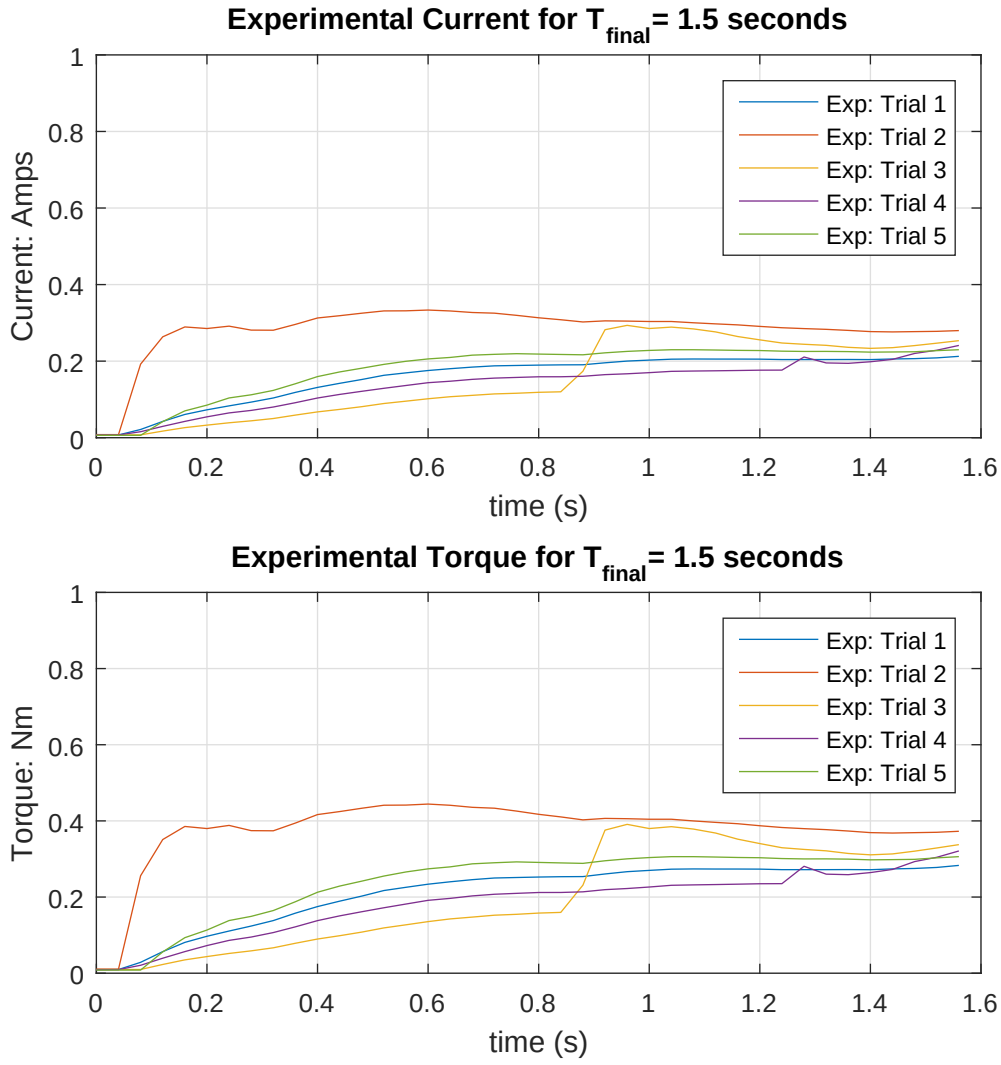

Figure 5.9: Experimental RRRP to RRRR- Current and Torque measurement, $t_f = 1.5$ seconds

RRRR to RRRP Configuration

The following section is the experimental data gathered from the prototype Mechanism for the RRRR to RRRP configuration. Table 5.3 parameters are the initial conditions of the third-order polynomial trajectory planner. The notation used in the table is consistent with Section 4.2 for trajectory generation. The trajectory planner are the input set points to the controller. The only parameter changed for each set of experimental trials was the final generated trajectory time (t_f or T_{final} in the figures). Figure 5.12 uses the data from trial one with a t_f of 1.0 seconds. The data set is comparable to other values at a t_f of 1.5 seconds.

Table 5.3: Desired Trajectory Parameters for RRRR to RRRP Simulation

Description	Value	Units
Desired Starting Angular Position	$\theta_i(t_i) = 46^\circ$	deg
Desired Ending Angular Position	$\theta_f(t_f) = 179^\circ$	deg
Desired Starting Angular Velocity	$\dot{\theta}_i(t_i) = 0$	deg/s
Desired Ending Angular Velocity	$\dot{\theta}_f(t_f) = 0$	deg/s

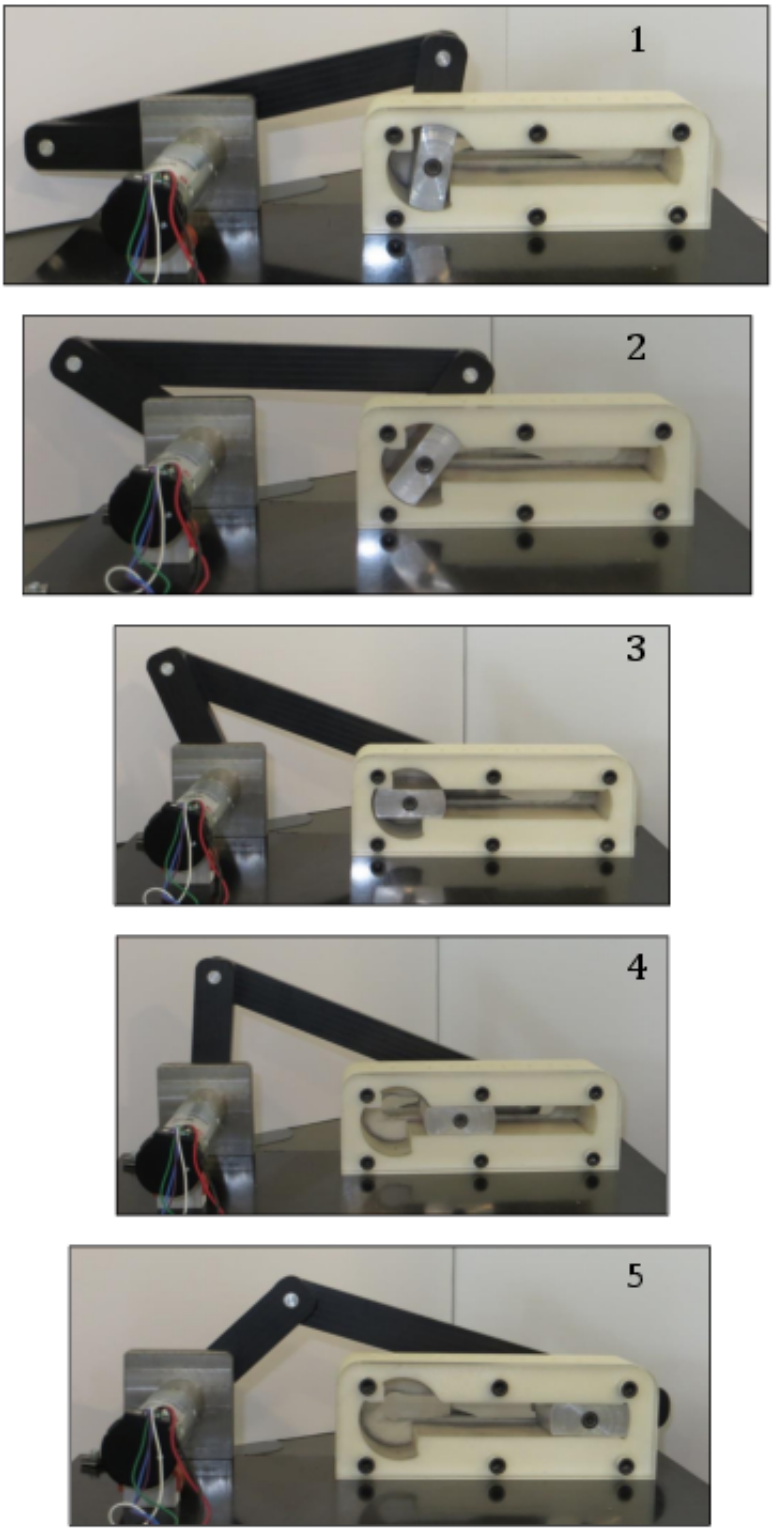

Figure 5.10: Compiled Pictures of RRRR to RRRP Configuration

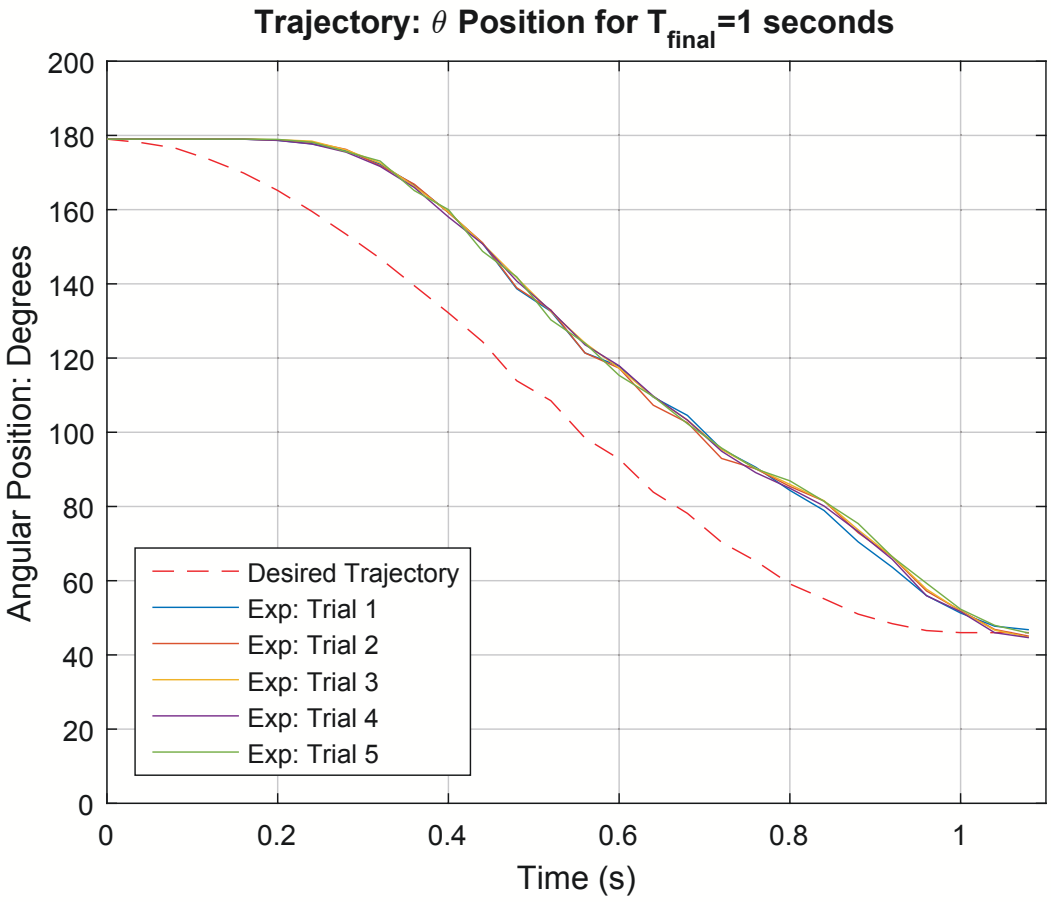

Figure 5.11: Experimental RRRR to RRRP- θ measurement, $t_f = 1.0$ seconds

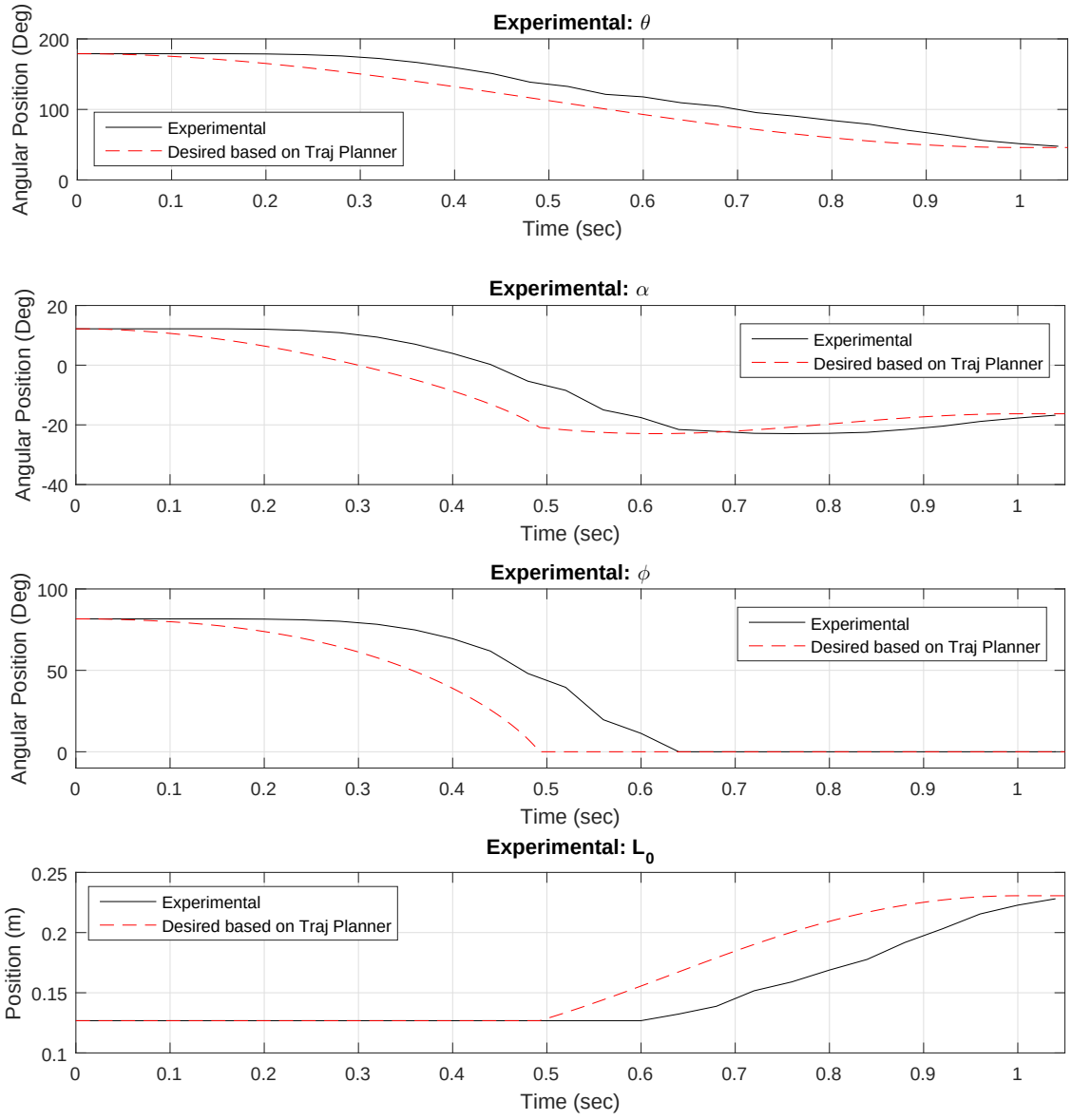

Figure 5.12: Experimental RRRR to RRRP- Complete Kinematics, $t_f = 1.0$ seconds

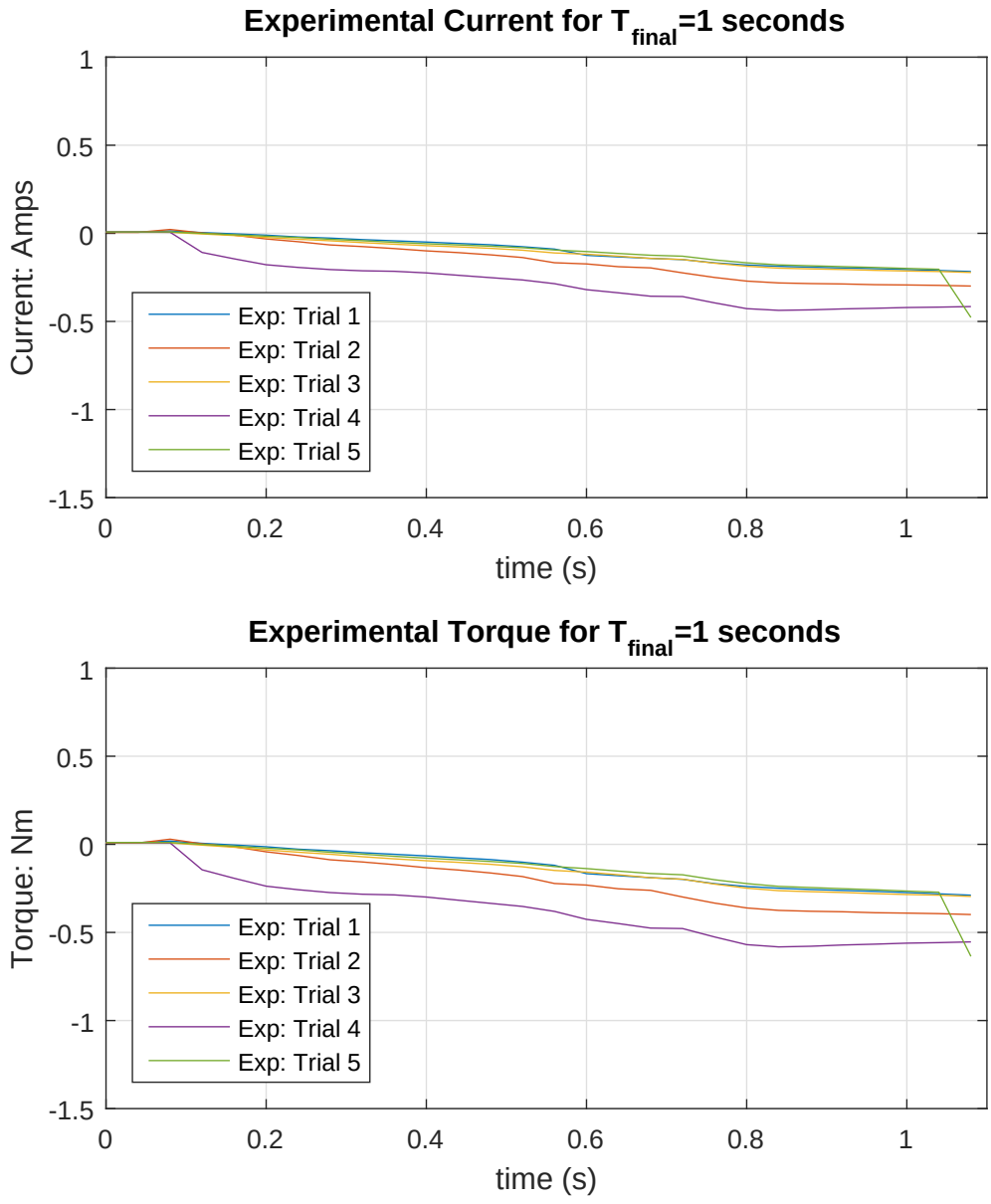

Figure 5.13: Experimental RRRR to RRRP- Current and Torque measurement, $t_f = 1.0$ seconds

5.4 Discussion of Experimental Results

In the following sub-sections are discussion of the RRRP to RRRR Configuration and the RRRR to RRRP Configuration.

5.4.1 RRRP to RRRR Configuration

Several different final times were examined for the desired trajectory. The following times final times (t_f) were considered: 0.75 seconds, 1.0 seconds, 1.5 seconds, 3.0 seconds, and 6.0 seconds. Five trials were conducted at each final time providing 25 data sets of the angles for the RRRP to RRRR configuration. At all of the final times the Mechanism was able to change from the RRRP configuration to the RRRR configuration. Numerous trials were completed to verify accurate measurement and consistent results.

First, the 0.75 second case was considered for the final time. After conducting the experiments five times, the experimental angular position data shows that that θ has a delayed start and overshoots the desired trajectory. A large current spike also occurs at 0.45 seconds. The error becomes very large at 0.45 seconds and causes the maximum output from the control system which translates to higher current output readings. In addition, with a final time of 0.75 seconds there are only 19 data points for the desired trajectory; the cRIO has a loop rate of 0.04 seconds creating almost an effective step input to the system. If a final time under 0.75 seconds was selected it could be expected that the angular position would over shoot and the current measurements would spike.

Next, 1.0 seconds and 1.5 seconds cases are examined. The results are very comparable. Both reach the desired position at the approximate desired time. A time delay is present in both data sets as well. The current readings are both very similar. The 1.0 second experimental results have slightly higher values. The

result is expected as the system is required to move the same distance in a shorter time. This translates to more current being supplied to the DC motor to keep up with the demand.

Finally, 3.0 seconds and 6.0 seconds are examined. The results are very comparable. Both undershoot the desired position at the desired time. A time delay is present in both data sets as well. A bump in the data can be seen; the bump is where the mechanism transitions from the RRRP configuration to the RRRR configuration. The Mechanism could stop moving and have to overcome the higher breakaway friction value. The current readings are both very similar and a higher current is seen at the transition point. A higher current value at the transition point indicates that the motor is required to supply more torque to the Mechanism to try to follow the desired trajectory.

Overall, the best final time for the RRRP to RRRR configuration is either 1.0 seconds or 1.5 seconds while in the specific application. Either one will produce highly accurate results. The 1.0 second final time achieves minimal steady state error while the 1.5 seconds final time tracks the desired trajectory very well. One draw back to the 1.5 seconds is that it undershoots slightly.

5.4.2 RRRR to RRRP Configuration

Several different final times were examined for the desired trajectory. Numerous trials were completed to verify accurate measurement and consistent results. The following times final times (t_f) were considered: 0.5 seconds, 0.75 seconds, 1.0 seconds, 1.5 seconds, 3.0 seconds, and 6.0 seconds. Five trials were conducted at each final time providing 30 data trials of the RRRR to RRRP configuration. At all of the final times the Mechanism was able to change from the RRRR configuration to the RRRP configuration.

First, the 0.75 seconds was considered for the final time. After conducting the experiments five times, the experimental angular position data shows that that θ has a delayed start and achieved an adequate response. The final time was then set to 0.5 seconds and 1 seconds respectively. Through experimentation, the researcher determined that the final time of 0.5 and 0.75 seconds produces some overshoot.

For trials with a final time of 1.5, 3.0 and 6 seconds, the slider became stuck in the transition point until the torque was high enough to overcome the force opposing it. The specific phenomenon can be seen by the elevated current and is shown in Appendix Figure D.14. The current is directly related to the torque. Once the necessary torque was achieved, the system became free of the transition point and overshoots the desired position. Once the system overshoots, the controller takes over and drives the slider back to the desired position. Through experimentation, a final time of less than 1.5 seconds is suggested to obtain the best results.

5.4.3 Observations of Prototype

There are several potential reasons that the slider could be getting stuck in the transition phase. One possibility are the tolerances of the prototype. The 3D printer used has accuracies up to $\pm$ 2.54 millimeters ($\pm$ 0.01 inches) [37]. The tolerances are adequate but does leave room for slop. Over, 150 trials have been conducted using the prototype and wear is noticeable on the contact surfaces. The surfaces include the transition point and the surface when the Mechanism is in the RRRP configuration. The aluminum shows no signs of wear while the ABS variable joint block does. For future Mechanisms, a block should be machined out of either aluminum or steel. Doing this will eliminate the potential failure to wear.

In addition, assembly is another potential opportunity for improvement. In the prototype, the links are currently connected together with a snap ring and a pin with a groove. The pins on some of the links have started to become loose and the press fit failing. With the loose pins, the forces are not transmitted properly though the Mechanism causing an issue. One way to eliminate the issue is to redesign the links with minimal out of plane movement.

5.5 Experimental Summary

In summary, the experimental software and hardware configurations were presented. LabView with a P controller was implemented to control the Mechanism. Numerous trials of experimental datal were logged for verification. The Mechanism was experimentally tested from the RRRP configuration to the RRRR configuration and vice-versa. In the next chapter, the experimental results will compared to the simulations results and discussed in detail.

CHAPTER 6

COMPARISON OF SIMULATION AND EXPERIMENTAL RRRR-RRRP MECHANISM RESULTS

6.1 Introduction

The Mechanism was previously modeled with two different cases in Chapter 4. In addition, the prototyped Mechanism was physically tested in Chapter 5. Now, the models and prototyped Mechanism will be compared for validation. With the validation of a plant model, future RRRR-RRRP Mechanisms can be designed and analyzed easily. The goal of the models are to be able to conduct simulated "physical" experiments in Matlab. The approach taken for modeling was very similar to the experimental prototype implementation.

For validation, the Mechanism will be tested in two different starting configurations using the developed control system and trajectory planner. For the first test, the Mechanism will start in the RRRR configuration and transition to the RRRP configuration. For the second test, the Mechanism will start in the RRRP configuration and transition to the RRRR configuration. The starting and ending time and angular positions will be specified for each test. The kinematics, kinetics, and current will be logged or calculated for both the experimental test. Once logged, the data will be compared to one trial; then the data will be compared to the average data gathered. A recommendation for the optimal plant model will be made.

6.2 Simulation and Experimental RRRR-RRRP Mechanism Results

As stated previously the Mechanism will be tested in two different starting positions. First, the RRRR to RRRP configuration will be examined and then the RRRP to RRRR configuration. All simulation solvers and details have been

outlined in Section 4.5 and will remain consistent for this chapter. Table 6.1 are the parameters for the Mechanism and are used for both the simulations and physical testing. The parameters come from the prototyped physical Mechanism. These parameters are necessary for understanding the kinematics and kinetics of the system. Note, M_3 and L_{3c} have been examined and calculated based on link length three (L_3) and the mass of the slider. The effective center of mass and mass of the two together were found. The two were modeled in this nature to account for the two being a rigidly connected. If the slider and link three are not parallel the current values do not hold true. L_0 presents the fixed length from the origin plus any additional change (ΔL_0). Note, all figures that reference Trajectory Planner use the trajectory planner's θ as the input for the kinematics. The kinematics are then calculated and the result plotted. These calculations do not include kinetics and are assume the kinematics to be ideal.

Table 6.1: Experimental and Simulation Parameter Inputs

Parameter	Units	Numeric
Link Lengths	m	$L_0 = 0.127 + \Delta L_0$
Link Lengths	m	L_1=0.0890, L_2=0.2280, L_3=0.0503
Mass Centers	m	L_{ic}=$L_i/2$, i=1,2
Mass Centers	m	L_{3c}=0.0106
Link masses	kg	M_1=0.0600, M_2= 0.1330 ,M_3=0.1320
Moment of Inertia	$\text{kg} \cdot \text{m}^2$	I_i=$M_i L_i^2/12$, i=1,2,3

6.2.1 Test One: RRRP to RRRR Configuration

Test one will examine the Mechanism moving from the RRRP configuration to the RRRR configuration. Outlined in Table 6.2 are the values input into the third-order trajectory planner. The planner will generate a specific

path that the system must follow. At the end of t_f, the planner generates constant values of $\theta_f(t_f)$ for position for an additional 1.0 seconds. The additional values are to ensure the simulated and prototyped Mechanism are given enough time to reach the desired values. A time delay may be present in the system. A proportional controller will be used control the angular position of θ on the Mechanism in both simulation and in the physical experiment. The simulated models will first be compared to trial one of the previously found RRRP to RRRR prototyped results. These results are outlined in detail in Appendix Section D.2. Next, the simulation results will be compared to all five trials at that specific t_f. Presenting both sets of data shows insight into how the simulation compares to one set of data as well as many.

Table 6.2: Desired Trajectory Parameters for RRRP to RRRR Simulation

Description	Value	Units
Desired Starting Time	$t_i = 0$	s
Desired Ending Time	$t_f = 1.0$	s
Desired Starting Angular Position	$\theta_i(t_i) = 46^\circ$	deg
Desired Ending Angular Position	$\theta_f(t_f) = 179^\circ$	deg
Desired Starting Angular Velocity	$\dot{\theta}_i(t_i) = 0$	deg/s
Desired Ending Angular Velocity	$\dot{\theta}_f(t_f) = 0$	deg/s

Comparison of Trial One for t_f of 1.0 seconds

The following results are for only trial one of the RRRP to RRRR configuration with a t_f of 1.0 seconds. Figure 6.1 presents the results for comparison of the controlled angle θ. Figure 6.2 are the results for the calculated angles and lengths. Figure 6.3 presents the simulated voltage, measured current and calculated torque. The calculated torque is the torque at the output gearbox

shaft.

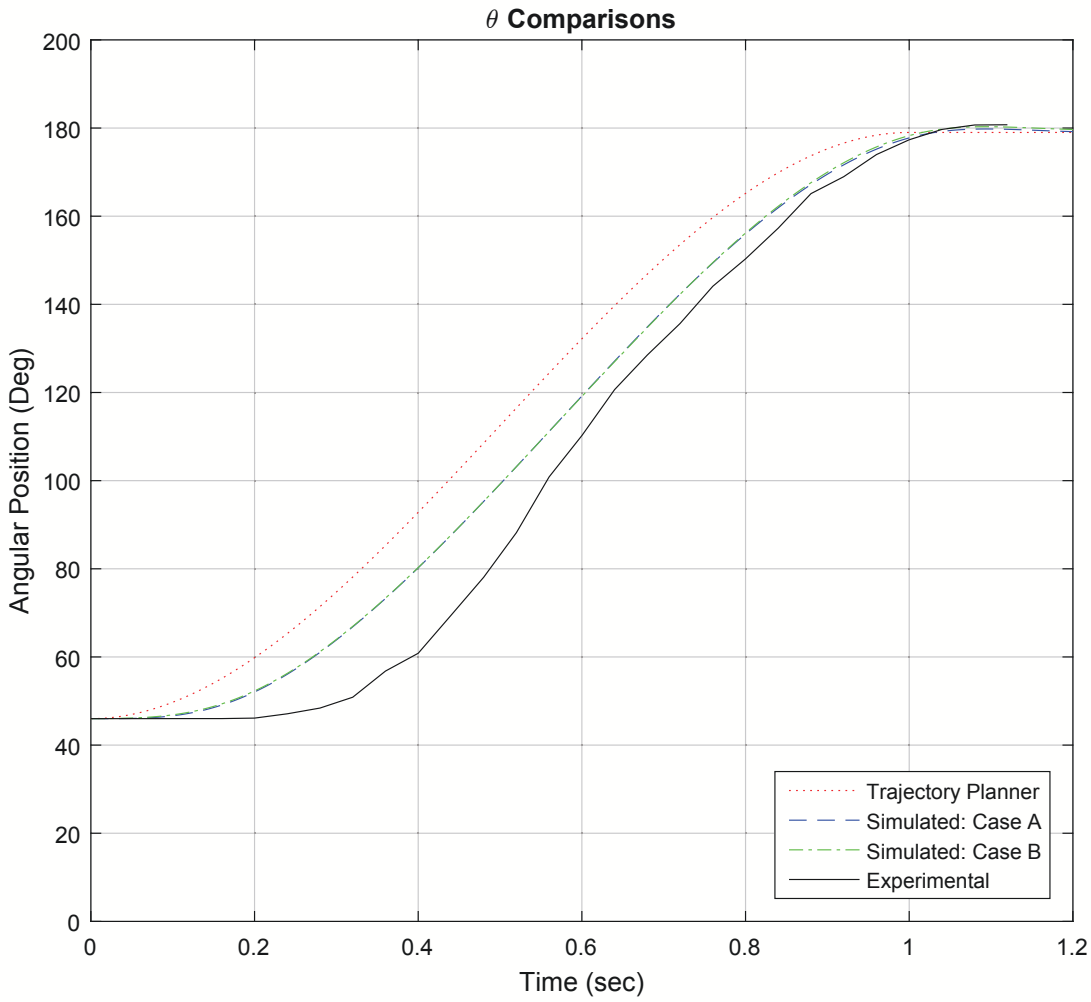

Figure 6.1: Comparison Results for RRRP to RRRR: θ

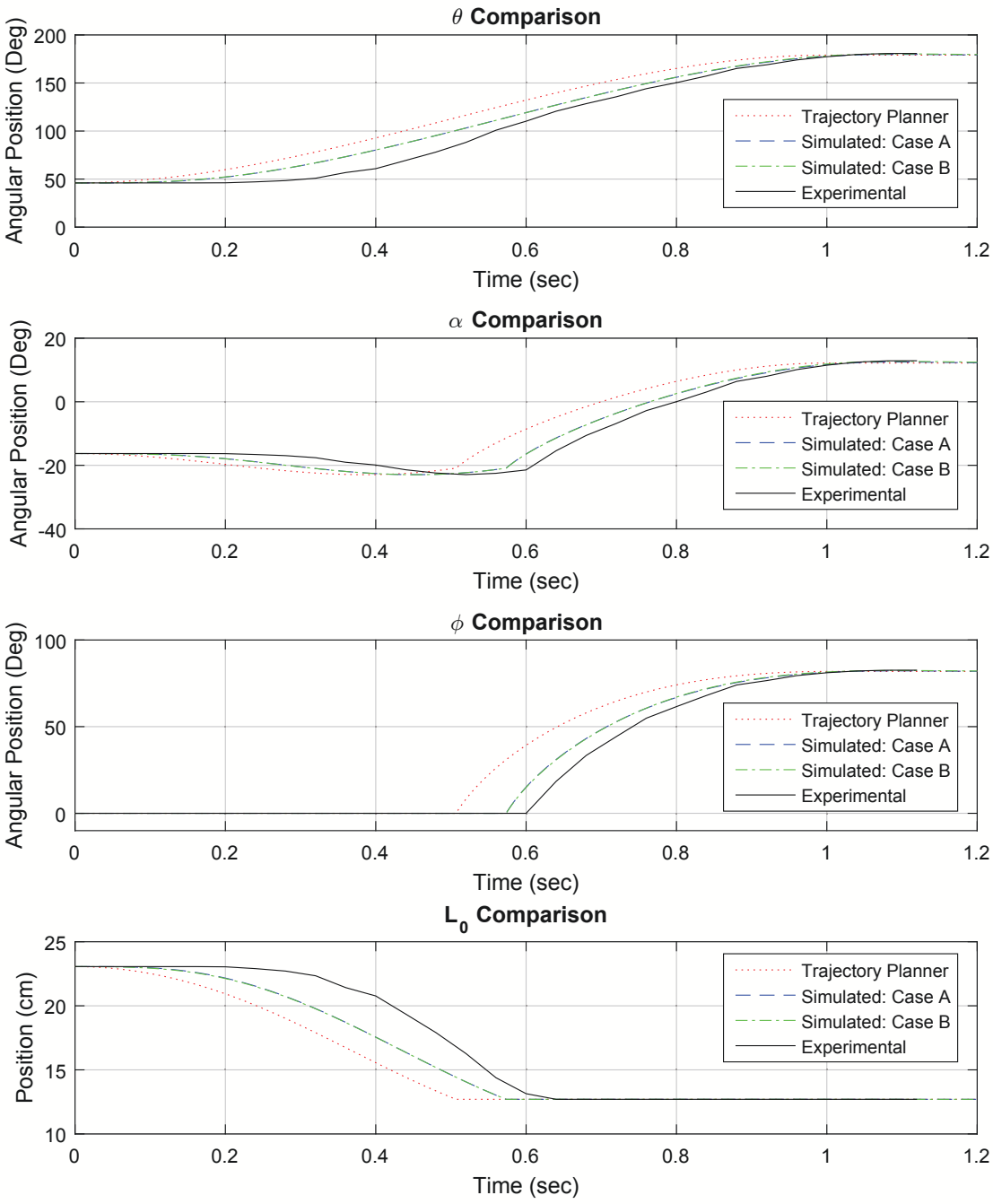

Figure 6.2: Comparison Results for RRRP to RRRR: Mechanism Positional Parameters

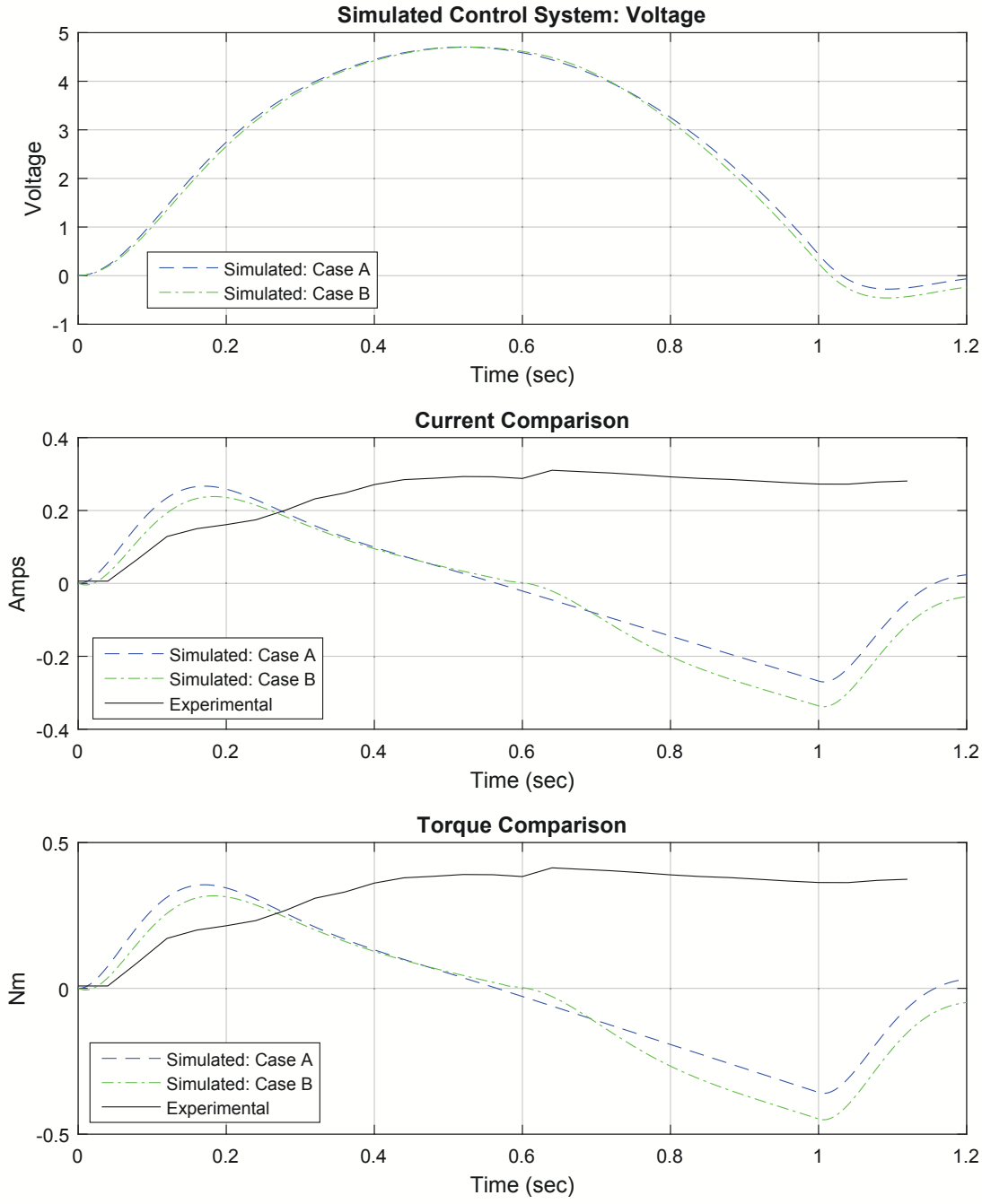

Figure 6.3: Comparison Results for RRRP to RRRR: Voltage, Current and Torque

Comparison of all Trials for t_f of 1.0 second

The following results are for all five trials of the RRRP to RRRR configuration with a t_f of 1.0 seconds. Figure 6.4 presents the results for comparison of the controlled angle θ. Figure 6.5 presents the currents and calculated torques of the Mechanism. Again, the calculated torque is the torque at the output gearbox shaft.

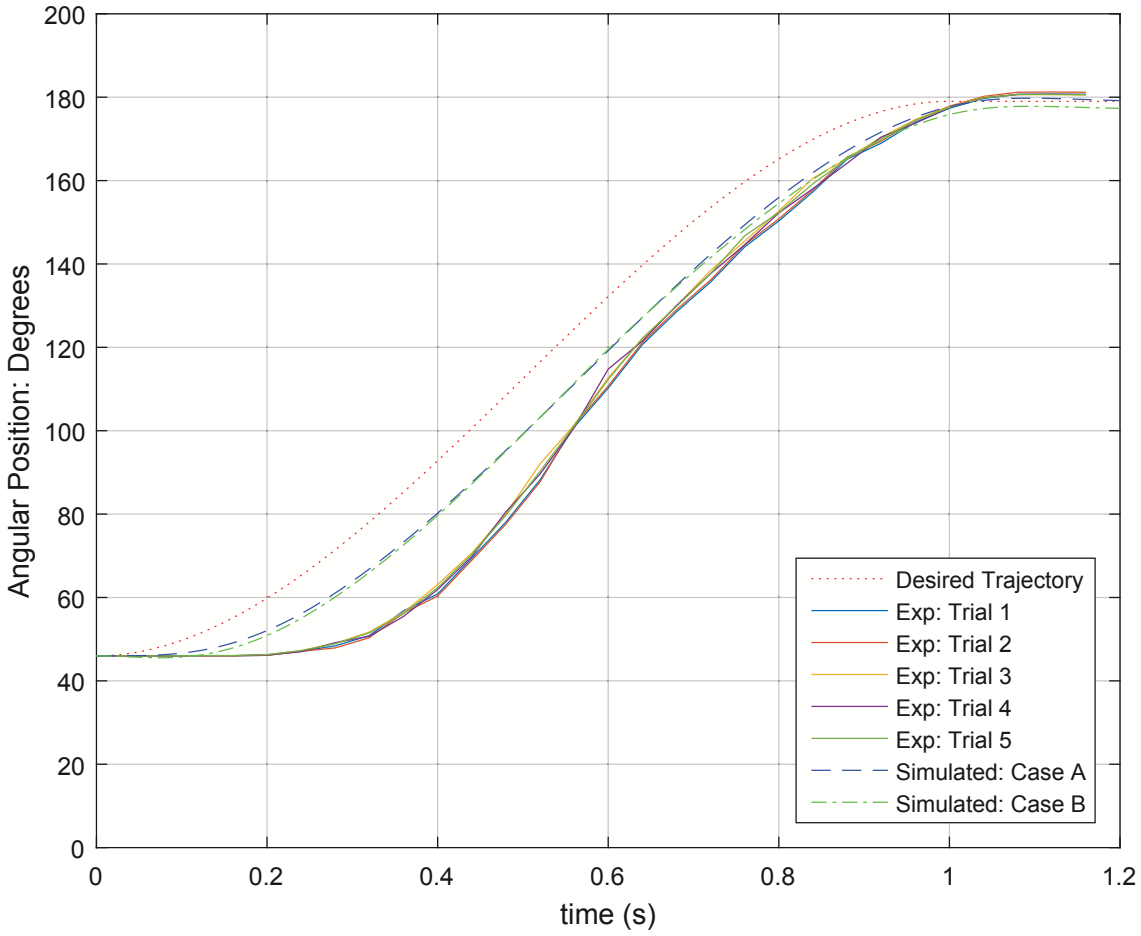

Figure 6.4: Comparison Results for RRRP to RRRR: θ for all trials at $t_f = 1.0$ seconds

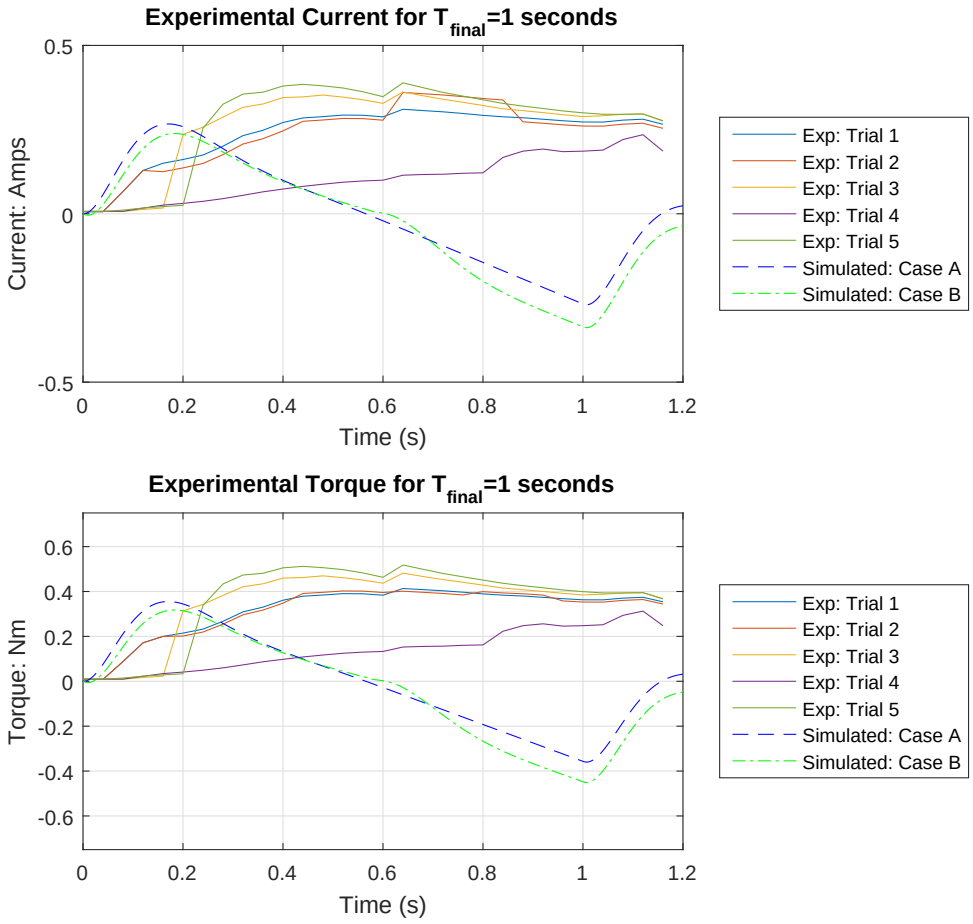

Figure 6.5: Comparison Results for RRRP to RRRR: Current and Torque for all trials at $t_f = 1.0$ seconds

6.2.2 Test Two: RRRR to RRRP Configuration

Test two will examine the Mechanism moving from the RRRR configuration to the RRRP configuration. Comparable to the previous section, Table 6.3 outlines the inputs for the third-order trajectory planner. The planner will generate a specific path that the system must follow. At the end of t_f, the planner generates constant values of $\theta_f(t_f)$ for position for an additional 1.0 seconds. The additional values are to ensure the simulated and prototyped

Mechanism are given enough time to reach the desired values. A time delay may be present in the system. A proportional controller will be used control the angular position of θ on the Mechanism in both simulation and in the physical experiment. The simulated models will first be compared to trial two of the previously found RRRR to RRRP prototyped results. These results are outlined in detail in Appendix Section D.3. Next, the simulation results will be compared to all five trials at that specific t_f. Presenting both sets of data shows insight into how the simulation compares to one set of data as well as many.

Table 6.3: Desired Trajectory Parameters for RRRR to RRRP Simulation

Description	Value	Units
Desired Starting Time	$t_i = 0$	s
Desired Ending Time	$t_f = 1.0$	s
Desired Starting Angular Position	$\theta_i(t_i) = 46^\circ$	deg
Desired Ending Angular Position	$\theta_f(t_f) = 179^\circ$	deg
Desired Starting Angular Velocity	$\dot{\theta}_i(t_i) = 0$	deg/s
Desired Ending Angular Velocity	$\dot{\theta}_f(t_f) = 0$	deg/s

Comparison of Trial 2 for 1.0 seconds

The following results are for only trial two of the RRRR to RRRP configuration with a t_f of 1.0 seconds. Figure 6.6 presents the results for comparison of the controlled angle θ. Shown in Figure 6.7 are the results for the calculated angles and lengths. Figure 6.8 presents the simulated voltage, measured current and calculated torque. The calculated torque is the torque at the output gearbox shaft.

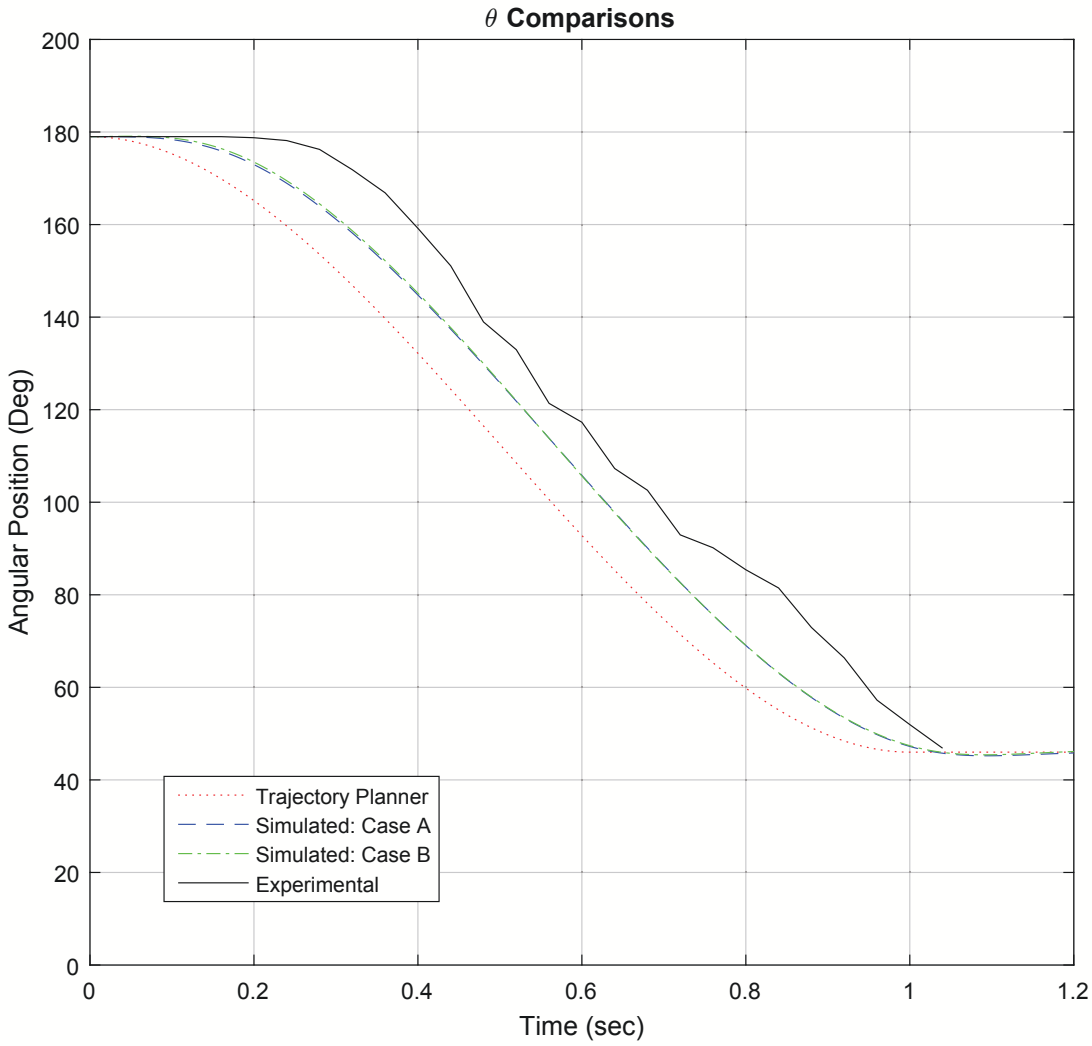

Figure 6.6: Comparison Results for RRRR to RRRP: θ

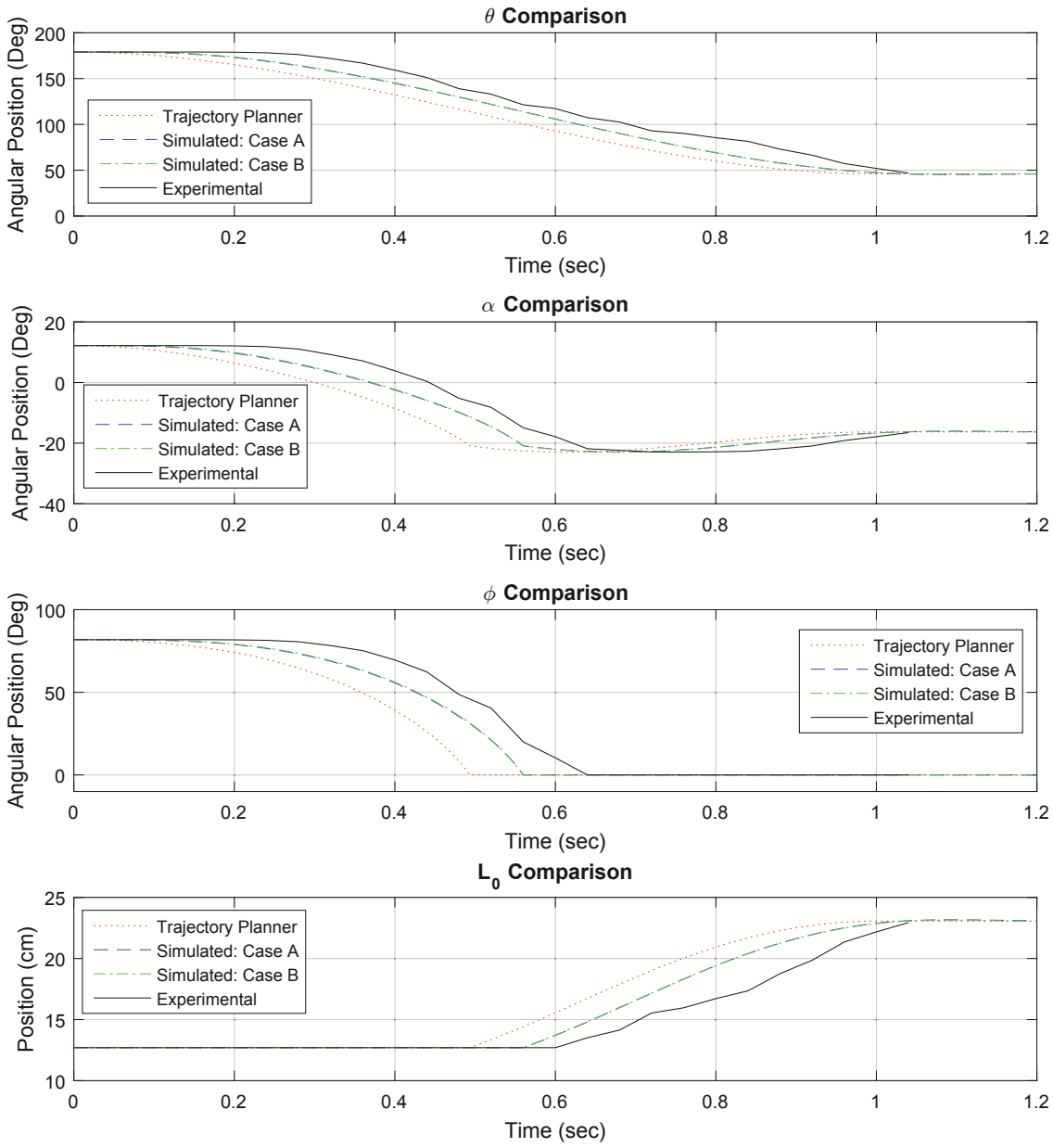

Figure 6.7: Comparison Results for RRRR to RRRP: Mechanism Positional Parameters

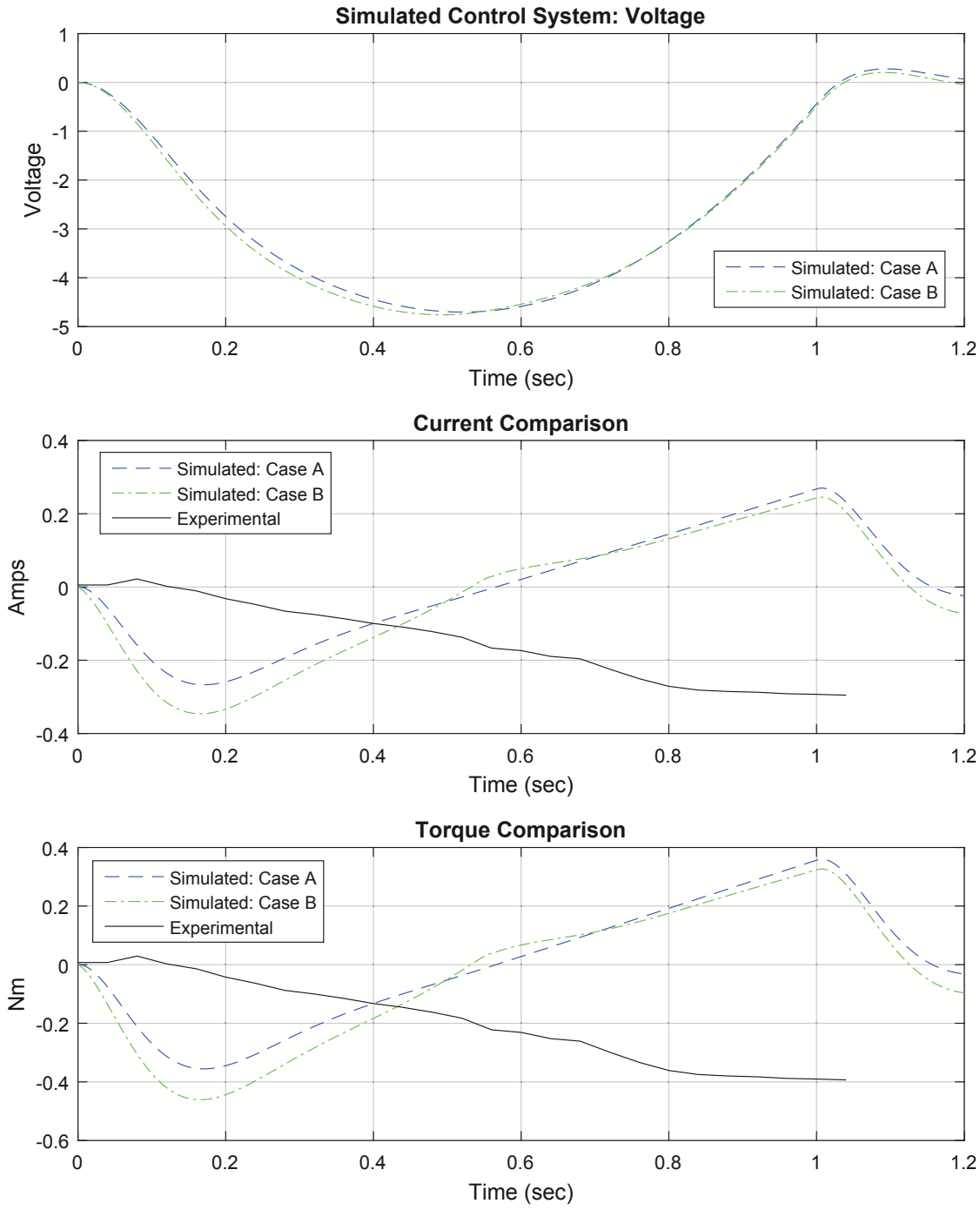

Figure 6.8: Comparison Results for RRRR to RRRP: Voltage, Current and Torque

Comparison of all Trials for t_f of 1 second

The following results are for all five trials of the RRRP to RRRR configuration with a t_f of 1.0 seconds. Figure 6.4 presents the results for comparison of the controlled angle θ. Shown in Figure 6.5 presents the currents and calculated torques of the Mechanism. Again, the calculated torque is the torque at the output gearbox shaft.

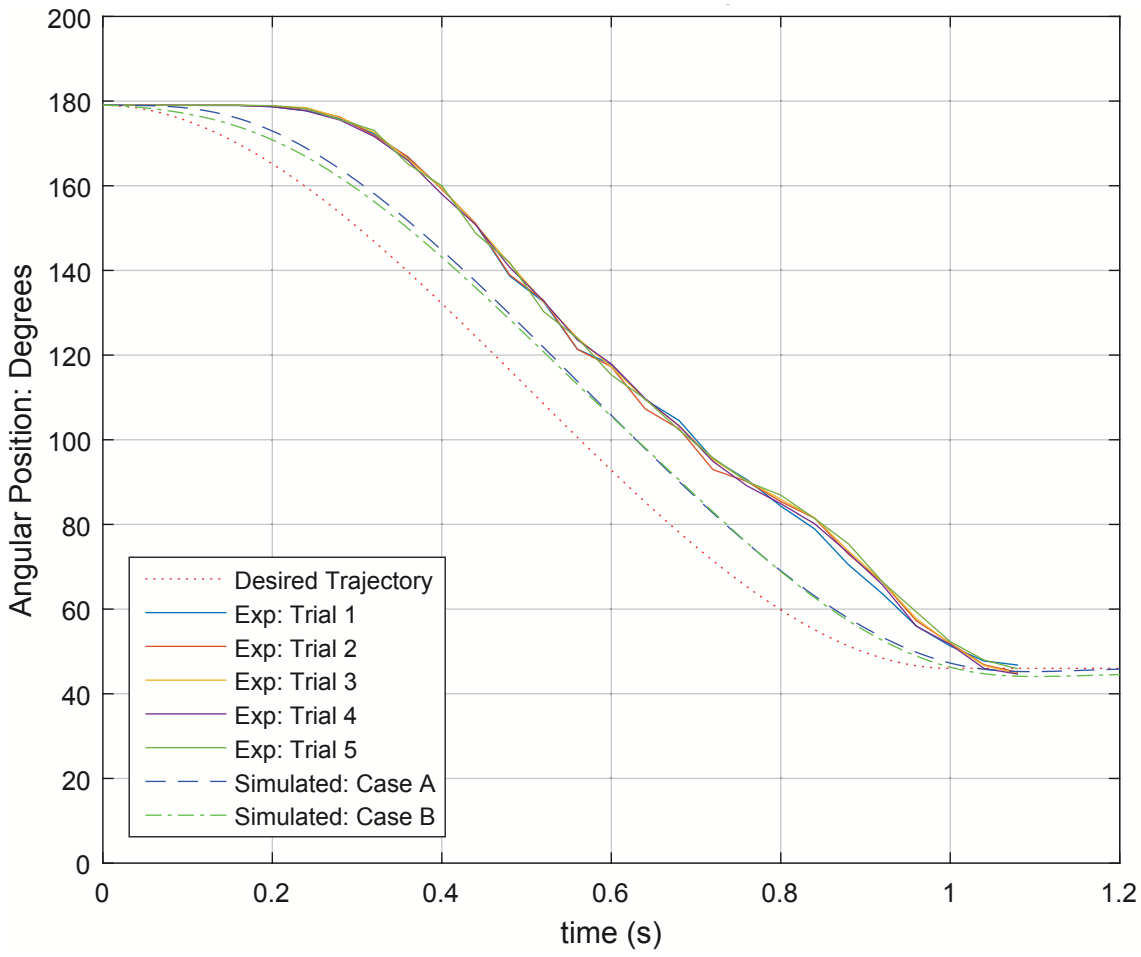

Figure 6.9: Comparison Results for RRRR to RRRP: theta all trials

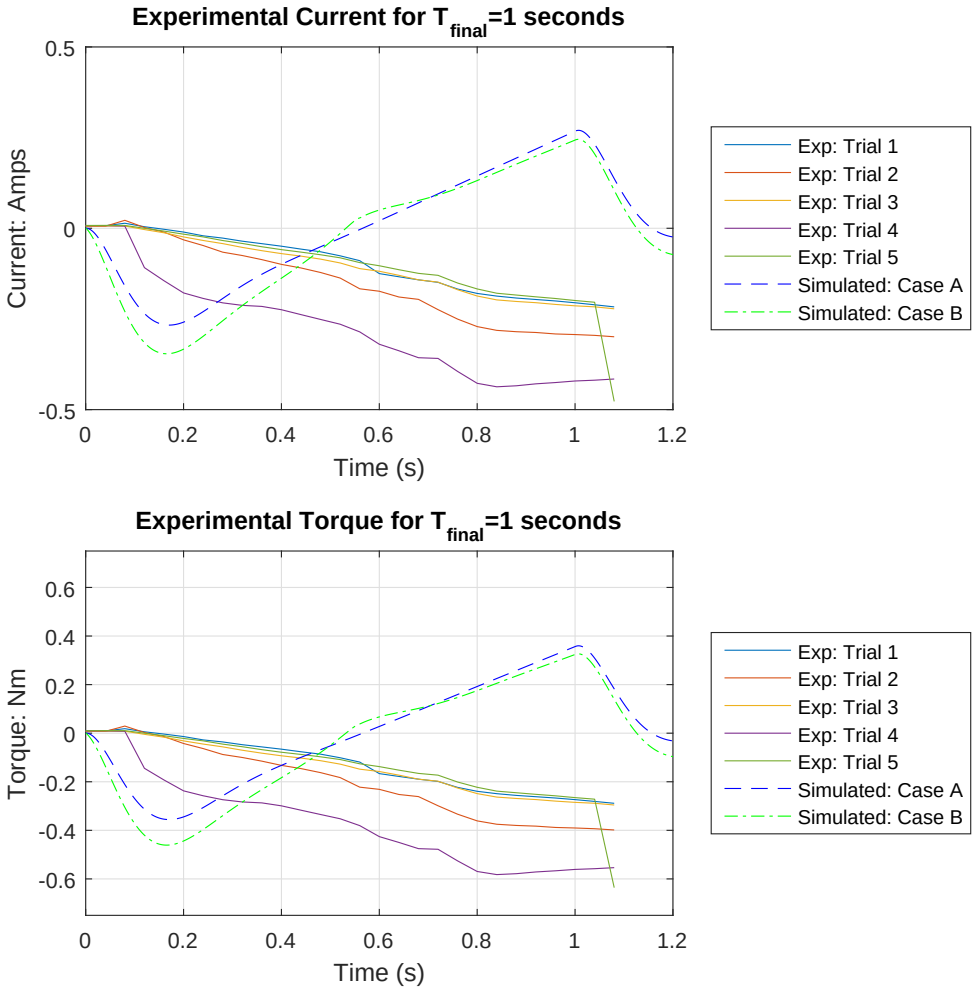

Figure 6.10: Comparison Results for RRRR to RRRP: Current All trials

6.3 Discussion of Simulation and Experimental RRRR-RRRP Mechanism Results

The following section in split into two sub-sections: RRRP to RRRR configuration results discussion and RRRR to RRRP configuration results discussion. There are several key areas to examine when evaluating the models and physical data. First, the timing of the models and physical results should be compared to the desired trajectory. Second, the overall shape of the response

needs to be comparable to the desired trajectory. If so, further analysis is needed. The overshoot or undershoots will be compared. Also, examination of the transition point between models should further be investigated. The transition point is when the Mechanism switches configurations. In addition, the current measurement should be evaluated and the magnitudes compared. Examining the current will predict the torque of the motor output. All of these items are vital to validating the models and ultimately selected the optimal one.

6.3.1 Discussion of Results: RRRP to RRRR Configuration

The RRRP to RRRR Configuration will be examined. The experimental prototype and the simulated models used same initial conditions and are shown in Table 6.2. The figures shown in Section 6.2.1 are the comparison of the simulated results to the experimental results for RRRP to RRRR configuration.

First, Figures 6.1 and 6.4 will be examined in detail. A time delay is present in both the experimental system and the simulated models. The delay is larger in the experimental results than the simulated models. The time delay for the experimental system changes as times goes. Initially, the delay is about 0.2 seconds but at the end of test it is about 0.1 seconds. Comparatively, the time delay for both models is about 0.1 seconds. Second, the overall shape of experimental and simulated results is sufficient. The control system drives the response of the system based on the desired θ. The experimental system overshoots slightly (less than 2%) at the end of the run. Case A overshoots as well but is even smaller than the experimental results. Case B undershoots the trajectory planner but again this is negligible. Some chatter is seen in the experimental run but overall the control system tracks the desired path extremely well.

From kinematics of the specific configuration being examined, the Mechanism should transition from the RRRP configuration to the RRRR configuration when $\theta = 114^{\circ}$. The transition point occurs at 0.45 seconds, 0.55 seconds and 0.60 seconds for the trajectory planner, simulated models and experimental data, respectively. The time delay plays a major role in when the Mechanism changes configurations. Examining Figure 6.2 one can clearly see the transition occur in α, ϕ, and L_0 at the respective times.

Next, the voltage will be examined. The simulated voltages are consistent with expectations. Experimental verification could be completed if a voltage measurement driver was purchased from NI. For a quick check, the experimental voltage was read via a multi-meter and provided comparable results. However, exact comparison is not possible using the multi-meter. In future experiments, a voltage measurement device will be explored.

Furthermore, the current was measured experimentally and simulated. Figure 6.5 shows the comparisons of current. The experimental results, Case A and Case B start comparably. All elevate initially until they reach their peak. The experimental data reached an average peak of approximately 0.4 amps. Case A reached a peak of approximately 0.27 amps. Case B reached a peak of approximately 0.24 amps. Overall, the magnitudes are comparable. Once the simulations reach their peaks they both have a negative slope. When Case B reaches the transition point (0.58 sec) a jump in the current can be sign. This is due to the transition point in the Mechanism; the model cause the change in the current. The jump can also be seen in the experimental data at 0.6 seconds. For the experimental data, the NI 9505 works well over one amps. However, the noise was present in the experimental data and a smoothing filter was used. A better experimental current measurement system could increase the fidelity of the experimental results. The torque is then calculated via the current. Similar results

are found in the current measurements.

Case A and B represent the kinematics and kinetics of the Mechanism very well. The current and voltage readings need to be further validate before any definitive results can be concluded. In addition, the model is best used when t_f is between 1.0 and 1.5 seconds. Outside of this range, the results can not be predicted. For example, if t_f is 3.0 seconds or higher the Mechanism sticks in the transition point until it receives enough torque to overcome the friction. These experimental results are shown in Appendix Section D.2. Both Case A and Case B do not account for the jamming in the transition point. Jamming in the transition point is very difficult to model. Even though the results are promising, only one prototype was experimentally examined. More prototypes with tighter manufacturing tolerances are necessary. The current prototype has some slop in the assembly and could potentially cause jamming. The slop is due to wear on the pins and 3D printed housing of the Mechanism. Overall, Case A best represents the RRRP to RRRR configuration for a t_f of 1.0 seconds to 1.5 seconds. Case A is better because less parameters are necessary for completing the model.

6.3.2 Discussion of Results: RRRR to RRRP Configuration

The RRRP to RRRR Configuration will be examined. The experimental prototype and the simulated models used same initial conditions and are shown in Table 6.2. The figures shown in Section 6.2.2 are the comparison of the simulated results to the experimental results for RRRR to RRRP configuration. The experimental results and findings are very comparable to the previous section but will still be examined for clarity.

First, Figures 6.6 and 6.9 will be examined in detail. A time delay is present again in both the experimental system and the simulated models. The delay is larger in the experimental results than the simulated models. Second, the overall

shape of experimental and simulated results is sufficient. The control system drives the response of the system based on the desired θ. The experimental system overshoots slightly (less than 2%) at the end of the run again. Case A overshoots as well but is even smaller than the experimental results. Case B undershoots the trajectory planner but again this is negligible. Some chatter is seen in the experimental run but overall the control system tracks the desired path extremely well.

From kinematics of the specific configuration being examined, the Mechanism should transition from the RRRR configuration to the RRRP configuration when $\theta = 114^{\circ}$. The transition point occurs at 0.50 seconds, 0.56 seconds and 0.62 seconds for the trajectory planner, simulated models and experimental data, respectively. The time delay plays a major role in when the Mechanism changes configurations. Examining Figure 6.7 one can clearly see the transition occur in α, ϕ, and L_0 at the respective times.

Next, the voltage will be examined. The simulated voltages are consistent with expectations and were further discussed in the previous section. The current was measured experimentally and simulated. Figure 6.10 shows the comparisons of current. The experimental results, Case A, and Case B start comparable. All elevate initially until they reach their peak. The experimental data reached an average peak of approximately -0.3 amps. Case A reached a peak of approximately -0.25 amps. Case B reached a peak of approximately -0.35 amps. Overall, the magnitudes are comparable. Once the simulations reach their peaks they both have a positive slope. When Case B reaches the transition point (0.58 sec) a jump in the current can be sign. The jump can not be seen in the experimental data for the RRRR to RRRP configurations. This results is interesting as the jump at the transition point was seen in the RRRP to RRRR configurations. As discussed previously, further experimentation of the current is

necessary to validate either of the models. The torque is then calculated via the current. Similar results are found in the current measurements.

Case A and B represent the kinematics and kinetics of the Mechanism very well. The current and voltage readings need to be further validated before any definitive results can be concluded. In addition, the model is best used when t_f is between 0.5 and 1.0 seconds. Outside of this range, the results can not be predicted. For example, if t_f is 1.5 seconds or higher the Mechanism sticks in the transition point until it receives enough torque to overcome the friction. These experimental results are shown in Appendix Section D.3. The jamming that occurs in the RRRR to RRRP configuration differs drastically than that of the RRRP to RRRR configuration. The sticking in the RRRP to RRRR configuration is minimal. In the RRRR to RRRP configuration, cases occurred where the Mechanism jammed completely and had to be manually moved to overcome the jam. Again, both Case A and Case B do not account for the jamming in the transition point. As discussed before the results are promising, however, only one prototype was experimentally examined. More prototypes with tighter manufacturing tolerances are necessary. The current prototype has some slop in the assembly and could potentially cause jamming. The slop is to do wear on the pins and 3D printed housing of the Mechanism. Overall, Case A best represents the RRRP to RRRR configuration for a t_f of 0.5 seconds to 1.0 seconds. Case A is better because less parameters are necessary for completing the model.

6.4 Comparison Summary

In summary, two different experimental cases were examined. The first examined was the RRRP to RRRR configuration and the second was the RRRR to RRRP configuration. For the RRRP to RRRR configuration, Case A and Case B represent the experimental results for a t_f of 1.0 seconds to 1.5 seconds. For the

RRRR to RRRP configuration, Case A and Case B represent the experimental results for a t_f of 0.5 seconds to 1.0 seconds. Case A is ideal because less parameters are necessary for completing the model. In future experiments, voltage and current measurements should be conducted to further validate the models. Overall, an accurate representation of the Mechanism was generated. The next chapter will outline the uses of the developed model.

CHAPTER 7

DESIGN AND ANALYSIS TOOLS FOR A RRRR-RRRP MECHANISM

7.1 Introduction

Synthesis is the process of generating new ideas or concepts. Within the context of mechanism design, one of the most challenging parts is synthesis. The process of creating a mechanism from nothing is very difficult. For example, how does one select the proper configuration, link lengths or masses. In classical mechanism design, kinematics and kinetics have helped solved these problems. Within reconfigurable mechanisms, these specific techniques tend to be tedious and challenging. In the following chapter, design tools will be developed for one specific reconfigurable mechanism (RRRR-RRRP Mechanism).

These specific design tools for the Mechanism will help make the synthesis process easier. In addition, the design tools will give the designer freedom to experiment in simulation before physically testing. Model based design helps to reduce cost and lead times on projects. Furthermore, a better design is usually achieved through the in-depth understanding of the design. Specifically, the design tools for the Mechanism could reduce design time of the new mechanism. In addition, more tools and virtual testing can be conducted from the developed design tools. The continuation of this work will be discussed in the Future Works section.

The analytical models developed to represent the RRRR-RRRP Mechanism will now be developed into design tools. Specifically two different design tool sets have arisen from the modeling of the Mechanism. The first set uses the generated equations of motion. From the equations of motion, a designer is able to understand the acceleration at the center of mass of each link. By varying the

link lengths and masses, the forcing acting through the center of mass will change. Understanding the forces acting at the center of mass will allow the designer to better understand the stresses in the Mechanism. The equations of motion can also be used to find the torque needed to drive the mechanism which allows a designer to properly size the motor.

The next set of tools derives from the validation of the individual dynamic models in SimMechanics. Using SimMechanics, a designer is able to define a trajectory that the Mechanism must follow. The Mechanism follows this trajectory and provides the torque necessary to achieve this motion profile in the allotted time. This feature is a good check to the derived model previously discussed. In addition, the SimMechanics method is faster. Furthermore, using SimMechanics allows a designer to find the internal forces of the joints.

In the following sections these tools will be examined. First, the force analysis at the center of mass of the links is examined. Second, the torque from the equations of motion is investigated. Next, SimMechanics tools are further explored. The torque from a prescribed motion path is found through analysis. Next, the internal forces are examined using SimMechanics. All of these tools will provide more efficient design of RRRR-RRRP Mechanisms. Finally, the design tools will be demonstrate their usefulness through a preliminary parameter variation analysis.

7.2 Equations of Motion Analysis and Design Tools

As discussed previously, there are two tools that can be derived from the equations of motion of the Mechanism. The first is the Force Analysis Tool at the Center of Mass. The second is the torque required to drive the Mechanism. For each tool an example is presented and discussed. Figure 7.1 shows an example desired trajectory of the Mechanism where the Mechanism will switch from the

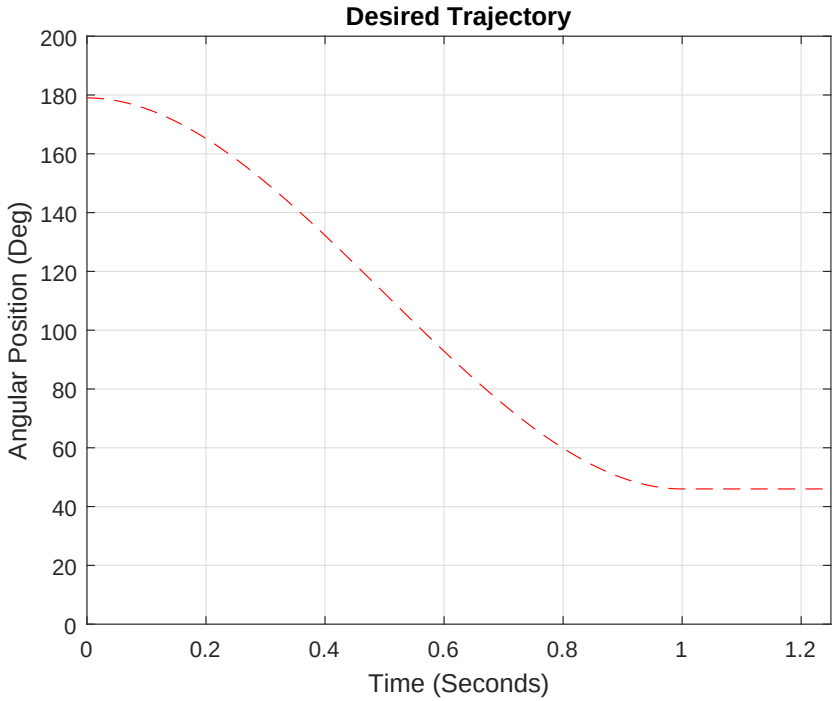

Figure 7.1: Desired trajectory for θ

RRRR to RRRP configuration. All parameters such as link lengthes and others can be found in Table 6.1. The table are the values for the prototyped Mechanism.

7.2.1 Force Analysis Tool at the Center of Mass

Using the previously derived kinematic equations, the angular acceleration of each joint was solved for numerically. Once solved for, the angular acceleration vector was used to solve for the force vector for each center of mass. The center of mass of link one and two were easily found. The center of mass combines link three and the slider because they are rigidly attached.

Force Analysis Tool at the Center of Mass: Example

Using the previously defined prototype Mechanism, the forces were found using the simulated model. The Mechanism transitions from the RRRR to RRRP

configuration. Figure 7.2 shows the forces as a function of time acting on the center of masses on the links. F_i correlates to the force in the global x-axis. F_j correlates to the force in the global y-axis. F_{mag} correlates to the magnitude of the force vector.

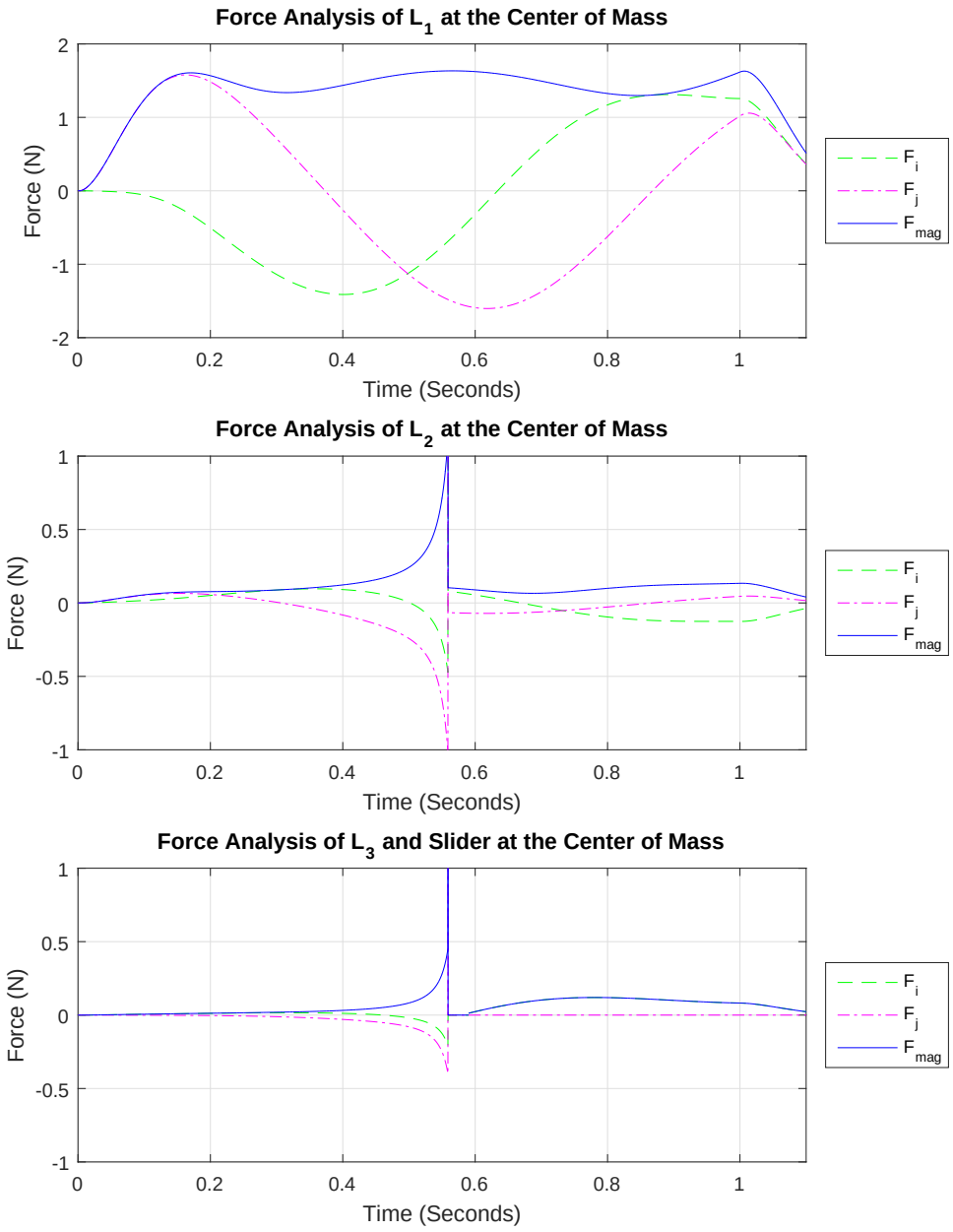

Figure 7.2: Mechanism Center of Mass Force Analysis

7.2.2 Torque from the EOM Tool

An additional design tool is being able to understand the required torque necessary to move the Mechanism. The required torque is a by-product of solving the forward dynamics. The forward dynamics product the motion of a body from an applied joint torque or force [33]. A designer could use this torque to size a motor appropriately. This method has previously been demonstrated and is shown in the appendices.

7.3 SimMechanics Analysis and Design Tools

SimMechanics is a helpful tool for solving complex dynamics. It is especially useful when solving parallel mechanisms. Two different tools will be examined. The first is understanding the necessary torque for a specified motion path. The second solves for the internal forces of the Mechanism. Unfortunately, SimMechanics does not allow for the simulation of the Mechanism in its entirety. The Mechanism must be split into the RRRR and RRRP configurations in order to simulate. This approach is consistent with Chapter 3.

7.3.1 Torque Analysis from θ input

As discussed previously, the forward dynamics are inherently solved through the equations of motion. The inverse dynamics can easily be found using SimMechanics. A motion path is specified and the forces and torques required to create that motion are found. In other words, a torque is output that is required to achieve the desired path. This tool is very beneficial in motor selection as one needs to know what the desired.

Using the previously defined prototype Mechanism, the necessary torque at the input joint θ is found. In this example, the Mechanism transitions from the

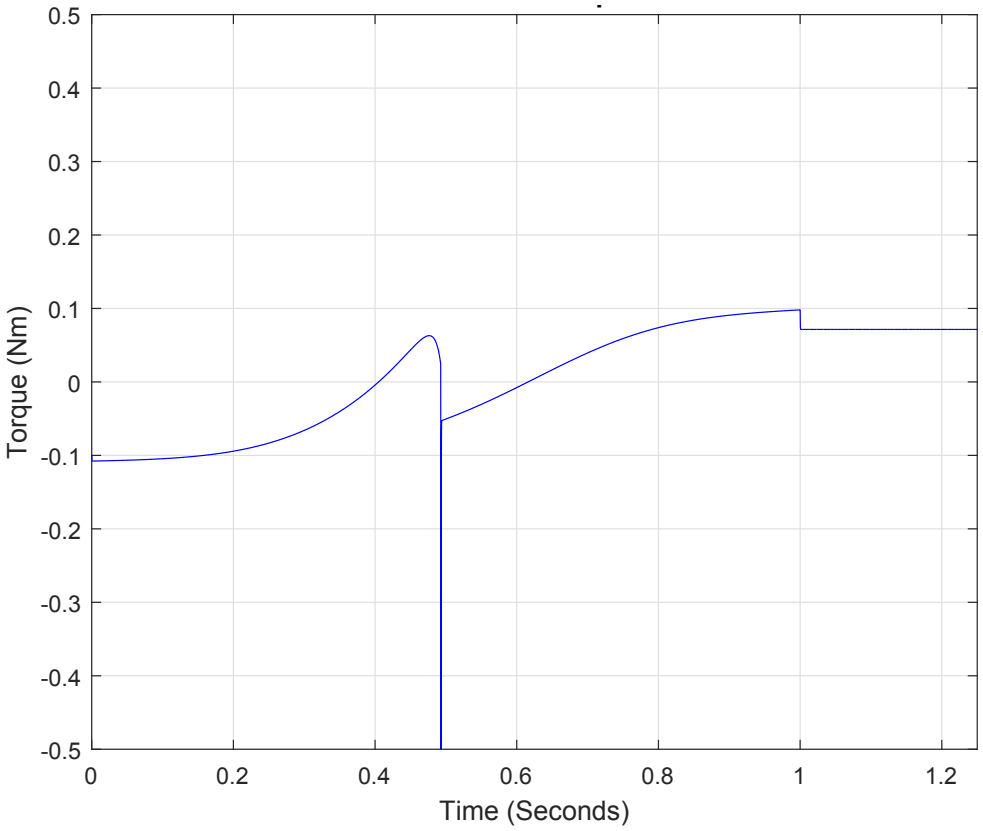

Figure 7.3: Actuated Torque Analysis

RRRR to RRRP configuration. Figure 7.3 shows the actuated torque as a function of time. A jump is seen where the Mechanism changes configurations.

7.3.2 Internal Force Analysis

In addition to being apply to solve the forward and inverse dynamics, SimMechanics can also solve for internal forces at joints. Understanding the direction and magnitude of a force in time will provide design insight.

Internal Force Analysis: Example

Using the previously defined prototype Mechanism, the internal forces acting on the base of link one were found; other forces could easily be found.

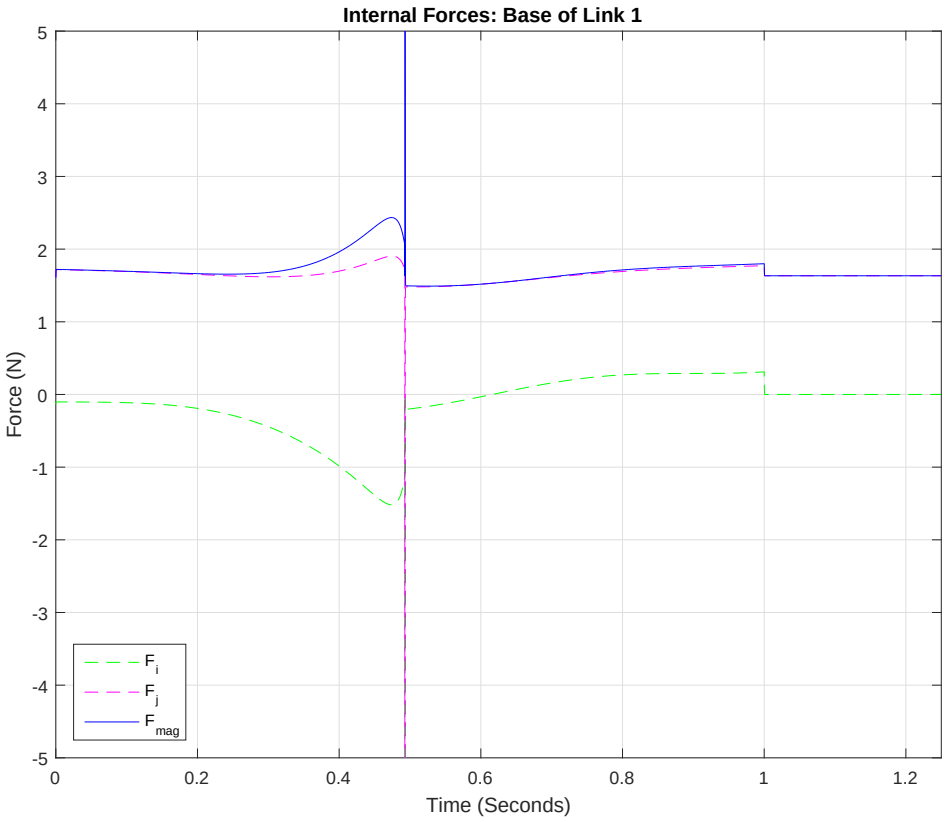

Figure 7.4: Internal Force Analysis

Only one set of forces is shown in Figure 7.4. One key thing when analyzing the forces is ensuring that reference frames within SimMechanics are properly aligned. If the frames are misaligned, the forces could be out of plane and not provide a true representation. Figure 7.4 shows the internal forces of the base as a function of time. A jump is seen where the Mechanism changes configurations. The forces could be used to properly size a mounting plate and bearings for the Mechanism.

7.4 Design Tools with Parameter Variations

Using the developed tools in the previous sections further design insight can be achieved. Using the SimMechanics tools developed a parameter variation study can be completed to determine how the variation will affect the response of the Mechanism. Being able to vary the parameters of the Mechanism and understand the forces or torques acting will allow a designer to effectively construct other Mechanisms.

For this specific example, the mass and length of link one were varied while the others were held constant. A possible design goal could be to minimize the force or torque jump between configurations. With a minimized jump, a smoother Mechanism motion can be achieved. The force and torque jump were examined at the transition point. The force examined was the internal force acting on the link one base. Any other force at the joints could easily be tested. In addition, the transmission angle was also examined at the transmission point. In classical four bar mechanism research, the transmission angle allows a designer to determine the effectiveness of the mechanism from a force transfer perspective.

For this particular example, the mass of link one (M_1) was varied from 0.05 to 1 kg. The length of link one (L_1) was varied from 0.09 to 0.15 m. The other constants can be found in Table 6.1. A desired trajectory was selected and is shown in Figure 7.1.Figure 7.5 shows the internal force jump at the transition point. Figure 7.5 is interesting because a maximum was found for the range. However, no minimum was specifically found. From the results its appears that the link length has more importance than the mass on the internal force jump. Figure 7.6 shows the torque jump at the transition point for link one attaching on the left fixed base. Comparable to before, the link length affects the result drastically compared to the mass for the change in torque between configurations.

Figure 7.7 shows the transmission angle at the transition point for link one attached to the left fixed base. Again, the link length affects the transmission angle more than the mass. The result was expected as the transmission angle is a function of the kinematics. Figure 7.8 is the transmission angle vs force change at the transition point for link one. In summary, varying the parameters of the Mechanism can provided greater insight into the optimal design.

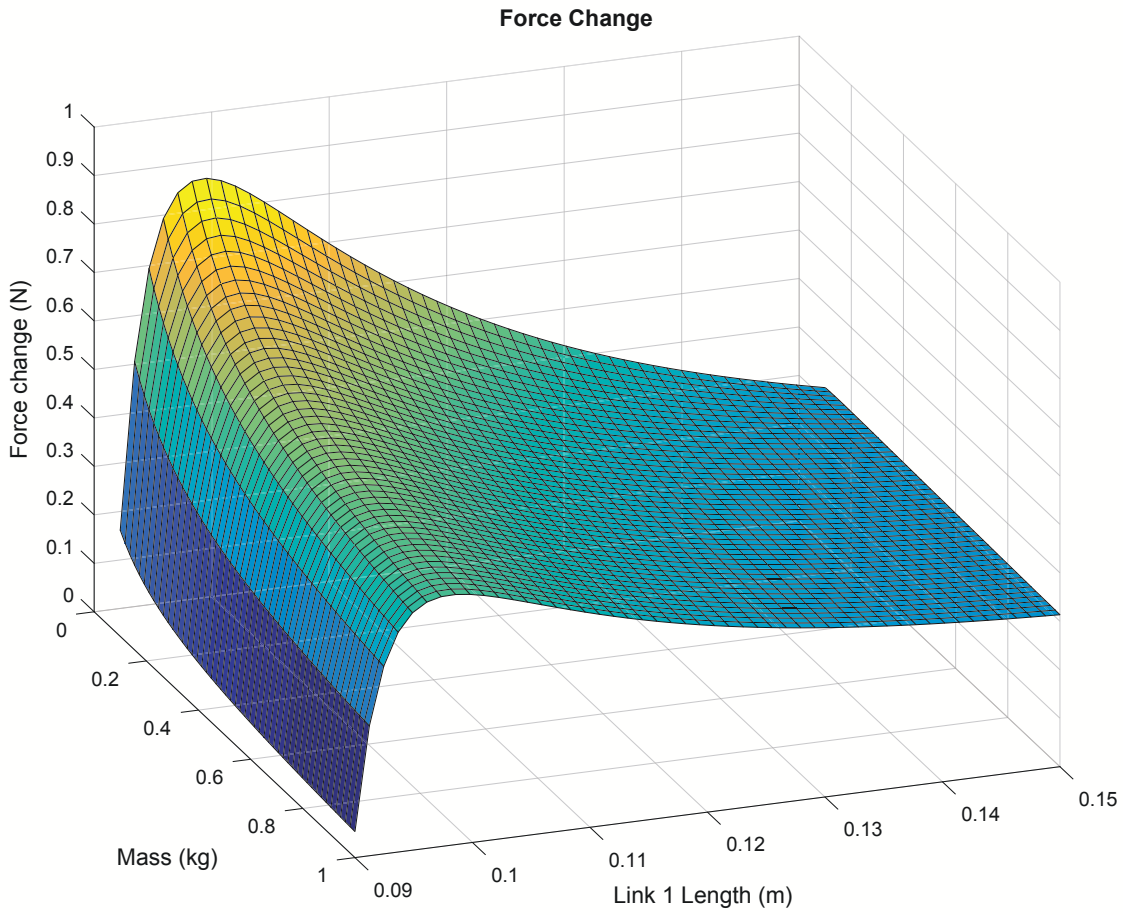

Figure 7.5: Internal Force Jump at the Transition Point for Link One attaching on the Left Fixed Base

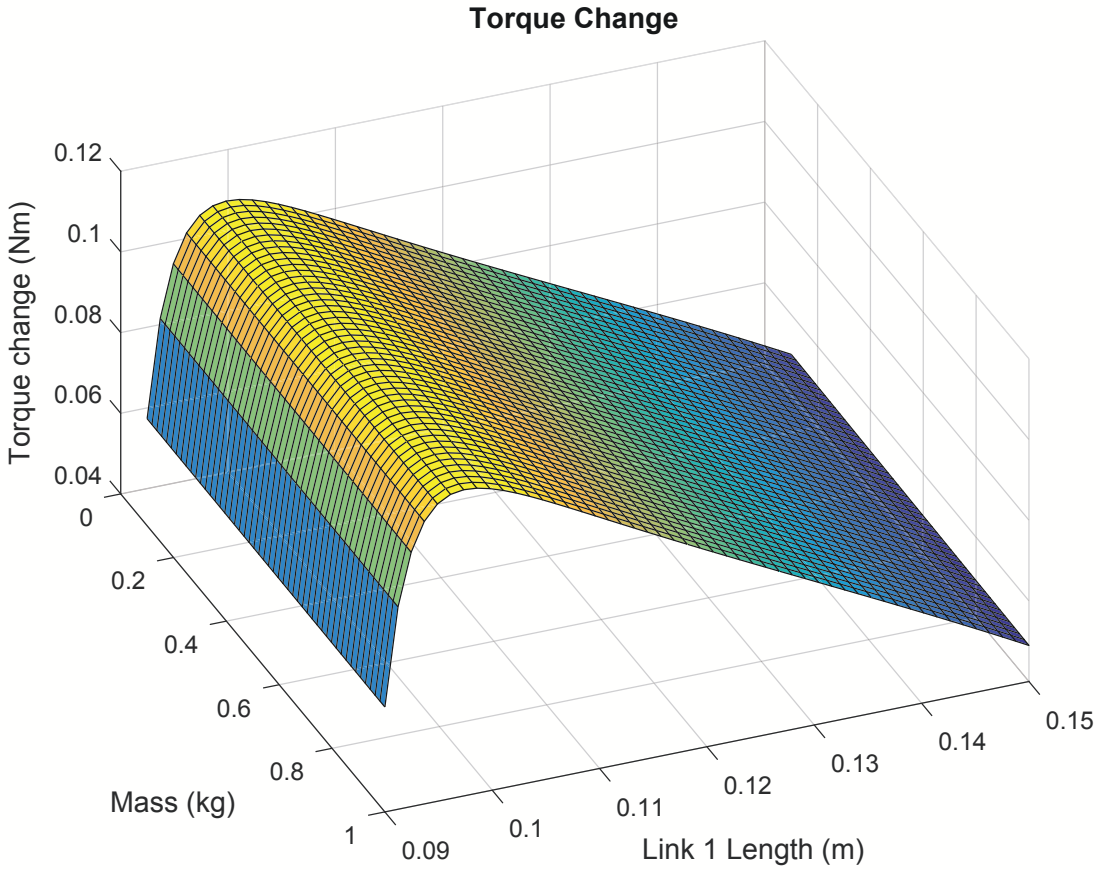

Figure 7.6: Torque Jump at the Transition Point for Link One attaching on the Left Fixed Base

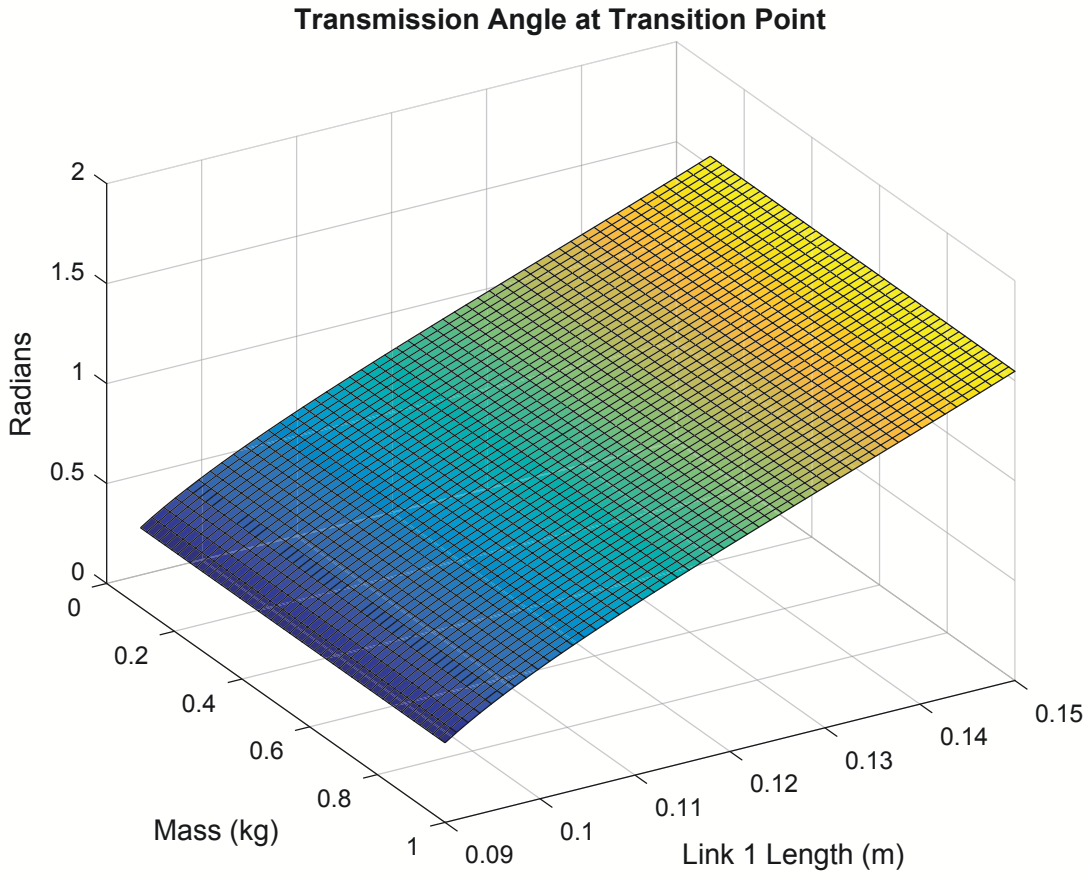

Figure 7.7: Transmission Angle Analysis at the Transition Point for Link One attaching on the Left Fixed Base

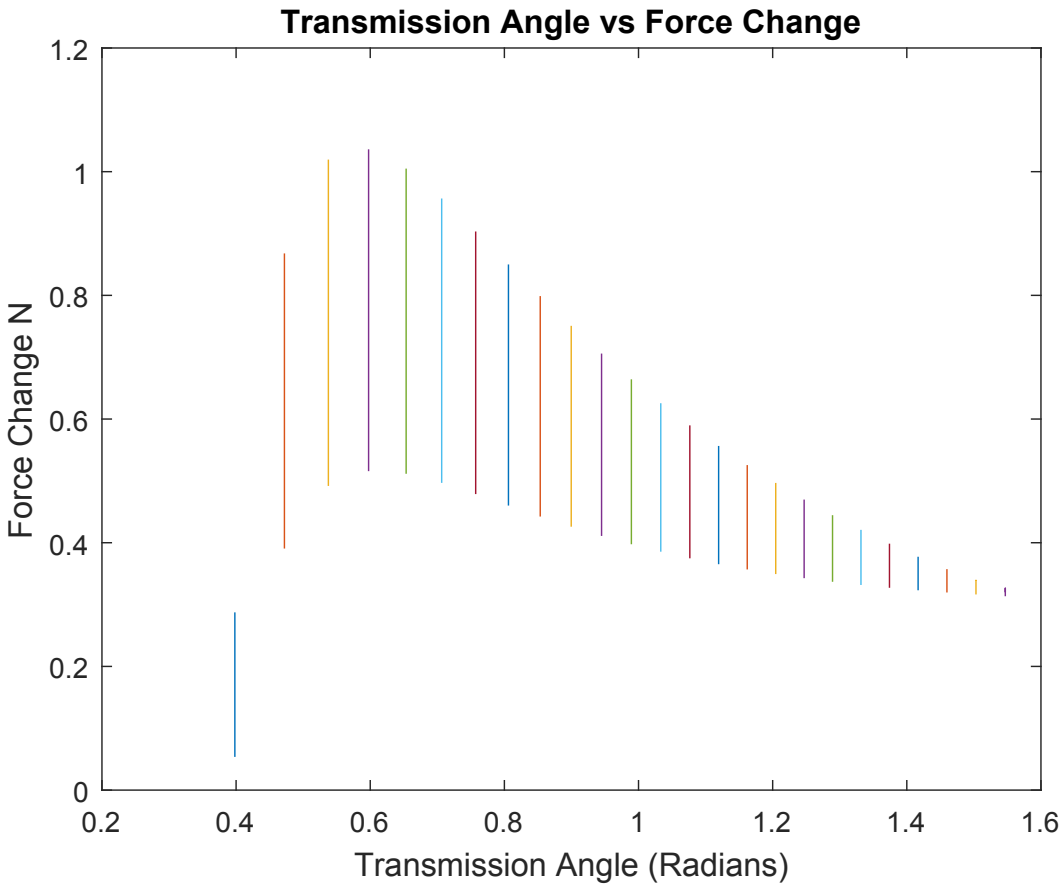

Figure 7.8: Transmission Angle vs Force Change at the Transition Point for Link One attaching on the Left Fixed Base

7.5 Summary

In summary, a suite of tools for understanding and designing the Mechanism were developed. A designer is able to find the forces at the center of mass and joints. Knowing the forces acting on the links and joints will allow a designer to fully analyze and design the mechanical structure. In addition, a designer is able to understand the necessary torque to drive the Mechanism. Understanding the torque will allow a user to select or build a motor to those requirements. The designer is also able to perform variation of parameters and examine the force change between configurations. Overall, the design tools will provide more insight into the synthesis and analysis of a RRRR-RRRP Mechanism.

CHAPTER 8

CONCLUSION AND FUTURE WORKS

8.1 Conclusion

From the research several different conclusions can be drawn from the research. First, the Mechanisms developed models are valid from 0.5 seconds to 1.5 seconds pending the configuration. Case A and B both accurately represent the Mechanism. Case A is ideal because less parameters are needed to model. The modeling technique works well for the positional analysis and it could potentially be applied to other reconfigurable mechanisms.

In addition, the experimental data was compared to the simulation for analysis. From the results, it was found that the mathematical models accurately represent the kinematics of the system. In addition, the peak magnitude of the torque is comparable. From the models, it was found that the simplified dynamic model proved sufficient in the case of the prototyped Mechanism. More Mechanisms need to be built with varying masses and link lengths to fully conclude that the simplified dynamic representation is best. One advantage of the simplified dynamic model is that only the mass and link length of the first link are necessary.

In summary, mathematical models for the RRRR-RRRP reconfigurable mechanism were developed. The mechanism switches between the RRRR and RRRP configurations using a kinematically reconfigurable variable joint. The kinematics of the Mechanism were analyzed. In addition, a Lagrangian approach was used to model the dynamics of the mechanism. The dynamics were independently verified using SimMechanics. Once verified, the dynamics were used to develop a full dynamics plant model of the Mechanism. In addition, a

simplified dynamics model was also developed. Through the plant modeling, a general geared DC motor was modeled. A friction model was developed as well to represent the friction in the motor. Furthermore, the DC motor model was verified through open loop experimentation. With the plant models developed, a proportional controller was implemented to control the system. A third-order cubic polynomial trajectory planner was used to specify the desired angular position of the input shaft. Sufficient control and response were seen.

A prototype RRRR-RRRP Mechanism was built to verify the mathematical models. Using the prototyped Mechanism, it was positioned in two different starting positions for the experimental testing. First, the Mechanism was positioned in the RRRP configuration then moved using the DC motor to the RRRR configuration. A cubic polynomial trajectory was generated a priori and then implemented in real time with the motor control system. Second, the Mechanism was positioned in the RRRR configuration then moved using the DC motor to the RRRP configuration using a similar generated trajectory. The positional data for the experimental testing was logged for examination and the kinematics were calculated based on the input angle θ. Results were generated.

Using the developed equations of motion and SimMechanics models, a suite of analysis and design tools were developed. The tools will assist in the creation and understanding of future RRRR-RRRP Mechanisms. One of the tools allow a designer to be able to understand the necessary torque to drive the Mechanism. Understanding the torque will allow a user to select or build a motor to those requirements. Another tool allows a designer is able to find the forces at the center of mass and internal joint forces. These tools will increase design speed as well as provided insight into how RRRR-RRRP Mechanisms function. Overall, the design tools will provide more understanding of RRRR-RRRP Mechanisms.

In summary, the RRRR-RRRP mechanism was mathematical modeled and verified through experimentation. Using the developed models, a suite of tools were created to assist with the analysis and future development of RRRR-RRRP Mechanisms.

8.2 Future Work

While the RRRR-RRRP Mechanism was effectively modeled, there is always more work to be done. Specifically, the mathematical models can be further validated by comparing them to other prototypes. More validation will increase the fidelity of the model.

In addition to verification of models, future prototypes can be improved. First, the Mechanism's 3D printed block is showing signs of wear. A steel or aluminium block should be machined as a replacement. Once machined, dry or wet lubrication should be considered. Also, the press fit pins were showing signs of wear and beginning to loosen. These are just some of the physical components that should be revaluated when designing the next prototype.

A different motor could be also examined. One suggestion would be to use a higher geared motor. Using a higher geared motor will reduce the dynamic load felt by the motor but will slow down the response. In addition, a better current measurement system should be considered. While costly, it could assist in validation of the Mechanism plant models. Also, a NI voltage reader compatible with the cRIO should be purchased. Again, the unit is costly but would improve the model validation. Furthermore, any control system can be further improved. This is the same case for the Mechanism. A P controller was sufficient but other control algorithms could be better such as gain scheduling for PID control or model predictive control.

The design tools can be further examined and tested. Experimental verification of the design tools could also be completed. For example, comparison of the desired torque to the measured torque would help validate the tool. An accelerometer and inclinometer could also be placed on the slider to help validate the dynamics even more.

Overall, the work conducted in the thesis was insightful but more work is necessary. The developed techniques now need to be expanded to other reconfigurable mechanisms for further understanding.

BIBLIOGRAPHY

[1] B. Slaboch. *Profile synthesis of planar variable joints*. Phd thesis, Marquette University, 2013.

[2] J. Prisco. Dynamic modeling of a belt driven elctromechanical xy plotter cutter. Master's thesis, Marquette University, 2009.

[3] J.S. Dai and J.R. Jones. Mobility in metamorphic mechanisms of foldable/ erectable kinds. *Journal of Mechanical Design*, (121):375–381, September 1999.

[4] K. Hsiao and H. Yan. Structural synthesis of ancient chinese chu state repeating crossbow. In J. Dai, M. Zoppi, and X. Kong, editors, *Advances in Reconfigurable Mechanisms and Robots I*, pages 749–758, New York, 2012.

[5] K. Wohlhart. Kinematotropic linkages. In J. Lenarcic and V. Parenti-Castelli, editors, *Recent Advances in Robot Kinematics*, pages 359–368, The Netherlands, 1996. Kluwer Academic.

[6] K. Wohlhart. Degrees of shakiness. In J. Lenarcic and V. Parenti-Castelli, editors, *Mechanism and Machine Theory*, pages 1103–1126, New York, 1999.

[7] C. Galletti and P. Fanghella. Single-loop kinematotropic mechanisms. pages 743–761, October 2001.

[8] C. Galletti and P. Fanghella. Multiloop kinematotropic mechanisms. In *Proceedings of the ASME DETC*, 2002.

[9] C.H. Kuo and H.S. Yan. On the mobility and configuration singularity of mechanisms with variable topologies. *ASME Journal of Mechanical Design*, (129):617–624, June 2007.

[10] C. Gosselin. Determination of the workspace of 6-dof parallel manipulators. *ASME Journal of Mechanical Design*, 113(331-336), 1990.

[11] C. Gosselin and et al. The synthesis of manipulators with prescribed workspace. *ASME Journal of Mechanical Design*, 113(451-455), 1991.

[12] C. Gosselin and et al. On the kinematic design of sphereical there-degree-of freedom parallel manipulators. *The International Journal of Robotics Research*, 12(4):394–402, 1993.

[13] L. Howell. *Compliant Mechanisms*. Wiley-Interscience, 2001.

[14] H.S. Yan and C.H. Kuo. Topological representations and characteristics of variable kinematic joints. *ASME Journal of Mechanical Design*, (128):384–391, March 2006.

[15] A.P. Murray, J.P. Schmiedeler, and B.M. Korte. Kinematic synthesis of planar, shape-changing rigid-body mechanisms. *Journal of Mechanical Design*, 130(1-10), 2008.

[16] T. Ritchey. Analysis and synthesis on scientific method - based on a study by bernhard riemann. *Systems Research*, 8(4), 1991.

[17] B. Slaboch and P. Voglewede. Mechanism state matrices for planar reconfigurable mechanisms. *Journal of Mechanisms and Robotics*, Transactions of the ASME(3), February 2011.

[18] C.H. Kuo. Structural characteristics of mechanisms with variable topologies taking into account the configuration singularity. Master's thesis, National Cheng Kung University, 2004.

[19] H.S. Yan and C.H Kuo. Representations and identifications of structural and motion state characteristics of mechanisms with variable topologies. In *Transactions of the Canadian Society of Mechanical Engineering*, volume 30, pages 19–40, March 2006.

[20] H.S. Yan and N.T. Liu. Finite-state-machine representations for mechanisms and chains with variable topologies. In *In Proceedings of the 26th ASME Mechanisms Conference*, number DETC2000/MECH-14054, Baltimore, MD, 2000.

[21] J.S. Dai and J.R. Jones. Matrix representation of topological changes in metamorphic mechanisms. *Journal of Mechanical Design*, (127):837–840, July 2005.

[22] Z. Lan and R. Du. Representation of topological changes in metamorphic mechanisms with matrices of the same dimension. *Journal of Mechanical Design*, (130), July 2008.

[23] C. Kuo and L. Chang. Structure decomposition and homomorphism identification of planar variable topology mechanisms. *Journal of Mechanisms and Robotics, Transactions of the ASME*, 8, 2014.

[24] J. Ginsberg. *Engineering Dynamics*. Cambridge University Press, 2008.

[25] D. Gan and et al. Variable motion/force transmissibility of a metamorphic parallel mechanism with reconfigurable 3t and 3r motion. In *In Proceedings of the 2015 ASME IDETC*, 2015.

[26] P. Malak and P. Voglewede. Dynamic analysis of a planar mechanism with variable topology. In *In Proceedings of the 2015 ASME IDETC*, 2015.

[27] T. Yang and et al. Comparative study of two methods for type synthesis of robot mechanisms. In *Proceedings of the 2009 Reconfigurable Mechanisms and Robotics Conference*, page 205214, 2009.

[28] L. Ma and et al. A method for structure syntheiss of reconfigurable mechanism based on genetic optimization algorithm. In *Proceedings of the 2009 Reconfigurable Mechanisms and Robotics Conference*, pages 148–152, 2009.

[29] B. Slaboch. Synthesis of a reconfigurable four-bar mechanism with variable joints. In *Proceedings of the 2014 ASME Design Engineering Technical Conference*, number DETC2014-34924, Buffalo, NY, 2014.

[30] S. Niku. *Introduction to Robotics: Analysis, Control, Applications*. John Wiley and Sons, Inc., 2nd edition, 2011.

[31] C. Tang. Lagrangian dynamic formulation of a four-bar mechanism with minimal coordinates. Nonholonomic, 2006.

[32] The MathWorks Inc. Simmechanics: Model and simulate multibody mechanical systems. Website, February 2016.

[33] W. Palm. *System Dynamics*. McGraw Hill, 3rd edition, 2014.

[34] Pittman-Ametek. Brush commutated dc servo motors: 8543 series. Electronic, 2016.

[35] I. Virgala, P. Frankovsky, and M. Kenderova. Friction effect analysis of a dc motor. *American Jornal of Mechanical Engineering*, 1(1):1–5, January 2013.

[36] R. Dorf and R. Bishop. *Modern Control Systems*. Pearson Eduation Inc., 12th edition, 2011.

[37] Marquette University-Opus College of Engineering. 3d printing. Electronic, April 2016.

[38] The MathWorks Inc. Mathematical functions: atan2. Website, February 2016.

APPENDIX A

RRRR MECHANISM: MECHANICAL DERIVATION

A.1 Introduction

The following is a full derivation of the planar kinematics and kinetics of the RRRR configuration. A Lagrangian approach was used for the kinetics. The RRRR configuration (Figure A.1) is a one degree of freedom mechanism. If the input angle (θ) is known, all other angles and positions can be found. The kinematics are necessary in understanding the dynamics of the system. A fixed coordinate system is located at the left revolute joint following the right hand rule. The analysis will be completed in a planar frame.

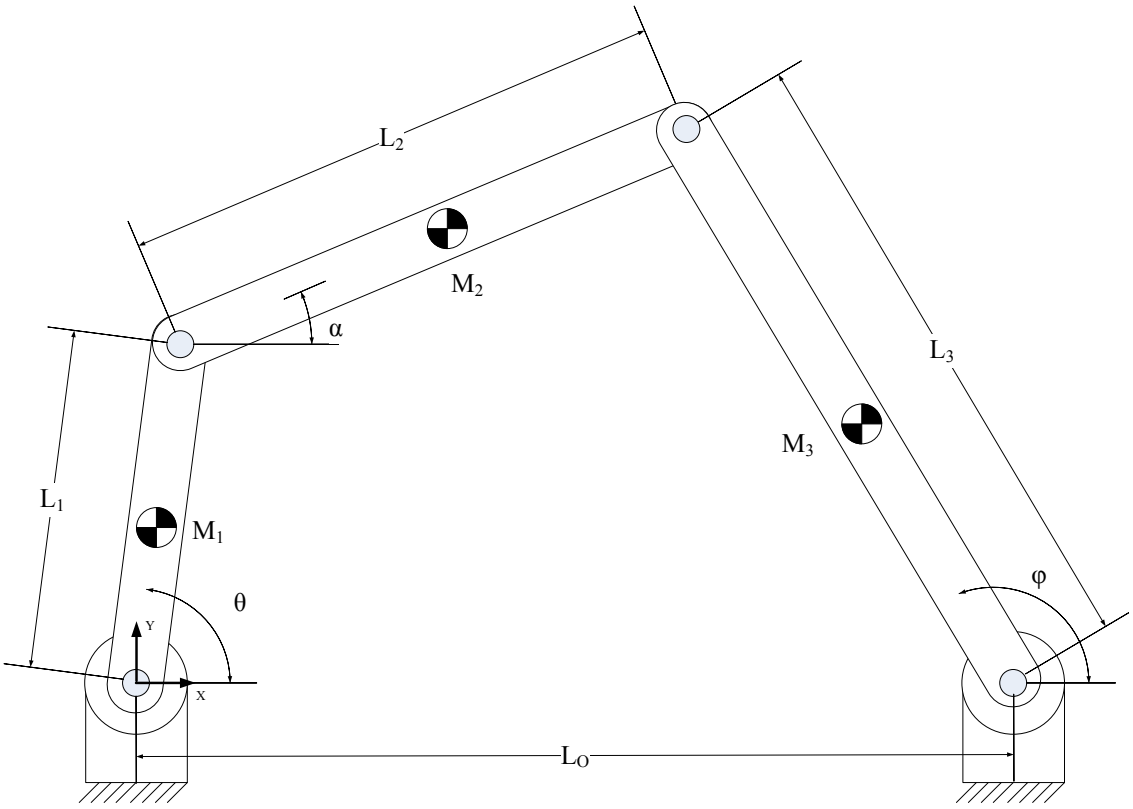

Figure A.1: RRRR Configuration

A.2 Kinematics

A.2.1 Kinematics: Position Analysis

Through the kinematics of the mechanism, the specified angles can be found. This requires some manipulation of mathematical principles but is necessary for understanding the mechanism.

Using the vector loop method, kinematic equations were developed for the RRRR mechanism.

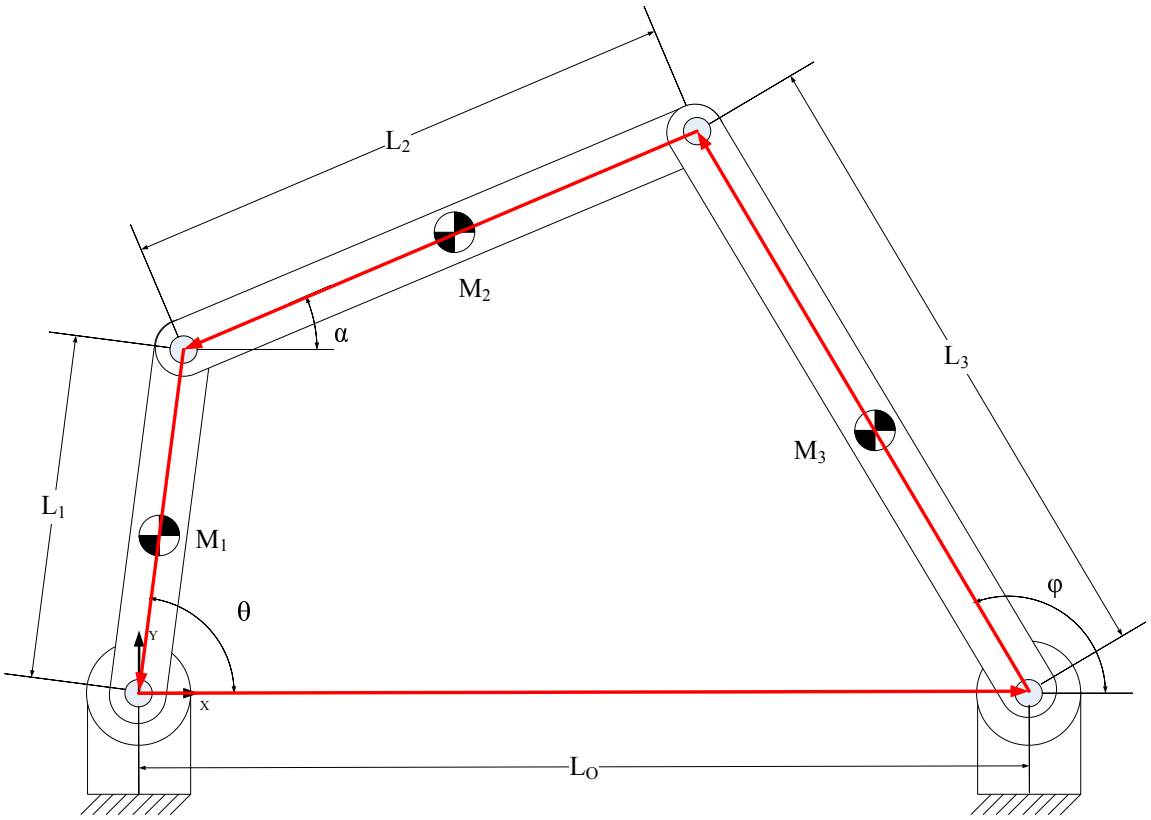

Figure A.2: RRRR Configuration

Vector Loop

Using the vector loop method, kinematic equations were developed for the RRRR mechanism [31]. Reference Figure A.2 for loop closure vectors. The naming convention is consistent with the link lengths.

$$\vec{0} = \vec{r_1} + \vec{r_2} + \vec{r_3} - \vec{r_4} \tag{A.1}$$

Now using the Vector loop equation, it can be broken into x components and y components. *For x:*

$$0 = -L_1 \cos\theta - L_2 \cos\alpha + L_3 \cos\phi + L_0 \tag{A.2}$$

For y:

$$0 = -L_1 \sin\theta - L_2 \sin\alpha + L_3 \sin\phi \tag{A.3}$$

θ, $\dot{\theta}$ are assumed as the initial conditions of the mechanism. In addition, it is assumed all link lengths are known. α, $\dot{\alpha}$, ϕ, $\dot{\phi}$ are unknown and will be expressed in terms of θ to fully describe the position of the mechanism in one coordinate.

Solve for ϕ

Rearrange Equations A.2, A.3 in terms of α:

$$L_2 \cos\alpha = L_0 - L_1 \cos\theta + L_3 \cos\phi \tag{A.4}$$

$$L_2 \sin\alpha = -L_1 \sin\theta + L_3 \sin\phi \tag{A.5}$$

Now squaring Equations A.4, A.5 then adding together:

$$0 = R_1(\theta)\sin\theta + R_2(\theta)\cos\phi + R_3(\theta) \tag{A.6}$$

Where A:

$$R_1(\theta) = -2L_1L_3\sin\theta \tag{A.7}$$

$$R_2(\theta) = 2L_3(L_0 - L_1\cos\theta) \tag{A.8}$$

$$R_3(\theta) = L_0^2 + L_1^2 - L_2^2 + L_3^2 - 2L_0L_1\cos\theta \tag{A.9}$$

Equation A.6 is a Freudenstein equation, which can be solved in closed form. Knowing this, ϕ can now be solved in terms of θ.

$$w = \tan\frac{\phi}{2} \tag{A.10}$$

$$\sin\phi = \frac{2w}{1+w^2} \tag{A.11}$$

$$\cos\phi = \frac{1-w^2}{1+w^2} \tag{A.12}$$

Now substituting to create a quadratic:

$$0 = (R_3 + R_2)w^2 + 2R_1w + (R_3 + R_2) \tag{A.13}$$

$$w = \frac{-R_1 \pm \sigma\sqrt{R_1^2 + R_2^2 - R_3^2}}{R_3 - R_2} \tag{A.14}$$

Where $\sigma = \pm 1$ depends on the mode which the RRRR mechanism is in. σ changes the kinematic configuration. The derivation of ϕ only has a valid range of $-\pi \leq \phi \leq \pi$. Substituting Equation A.10 into Equation A.14 to get ϕ:

$$\boxed{\phi(\theta) = 2 \cdot atan2(-R_1 + \sigma\sqrt{R_1^2 + R_2^2 - R_3^2}, R_3 - R_2)} \tag{A.15}$$

Note: $atan2$ is a specialized Matlab function provide the four quadrant inverse tangent [38].

Solve for α

By dividing Equation A.5 by Equation A.4:

$$\boxed{\alpha(\theta, \phi) = arctan2(-L_1 \sin\theta + L_3 \sin\phi, L_0 - L_1 \cos\theta + L_3 \cos\phi)} \tag{A.16}$$

θ, ϕ, and α can now fully describe the position of the mechanism in one coordinate (θ).

A.2.2 Kinematics: Velocity Analysis

Deriving the positional equations of the mechanism are necessary in order to get the velocity equations of the mechanism. Taking the derivative of the positional vector loop equations provides the necessary velocities after some manipulation. This yields the following results.

Differentiating Equations A.2 and A.3 result in the following matrix:

$$\begin{bmatrix} L_1 \sin\theta & L_2 \sin\alpha & L_3 \sin\phi \\ -L_1 \cos\theta & -L_2 \cos\alpha & L_3 \cos\phi \end{bmatrix} \begin{bmatrix} \dot{\theta} \\ \dot{\alpha} \\ \dot{\theta} \end{bmatrix} = \begin{bmatrix} 0 \\ 0 \end{bmatrix} \tag{A.17}$$

Rearranging Equation A.17:

$$\begin{bmatrix} L_2 \sin\alpha & L_3 \sin\phi \\ -L_2 \cos\alpha & L_3 \cos\phi \end{bmatrix} \begin{bmatrix} \dot{\theta} \\ \dot{\alpha} \end{bmatrix} = \begin{bmatrix} L_1 \sin\theta \\ -L_1 \cos\theta \end{bmatrix} \dot{\theta} \tag{A.18}$$

$$\begin{bmatrix} \dot{\theta} \\ \dot{\alpha} \end{bmatrix} = \begin{bmatrix} Q_1(\theta, \alpha, \phi) \\ Q_2(\theta, \alpha, \phi) \end{bmatrix} \dot{\theta} \tag{A.19}$$

where:

$$Q_1(\theta, \alpha, \phi) = \frac{\partial \alpha}{\partial \theta} = \frac{L_1 \sin(\phi - \theta)}{L_2 \sin(\alpha - \phi} \tag{A.20}$$

$$Q_2(\theta, \alpha, \phi) = \frac{\partial \phi}{\partial \theta} = \frac{L_1 \sin(\phi - \theta)}{L_3 \sin(\alpha - \phi} \tag{A.21}$$

Solve for $\dot{\alpha}$

$$\dot{\alpha}(\theta, \dot{\theta}, \phi, \alpha) = \frac{L_1 \sin(\phi - \theta)}{L_2 \sin(\alpha - \phi)} \dot{\theta} \tag{A.22}$$

Solve for $\dot{\phi}$

$$\dot{\phi}(\theta, \dot{\theta}, \phi, \alpha) = \frac{L_1 \sin(\alpha - \theta)}{L_3 \sin(\alpha - \phi)} \dot{\theta} \tag{A.23}$$

A.2.3 Kinematics: Velocity Analysis for Link Center of Mass

For links $i = 1 - 3$:

$$L_{ci} = \frac{L_i}{2} \tag{A.24}$$

For Link 1:

$$x_{g1} = L_{c1} \cos(\theta) \tag{A.25}$$

$$y_{g1} = L_{c1} \sin(\theta) \tag{A.26}$$

$$x\vec{y}_{g1} = [L_{c1} \cos(\theta)]\hat{i} + [L_{c1} \sin(\theta)]\hat{j} \tag{A.27}$$

$$v_{g1_x} = -L_{c1}\sin(\theta)\dot{\theta} \tag{A.28}$$

$$v_{g1_y} = L_{c1}\cos(\theta)\dot{\theta} \tag{A.29}$$

$$\vec{v_{g1}} = [L_{c1}\sin(\theta)\dot{\theta}]\hat{i} + [L_{c1}\cos(\theta)\dot{\theta}]\hat{j} \tag{A.30}$$

$$|v_{g1}|^2 = L_{c1}^2\dot{\theta}^2 \tag{A.31}$$

For Link 2:

$$x_{g2} = L_1\cos(\theta) + L_{c2}\cos(\alpha) \tag{A.32}$$

$$y_{g2} = L_1\sin(\theta) + L_{c2}\sin(\alpha) \tag{A.33}$$

$$x\vec{y}_{g2} = [L_1\cos(\theta) + L_{c2}\cos(\alpha)]\hat{i} + [L_1\sin(\theta) + L_{c2}\sin(\alpha)]\hat{j} \tag{A.34}$$

$$v_{g2_x} = -L_1\sin(\theta)\dot{\theta} - L_{c2}\sin(\alpha)\dot{\alpha} \tag{A.35}$$

$$v_{g2_y} = L_1\cos(\theta)\dot{\theta} + L_{c2}\sin(\alpha)\dot{\alpha} \tag{A.36}$$

$$\vec{v_{g2}} = [-L_1\sin(\theta)\dot{\theta} - L_{c2}\sin(\alpha)\dot{\alpha}]\hat{i} + [L_1\cos(\theta)\dot{\theta} + L_{c2}\sin(\alpha)\dot{\alpha}]\hat{j} \tag{A.37}$$

$$|v_{g2}|^2 = L_1^2\dot{\theta}^2 + L_{c2}^2\dot{\alpha}^2 + 2L_1L_{c2}\cos(\theta-\alpha)\dot{\theta}\dot{\alpha} \tag{A.38}$$

For Link 3:

$$x_{g3} = L_{c3}\cos(\phi) \tag{A.39}$$

$$y_{g3} = L_{c3}\sin(\phi) \tag{A.40}$$

$$x\vec{y}_{g3} = [L_{c3}\cos(\phi)]\hat{i} + [L_{c3}\sin(\phi)]\hat{j} \tag{A.41}$$

$$v_{g3_x} = -L_{c3}\sin(\phi)\dot{\phi} \tag{A.42}$$

$$v_{g3_y} = L_{c3}\cos(\phi)\dot{\phi} \tag{A.43}$$

$$\vec{v_{g3}} = [-L_{c3}\sin(\phi)\dot{\phi}]\hat{i} + [L_{c3}\cos(\phi)\dot{\phi}]\hat{j} \tag{A.44}$$

$$|v_{g3}|^2 = L_{c3}^2\dot{\phi}^2 \tag{A.45}$$

A.3 Kinetics: Lagrangian Dynamics

A.3.1 Introduction

Rather than using constrained coordinates, the dynamics for each configuration are analyzed using a single constrained coordinate following the approach by Tang [31]. While a single dynamic equation is only needed to fully describe a system with one degree of freedom, these equations can be quite complicated due to the inherent kinematic vector loop equations. Mathematical gymnastics are often necessary in order to complete this for closed kinematic chains.

The link lengths and link masses are known. Only a single angle input and its first derivative is needed to completely describe each system. A torque (τ) will be applied at the revolute joint described by angle θ in the model. Thus, the model was evaluated using the generalized coordinate θ. Friction in the joints was neglected for the analysis. In addition, the torque supplied was considered an ideal source.

A.3.2 Kinetics: Energy Analysis

The following equations represent the potential energy (V) and kinetic energy (T)equations.

Potential Energy:

The general potential energy equation is shown in Equation A.46.

$$V = M_i g h_i \tag{A.46}$$

$$V = V_1 + V_2 + V_3 \tag{A.47}$$

where:

$$V_1 = \frac{1}{2} L_1 M_1 g \sin\theta \tag{A.48}$$

$$V_2 = M_2 g (L_1 \sin\theta + \frac{L_1}{2} \sin\alpha) \tag{A.49}$$

$$V_3 = \frac{1}{2} M_3 g L_3 \sin\phi \tag{A.50}$$

Kinetic Energy:

The general kinetic energy equation is shown in Equation A.51

$$T = \frac{1}{2} M_i |v_{gi}|^2 + \frac{1}{2} I_i |\omega_i|^2 \tag{A.51}$$

$$T = T_1 + T_2 + T_3 \tag{A.52}$$

Velocity squared terms from before:

$$|v_{g1}|^2 = L_{c1}^2 \dot{\theta}^2 \tag{A.53}$$

$$|v_{g2}|^2 = L_1^2 \dot{\theta}^2 + L_{c2}^2 \dot{\alpha}^2 + 2 L_1 L_{c2} \cos(\theta - \alpha) \dot{\theta} \dot{\alpha} \tag{A.54}$$

$$|v_{g3}|^2 = L_{c3}^2 \dot{\phi}^2 \tag{A.55}$$

$$T_1 = \frac{1}{8} M_1 L_1^2 \dot{\theta}^2 + \frac{1}{2} I_1 \dot{\theta}^2 \tag{A.56}$$

$$T_2 = \frac{1}{2} M_2 L_1^2 \dot{\theta}^2 + \frac{1}{8} M_2 L_2^2 \dot{\alpha}^2 + \frac{1}{2} I_2 \dot{\theta}^2 + M_2 L_1 L_2 \cos(\theta - \alpha) \dot{\theta} \dot{\alpha} \tag{A.57}$$

$$T_3 = \frac{1}{8} M_3 L_3^2 \dot{\phi}^2 + \frac{1}{2} I_3 \dot{\phi}^2 \tag{A.58}$$

A.3.3 Kinetics: Lagrangian

The energy parameters can be placed into Lagranges equation [24].

Lagrangian:

$$\mathcal{L} = T - V \tag{A.59}$$

$$\mathcal{L} = T_1 + T_2 + T_3 - V_1 - V_2 \tag{A.60}$$

$$\mathcal{L} = B_1\dot{\theta}^2 + B_2\dot{\alpha}^2 + B_3\dot{\alpha}^2 + N_1 D_1(\theta,\alpha)\,\dot{\theta}\dot{\alpha} + H(\theta,\alpha,\phi) \tag{A.61}$$

where:

$$B_1 = \frac{1}{2}\left(M_1 L_{c1}^2 + I_1 + M_1 L_1^2\right) \tag{A.62}$$

$$B_2 = \frac{1}{2}\left(M_2 L_{c2}^2 + I_2\right) \tag{A.63}$$

$$B_3 = \frac{1}{2}\left(M_3 L_{c3}^2 + I_3\right) \tag{A.64}$$

$$N_1 = M_2 L_1 L_{c2} \tag{A.65}$$

$$D_1(\theta,\alpha) = \cos(\theta - \alpha) \tag{A.66}$$

$$H(\theta,\alpha,\phi) = (-M_1 g L_{c1} - M - 2gL_1)\sin\theta - M_2 g L_{c2}\sin\alpha - M_3 g L_{c3}\sin\phi \tag{A.67}$$

Simplify:

$$\mathcal{L} = B_1\dot{\theta}^2 + B_2\dot{\alpha}^2 + B_3\dot{\alpha}^2 + N_1 D_1\dot{\theta}\dot{\alpha} + H \tag{A.68}$$

Now eliminate $\dot{\alpha}$ from Equation A.68 using Equation A.22

$$\boxed{\mathcal{L} = \left(B_1 + B_2 Q_1^2 + B_3 Q_2^2 + N_1 D_1 Q_1\right)\dot{\theta}^2 + H} \tag{A.69}$$

A.3.4 Kinetics: Equation of Motion

$$\tau_{external} = \frac{d}{dt}\left(\frac{\partial\mathcal{L}}{\partial\dot{\theta}}\right) - \frac{\partial\mathcal{L}}{\partial\theta} \tag{A.70}$$

After taking the derivatives and simplifying:

$$\boxed{F(\theta)\ddot{\theta} + A\left(\theta,\dot{\theta}\right)\dot{\theta}^2 + H_{partial} = \tau_{external}} \tag{A.71}$$

where:

$$F = 2\left[B_1 + B_2 {Q_1}^2 + N_1 D_1 Q_1 + N_2 D_2 Q_1\right] \tag{A.72}$$

$$A = \left[2B_2Q_1\left(\frac{\partial Q_1}{\partial\theta} + Q_1\frac{\partial Q_1}{\partial\alpha} + Q_2\frac{\partial Q_1}{\partial\theta}\right) + 2B_3Q_2\left(\frac{\partial Q_2}{\partial\theta} + Q_1\frac{\partial Q_2}{\partial\alpha} + Q_2\frac{\partial Q_2}{\partial\theta}\right) + N_1\left(D_1\left(\frac{\partial Q_1}{\partial\theta} + Q_1\frac{\partial Q_1}{\partial\alpha} + Q_2\frac{\partial Q_1}{\partial\phi}\right) + Q_1\left(\frac{\partial D_1}{\partial\theta} + S_1\frac{\partial D_1}{\partial\alpha}\right)\right)\right] \quad \text{(A.73)}$$

$$H_{partial} = \left[-\frac{\partial H}{\partial\theta} - \frac{\partial H}{\partial\alpha}\frac{\partial\alpha}{\partial\theta} - \frac{\partial H}{\partial\phi}\frac{\partial\phi}{\partial\theta}\right] \quad \text{(A.74)}$$

Derivative Terms:

$$\frac{\partial Q_1}{\partial \theta} = \frac{L_1 \sin(\phi - \theta)}{L_2 \sin(\alpha - \phi)} \tag{A.75}$$

$$\frac{\partial Q_1}{\partial \alpha} = -\frac{L_1 \sin(\phi - \theta)\cos(\alpha - \phi)}{L_2 \sin(\alpha - \phi)^2} \tag{A.76}$$

$$\frac{\partial Q_1}{\partial \phi} = -2\frac{L_1 \sin(\alpha - \theta)}{-L_2 + L_2(\cos(2\alpha - 2\phi))} \tag{A.77}$$

$$\frac{\partial Q_2}{\partial \theta} = -\frac{L_1 \cos(\alpha - \theta)}{L_3 \sin(\alpha - \phi)} \tag{A.78}$$

$$\frac{\partial Q_2}{\partial \alpha} = 2\frac{L_1 \sin(\phi - \theta)}{-L_3 + L_3 \cos(2\alpha - 2\phi)} \tag{A.79}$$

$$\frac{\partial Q_2}{\partial \phi} = -\frac{L_1 \sin(\alpha - \theta)\cos(\alpha - \phi)}{L_3 \sin(\alpha - \phi)^2} \tag{A.80}$$

C_1 terms:

$$\frac{\partial C_1}{\partial \theta} = \sin(\alpha - \theta) \tag{A.81}$$

$$\frac{\partial C_1}{\partial \alpha} = -\sin(\alpha - \theta) \tag{A.82}$$

G terms:

$$\frac{\partial G}{\partial \theta} = (-M_1 L_{c1} - M_2 L_1)\, g \cos\theta \tag{A.83}$$

$$\frac{\partial G}{\partial \alpha} = -M_2 g \mathrm{L_{c2}} \cos\alpha \tag{A.84}$$

$$\frac{\partial G}{\partial \phi} = -M_3 g \mathrm{L_{c3}} \cos\phi \tag{A.85}$$

APPENDIX B

RRRP MECHANISM: MECHANICAL DERIVATION

B.1 Introduction

The following is a full derivation of the kinematics and kinetics of the RRRP configuration. A Lagrangian approach was used for the kinetics. The RRRP configuration (Figure B.1) is a one degree of freedom mechanism. If the input angle (θ) is known, all other angles and positions can be found. The kinematics are necessary in understanding the dynamics of the system. A fixed coordinate system is located at the left revolute joint following the right hand rule. The analysis will be completed in a planar frame.

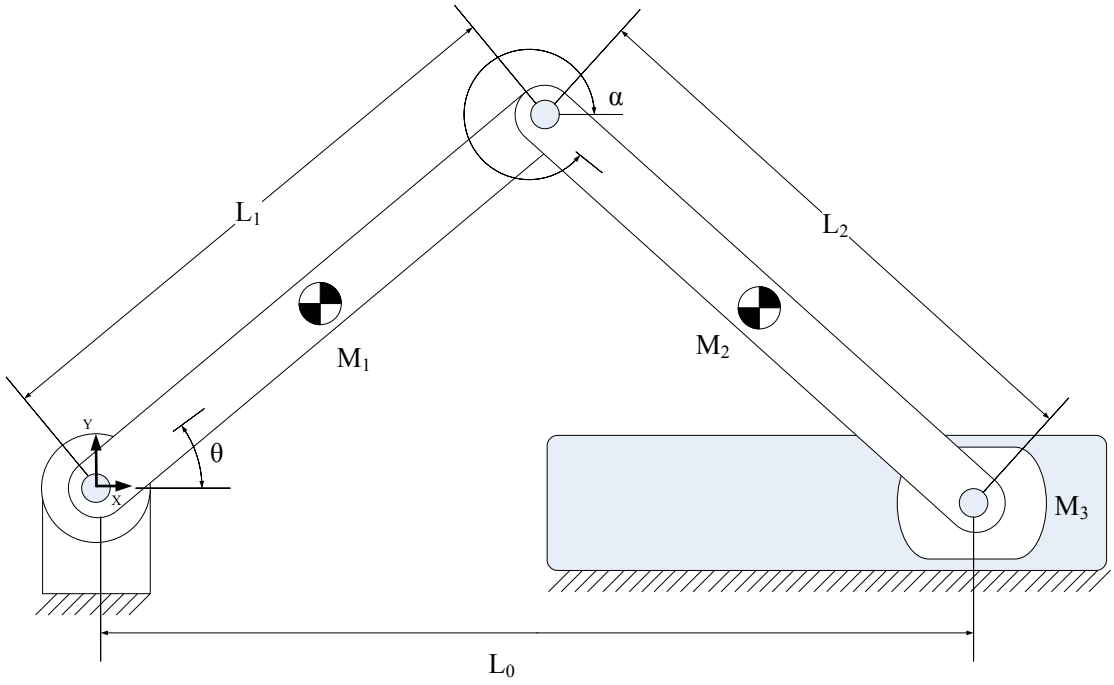

Figure B.1: RRRP Configuration

B.2 Kinematics

B.2.1 Kinematics: Position Analysis

Through the kinematics of the mechanism, the specified angles can be found. This requires some manipulation of mathematical principles but is necessary for understanding the mechanism.

Using the vector loop method, kinematic equations were developed for the RRRP mechanism.

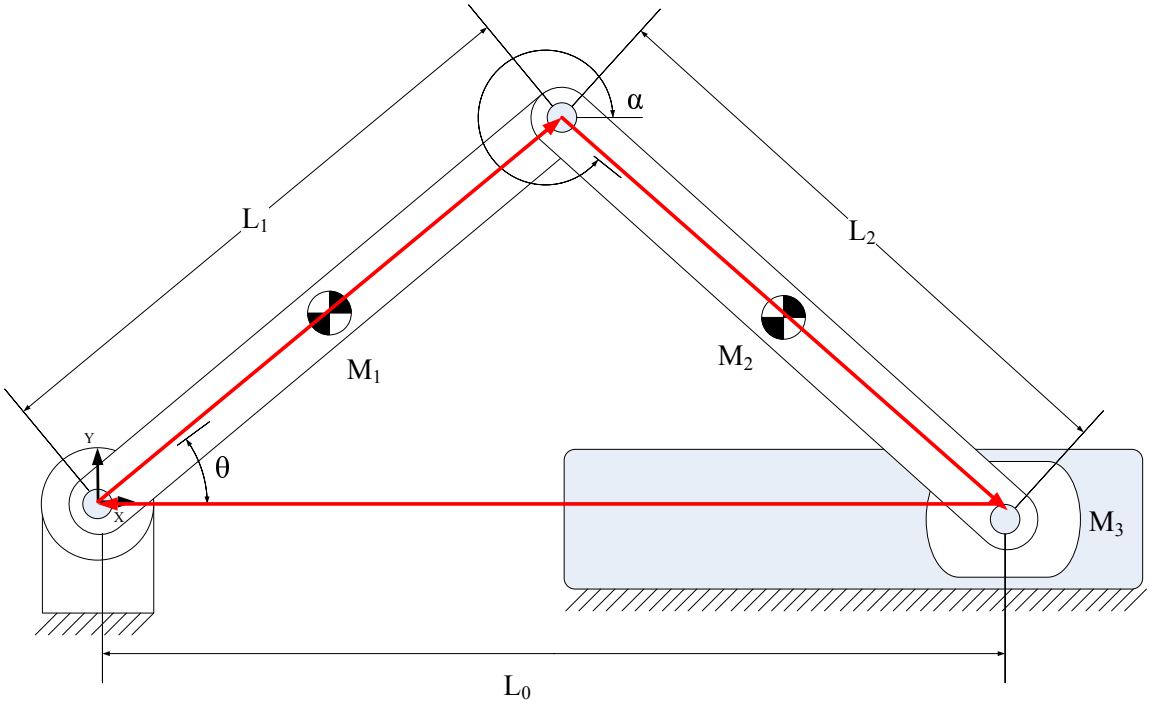

Figure B.2: RRRP Configuration: Vector Loop

Vector Loop

Using the vector loop method, kinematic equations were developed for the RRRP mechanism [31]. Reference Figure B.2 for loop closure vectors. The naming convention is consistent with the link lengths.

$$\vec{0} = \vec{r_1} + \vec{r_2} - \vec{r_3} \tag{B.1}$$

Now using the Vector loop equation, it can be broken into x components and y components. *For x:*

$$0 = L_1 \cos\theta + L_2 \cos\alpha - L_0 \tag{B.2}$$

For y:

$$0 = L_1 \sin\theta + L_2 \sin\alpha \tag{B.3}$$

θ, $\dot{\theta}$ are assumed as the initial conditions of the mechanism. In addition, it is assumed all link lengths are known. α, $\dot{\alpha}$, L_0, $\dot{L_0}$ are unknown and will be expressed in terms of θ to fully describe the position of the mechanism in one coordinate.

Solve for L_0 :

Rearrange in terms of α :

$$L_2 cos\alpha = L_0 - L_1 \cos\theta \tag{B.4}$$

$$L_2 sin\alpha = -L_1 \sin\theta \tag{B.5}$$

Square Equations B.4 and B.5 then add together

$$0 = {L_0}^2 + k_1 L_0 + k_2 \tag{B.6}$$

where:

$$k_1 = \ -2L_1 cos\theta \tag{B.7}$$

$$k_2 = L_1^2 - L_2^2 \tag{B.8}$$

$$\boxed{L_0(\theta) = L_1 \cos\theta \pm \sqrt{L_1^2 \cos\theta^2 - L_1^2 + L_2^2}} \tag{B.9}$$

Solve for α :

Divide Equation B.5 by B.4

$$\boxed{\alpha(\theta, L_0) = arctan2(-L_1 \sin\theta, L_0 - L_1 \cos\theta)} \tag{B.10}$$

B.2.2 Kinematics: Velocity Analysis

Taking the derivative of the vector loop equations provides the necessary velocities. This yields the following results for the RRRP configuration.

Solve for $\dot{L_0}$:

Differentiating Equation B.9 with respect to time yields:

$$\boxed{\dot{L_0}(\theta, \dot{\theta}) = -L_1 sin\theta\ \dot{\theta} \overline{+} \frac{-L_1^2 sin\theta\ cos\theta\ \dot{\theta}}{\sqrt{{L_1}^2\ (cos\theta\ )^2 - {L_1}^2 + {L_2}^2}}} \tag{B.11}$$

Solve for $\dot{\alpha}$:

Differentiating Equation B.10 with respect to time yields:

$$\boxed{\dot{\alpha}(\theta, \dot{\theta}) = \left(\frac{-L_1 cos\theta}{\sqrt{{L_1}^2\ (cos\theta\ )^2 - {L_1}^2 + {L_2}^2}} \right) \dot{\theta}} \tag{B.12}$$

B.2.3 Kinematics: Velocity Analysis for Link Center of Mass

For links $i = 1 - 3$:

$$L_{ci} = \frac{L_i}{2} \tag{B.13}$$

For Link 1:

$$x_{g1} = L_{c1} \cos(\theta) \tag{B.14}$$

$$y_{g1} = L_{c1} \sin(\theta) \tag{B.15}$$

$$x\vec{y}_{g1} = [L_{c1}\cos(\theta)]\hat{i} + [L_{c1}\sin(\theta)]\hat{j} \tag{B.16}$$

$$v_{g1_x} = -L_{c1}\sin(\theta)\dot{\theta} \tag{B.17}$$

$$v_{g1_y} = L_{c1}\cos(\theta)\dot{\theta} \tag{B.18}$$

$$\vec{v_{g1}} = [L_{c1}\sin(\theta)\dot{\theta}]\hat{i} + [L_{c1}\cos(\theta)\dot{\theta}]\hat{j} \tag{B.19}$$

$$|v_{g1}|^2 = L_{c1}^2\dot{\theta}^2 \tag{B.20}$$

For Link 2:

$$x_{g2} = L_1\cos(\theta) + L_{c2}\cos(\alpha) \tag{B.21}$$

$$y_{g2} = L_1\sin(\theta) + L_{c2}\sin(\alpha) \tag{B.22}$$

$$x\vec{y}_{g2} = [L_1\cos(\theta) + L_{c2}\cos(\alpha)]\hat{i} + [L_1\sin(\theta) + L_{c2}\sin(\alpha)]\hat{j} \tag{B.23}$$

$$v_{g2_x} = -L_1\sin(\theta)\dot{\theta} - L_{c2}\sin(\alpha)\dot{\alpha} \tag{B.24}$$

$$v_{g2_y} = L_1\cos(\theta)\dot{\theta} + L_{c2}\sin(\alpha)\dot{\alpha} \tag{B.25}$$

$$\vec{v_{g2}} = [-L_1\sin(\theta)\dot{\theta} - L_{c2}\sin(\alpha)\dot{\alpha}]\hat{i} + [L_1\cos(\theta)\dot{\theta} + L_{c2}\sin(\alpha)\dot{\alpha}]\hat{j} \tag{B.26}$$

$$|v_{g2}|^2 = L_1^2\dot{\theta}^2 + L_{c2}^2\dot{\alpha}^2 + 2L_1L_{c2}\cos(\theta-\alpha)\dot{\theta}\dot{\alpha} \tag{B.27}$$

For Link 3:

$$x_{g3} = L_1 cos\theta \ + L_2 cos\alpha \tag{B.28}$$

$$y_{g3} = 0 \tag{B.29}$$

$$x\vec{y}_{g3} = [L_1 cos\theta \ + L_2 cos\alpha \ ]\hat{i} \tag{B.30}$$

$$v_{g3_x} = \ -L_1 sin\theta \ \dot{\theta} - \ L_2 sin\alpha \ \dot{\alpha} \tag{B.31}$$

$$v_{g3_y} = 0 \tag{B.32}$$

$$\vec{v_{g3}} = [-L_{c3}\sin(\phi)\dot{\phi}]\hat{i} \tag{B.33}$$

$$|v_{g3}|^2 = {L_1}^2\dot{\theta}^2(sin\theta\ )^2 + {L_2}^2\dot{\alpha}^2(sin\alpha\ )^2 + 2L_1L_2\dot{\alpha}\ \dot{\theta}sin\alpha\ sin\theta \tag{B.34}$$

B.3 Kinetics: Lagrangian Dynamics

B.3.1 Introduction

Rather than using constrained coordinates, the dynamics for each configuration are analyzed using a single constrained coordinate following the approach by Tang [31]. While a single dynamic equation is only needed to fully describe a system with one degree of freedom, these equations can be quite complicated due to the inherent kinematic vector loop equations. Mathematical gymnastics are often necessary in order to complete this for closed kinematic chains.

The link lengths and link masses are known. Only a single angle input and its first derivative is needed to completely describe each system. A torque (τ) will be applied at the revolute joint described by angle θ in the model. Thus, the model was evaluated using the generalized coordinate θ. Friction in the joints was neglected for the analysis. In addition, the torque supplied was considered an ideal source.

B.3.2 Kinetics: Energy Analysis

The following equations represent the potential energy (V) and kinetic energy (T)equations.

Potential Energy

The general potential energy equation is shown in Equation A.34

$$V = M_i g h_i \tag{B.35}$$

$$V = V_1 + V_2 + V_3 \tag{B.36}$$

where:

$$V_1 = \frac{1}{2} M_1 g \sin\theta L_1 \tag{B.37}$$

$$V_2 = M_2 g (L_1 \sin\theta + \frac{L_1}{2} \sin\alpha) \tag{B.38}$$

$$V_3 = 0 \tag{B.39}$$

Kinetic Energy

The general kinetic energy equation is shown in Equation A.37

$$T = \frac{1}{2} M_i |v_{gi}|^2 + \frac{1}{2} I_i |\omega_i|^2 \tag{B.40}$$

$$T = T_1 + T_2 + T_3 \tag{B.41}$$

Velocity squared terms from before:

$$|v_{g1}|^2 = L_{c1}^2 \dot{\theta}^2 \tag{B.42}$$

$$|v_{g2}|^2 = L_1^2 \dot{\theta}^2 + L_{c2}^2 \dot{\alpha}^2 + 2 L_1 L_{c2} \cos(\theta - \alpha) \dot{\theta} \dot{\alpha} \tag{B.43}$$

$$|v_{g3}|^2 = {L_1}^2 \dot{\theta}^2 (sin\theta\ )^2 + {L_2}^2 \dot{\alpha}^2 (sin\alpha\ )^2 + 2 L_1 L_2 \dot{\alpha}\ \dot{\theta} sin\alpha\ sin\theta \tag{B.44}$$

where:

$$T_1 = \frac{1}{2} M_1 \left(\frac{L_1}{2} \right)^2 \dot{\theta}^2 + \frac{1}{2} I_1 \dot{\theta}^2 \tag{B.45}$$

$$T_2 = \frac{1}{2} M_2 \left({L_1}^2 \dot{\theta}^2 + \left(\frac{L_2}{2} \right)^2 \dot{\alpha}^2 + 2 L_1 \left(\frac{l_2}{2} \right) \dot{\alpha}\ \dot{\theta} cos\ (\theta - \alpha) \right) + \frac{1}{2} I_2 \dot{\alpha}^2 \tag{B.46}$$

$$T_3 = \frac{1}{2} M_3 \left({L_1}^2 \dot{\theta}^2 (sin\theta\ )^2 + {L_2}^2 \dot{\alpha}^2 (sin\alpha\ )^2 + 2 L_1 L_2 \dot{\alpha}\ \dot{\theta} sin\alpha\ sin\theta \right) \tag{B.47}$$

B.3.3 Kinetics: Lagrangian

The energy terms be placed into Lagranges equation [24]. *Lagrangian:*

$$\mathcal{L} = T - V \tag{B.48}$$

$$\mathcal{L} = T_1 + T_2 + T_3 - V_1 - V_2 \tag{B.49}$$

The rest of the equations were manipulated in MuPad and then moved to Matlab for simulation. Only the general steps will be shown here.

B.3.4 Kinetics: Equation of Motion

$$\tau_{external} = \frac{d}{dt}\left(\frac{\partial \mathcal{L}}{\partial \dot{\theta}}\right) - \frac{\partial \mathcal{L}}{\partial \theta} \tag{B.50}$$

$$\boxed{A(\theta)\ddot{\theta} + B\left(\theta,\ \dot{\theta}\right)\dot{\theta}^2 - C = \tau_{external}} \tag{B.51}$$

Where A, B, C represent specific terms derived in MuPad

APPENDIX C

PLANT MODELING: RRRR-RRRP MECHANISM

C.1 Introduction

The following is the development of the Plant Model for the control system. The goal of the plant model is to model a DC motor with a gearbox attached to the input driver (θ) of the Mechanism. In order to complete the plant model several steps are necessary. First, a direct current (DC) motor with a gearbox is modeled. Within the DC motor model, a general DC motor electrical circuit is developed and is consistent with industry standards [30, 33]. The DC motor model is then verified through open loop experimentation using a Pittman Ametek 8543 series 24.0 Volt motor [34].

Once the open loop DC motor model is verified, two different models are developed to represent the RRRR-RRRP Mechanism. The two different cases are Case A: Mechanical Modeling with Simplified Dynamics and Case B: Mechanical Modeling with Full Dynamics. Case A: Mechanical Modeling with Simplified Dynamics represents a single external link attached to the output shaft of the motor. Case B: Mechanical Modeling with Full Dynamics represents the entire Mechanism attached to the output shaft of the motor. Using the dynamics previously developed in Appendices A and B, the effective load applied can be determined in each case. Finally, the general electrical motor circuit can be combined with each case to develop state equations that represent the plant model. In summary, two different plant models are developed. Case A is a simplified representation of the Mechanism and Case B is the more complex more realistic model.

C.2 DC Motor Modeling

The modeling of the DC motor is examined as two systems (electrical and mechanical). First, an electrical derivation of a general DC motor is completed. Second, the mechanical modeling of a DC motor with a gearbox is completed. Initially, a generic mechanical model is developed and then revised based on open loop experimentation using a Pittman-Ametek 8543 motor. The revised DC motor model is then verified through experimentation.

C.2.1 DC Motor: Electrical Modeling

Shown in Figure C.1 is a general DC motor model. The electrical circuit will be modeled for future use. The mechanical side is currently represented by a basic general DC motor. The following sections will examine the mechanical side in detail and revise the current representation. Figure C.1 parameters are defined in Table C.1.

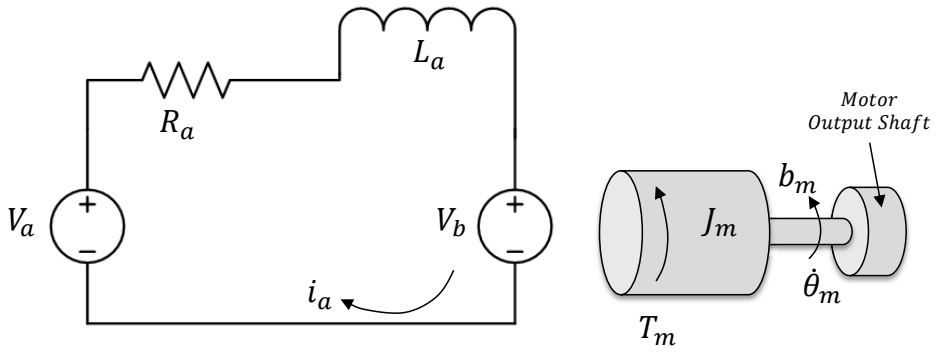

Figure C.1: Electrical Circuit of DC Motor Model

Table C.1: Figure C.1 Parameters

Variable	Variable Description	Units
V_a	Supply Voltage	V
R_a	Motor Resistance	Ω
L_a	Motor Inductance	H
V_b	Motor Back EMF Voltage	V
i_a	Motor Current	A
T_m	Motor Torque	$\mathrm{N \cdot m}$
J_m	Rotor Inertia	$\mathrm{kg \cdot m^2}$
b_m	Viscous Damping Factor	$\mathrm{N \cdot m \cdot s/rad}$
θ_m	Angular Position	rad
$\dot{\theta}_m$	Angular Velocity	rad/s
$\ddot{\theta}_m$	Angular Acceleration	$\mathrm{rad/s^2}$

The following is the development of the equation of motion for the DC motors electrical circuit. Using Kirchoff's Voltage Law (KVL):

$$0 = V_a - R_a i_a - L_a \frac{di_a}{dt} - V_b \tag{C.1}$$

Using the known principle of: $V_b = K_b \dot{\theta}_m$, Equation C.1 can be rewritten.

$$0 = V_a - R_a i_a - L_a \frac{di_a}{dt} - K_b \dot{\theta}_m \tag{C.2}$$

Now solving for $\frac{di_a}{dt}$:

$$\boxed{\frac{di_a}{dt} = \frac{1}{L_a} V_a - \frac{R_a}{L_a} i_a - \frac{K_b}{L_a} \dot{\theta}_m} \tag{C.3}$$

C.2.2 DC Motor: Mechanical Modeling

The following section is the development of the mechanical model of a DC motor with a gearbox. The motor will be modeled will no additional load on the output shaft of the motor. Modeling no additional load on the motor will allow for verification of the motor in experiment. Figure C.2 parameters are explained

in Table C.2. The mechanical model is coupled with the previously developed electrical model.

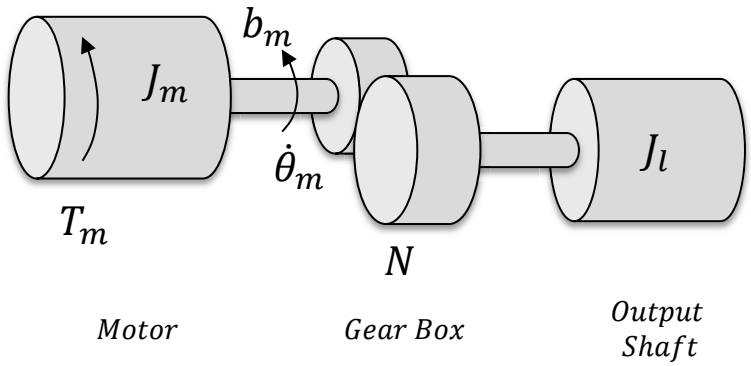

Figure C.2: Mechanical DC Motor Model with Gearbox

Table C.2: Figure C.10 Parameters

Variable	Representation	Units
T_m	Motor Torque	$\mathrm{N \cdot m}$
J_m	Rotor Inertia	$\mathrm{kg \cdot m^2}$
b_m	Viscous Damping Factor	$\mathrm{N \cdot m \cdot s/rad}$
N	Gear Ratio	-
J_l	Inertia of gearbox shaft	$\mathrm{kg \cdot m^2}$
θ_m	Angular Position	rad
$\dot{\theta}_m$	Angular Velocity	rad/s
$\ddot{\theta}_m$	Angular Acceleration	$\mathrm{rad/s^2}$

DC Motor: Kinematics

Using the kinematics of the motor with the gearbox, the motion of the motor shaft can be related to the output shaft motor.

$$r_l\theta_l = r_m\theta_m \tag{C.4}$$

Gear Ratio:

$$N = \frac{r_l}{r_m} \tag{C.5}$$

Relating Motor to the load:

$$\theta_m = N\theta_l \tag{C.6}$$

$$\dot{\theta}_m = N\dot{\theta}_l \tag{C.7}$$

$$\ddot{\theta}_m = N\ddot{\theta}_l \tag{C.8}$$

DC Motor: Kinetics

A Newtonian approach was used to solve the DC motor's kinetics. The motor was split into two different free body diagrams and analyzed. Once analyzed independently, the equations were combined together to solve for the final equations of motion. Shown in Figure C.3 is the first free body diagram with its corresponding equations. Shown Figure C.4 is the second free body diagram with its corresponding equations. Once both sets of equations were solved, they were combined together to solve for the final mechanical equation of motion, shown in Equation C.20.

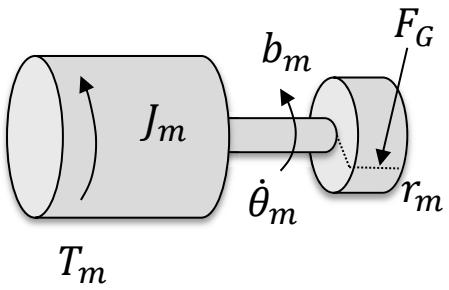

Figure C.3: DC Motor Model with Gearbox- Free Body Diagram One

$$\sum M_m = J_m \ddot{\theta}_m \tag{C.9}$$

$$J_m \ddot{\theta}_m = T_m - b_m \dot{\theta}_m - F_g r_m \tag{C.10}$$

$$F_g = -\frac{1}{r_m} T_m + \frac{b_m}{r_m} \dot{\theta}_m + \frac{J_m}{r_m} \ddot{\theta}_m \tag{C.11}$$

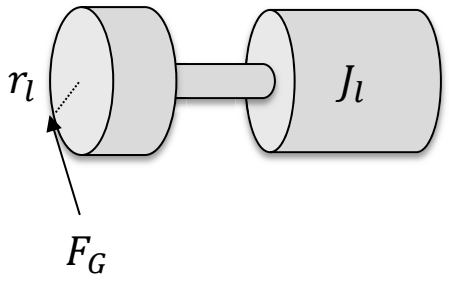

Figure C.4: DC Motor Model with Gearbox- Free Body Diagram Two

$$\sum M_m = J_l \ddot{\theta}_l \tag{C.12}$$

$$J_l \ddot{\theta}_l = F_g r_l \tag{C.13}$$

$$F_g r_l = J_l \ddot{\theta}_l \tag{C.14}$$

Combine Equations to solve for $\ddot{\theta}_l$: Substituting Equation C.11 into Equation C.14 to eliminate F_g:

$$0 = r_l\left(-\frac{1}{r_m}T_m + \frac{b_m}{r_m}\dot{\theta}_m + \frac{J_m}{r_m}\ddot{\theta}_m \right) - J_l\ddot{\theta}_l \tag{C.15}$$

$$0 = -\frac{r_l}{r_m}T_m + \frac{r_l}{r_m}b_m\dot{\theta}_m + \frac{r_l}{r_m}J_m\ddot{\theta}_m - J_l\ddot{\theta}_l \tag{C.16}$$

Now substituting the known kinematic equations into Equation C.37, a simplified result in terms of θ_l is solved.

$$0 = -NT_m + Nb_m\dot{\theta}_m + NJ_m\ddot{\theta}_m - J_l\ddot{\theta}_l \tag{C.17}$$

$$0 = -NT_m + (N^2b_m)\dot{\theta}_l + (N^2J_m - J_l)\ddot{\theta}_l \tag{C.18}$$

Using the relationship $T_m = K_t i_a$ Equation C.18 can be further simplified.

$$(N^2J_m - J_l)\ddot{\theta}_l = (NK_t)i_a - (N^2b_m)\dot{\theta}_l \tag{C.19}$$

Solving for $\ddot{\theta}_l$:

$$\boxed{\ddot{\theta}_l = \frac{NK_t}{N^2J_m - J_l}i_a - \frac{N^2b_m}{N^2J_m - J_l}\dot{\theta}_l} \tag{C.20}$$

DC Motor: Kinetics: State Space Representation

The state variables are $\theta_l, \dot{\theta}_l, i_a$. Collecting all of the terms from the previously developed equations, they are now now listed:

$$\frac{di_a}{dt} = \frac{1}{L_a}V_a - \frac{R_a}{L_a}i_a - \frac{K_b}{L_a}N\dot{\theta}_l \tag{C.21}$$

$$\dot{\theta}_l = \frac{d\theta_l}{dt} \tag{C.22}$$

$$\ddot{\theta}_l = \frac{NK_t}{N^2J_m - J_l}i_a - \frac{N^2b_m}{N^2J_m - J_l}\dot{\theta}_l \tag{C.23}$$

Now representing state equations in State-Space form:

$$\frac{d}{dt}\begin{bmatrix}\theta_l\\ \dot{\theta}_l\\ i_a\end{bmatrix} = \begin{bmatrix}0 & 1 & 0\\ 0 & -\frac{N^2b_m}{N^2J_m - J_l} & \frac{NK_t}{N^2J_m - J_l}\\ 0 & -\frac{K_b}{L_a}N & -\frac{R_a}{L_a}\end{bmatrix}\begin{bmatrix}\theta_l\\ \dot{\theta}_l\\ i_a\end{bmatrix} + \begin{bmatrix}0 & 0 & 0\\ 0 & 0 & 0\\ 0 & 0 & \frac{1}{L_a}\end{bmatrix}\begin{bmatrix}0\\ 0\\ V_a\end{bmatrix} \tag{C.24}$$

DC Motor: Friction Modeling

The developed DC Motor Model was simulated and then compared to experimental results. It was found that additional parameters were necessary for increased fidelity of the model. First, the friction modeling of the model was examined. In the next section, the inertia of the motor and gearbox is examined.

Initially, only the viscous friction ($b_{motor}\dot{\theta}$) and static Coulomb friction torque ($T_{fs_{motor}}$) were modeled. These were the only parameters provided in the data sheet [34] and are only for the motor. These parameters do not account for the addition of the gearbox which will significantly affect the the viscous friction. In addition, the dynamic Coulomb friction torque was not provided. Shown in Table C.3 are the provided parameters in tabular format.

Shown in Figure C.5 is an ideal model of friction in a DC motor. An experimental process to find the various friction terms, viscous friction (B_{Total}), static Coulomb friction torque (T_{fs}) and dynamic Coulomb friction torque (T_{fd}), was conducted. Viscous friction is related linearly to the speed ($\dot{\theta}$). Static Coulomb friction torque is the torque required to start motion. Static Coulomb friction torque is also referred to as the breakaway force [35]. Dynamic Coulomb friction torque is the torque that is in constant opposition when the motor is moving. This friction is independent of the velocity and only dependent on the direction of motion [35]. The experimental process used is outlined in detail in Prisco's work [2]. The Stribeck effect was neglected as the measurement devices could not adequately capture the phenomenon. In addition, this will not be a factor when the experimentation of the Mechanism is conducted. The following $T_{friction}$ term was adapted from Prisco's work [2] and represents the various friction terms. In addition, (B_{Total}) represents the total viscous friction in the motor and the gearbox.

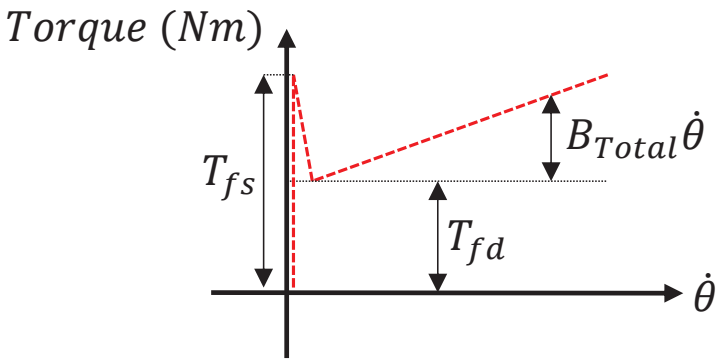

Figure C.5: Theoretical Friction Modeling (Adapted from [2])

$$T_{friction} = \left\{ \begin{array}{l} \dot{\theta}_l = 0 \rightarrow T_{fs} : \text{Static Coulomb friction torque} \\ \dot{\theta}_l \neq 0 \rightarrow T_{fd} : \text{Dynamic Coulomb friction torque} \\ \dot{\theta}_l = 0 \rightarrow -T_{fs} < T_{friction} < -T_{fs} : \text{For static equilibrium} \end{array} \right\} \quad \text{(C.25)}$$

Through the experimentation an improved model of friction was developed. Shown in Figure C.6 is the experimental data and the provided data sheet friction model [34]. Through the analysis it was found that the provided friction model from the Pittman data sheet was not accurate for a motor with a gearbox. Table C.3 provides a comparison of the data sheet values and the experimental motor friction values. The viscous friction terms varied significantly. The variation is directly related to the addition of the gearbox to the motor. In addition, the static Coulomb friction torque was determined and allows for increased fidelity in the model. The experimental results correlate directly to the idealized friction model provide in literature [35, 2].

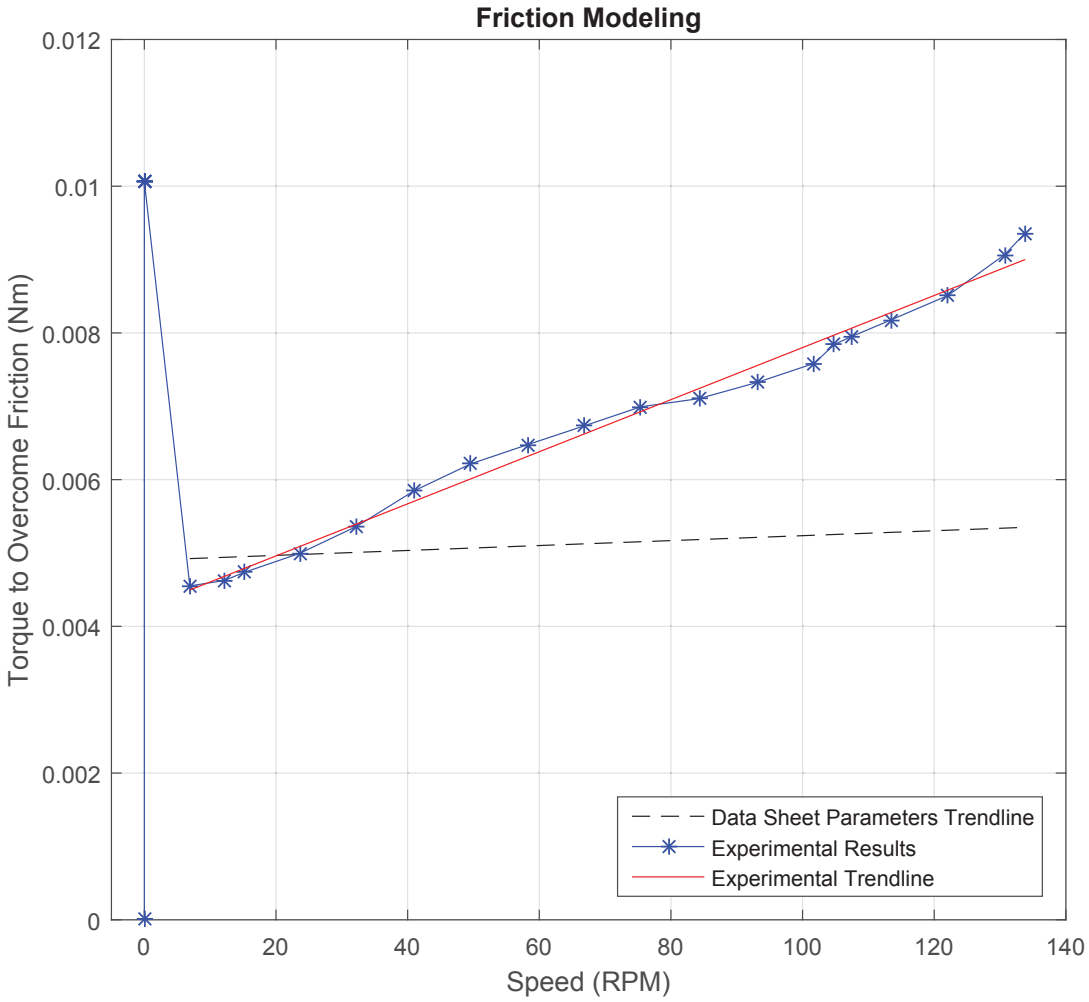

Figure C.6: Experimental Friction Modeling

Table C.3: Comparison of Friction Parameters

Variable	Data Sheet	Experimental	Units
T_{fs}	Not Provided	0.0101	$\mathrm{N \cdot m}$
T_{fd}	0.0049	0.0045	$\mathrm{N \cdot m}$
b_{motor}	$3.36E-6$	-	$\mathrm{N \cdot m \cdot s/rad}$
B_{Total}	Not Provided	$3.55E-5$	$\mathrm{N \cdot m \cdot s/rad}$

DC Motor: Inertia Correction Term

With the updated friction term, the DC Motor Model was simulated and then compared to experimental results. It was found that the motor model responded too fast. Upon examination, the gearbox inertia was not accounted for in the provided data sheet inertia, thus an effective motor inertia was experimentally determined.

The DC motor was set to several voltages and given a step input. The rise time of three trials from the various voltages was recorded. A looping method was used to compare the motor model simulation's rise time to the experimental rise time based on the various input voltages. If the rise times differed, the inertia of the model was varied by a defined increment and the simulation rerun. Once the simulations rise time was within one percent of experimental rise time the inertia was recorded. The new inertia is the inertia that best represents the specific Pittman 8543 motor and is named the Inertia correction term (J_c).

DC Motor: Updated EOM

As discussed in the previous section, adaptation of the original motor is necessary. Updating Equations C.21, C.22, and C.23 the following equations accurately represent the Pittman 8543 DC motor.

$$\frac{di_a}{dt} = \frac{1}{L_a}V_a - \frac{R_a}{L_a}i_a - \frac{K_b}{L_a}N\dot{\theta}_l \tag{C.26}$$

$$\dot{\theta}_l = \frac{d\theta_l}{dt} \tag{C.27}$$

$$\ddot{\theta}_l = \frac{NK_t}{N^2(J_m + J_c) - J_l}i_a - B_{Total}\dot{\theta}_l + T_{friction} \tag{C.28}$$

Verification of Open Loop DC Motor Model

The following figures represent the verification of the open loop DC motor model. A step input at varying voltages was input to both the model and the physical motor. The response of the angular position and angular velocity was examined. Shown in Figure C.7 is the angular velocity response at a 22 volt step input. When viewing Figure C.7, the noise of the sensor is seen by the jagged points. If a better encoder was used a more accurate response could be seen. Shown in Figure C.8 is the angular position response at a 22 volt step input. Figure C.9 shows a comparison of the experimental results to simulated results for angular velocity at multiple voltages. Three trials for the experimental results were conducted at each voltage and then the steady state RPM was averaged and recorded. The averaging provides a more accurate representation and comparison to the simulated model. After the comparison of the experimentation and motor model, it was found that the simulation steady state value is an average of 7.37 RPM faster than the experimental results. The variation is consistent between voltages and can be seem in Figure C.9. While different, this error is insignificant. The DC motor model has now been validated.

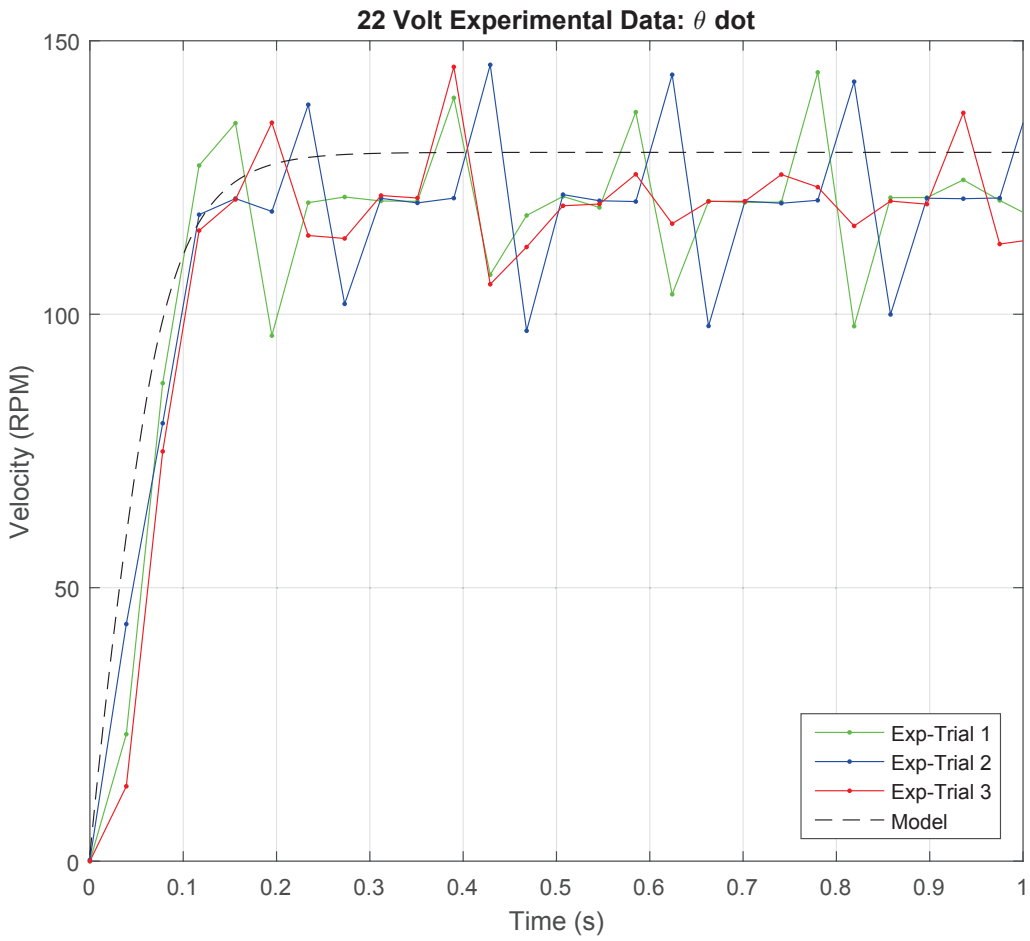

Figure C.7: Angular Velocity- Comparison of Experimental and Simulation Results at 22 Volts

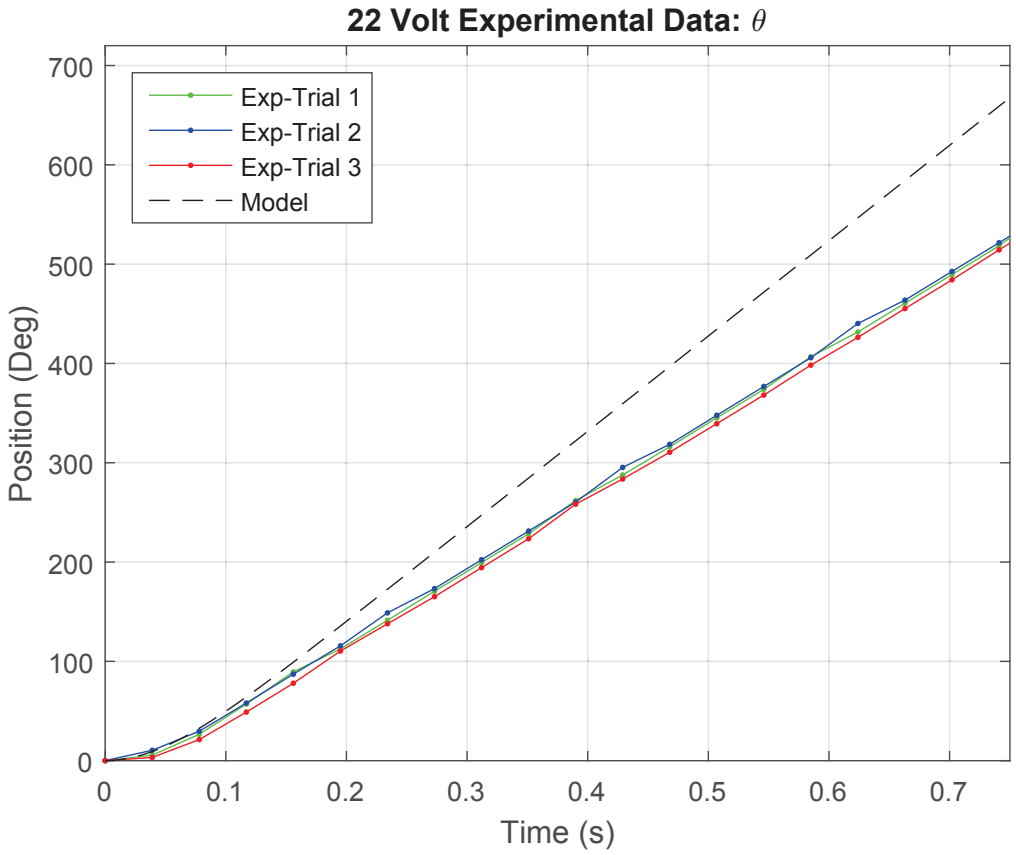

Figure C.8: Angular Position- Comparison of Experimental and Simulation Results at 22 Volts

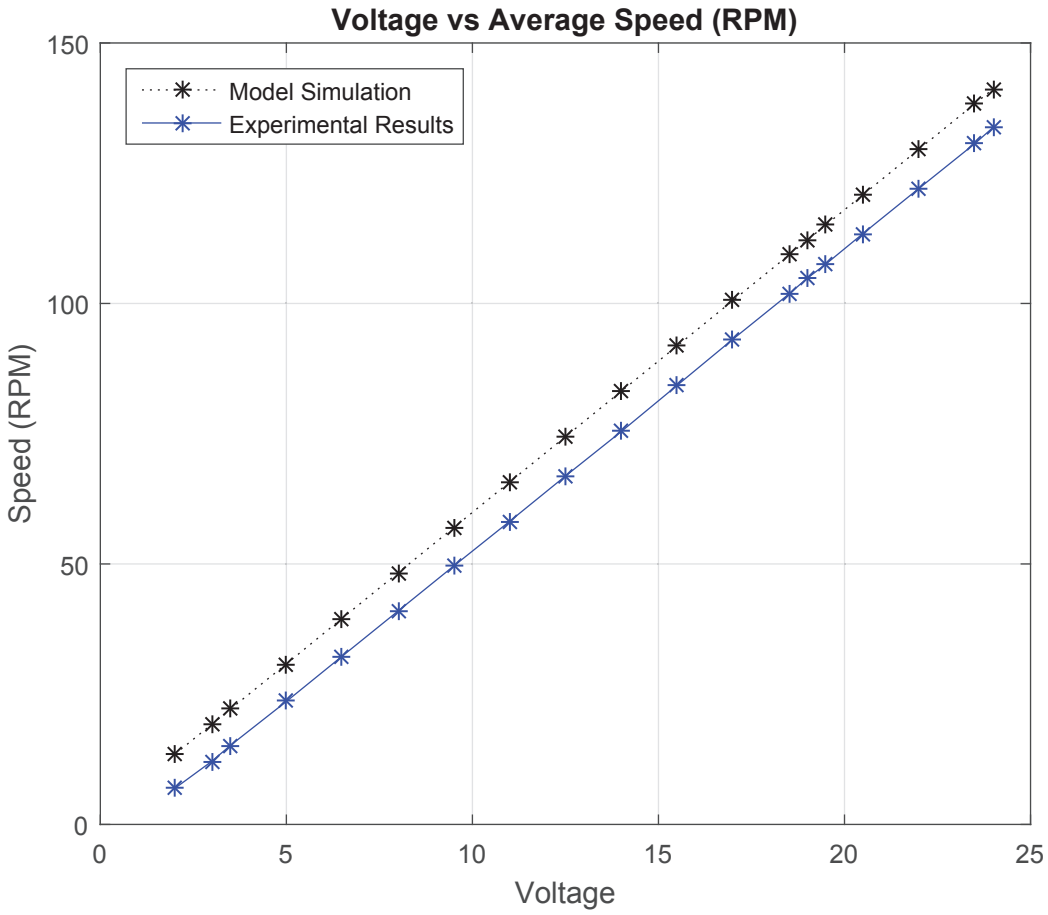

Figure C.9: Comparison of Experimental Results to Simulated Results for Angular Velocity

C.3 Mechanical Modeling with Simplified Dynamics (Case A)

Mechanical Modeling with Simplified Dynamics (Case A) represents a single external link attached to the output shaft of the motor. The mathematical model is extremely comparable to the previously derived DC motor model. An updated diagram of the mechanical side with an external link can be found in Figure C.10. The parameters of the figure are explained in Table C.4. First, the models equations of motion will be derived and then the additional terms (J_c, $T_{friction}$, B_{Total}) will be added to the model. This additional is done after the initial derivation to demonstrate the general form of the equations before any manipulation.

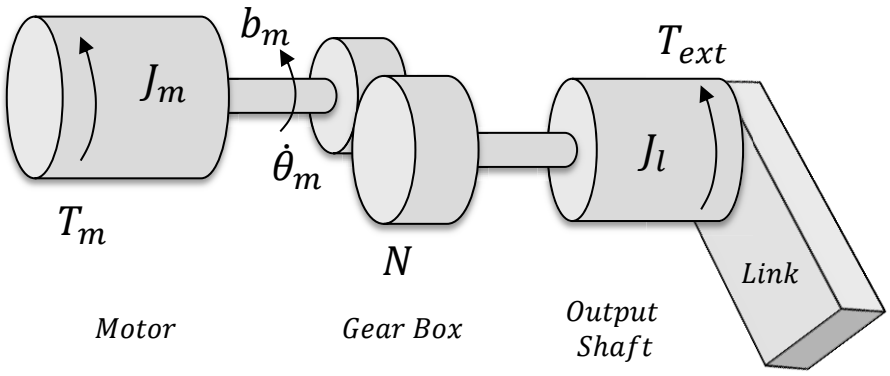

Figure C.10: Case A: Mechanical DC Motor Model with Simplified Dynamics

Table C.4: Figure C.10 Parameters

Variable	Representation	Units
T_m	Motor Torque	$N \cdot m$
J_m	Rotor Inertia	$kg \cdot m^2$
b_m	Viscous Damping Factor	$N \cdot m \cdot s/rad$
N	Gear Ratio	-
J_l	External Inertia of Link and Inertia of gear shaft	$kg \cdot m^2$
T_{ext}	External applied Torque	$N \cdot m$
θ_m	Angular Position	rad
$\dot{\theta}_m$	Angular Velocity	rad/s
$\ddot{\theta}_m$	Angular Acceleration	rad/s^2

C.3.1 Case A: Kinetics

Free Body Diagram One

Shown in Figure C.11 is free body diagram one.

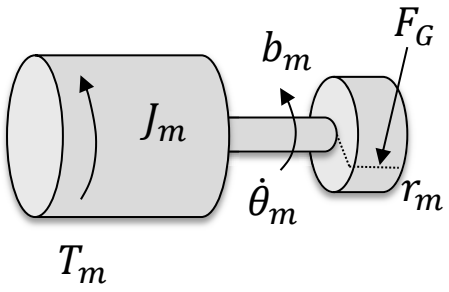

Figure C.11: Case A- Free Body Diagram One

$$\sum M_m = J_m \ddot{\theta}_m \tag{C.29}$$

$$J_m \ddot{\theta}_m = T_m - b_m \dot{\theta}_m - F_g r_m \tag{C.30}$$

$$F_g = -\frac{1}{r_m} T_m + \frac{b_m}{r_m} \dot{\theta}_m + \frac{J_m}{r_m} \ddot{\theta}_m \tag{C.31}$$

Free Body Diagram Two

Shown in Figure C.12 is free body diagram two.

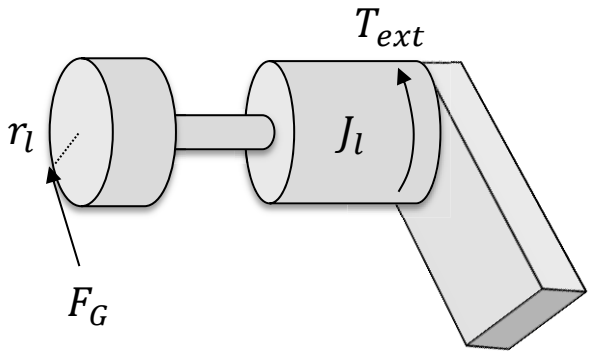

Figure C.12: Case A- Free Body Diagram Two

$$J_l = \frac{1}{12} m_1 L_1^2 + \frac{1}{12} m_{shaft} L_{shaft}^2 \tag{C.32}$$

Where m_1 and L_1 are the mass and length of the first link of the Mechanism, respectively. In addition, m_{shaft} and L_{shaft} are the mass and length of the gearbox shaft on the motor, respectively.

$$\sum M_m = J_l \ddot{\theta}_l \tag{C.33}$$

$$J_l \ddot{\theta}_l = F_g r_l - T_{ext} \tag{C.34}$$

$$F_g r_l = J_l \ddot{\theta}_l + T_{ext} \tag{C.35}$$

Solve for $\ddot{\theta}_l$:

Substituting Equation C.31 into Equation C.35 to eliminate F_g:

$$T_{ext} = r_l \left(-\frac{1}{r_m} T_m + \frac{b_m}{r_m} \dot{\theta}_m + \frac{J_m}{r_m} \ddot{\theta}_m \right) - J_l \ddot{\theta}_l \tag{C.36}$$

$$T_{ext} = -\frac{r_l}{r_m} T_m + \frac{r_l}{r_m} b_m \dot{\theta}_m + \frac{r_l}{r_m} J_m \ddot{\theta}_m - J_l \ddot{\theta}_l \tag{C.37}$$

Substituting the known kinematic equations into Equation C.37 to simplify and put in terms of θ_l.

$$T_{ext} = -NT_m + Nb_m\dot{\theta}_m + NJ_m\ddot{\theta}_m - J_l\ddot{\theta}_l \tag{C.38}$$

$$T_{ext} = -NT_m + (N^2b_m)\dot{\theta}_l + (N^2J_m - J_l)\ddot{\theta}_l \tag{C.39}$$

Using the relationship $T_m = K_t i_a$ to simplify Equation C.39.

$$(N^2J_m - J_l)\ddot{\theta}_l = T_{ext} + (NK_t)i_a - (N^2b_m)\dot{\theta}_l \tag{C.40}$$

Solving for $\ddot{\theta}_l$:

$$\boxed{\ddot{\theta}_l = \frac{1}{N^2J_m - J_l}T_{ext} + \frac{NK_t}{N^2J_m - J_l}i_a - \frac{N^2b_m}{N^2J_m - J_l}\dot{\theta}_l} \tag{C.41}$$

C.3.2 Case A: Equations of Motion

The state variables are $\theta_l, \dot{\theta}_l, i_a$. Applying $\dot{\theta}_m = N\dot{\theta}_l$ to Equation C.3 the equation can be rewritten. The state equations developed are now listed:

$$\frac{di_a}{dt} = \frac{1}{L_a}V_a - \frac{R_a}{L_a}i_a - \frac{K_b}{L_a}N\dot{\theta}_l \tag{C.42}$$

$$\dot{\theta}_l = \frac{d\theta_l}{dt} \tag{C.43}$$

$$\ddot{\theta}_l = \frac{1}{N^2J_m - J_l}T_{ext} + \frac{NK_t}{N^2J_m - J_l}i_a - \frac{N^2b_m}{N^2J_m - J_l}\dot{\theta}_l \tag{C.44}$$

In state space form:

$$\frac{d}{dt}\begin{bmatrix}\theta_l\\ \dot{\theta}_l\\ i_a\end{bmatrix} = \begin{bmatrix}0 & 1 & 0\\ 0 & -\frac{N^2b_m}{N^2J_m - J_l} & \frac{NK_t}{N^2J_m - J_l}\\ 0 & -\frac{K_b}{L_a}N & -\frac{R_a}{L_a}\end{bmatrix}\begin{bmatrix}\theta_l\\ \dot{\theta}_l\\ i_a\end{bmatrix} + \begin{bmatrix}0 & 0 & 0\\ 0 & \frac{1}{N^2J_m - J_l} & 0\\ 0 & 0 & \frac{1}{L_a}\end{bmatrix}\begin{bmatrix}0\\ T_{ext}\\ V_a\end{bmatrix} \tag{C.45}$$

C.3.3 Case A: Updated Equations of Motion

Adding in the the additional corrective terms (J_c, $T_{friction}$, B_{Total}) to the previous generated equations of motion result in the updated state equations. These equations are used in any simulation referenced as Case A.

$$\frac{di_a}{dt} = \frac{1}{L_a}V_a - \frac{R_a}{L_a}i_a - \frac{K_b}{L_a}N\dot{\theta}_l \tag{C.46}$$

$$\dot{\theta}_l = \frac{d\theta_l}{dt} \tag{C.47}$$

$$\ddot{\theta}_l = \frac{1}{N^2(J_m + J_c) - J_l}T_{ext} + \frac{NK_t}{N^2(J_m + J_c) - J_l}i_a - B_{Total}\dot{\theta}_l + T_{friction} \tag{C.48}$$

C.4 Mechanical Modeling with Full Dynamics (Case B)

Mechanical Modeling with Full Dynamics (Case B) represents the full Mechanism connected to the output shaft of the motor. An updated diagram of the mechanical side with a representation of the Mechanism is shown in Figure C.13. The parameters of the figure are explained in Table C.4. First, the models equations of motion will be derived and then the additional terms (J_c, $T_{friction}$, B_{Total}) will be added to the model. This additional is done after the initial derivation to demonstrate the general form of the equations before any manipulation.

Case B incorporates the EOM of the RRRR and RRRP configurations and will be parameterized as J_{mech}. The EOM of the configurations can be found in their entirety in Appendices A and B. A Matlab code was developed to select the configurations equations of motion based on the angle ϕ (Shown in Figure 3.3). If ϕ is greater than zero than the Mechanism is in the RRRR configuration. If ϕ is less than or equal to zero than the Mechanism is in the RRRP configuration. Figure C.14 is a graphical representations of the determination for the parameter

J_{mech}. J_{mech} will be incorporated into the step by step derivation of the equations of motion.

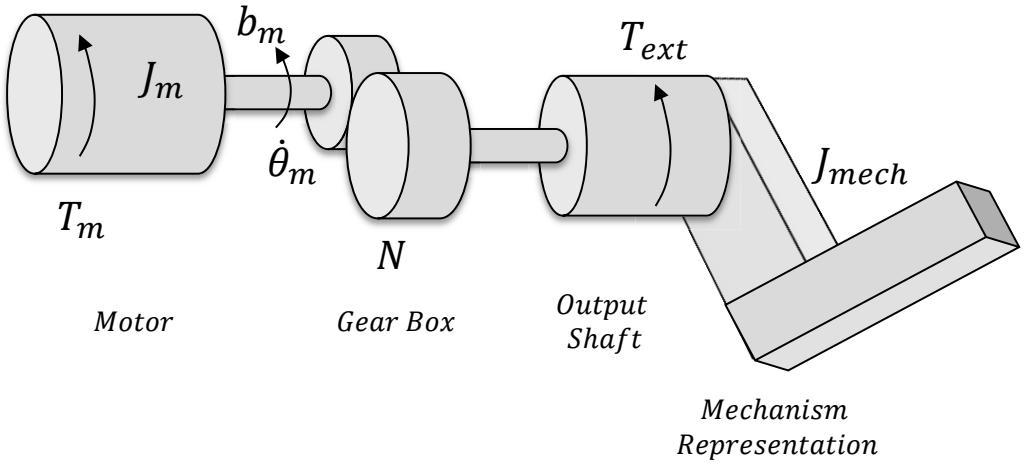

Figure C.13: Case B- Mechanical Modeling with Full Dynamics

Table C.5: Definition of Figure C.10 Parameters

Variable	Representation	Units
T_m	Motor Torque	$N \cdot m$
J_m	Rotor Inertia	$kg \cdot m^2$
b_m	Viscous Damping Factor	$N \cdot m \cdot s/rad$
N	Gear Ratio	-
J_{mech}	External Effective Inertia of Mechanism	$N \cdot m$
T_{ext}	External applied Torque	$N \cdot m$
θ_m	Angular Position	rad
$\dot{\theta}_m$	Angular Velocity	rad/s
$\ddot{\theta}_m$	Angular Acceleration	rad/s^2
J_{mech}	Mechanism's Dynamics	-

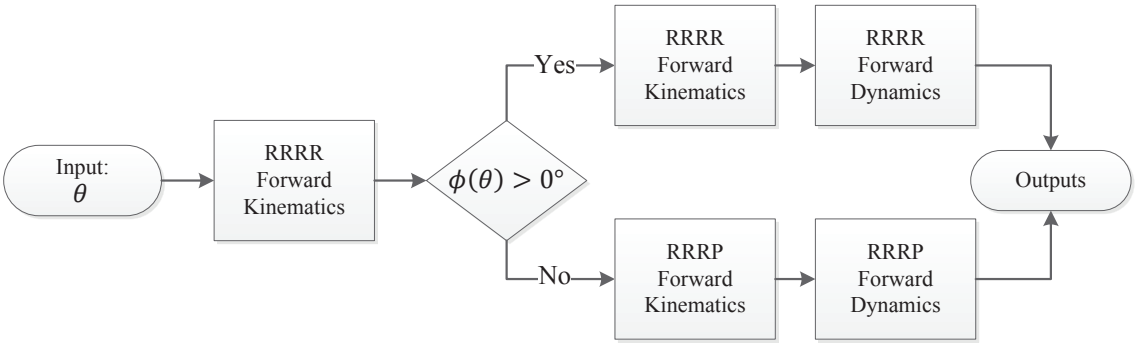

Figure C.14: Configuration Selector for the Mechanism

C.4.1 Case B: Kinematics

Using the kinematics of the motor with the gearbox the motion of the motor shaft can be related to the output shaft motor. r_l and r_m are the radius of the gears attached to the load and to the motor respectively.

$$r_l\theta_l = r_m\theta_m \tag{C.49}$$

Gear Ratio:

$$N = \frac{r_l}{r_m} \tag{C.50}$$

Relating Motor to the load:

$$\theta_m = N\theta_l \tag{C.51}$$

$$\dot{\theta}_m = N\dot{\theta}_l \tag{C.52}$$

$$\ddot{\theta}_m = N\ddot{\theta}_l \tag{C.53}$$

C.4.2 Case B: Kinetics

A Newtonian approach was used for the kinetics of the system.

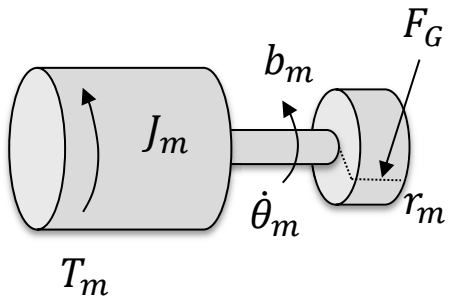

Figure C.15: Case B: Free Body Diagram One

Free Body Diagram One

$$\sum M_m = J_m \ddot{\theta}_m \tag{C.54}$$

$$J_m \ddot{\theta}_m = T_m - b_m \dot{\theta}_m - F_g r_m \tag{C.55}$$

$$F_g = -\frac{1}{r_m} T_m + \frac{b_m}{r_m} \dot{\theta}_m + \frac{J_m}{r_m} \ddot{\theta}_m \tag{C.56}$$

Free Body Diagram Two

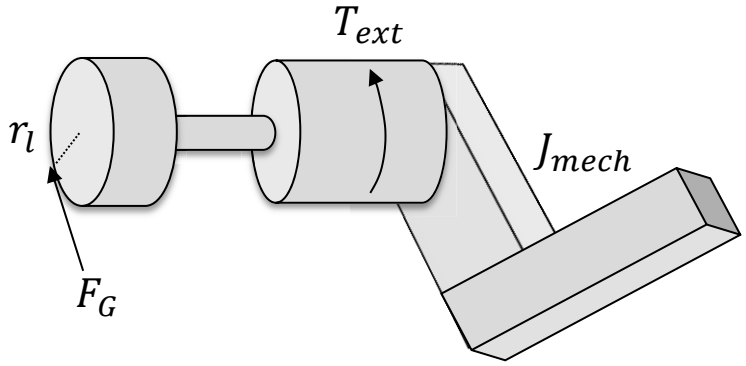

Figure C.16: Case B: Free Body Diagram Two

As stated previously, the Mechanism's dynamics are represented by J_{mech} where A, B, C are coefficients of the dynamics model. Depending on the configuration of the Mechanism A, B, C will change accordingly. Shown in Figure C.14 is a graphical representation for switching between configurations. J_{mech} is used as a representation until later when the equation has been simplified more.

$$J_{mech} = A\ddot{\theta}_l + B\dot{\theta}_l^2 + C \tag{C.57}$$

$$\sum M_m = J_{mech} \tag{C.58}$$

$$J_{mech} = F_g r_l - T_{ext} \tag{C.59}$$

$$F_g r_l = J_{mech} + T_{ext} \tag{C.60}$$

Combine Equations to Solve for $\ddot{\theta}_l$:

Substituting Equation C.56 into EquationC.60 to eliminate F_g:

$$T_{ext} = r_l\left(-\frac{1}{r_m}T_m + \frac{b_m}{r_m}\dot{\theta}_m + \frac{J_m}{r_m}\ddot{\theta}_m \right) - J_{mech} \tag{C.61}$$

$$T_{ext} = -\frac{r_l}{r_m}T_m + \frac{r_l}{r_m}b_m\dot{\theta}_m + \frac{r_l}{r_m}J_m\ddot{\theta}_m - J_{mech} \tag{C.62}$$

Substituting the known kinematic equations into C.62 to simplify. Put all terms into θ_l and eliminate θ_m .

$$T_{ext} = -NT_m + Nb_m\dot{\theta}_m + NJ_m\ddot{\theta}_m - J_{mech} \tag{C.63}$$

$$T_{ext} = -NT_m + (N^2 b_m)\dot{\theta}_l + (N^2 J_m)\ddot{\theta}_l - J_{mech} \tag{C.64}$$

Using the relationship $T_m = K_t i_a$ to simplify Equation C.64.

$$(N^2 J_m)\ddot{\theta}_l = J_{mech} + T_{ext} + (NK_t)i_a - (N^2 b_m)\dot{\theta}_l \tag{C.65}$$

Now substituting Equation C.57 into Equation C.65.

$$(N^2 J_m)\ddot{\theta}_l = A\ddot{\theta}_l + B\dot{\theta}_l^2 + C + T_{ext} + (NK_t)i_a - (N^2 b_m)\dot{\theta}_l \tag{C.66}$$

$$(J_m N^2 - A)\ddot{\theta}_l = B\dot{\theta}_l^2 + C + T_{ext} + (NK_t)i_a - (N^2 b_m)\dot{\theta}_l \tag{C.67}$$

Solve for $\ddot{\theta}_l$:

$$\boxed{\ddot{\theta}_l = \frac{B}{J_m N^2 - A}\dot{\theta}_l^2 + \frac{C}{J_m N^2 - A} + \frac{1}{J_m N^2 - A}T_{ext} + \frac{K_t N}{J_m N^2 - A}i_a - \frac{N_2 b_m}{J_m N^2 - A}\dot{\theta}_l} \tag{C.68}$$

C.4.3 Case B: Equations of Motion

All of the state variable ($\theta_l, \dot{\theta}_l, i_a$) equations have been collected and are provided.

$$\frac{di_a}{dt} = \frac{1}{L_a}V_a - \frac{R_a}{L_a}i_a - \frac{K_b}{L_a}N\dot{\theta}_l \tag{C.69}$$

$$\dot{\theta}_l = \frac{d\theta_l}{dt} \tag{C.70}$$

$$\ddot{\theta}_l = \frac{B}{J_m N^2 - A}\dot{\theta}_l^2 + \frac{C}{J_m N^2 - A} + \frac{1}{J_m N^2 - A}T_{ext} + \frac{K_t N}{J_m N^2 - A}i_a - \frac{N_2 b_m}{J_m N^2 - A}\dot{\theta}_l \tag{C.71}$$

C.4.4 Case B: Updated Equations of Motion

Adding in the the additional corrective terms (J_c, $T_{friction}$, B_{Total}) to the previous generated equations of motion result in the updated state equations. These equations are used in any simulation referenced as Case B.

$$\frac{di_a}{dt} = \frac{1}{L_a}V_a - \frac{R_a}{L_a}i_a - \frac{K_b}{L_a}N\dot{\theta}_l \tag{C.72}$$

$$\dot{\theta}_l = \frac{d\theta_l}{dt} \tag{C.73}$$

$$\ddot{\theta}_l = \frac{B}{(J_m + J_c)N^2 - A}\dot{\theta}_l^2 + \frac{C}{(J_m + J_c)N^2 - A} + \frac{1}{(J_m + J_c)N^2 - A}T_{ext} + \frac{K_t N}{(J_m + J_c)N^2 - A}i_a + T_{friction} - B_{Total}\dot{\theta}_l \tag{C.74}$$

APPENDIX D

EXPERIMENTAL DATA

D.1 Introduction

The following is the experimental data gathered from the prototype Mechanism. Five trials at varying lengths of time were recorded. θ and current were recorded via the cRIO measurement system. θ could be used to calculated the entire kinematics of the Mechanism. An example of the calculation is shown in the Chapter 5. All physical links and masses are constant for the experiments and are outlined in Chapter 5 in Table 5.1.

D.2 Experimental Data: RRRP to RRRR

The following is the experimental data gathered from the prototype Mechanism for the RRRR to RRRP configuration. Table D.1 parameters are the initial conditions of the third-order polynomial trajectory planner. The notation used in the table is consistent with Section 4.2 for trajectory generation. The trajectory planner are the input set points to the controller. The only parameter changed for each set of experimental trials was the final generated trajectory time (t_f or T_{final} in the figures).

Table D.1: Desired Trajectory Parameters

Description	Value	Units
Desired Starting Angular Position	$\theta_i(0) = 46^\circ$	deg
Desired Ending Angular Position	$\theta_f(t_f) = 179^\circ$	deg
Desired Starting Angular Velocity	$\dot{\theta}_i(0) = 0$	deg/s
Desired Ending Angular Velocity	$\dot{\theta}_f(t_f) = 0$	deg/s

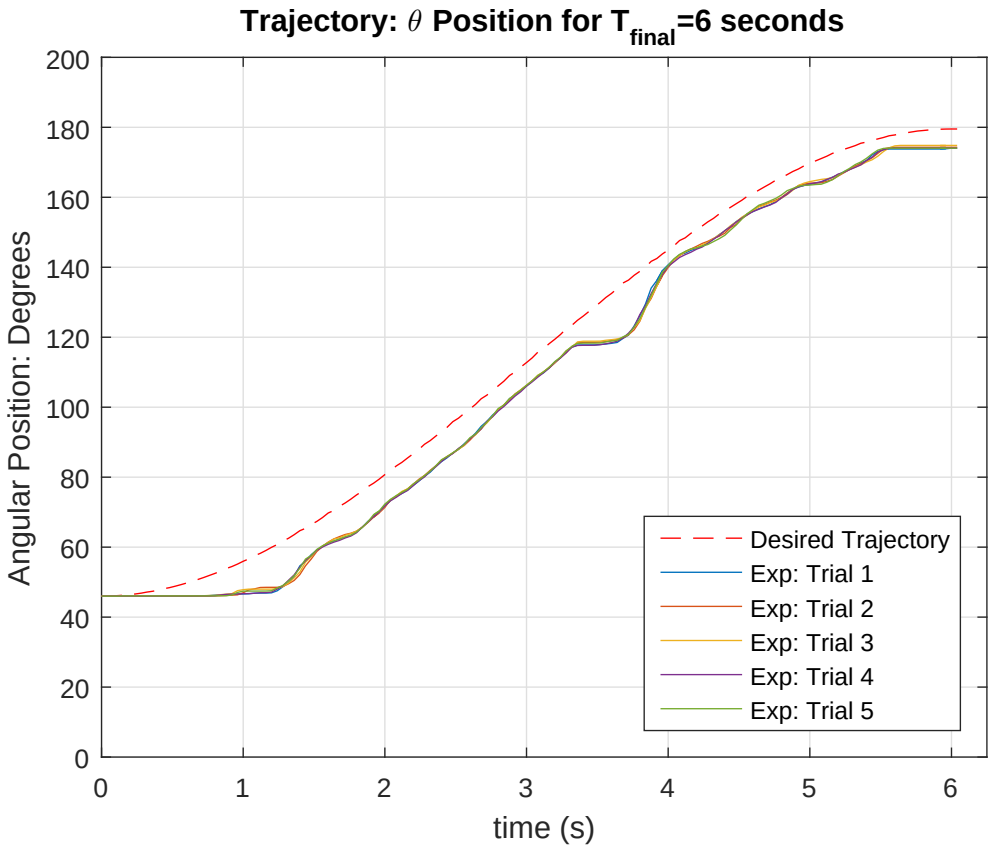

Figure D.1: Experimental RRRP to RRRR- θ measurement, $t_f = 6.0$ seconds

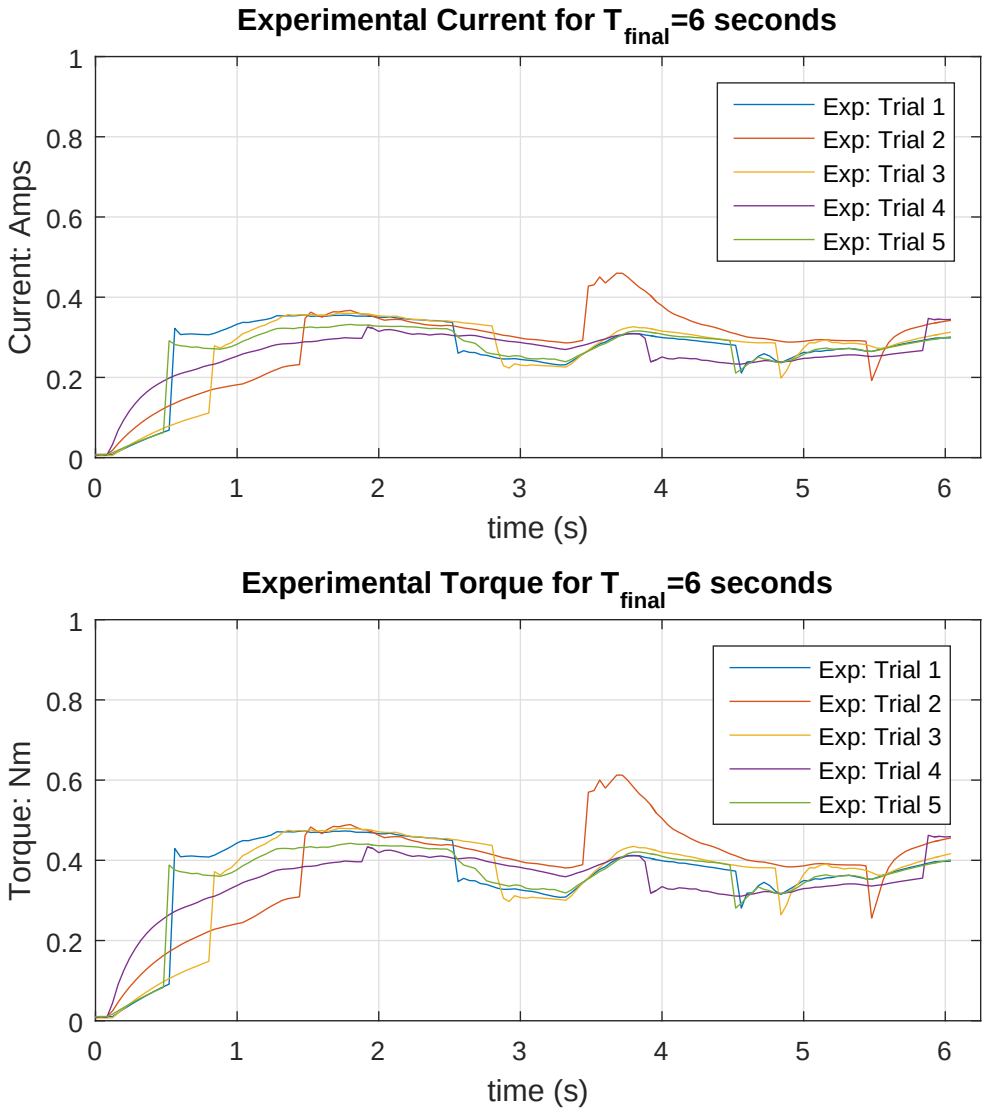

Figure D.2: Experimental RRRP to RRRR- Current and Torque measurement, $t_f = 6.0$ seconds

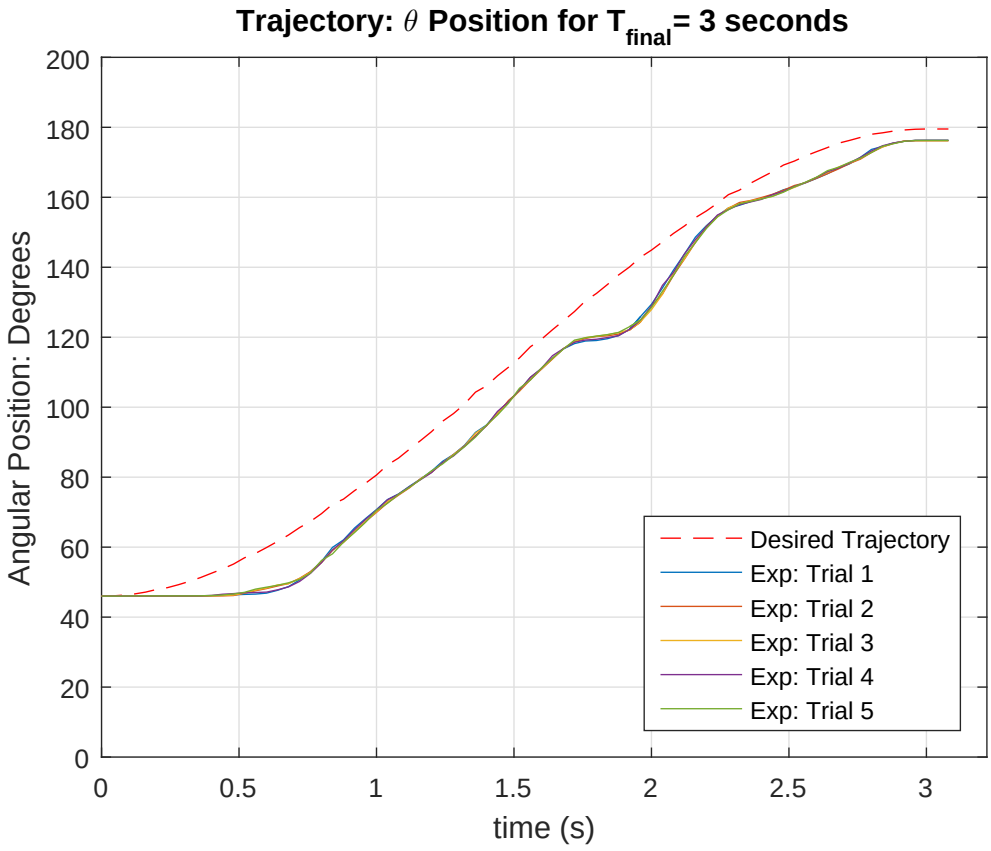

Figure D.3: Experimental RRRP to RRRR- θ measurement, $t_f = 3.0$ seconds

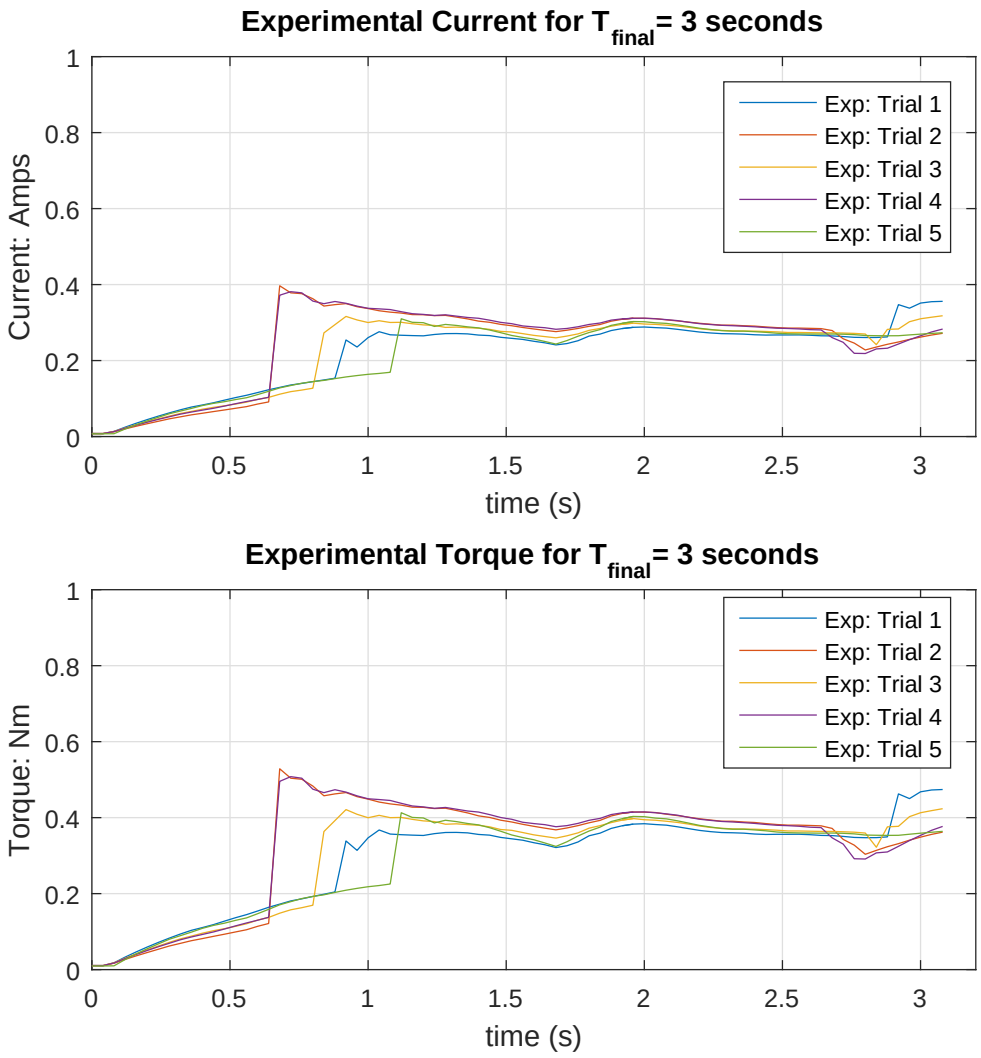

Figure D.4: Experimental RRRP to RRRR- Current and Torque measurement, $t_f = 3.0$ seconds

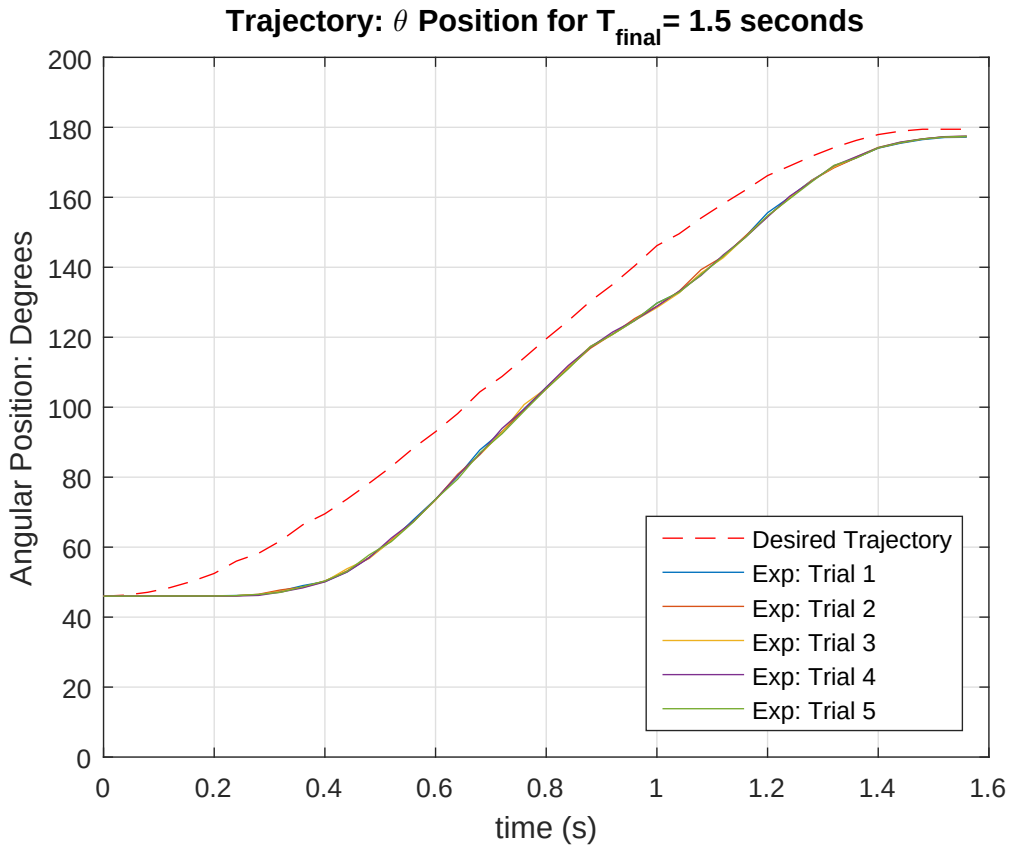

Figure D.5: Experimental RRRP to RRRR- θ measurement, $t_f = 1.5$ seconds

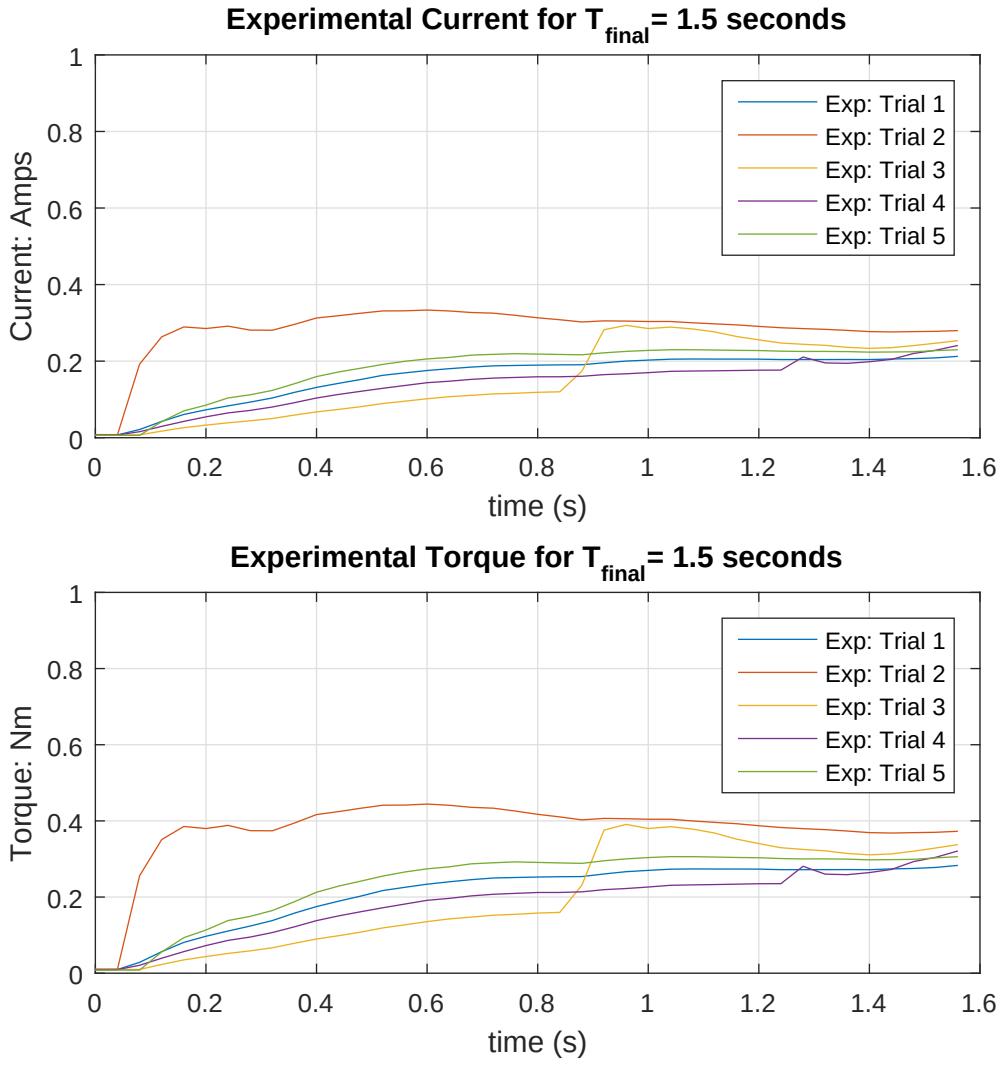

Figure D.6: Experimental RRRP to RRRR- Current and Torque measurement, $t_f = 1.5$ seconds

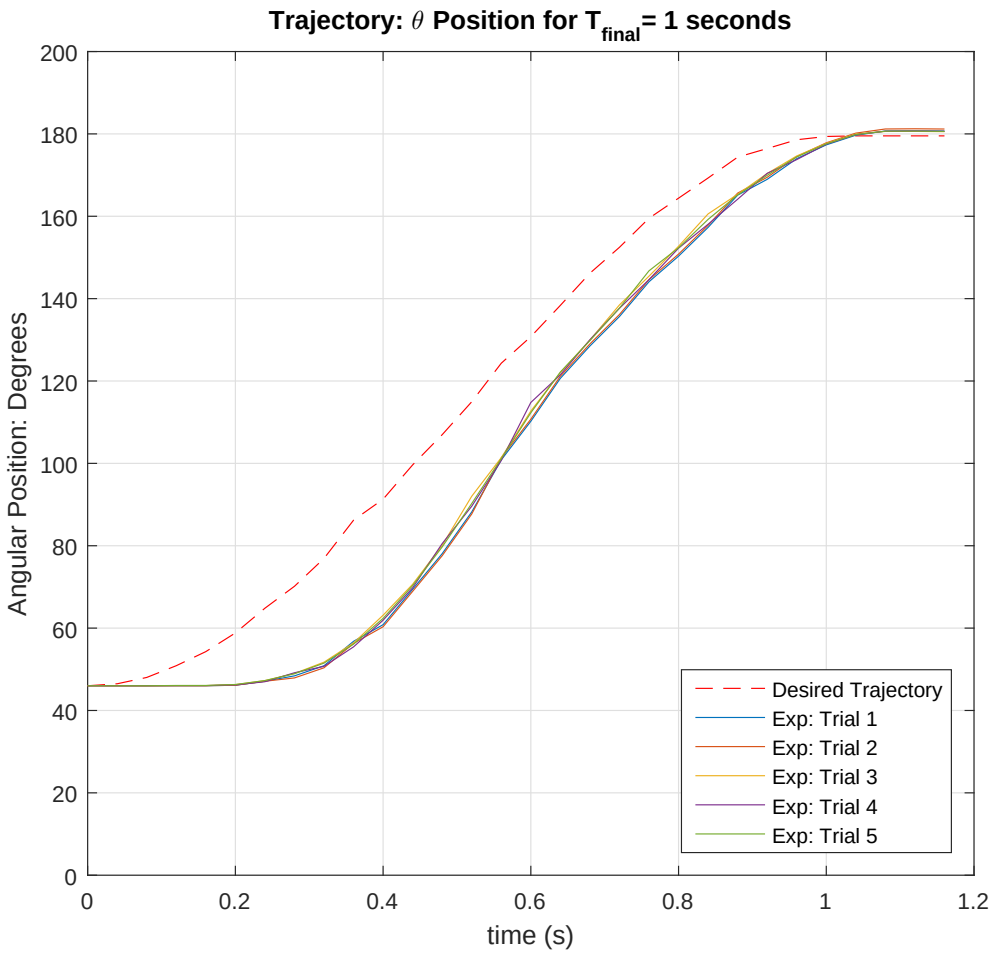

Figure D.7: Experimental RRRP to RRRR- θ measurement, $t_f = 1.0$ seconds

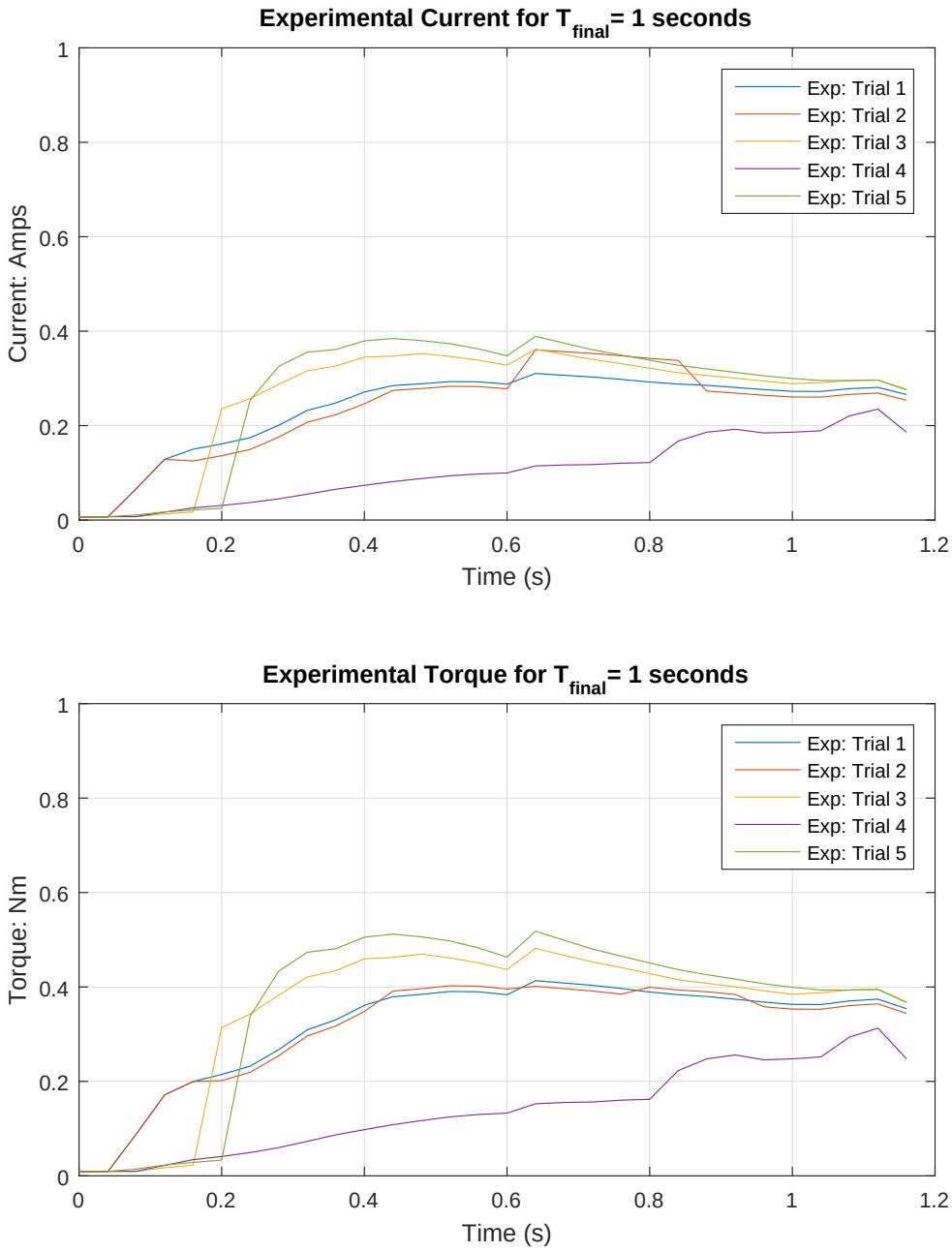

Figure D.8: Experimental RRRP to RRRR- Current and Torque measurement, $t_f = 1.0$ seconds

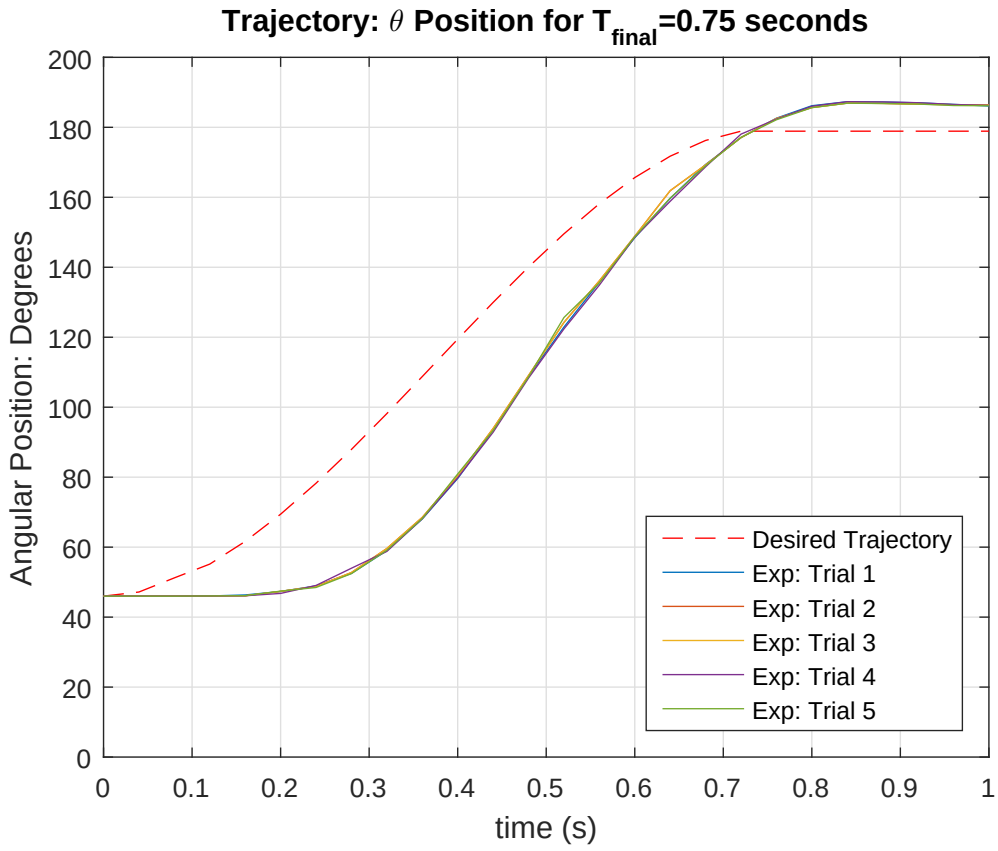

Figure D.9: Experimental RRRP to RRRR- θ measurement, $t_f = 0.75$ seconds

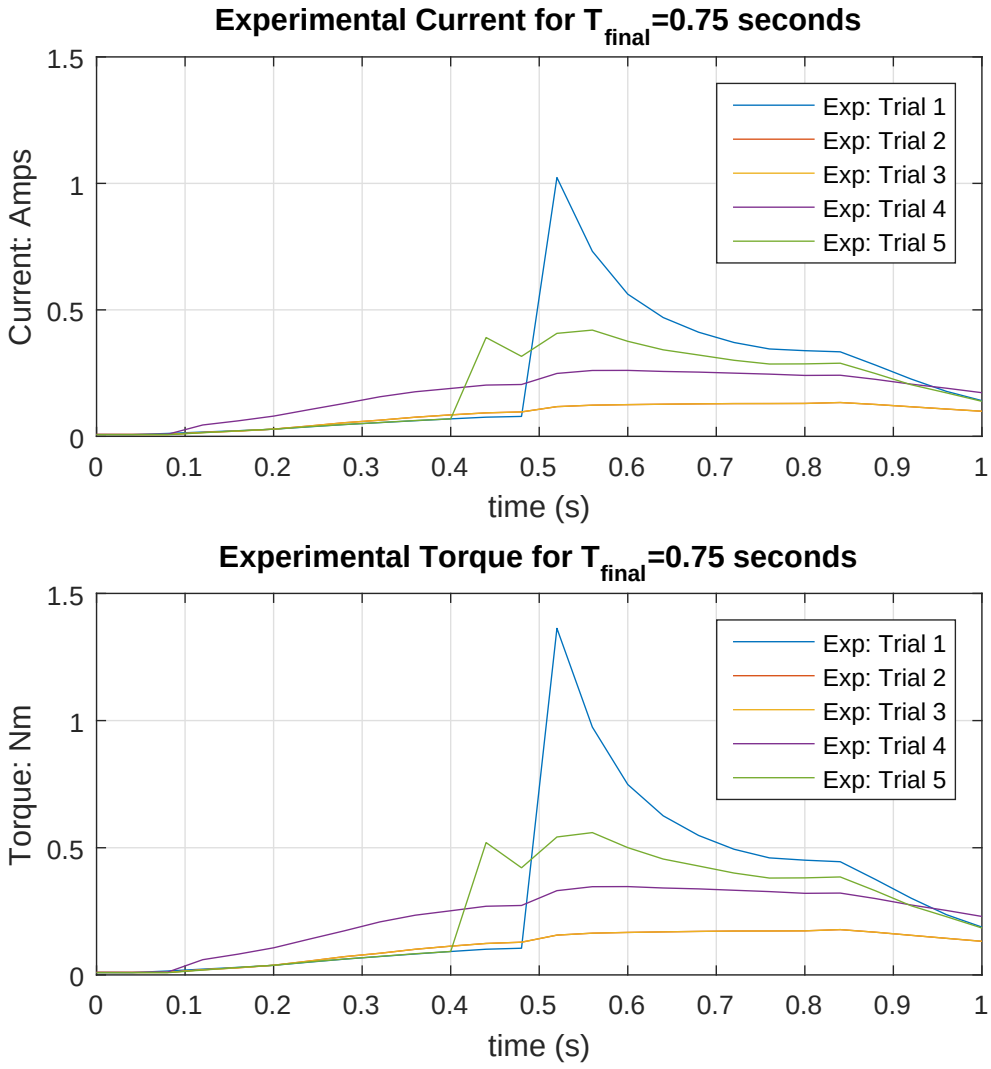

Figure D.10: Experimental RRRP to RRRR- Current and Torque measurement, $t_f = 0.75$ seconds

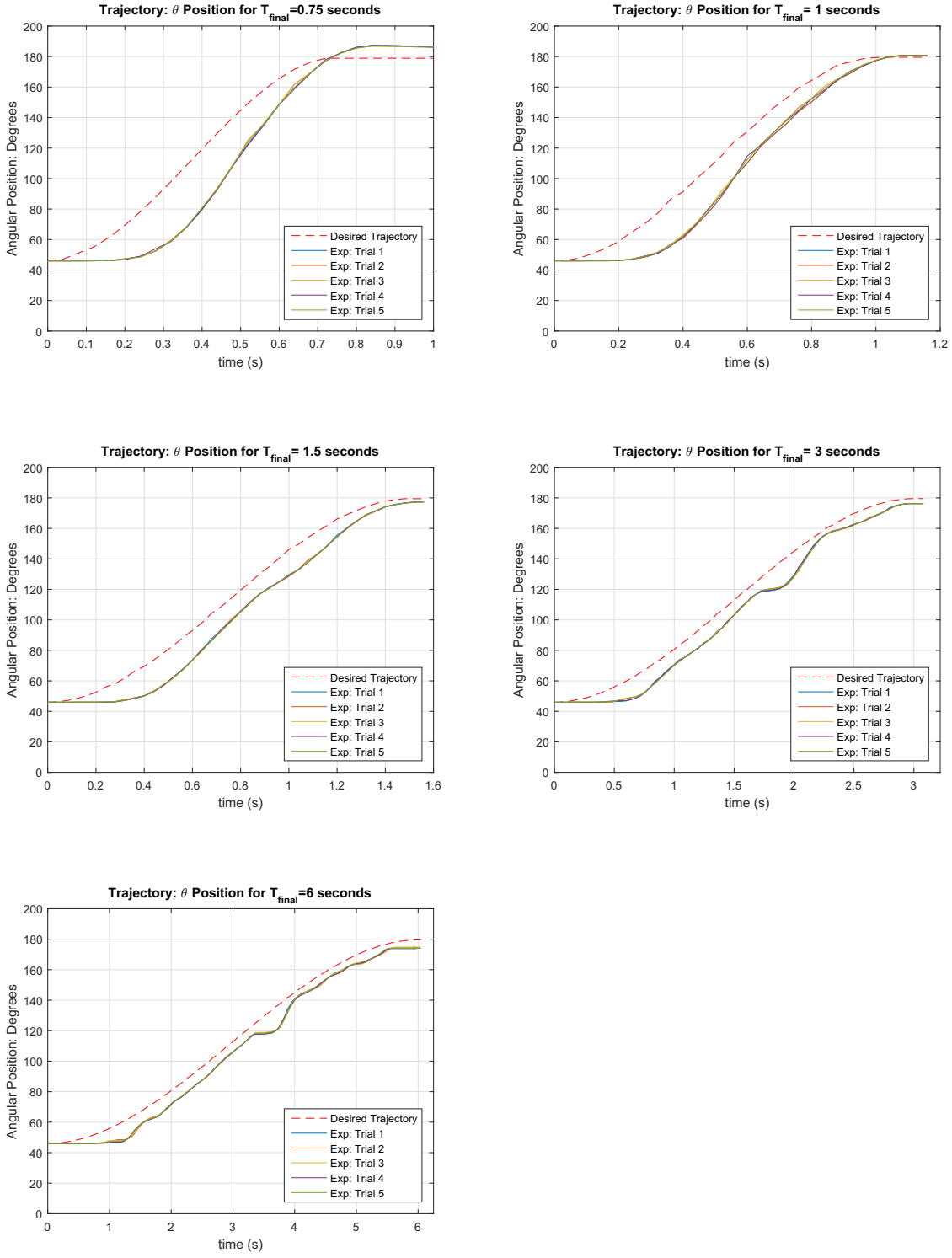

Figure D.11: Experimental RRRP to RRRR- Compiled θ data

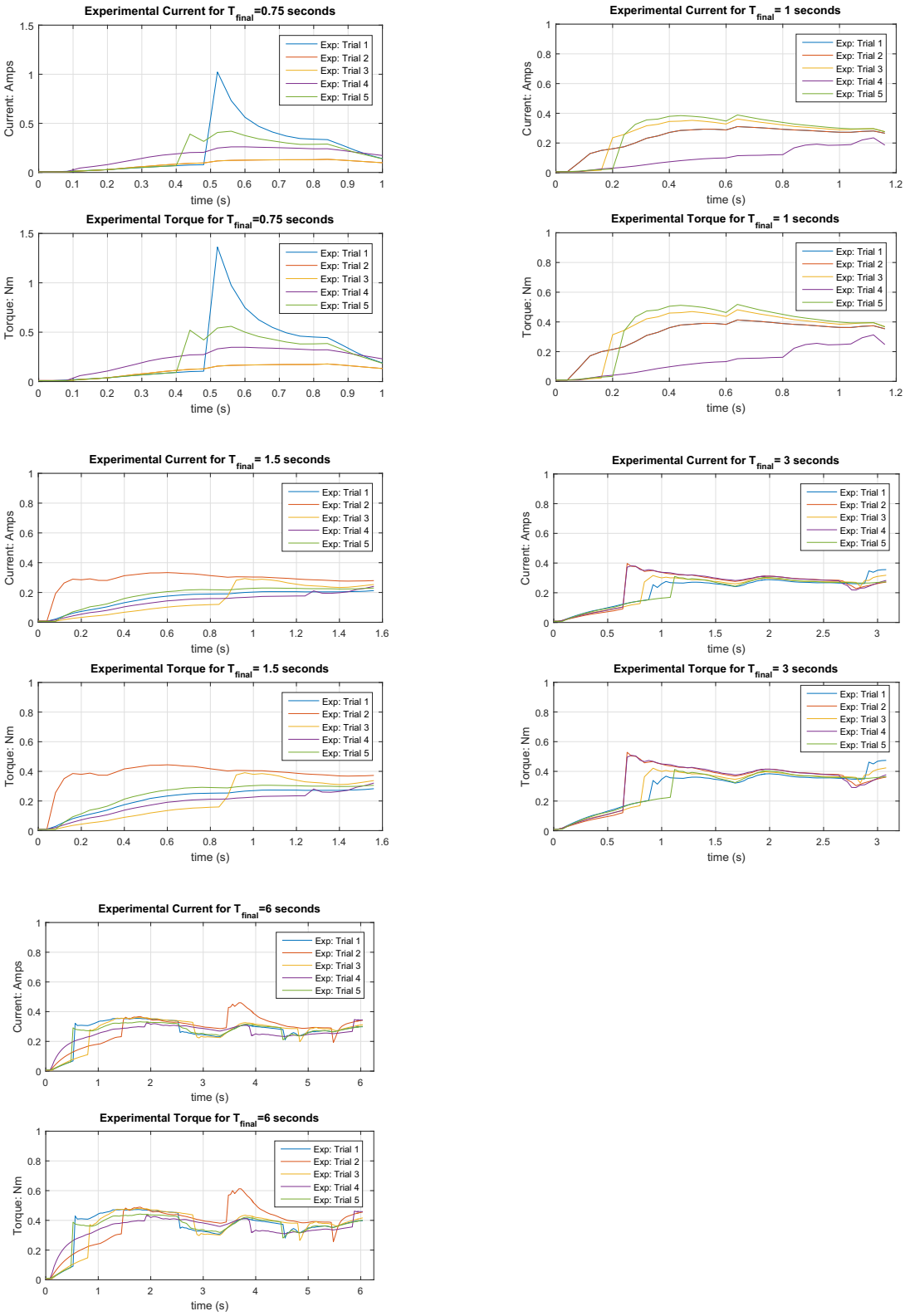

Figure D.12: Experimental RRRP to RRRR- Compiled Current and Torque data

D.3 Experimental Data: RRRR to RRRP

The following is the experimental data gathered from the prototype Mechanism for the RRRR to RRRP configuration. Table D.2 parameters are the initial conditions of the third-order polynomial trajectory planner. The notation used in the table is consistent with Section 4.2 for trajectory generation. The trajectory planner are the input set points to the controller. The only parameter changed for each set of experimental trials was the final generated trajectory time (t_f or T_{final} in the figures).

Table D.2: Desired Trajectory Parameters

Description	Value	Units
Desired Starting Angular Position	$\theta_i(0) = 179^\circ$	deg
Desired Ending Angular Position	$\theta_f(t_f) = 46^\circ$	deg
Desired Starting Angular Velocity	$\dot{\theta}_i(0) = 0$	deg/s
Desired Ending Angular Velocity	$\dot{\theta}_f(t_f) = 0$	deg/s

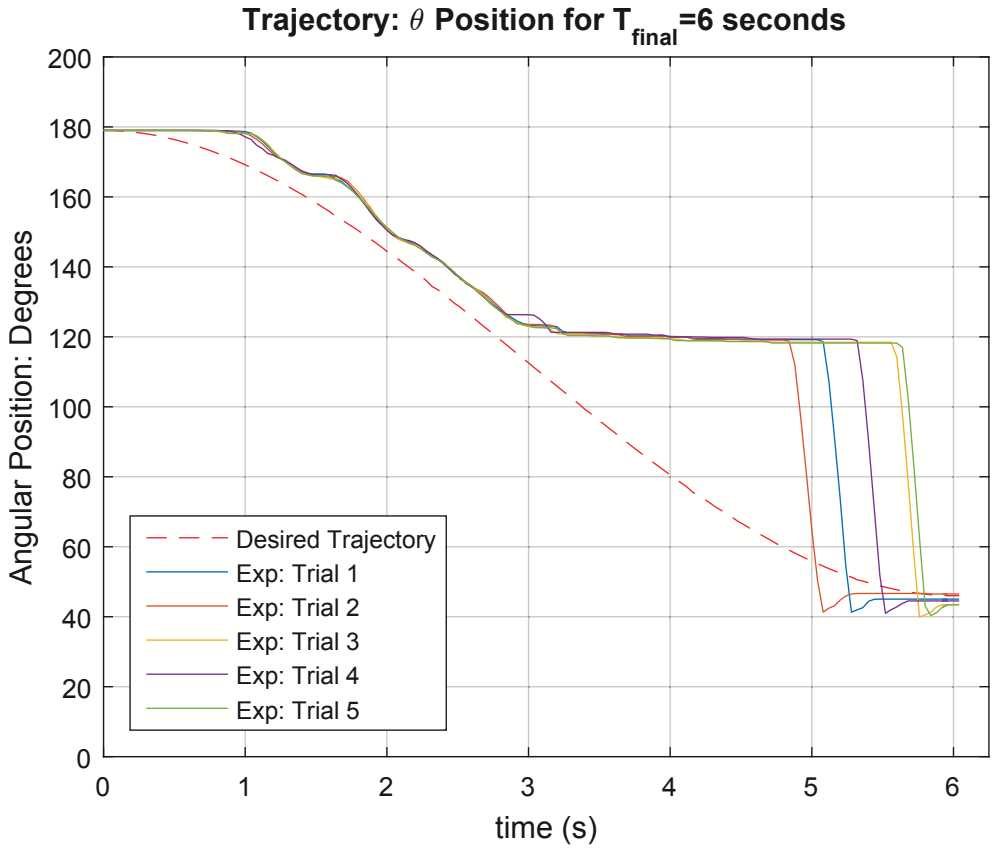

Figure D.13: Experimental RRRR to RRRP- θ measurement, $t_f = 6.0$ seconds

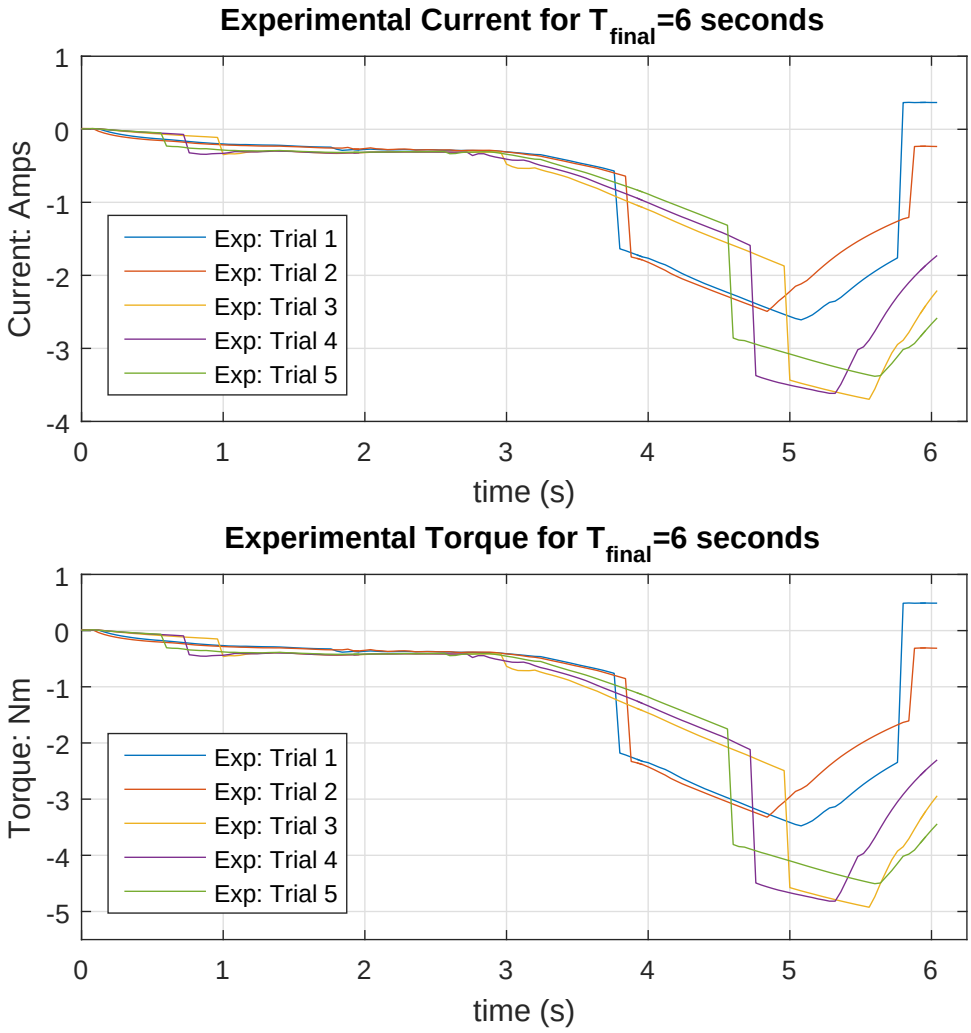

Figure D.14: Experimental RRRR to RRRP- Current and Torque measurement, $t_f = 6.0$ seconds

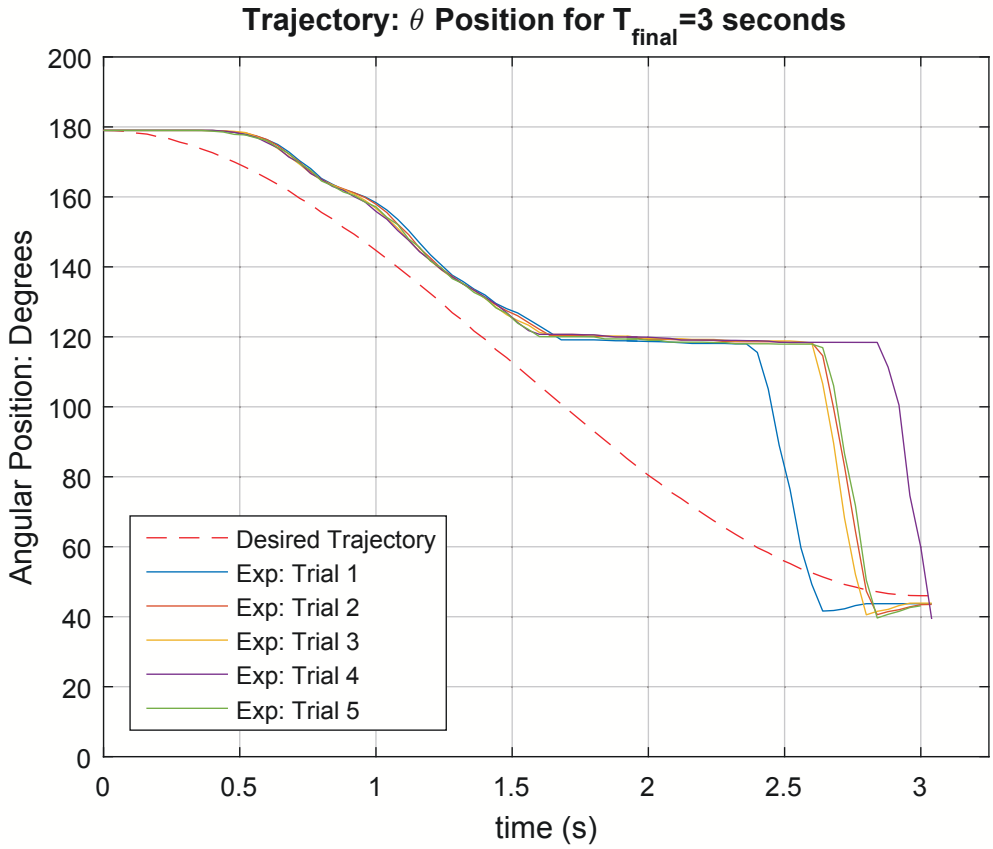

Figure D.15: Experimental RRRR to RRRP- θ measurement, $t_f = 3.0$ seconds

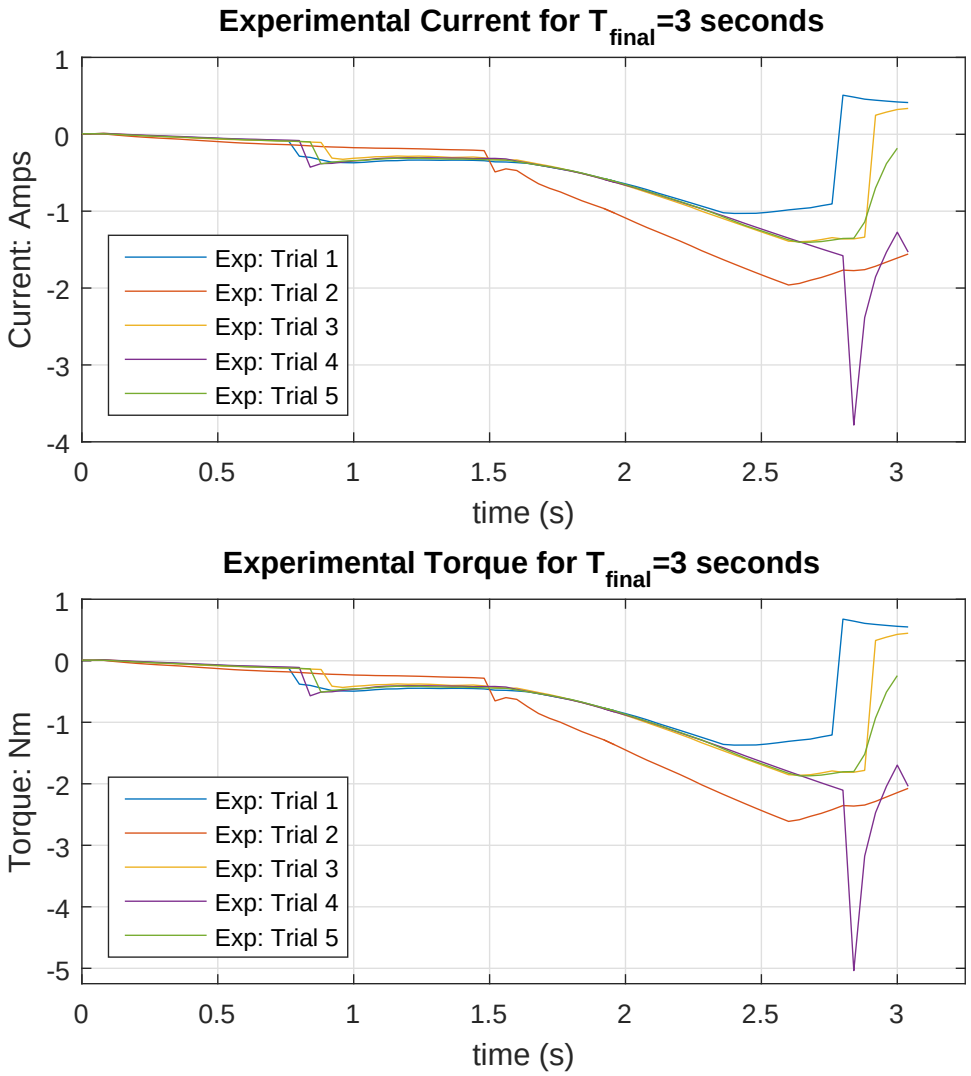

Figure D.16: Experimental RRRR to RRRP- Current and Torque measurement, $t_f = 3.0$ seconds

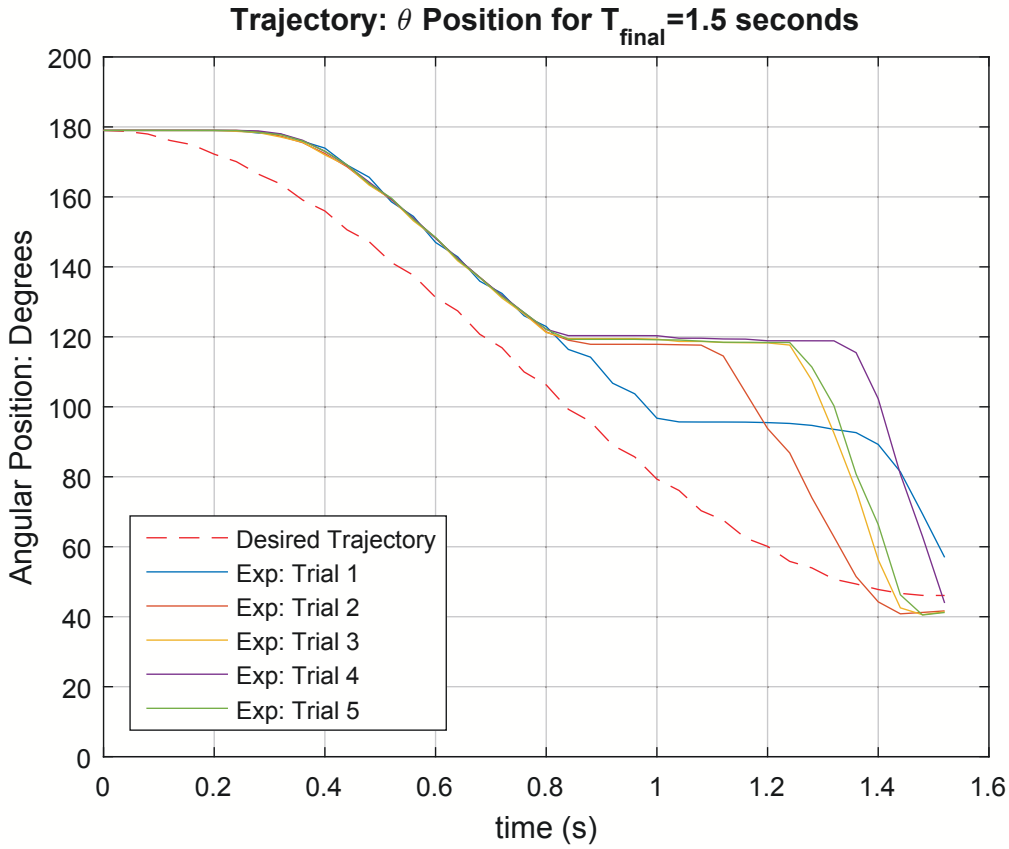

Figure D.17: Experimental RRRR to RRRP- θ measurement, $t_f = 1.5$ seconds

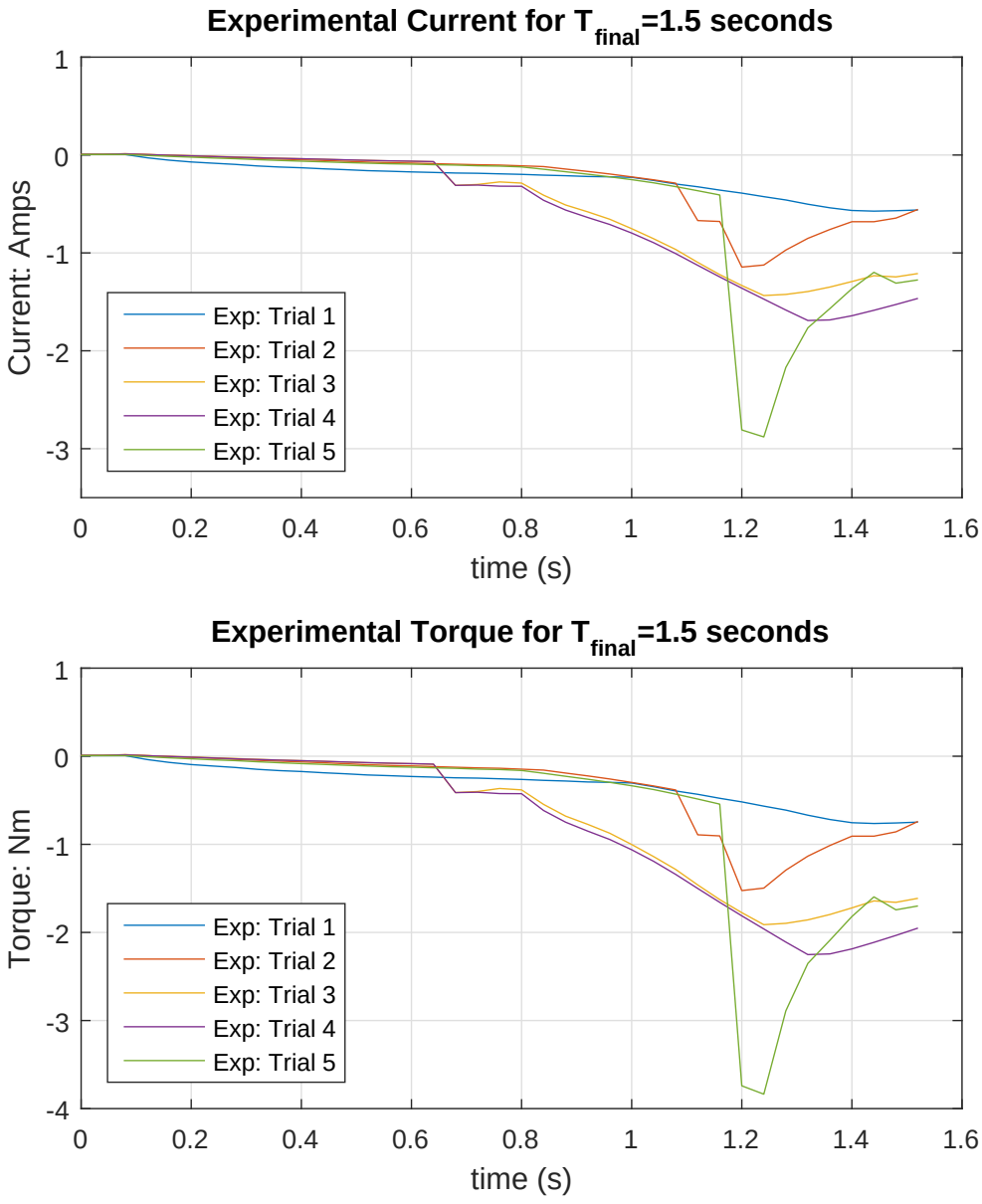

Figure D.18: Experimental RRRR to RRRP- Current and Torque measurement, $t_f = 1.5$ seconds

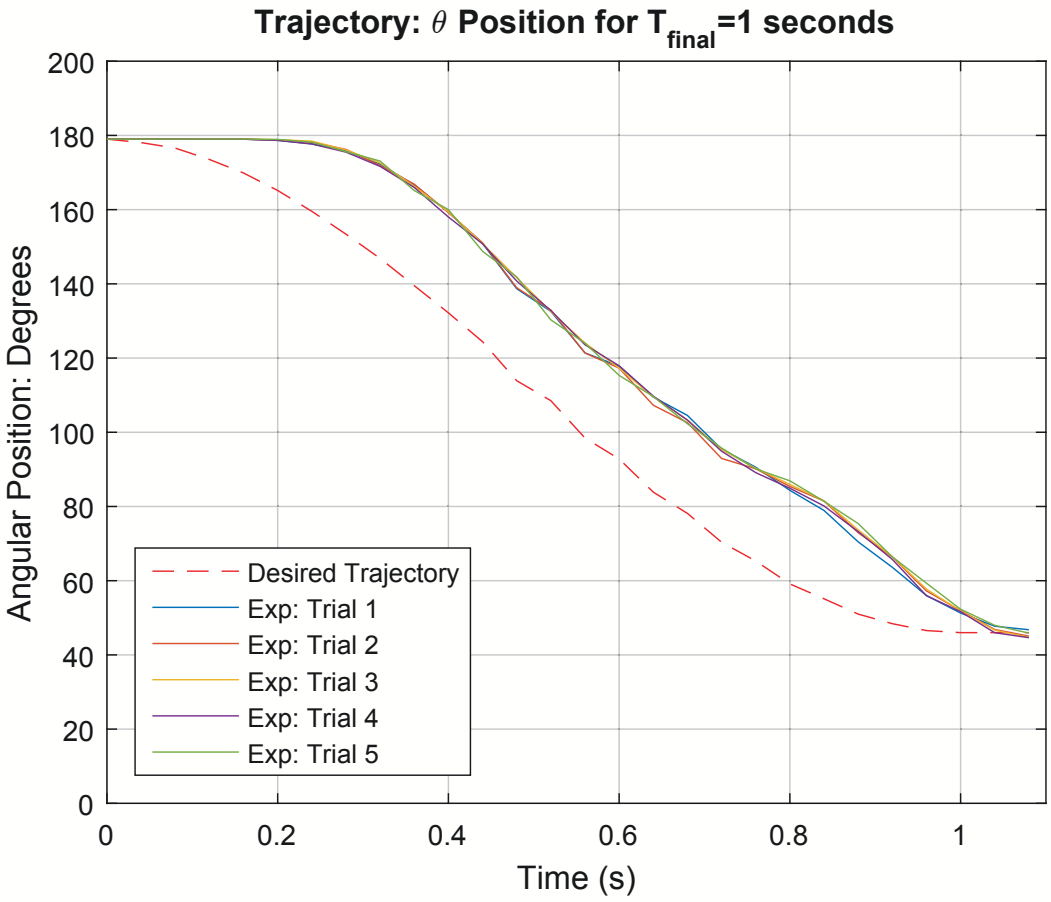

Figure D.19: Experimental RRRR to RRRP- θ measurement, $t_f = 1.0$ seconds

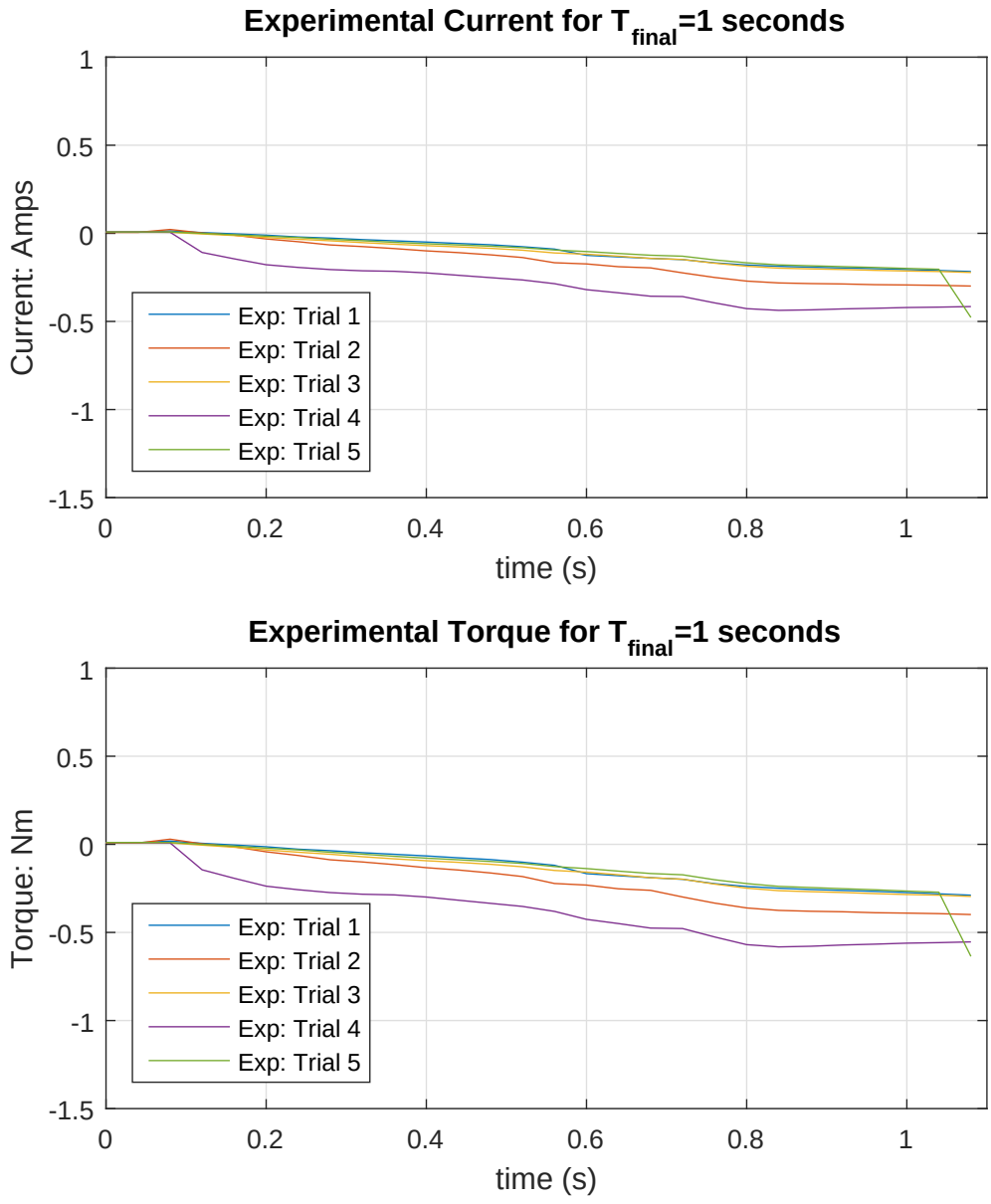

Figure D.20: Experimental RRRR to RRRP- Current and Torque measurement, $t_f = 1.0$ seconds

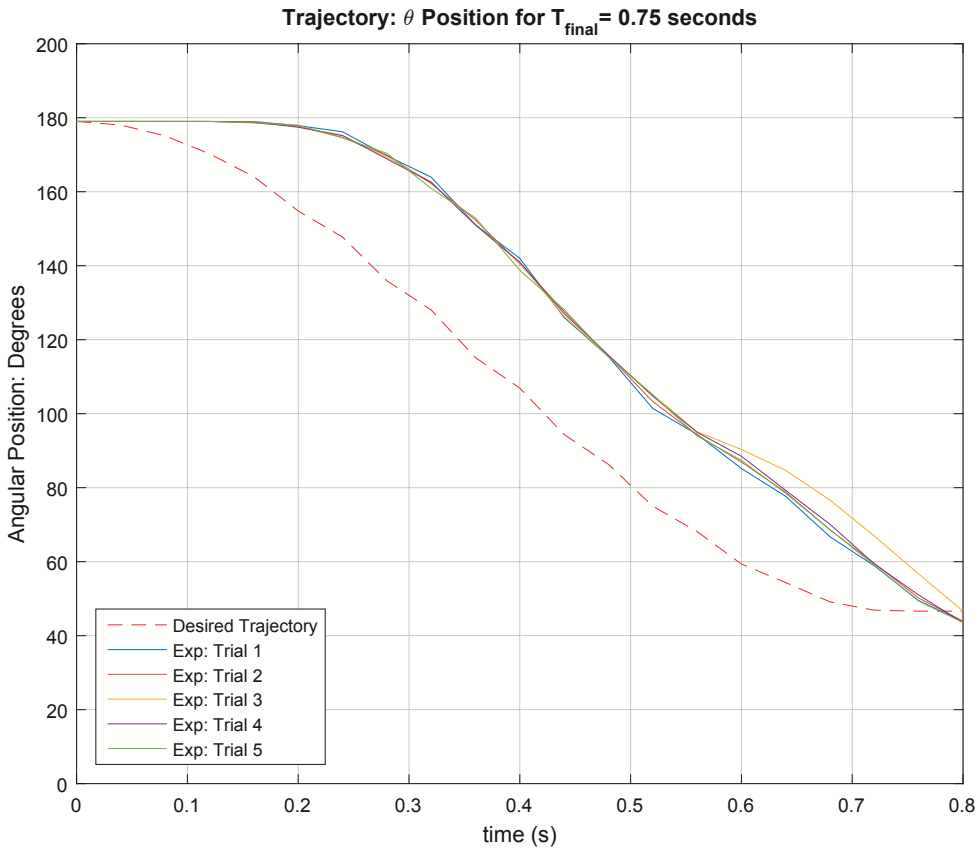

Figure D.21: Experimental RRRR to RRRP- θ measurement, $t_f = 0.75$ seconds

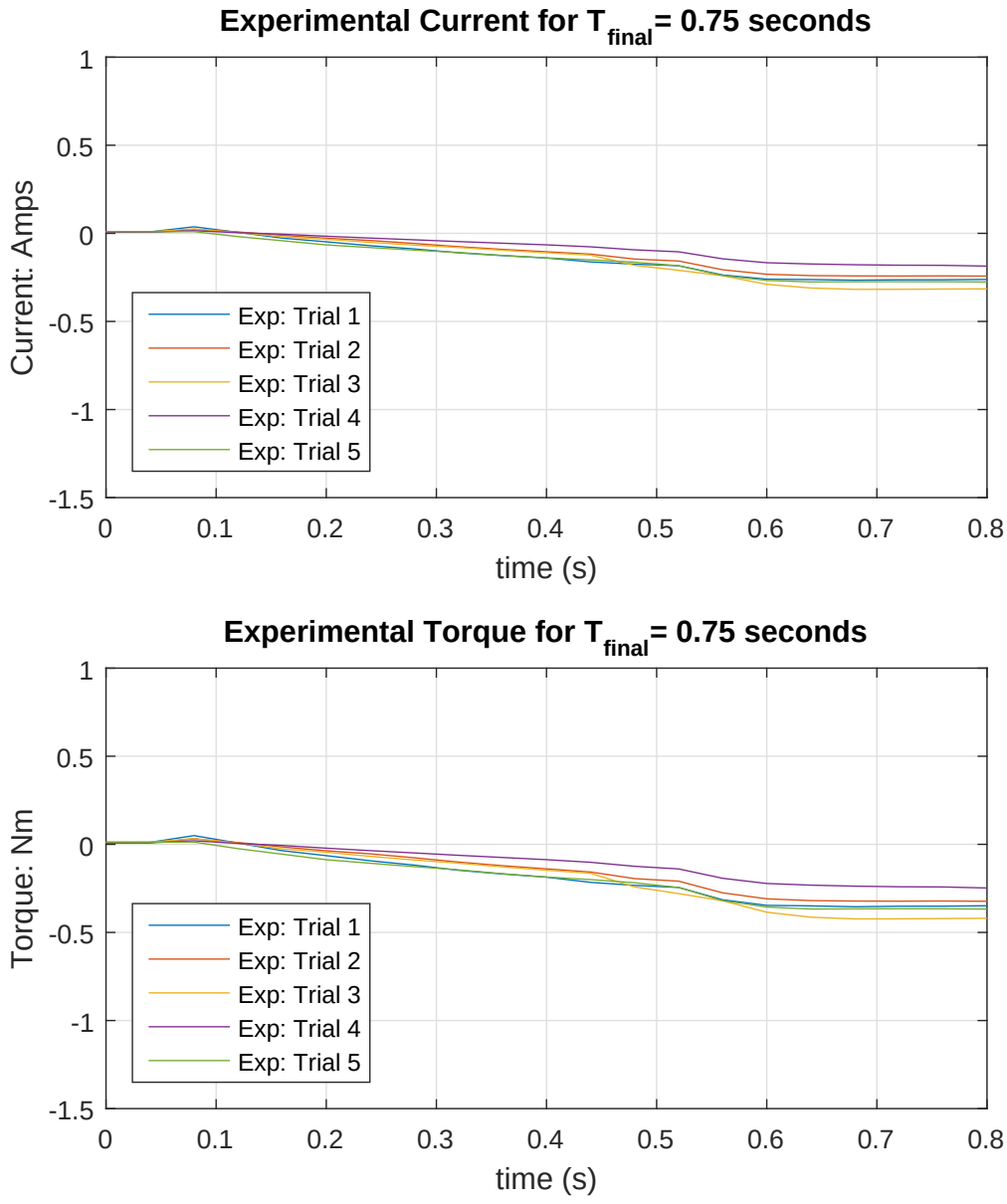

Figure D.22: Experimental RRRR to RRRP- Current and Torque measurement, $t_f = 0.75$ seconds

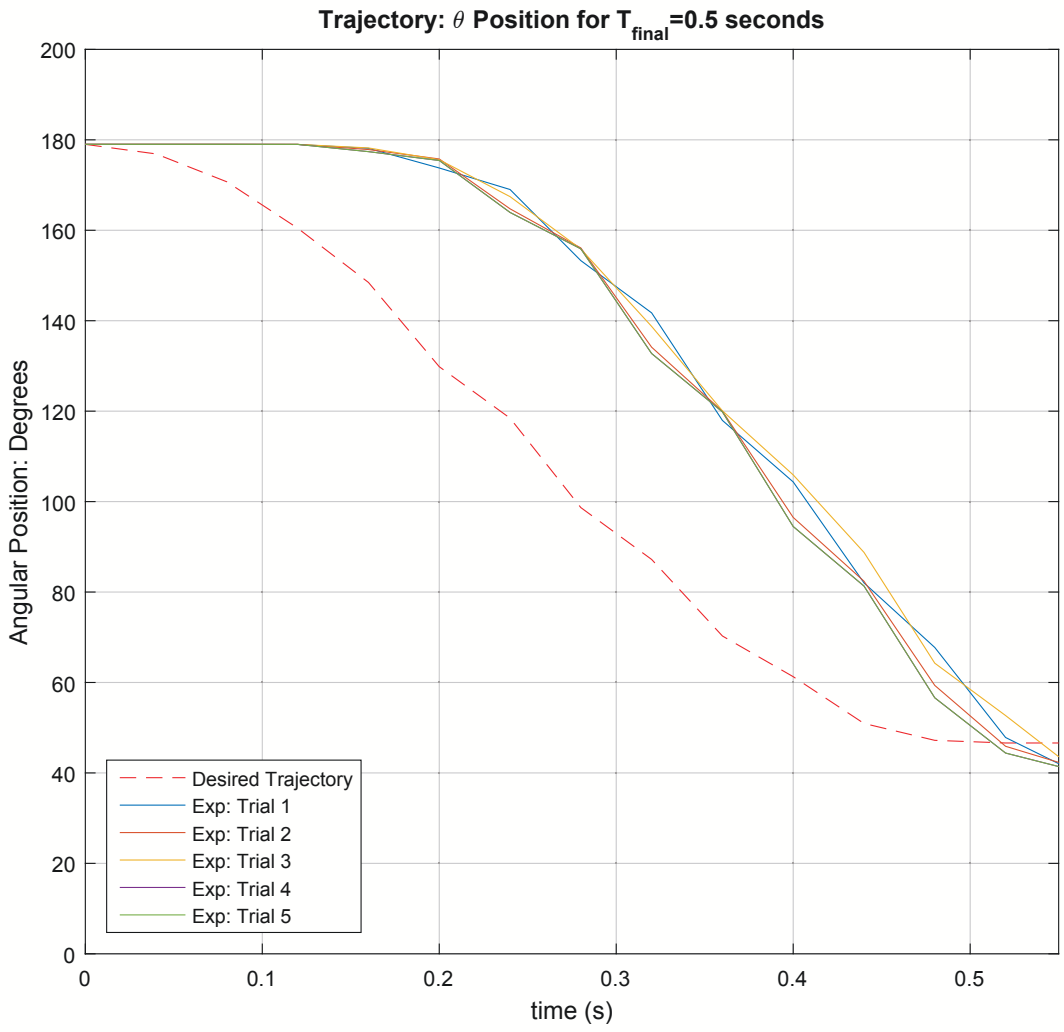

Figure D.23: Experimental RRRR to RRRP- θ measurement, $t_f = 0.5$ seconds

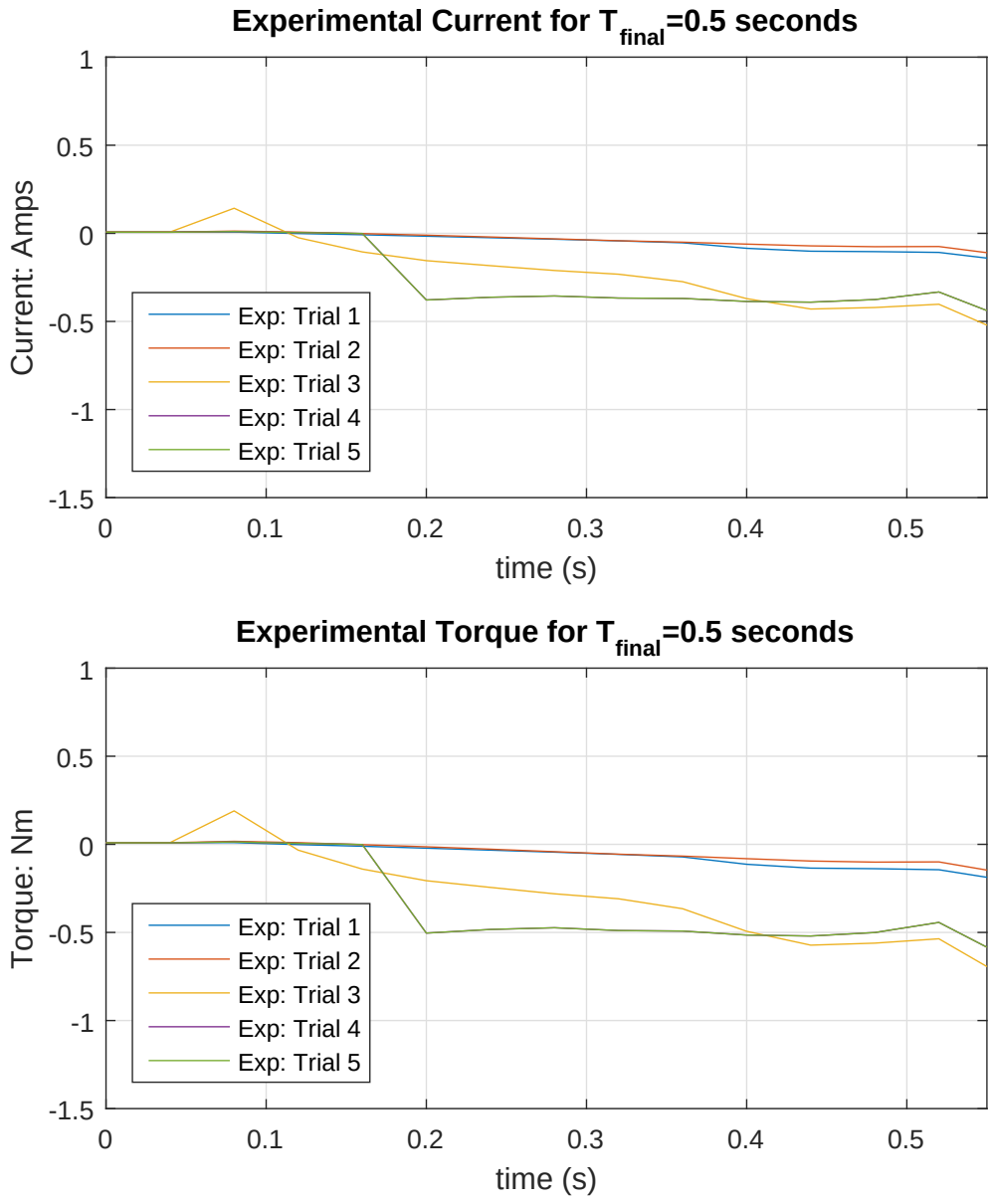

Figure D.24: Experimental RRRR to RRRP- Current and Torque measurement, $t_f = 0.5$ seconds

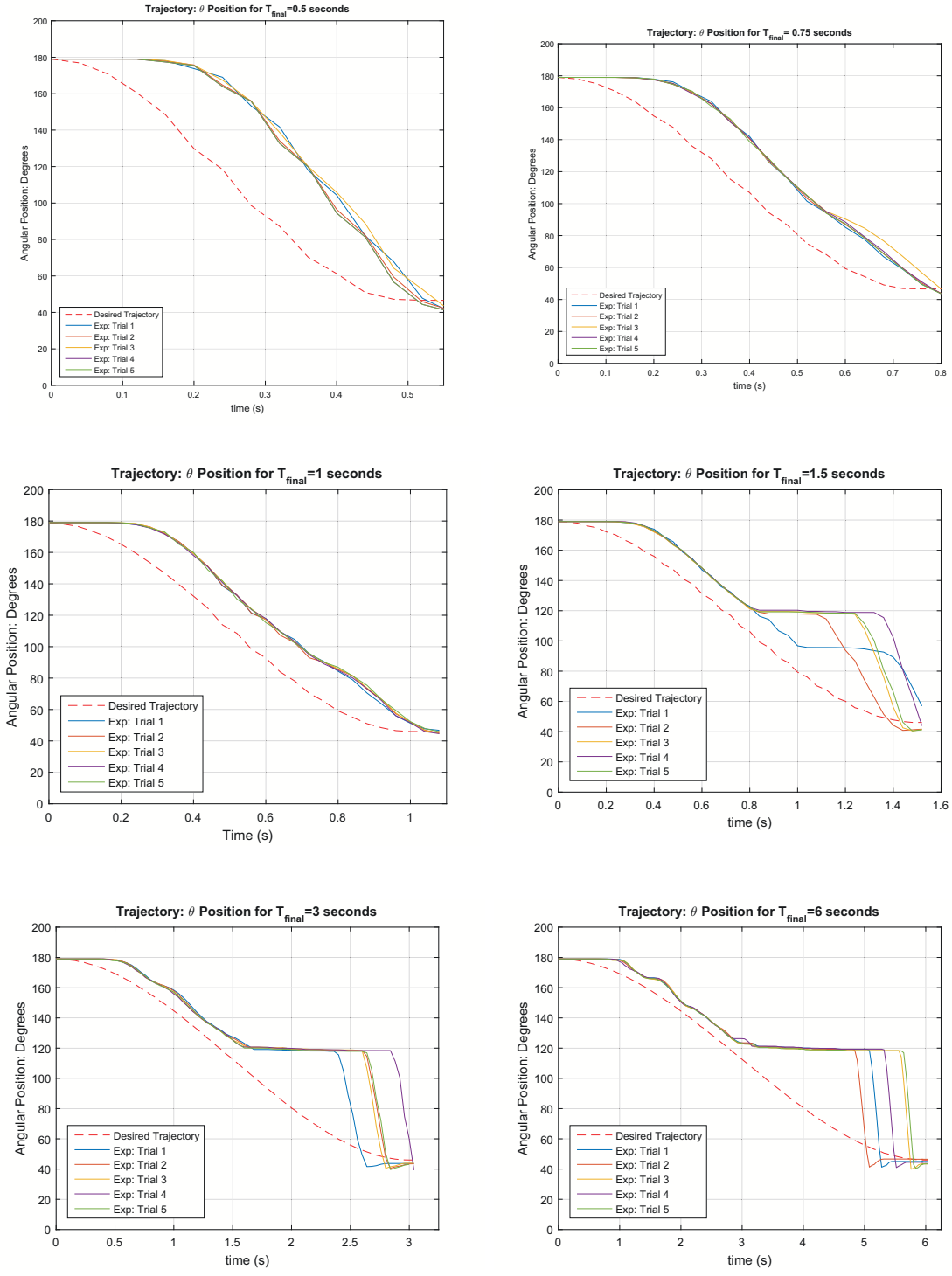

Figure D.25: Experimental RRRR to RRRP- Compiled θ data

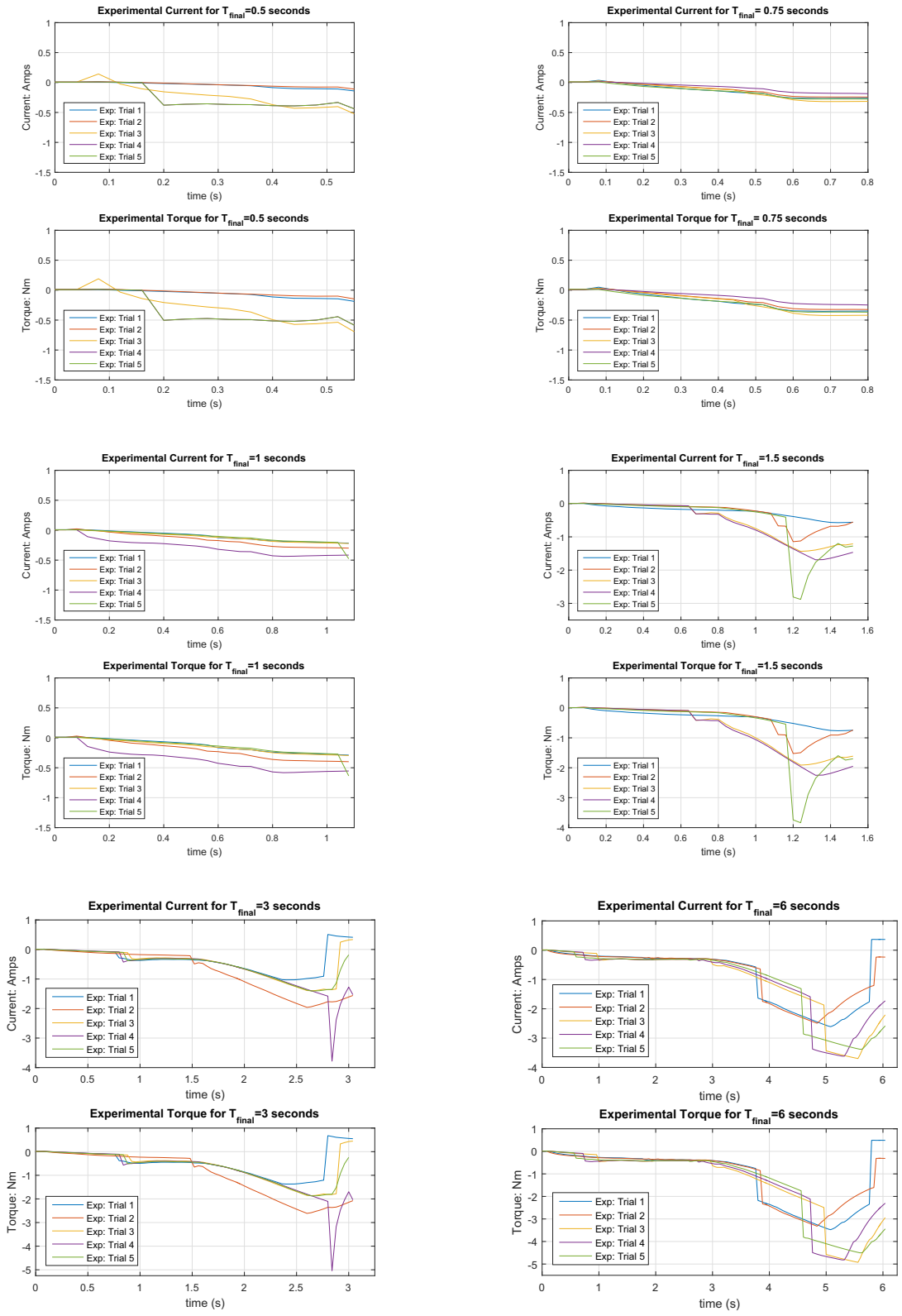

Figure D.26: Experimental RRRR to RRRP- Compiled Current and Torque data

D.4 Mechanism Prototype Pictures

The following are additional pictures of the manufactured prototype of the Mechanism.

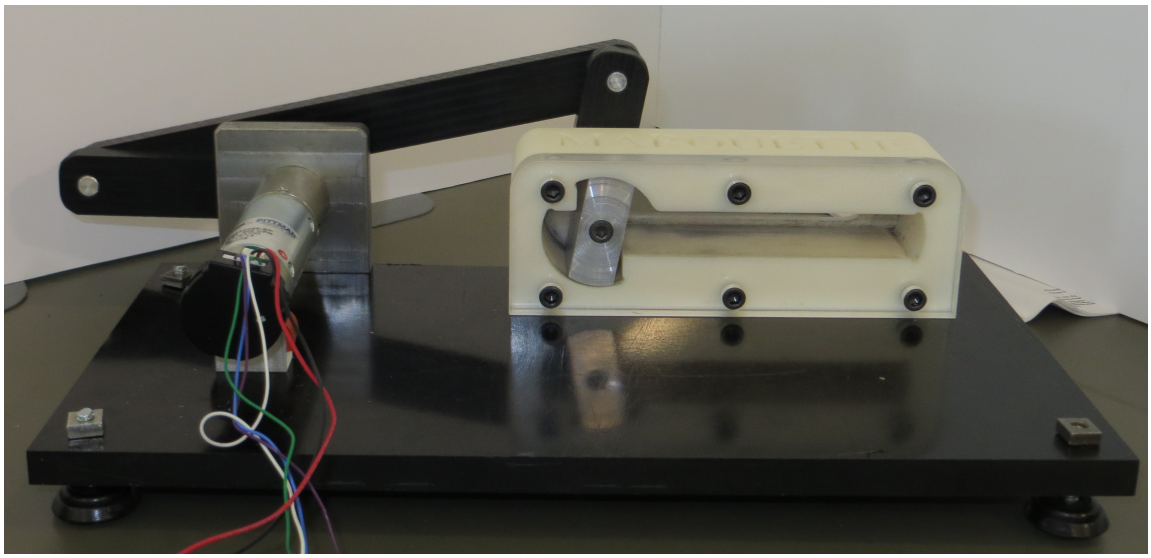

Figure D.27: Prototyped Mechanism

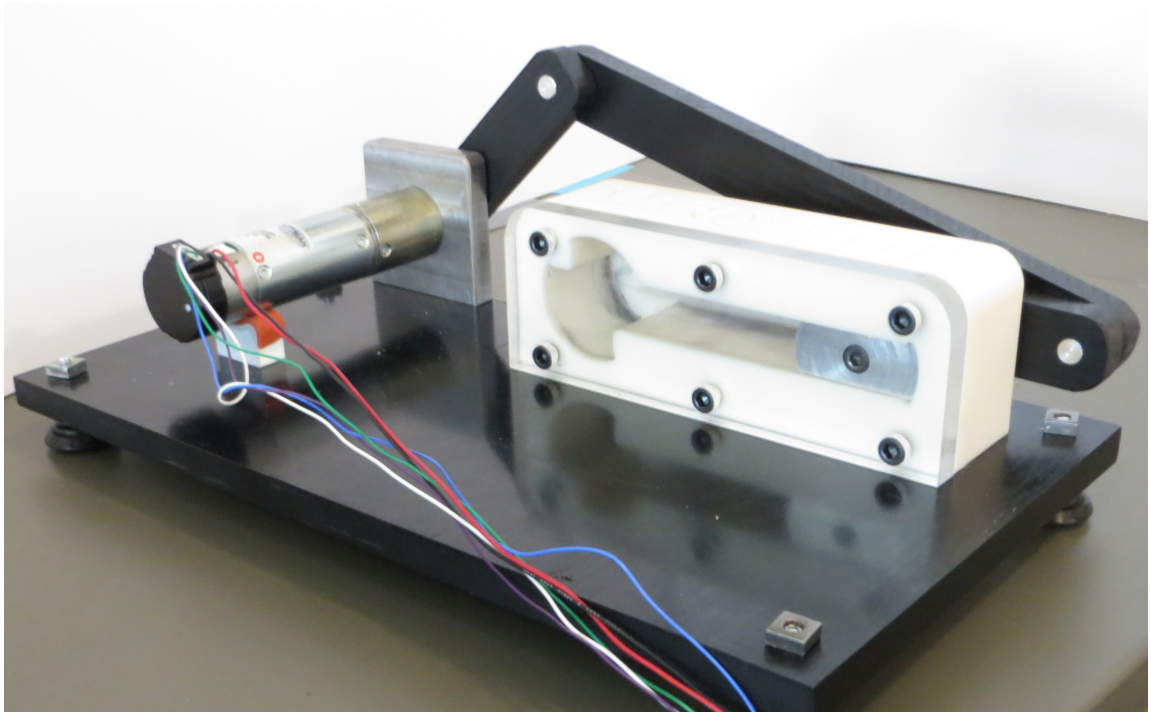

Figure D.28: Prototyped Mechanism

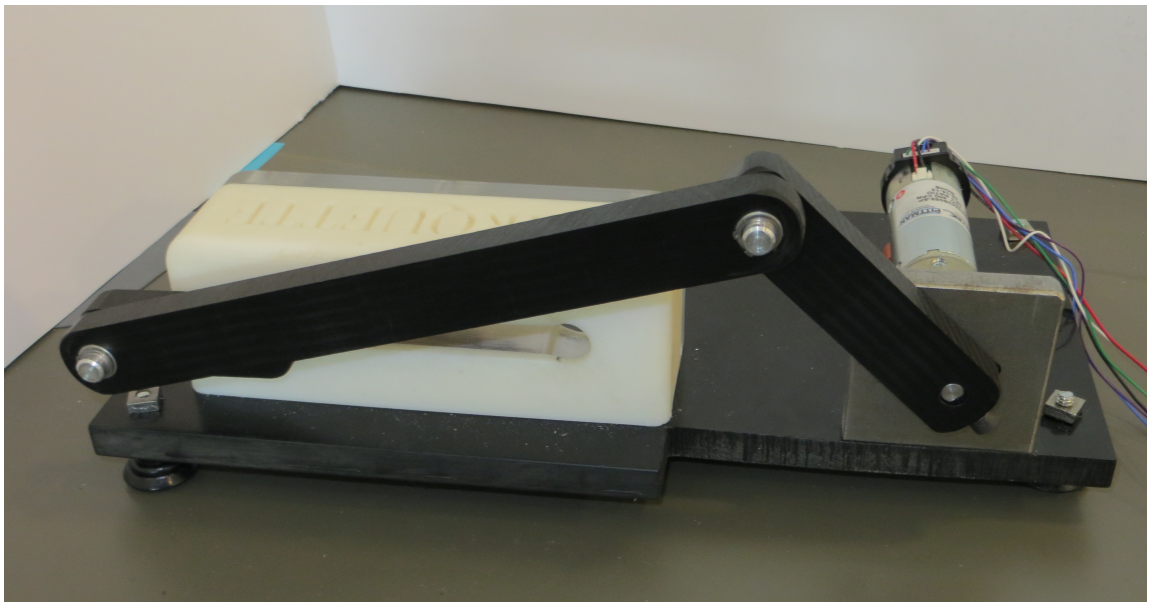

Figure D.29: Prototyped Mechanism

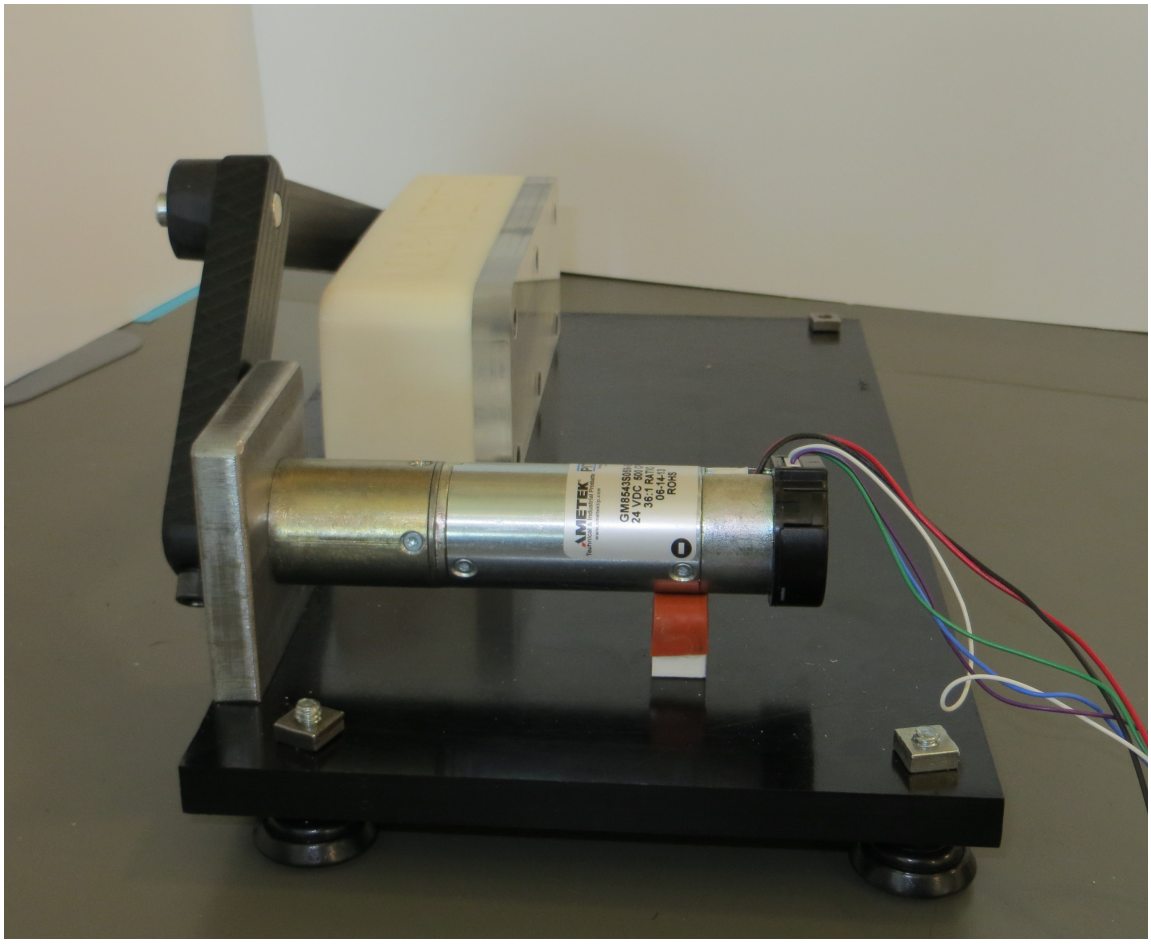

Figure D.30: Prototyped Mechanism